

**Particle size and morphology dependent magnetic  
properties of rare-earth manganites with potential  
multiferroic property**

**Thesis Submitted to AcSIR  
For the Award of the Degree of  
DOCTOR OF PHILOSOPHY  
In Chemical Sciences**



**By**  
Raja Das  
Registration Number: 10CC12J26025

**Under the guidance of**  
Dr. Pankaj Poddar  
Physical and Materials Chemistry Division  
CSIR-National Chemical Laboratory  
Dr. Homi Bhabha Road  
Pune 411008

*Dedicated to almighty God and  
my teachers*

# DECLARATION

I hereby declare that the work described in this thesis entitled “**Particle size and morphology dependent magnetic properties of rare-earth manganites with potential multiferroic property**” submitted for the degree of *Doctor of Philosophy in Chemical Sciences* has been carried out by me at the Physical and Materials Chemistry Division of the CSIR-National Chemical Laboratory, Pune, India under the supervision of Dr. Pankaj Poddar. Such materials as have been obtained by other sources have been duly acknowledged in this thesis. The work is original and has not been submitted in part or full by me for award of any other degree or diploma in any other University.

Date:

Place: Pune

**Raja Das**

(Research Student)

## *Acknowledgements*

---

*There are a great many people whom I would like to thank for their contributions and for the support they have provided me over the years which helped and supported me in preparing this thesis.*

*Dr. Pankaj Poddar, my supervisor has been very supportive since the day I joined CSIR-NCL, Pune. His valuable suggestions and fruitful discussions made significant contribution to make this thesis feasible. I would like to thank him for providing me the opportunity to work in various fields other than my Ph. D. area.*

*I also thank Mrs. Suguna Adhayantaya for her encouragements, valuable suggestions and helps in lab related matters. I would like to thank our collaborators Dr. Rahul Banerjee, Prof. S. K. Kulkarni, Prof. P. K. Bharadwaj, Dr. Sujit Ghosh for their help and believe in me.*

*I would also like to thank Dr. S. Pal, Director, CSIR-NCL and Dr. Anil Kumar, HoD, Physical & Materials Chemistry Division, for allowing me to carry out research at this Institute and providing with the required facilities. I am thankful to CSIR, DST, DRDO, India for the funding.*

*I must mention the good people that worked beside me in Lab No. 221, 236 over the years, my thanks for your great help and good times. I thank senior lab mates Umesh, Ramya, Imran, Adhish, Vivek, Neeraj, Lalita, Monalisha for their time, help and meaningful discussions. My fellow lab mates over the years Priya, Tuhin, Chandrashekhar, Shubha, Shubhdip, Guptaji, Mousumi, Padhye, Puneet, Anupam, Samir deserve the greatest thank*



*mainly for just putting up with me. I have enjoyed working with Adhish Jaiswal (who taught me how to remain calm in tense situation), Mousumi Sen (smart researcher), Anupam Biswas (good observer, always have an question on my opinion), Samir Sheikh (silent thinker).*

*I am extremely thankful to Mousumi, Preeti Gupta, Padhye and Puneet who took out time in order to help me with my thesis corrections.*

*I am very grateful for the good friends I made during my stay at CSIR-NCL. I thank Chandan, Manju (room-mates), Shuklaji, Pankajda, Mangesh, Khaja, Govind for their wonderful company. I would also like to thank my collaborators and friends Pradeep, Chandan, Tamos, Sanjog, Mukta, Rohini Mam, Mandar, Musheer, Bhaskar, Amey, Smita. I would like to thank my seniors and friends Thakuriada, Hemenda, Ajitda, Pankajda, Pranjaldada, Dipankardada, Nilutpalada, Bhaskar, Deepti with whom I have spend my lonely holidays.*

*I would like to thank my family for all their love and support and especially my parents who didn't really understood what I was doing but encouraged me anyway without asking any questions. I would like to thank my brothers (Tutan and Litu), didi, jamaibabu for their constant support during my Ph.D..*

*I would like to express my deepest gratitude to all my teachers for their blessings.*

---

*... Raja Das*

# Table of contents

---

Abstract	
List of abbreviations	i-ii
List of figures	I-X
List of tables	XI
<b>Chapter 1. Introduction</b>	<b>1-29</b>
1.1 Perovskite	2
1.2 Ferroelectricity	3
1.3 Ferromagnetism	4
1.4 Antiferromagnetism	4
1.5 Chemistry between ferroelectric and ferromagnetic ordering	5
1.6 Multiferroism	6
1.6.1 Types of multiferroics	7
1.6.1.1 Type-I multiferroics	8
1.6.1.11 Independent magnetic and ferroelectric system	8
1.6.1.12 Role of lone pairs	9
1.6.1.13 Ferroelectricity due to charge ordering	9
1.6.1.14 Geometric ferroelectricity	10
1.6.1.2 Type-II multiferroics	11
1.6.1.21 Ferroelectricity due to magnetic ordering	11
1.6.1.22 Exchange striction mechanism	14
1.7 Magnetoelectric effect	15
1.8 Why rare-earth manganites?	16
1.9 Rare-earth manganites	16
1.9.1 Why there is no Jahn-Teller distortion in hexagonal manganites	18
1.9.2 Structural change from orthorhombic to hexagonal with decreasing ionic radius of rare-earth ions	18

1.9.3 Phase diagram of $\text{RMnO}_3$	19
1.9.4 Properties of hexagonal manganites	20
1.9.5 Properties of orthorhombic manganites	21
1.10 Applications	22
1.11 Synthesis of nano crystalline rare-earth manganites	22
1.12 References	26
<b>Chapter 2. Characterization techniques</b>	<b>30-43</b>
2.1 Methods of synthesis	31
2.1.1 Hydrothermal synthesis	31
2.1.2 Solid-state synthesis	33
2.2 Characterization and measurement techniques	33
2.2.1 Powder X-ray diffraction (PXRD)	33
2.2.2 Transmission electron microscopy (TEM)	34
2.2.3 Scanning electron microscopy (SEM)	35
2.2.4 X-ray photoelectron spectroscopy (XPS)	36
2.2.5 Raman spectroscopy	37
2.2.6 UV-vis spectroscopy	38
2.2.7 Vibrating sample magnetometer (VSM)	39
2.2.8 AC Measurement System (ACMS)	40
2.2.9 Impedance spectroscopy	40
2.3 References	42

<b>Chapter 3. Hexagonal rare-earth manganites (RMnO<sub>3</sub>)</b>	<b>44-102</b>
<b>Section 3.1: R<sup>+3</sup> and Mn<sup>+3</sup> spin interaction: Er/YMnO<sub>3</sub></b>	<b>45-59</b>
3.1.1 Introduction	46
3.1.2 Synthesis	47
3.1.3 Structure and morphology	48
3.1.4 Magnetic study	50
3.1.5 Dielectric spectroscopy	57
3.1.6 Conclusion	58
<b>Section 3.2: Ionic chemistry and morphology dependent magnetic properties: YbMnO<sub>3</sub></b>	<b>60-80</b>
3.2.1. Introduction	61
3.2.2 Chemicals	63
3.2.3 Synthesis of YbMnO <sub>3</sub> nanorods	63
3.2.4 Structure and morphology	64
3.2.5 Magnetic properties of YbMnO <sub>3</sub> nanorods	65
3.2.6 Synthesis of YbMnO <sub>3</sub> nanoplates	70
3.2.7 Structure and morphology	70
3.2.8 Magnetic properties of YbMnO <sub>3</sub> nanoplates	71
3.2.9 Synthesis of YbMnO <sub>3</sub> micron sized particles	75
3.2.10 Structure and morphology	75
3.2.11 Magnetic properties of bulk YbMnO <sub>3</sub>	76
3.2.12 Mechanism of synthesis	77
3.2.13 Comparison between YbMnO <sub>3</sub> nanorods, plates and bulk	78
3.2.14 Conclusion	80

<b>Section 3.3: Effect of <math>R^{+3}</math> (<math>S=0</math>) on magnetic properties: <math>\text{LuMnO}_3</math></b>	<b>81-102</b>
3.3.1 Introduction	82
3.3.2 Synthesis	84
3.3.3 Structure and morphology	85
3.3.4 Raman spectroscopy	87
3.3.5 UV-vis-NIR spectroscopy	89
3.3.6 X-ray photoelectron spectroscopy (XPS)	90
3.3.7 Magnetic study	91
3.3.8 Conclusion	96
3.4 References	97

## **Chapter 4: Orthorhombic rare-earth manganites ( $\text{RMnO}_3$ )** **103-148**

### **Section 4.1: Study of manganites with spiral spin structure: $\text{Gd/DyMnO}_3$** **104-118**

4.1.1 Introduction	105
4.1.2 Synthesis	107
4.1.3 Structure and morphology	108
4.1.4 X-ray photoelectron spectroscopy (XPS)	111
4.1.5 Raman spectroscopy	111
4.1.6 Magnetic study	112
4.1.7 Conclusion	118

### **Section 4.2: Thermal hysteresis and exchange bias: $\text{EuMnO}_3$** **119-130**

4.2.1 Introduction	120
4.2.2 Synthesis	121
4.2.3 Structure and morphology	121

4.2.4 Magnetic study	123
4.2.5 Conclusion	130
<b>Section 4.3: Effect of calcination on size and properties TbMnO<sub>3</sub></b>	<b>131-148</b>
4.3.1 Introduction	132
4.3.2 Synthesis	134
4.3.3 Structure and morphology	134
4.3.4 Raman spectroscopy	136
4.3.5 X-ray photoelectron spectroscopy (XPS)	137
4.3.6 Magnetic study	138
4.3.7 Size dependent magnetic property	141
4.3.8 Conclusion	144
4.4 References	145
<b>Chapter 5. Effect of R and B site substitution on magnetic properties of RBO<sub>3</sub> (R=Gd, Dy and B=Mn, Cr)</b>	<b>149-171</b>
<b>Section 5.1 R-site substitution: Gd<sub>1-x</sub>Dy<sub>x</sub>MnO<sub>3</sub></b>	<b>150-160</b>
5.1.1 Introduction	151
5.1.2 Chemicals used	153
5.1.3 Synthesis	153
5.1.4 Crystal structure	153
5.1.5 Raman spectroscopy	154
5.1.6 Magnetic study	157
5.1.7 Conclusion	160

<b>Section 5.2 B-site substitution: DyMn<sub>1-x</sub>Cr<sub>x</sub>O<sub>3</sub></b>	<b>161-171</b>
5.2.1 Introduction	162
5.2.2 Chemicals used	163
5.2.3 Synthesis	163
5.2.4 X-ray diffraction	163
5.2.5 Raman spectroscopy	164
5.2.6 Magnetic study	165
5.2.7 Conclusion	168
5.3 References	169
<b>Chapter 6. Conclusion and future prospective</b>	<b>172-178</b>
6.1 Conclusion	173
6.2 Future prospective	177
Appendix I. List of publications	i-v

# Abstract

---

This thesis presents the study of rare-earth manganites in nano dimension. The materials studied in this thesis were synthesized using modified hydrothermal and solid-state reaction method. The main focus was to study the size and morphology dependent magnetic properties of nano dimensional rare-earth manganites.

Chapter 3 presents an investigation of the magnetic properties on hexagonal rare-earth manganites. Magnetic measurements on  $\text{ErMnO}_3$  nanoparticles revealed that triggering of  $\text{Er}^{+3}$  (4b) spin ordering by  $\text{Mn}^{+3}$  spins at  $T_N$  can be suppressed with an external field  $\geq 1500$  Oe. Single crystalline 1D and 2D *h*- $\text{YbMnO}_3$  nanocrystallites were synthesized by a complete ionic control, without the use of surfactant or template. Magnetic study of 1D, 2D and bulk  $\text{YbMnO}_3$  showed an influence of morphology. The field-dependent magnetic anomalies earlier predicted but never reported experimentally were observed in  $\text{LuMnO}_3$  nanoparticles.

Objective of chapter 4 is to study the magnetic properties of orthorhombic  $\text{RMnO}_3$  (R=Gd, Dy, Eu and Tb) in nano dimension. Ferromagnetism is observed in nanoparticles of  $\text{GdMnO}_3$  at low temperature due to surface uncompensated spins. Large exchange bias was observed in  $\text{EuMnO}_3$  nanoparticles, which was attributed to core-shell nature of antiferromagnetic core and ferromagnetic-like uncompensated surface spins. The increased value of magnetization in 2–3  $\mu\text{m}$  particles compared to nanoparticles of  $\text{TbMnO}_3$  was attributed to the double exchange interactions between  $\text{Mn}^{+3}$  and  $\text{Mn}^{+4}$  spins.

Chapter 5 presents the effect of R- and B-site substitution on the magnetic transitions of bulk  $\text{RBO}_3$  (R=Dy, Gd and B=Mn, Cr).

---



## List of abbreviations

---

1. Ferroelectricity	FE
2. Ferromagnetism	FM
3. Antiferromagnetic	AFM
4. Magnetoelectric	ME
5. Dzyaloshinskii-Moriya	DM
6. Nearest neighbor	NN
7. Jahn-Teller	JT
8. Orbital-ordering	O-O
9. Incommensurate	IC
10. Commensurate	CM
11. Magnetoelectric RAM	MERAM
12. X-ray diffraction	XRD
13. Transmission electron microscopy	TEM
14. Charge-coupled device	CCD
15. Selected area electron diffraction	SAED
16. High resolution transmission electron microscope	HR-TEM
17. Scanning electron microscopy	SEM
18. X-ray photoelectron spectroscopy	XPS
19. Vibrating sample magnetometer	VSM
20. Zero field cooled	ZFC
21. Field cooled	FC
22. AC measurement system	ACMS
23. Néel temperature	$T_N$

24. 1-dimensional	1D
25. 2-dimensional	2D
26. Magnetization vs field	M–H
27. Incommensurate antiferromagnetic	ICAFM
28. Canted <i>A</i> -type antiferromagnetic	<i>c</i> AAFM
29. First Fourier transform	FFT
30. Super exchange	SE
31. Paraelectric	PE
32. Full-width half maximum	FWHM
33. Magnetization vs. temperature	M–T
34. Coercivity	H <sub>C</sub>

---

## List of figures

---

**Figure 1.1:** Ideal cubic perovskite structure.

**Figure 1.2:** Ferromagnetic ordering in simple cubic structure.

**Figure 1.3:** Types of antiferromagnetic ordering in simple cubic structure.

**Figure 1.4:** Schematic showing no chemistry between ferroelectricity and ferromagnetism.

**Figure 1.5:** Multiferroic combine both magnetism and ferroelectricity.

**Figure 1.6:** Mixed perovskites with ferroelectrically active  $d^0$  ions (black circles) and magnetic  $d^n$  ions (blue arrows) [9].

**Figure 1.7:** Ordering of lone pairs (green lobes) of  $\text{Bi}^{+3}$  ions in  $\text{BiFeO}_3$ , direction of the polarization (black arrow) [11].

**Figure 1.8:** a) Site-centered charge order; b) bond centered charge order and c) a ferroelectric intermediate state. The charge-ordered structure in *c* which lacks inversion symmetry.

**Figure 1.9:** Schematic of  $\text{MnO}_5$  polyhedron, with Y layer above and below in hexagonal  $\text{YMnO}_3$ . a) paraelectric phase b) ferroelectric phase after tilting of  $\text{MnO}_5$  polyhedron [14].

**Figure 1.10:** Schematic of magnetic structure at Mn sites in the above figure paraelectric antiferromagnetic phase and below ferroelectric antiferromagnetic phase of  $\text{TbMnO}_3$  [17].

**Figure 1.11:** Inverse Dzyaloshinskii-Moriya (DM) interaction mechanism. A paramagnetic and paraelectric phase (above) and a non-collinear magnetic ordered ferroelectric phase (below). Purple circles represent the oxygen ions and black circles, the B-site ions [20].

**Figure 1.12:** The magneto-striction mechanism for the up-up-down-down collinear spin ordered phase. Purple and black circles represent oxygen ions and B-site ions, respectively [20].

**Figure 1.13:** Coupling of electric, elastic and magnetic degree of freedom in magnetoelectric materials.

**Figure 1.14:** The perovskite orthorhombic manganite structure. Black circle Mn cation, red circle R cation and violet circle oxygen anion.

**Figure 1.15:** Schematic of split of Mn 3d levels by crystal field and Jahn-Teller distortion.

**Figure 1.16:** Crystal field level of Mn<sup>+3</sup> in orthorhombic and hexagonal manganites.

**Figure 1.17:** a) Orbital and b) spin ordering temperature of RMnO<sub>3</sub> as a function of the in-plane Mn–O–Mn bond angle.

**Figure 1.18:** Temperature boundary that separates the stability ranges of rare-earth trihydroxides from the rare-earth oxide hydroxides in hydrothermal conditions.

**Figure 3.1.1:** Room temperature powder XRD pattern of ErMnO<sub>3</sub> from the JCPDS#140689 database (vertical line) and of as-prepared ErMnO<sub>3</sub> nanoparticles annealed at 700 °C.

**Figure 3.1.2:** Room temperature powder XRD pattern of YMnO<sub>3</sub> from the JCPDS#251709 database (vertical line) and of as-prepared YMnO<sub>3</sub> nanoparticles annealed at 700 °C.

**Figure 3.1.3:** A, B) TEM images C) HRTEM image of nanoparticle showing lattice fringes, D) SAED pattern of as-prepared ErMnO<sub>3</sub> shows that the particles are single crystalline.

**Figure 3.1.4:** A, B) TEM images C) HRTEM image of nanoparticle showing lattice fringes, D) SAED pattern of as-prepared YMnO<sub>3</sub>.

**Figure 3.1.5:** A) Magnetic hysteresis loops of ErMnO<sub>3</sub> nanoparticles B) M–H loops at 2 and 4 K in higher magnification.

**Figure 3.1.6:** A) Magnetic hysteresis loops of YMnO<sub>3</sub> nanoparticles B) M–H loops at 3 and 10 K in higher magnification.

**Figure 3.1.7:** Temperature dependence of ZFC–FC magnetization curves with an applied field of 500 Oe for A) ErMnO<sub>3</sub> nanoparticles B) YMnO<sub>3</sub> nanoparticles.

**Figure 3.1.8:** Expanded plots ZFC–FC magnetization curves showing the irreversibility below ~40 and ~20 K respectively for A) ErMnO<sub>3</sub> and B) YMnO<sub>3</sub> nanoparticles.

**Figure 3.1.9:** A, B) Temperature dependence of zero field cooling (ZFC) and field cooling (FC) magnetization curves for ErMnO<sub>3</sub> with different applied field.

**Figure 3.1.10:** Temperature dependence of ZFC–FC magnetization curves for YMnO<sub>3</sub> with different applied field.

**Figure 3.1.11:** Temperature dependence of the real part of the ac magnetization for A) ErMnO<sub>3</sub> B) YMnO<sub>3</sub> nanoparticles measured in 5 Oe ac field and various frequencies as indicated in figure.

**Figure 3.1.12:** A) Temperature dependence of imaginary part of the ac susceptibility measured in 5 Oe ac field for ErMnO<sub>3</sub> B) showing anomaly ~ 40 K.

**Figure 3.1.13:** Derivative of real part of ac susceptibility,  $dM'/dT$  for A) ErMnO<sub>3</sub>, B) YMnO<sub>3</sub> nanoparticles showing  $T_N$  at 69 and 82 K respectively.

**Figure 3.1.14:** Temperature dependent variation of A) real part of permittivity ( $\epsilon'$ ) and B) loss factor ( $\tan \delta$ ) of ErMnO<sub>3</sub> nanocrystals. Both real part of permittivity ( $\epsilon'$ ) and loss factor ( $\tan \delta$ ) showing anomaly at 70 K,  $T_N$  of ErMnO<sub>3</sub> nanocrystals.

**Figure 3.1.15:** Temperature dependent variation of real part of permittivity ( $\epsilon'$ ) of YMnO<sub>3</sub> nanocrystals showing anomaly at 85 K,  $T_N$ .

**Figure 3.2.1:** X-ray diffraction patterns of YbMnO<sub>3</sub> nanorods and the reference data from JCPDS card No. 801704 for the hexagonal phase with  $P6_3cm$  symmetry. The X-ray diffraction shows the formation of single phase YbMnO<sub>3</sub> crystal.

**Figure 3.2.2:** A, B, C) TEM images of YbMnO<sub>3</sub> nanocrystals at different scales taken from various parts of the same TEM grid D) HRTEM image of nanocrystals F) selected area diffraction pattern of YbMnO<sub>3</sub> nanocrystals E) corresponding TEM image of SAED pattern.

**Figure 3.2.3:** A) M–H loops at various temperatures, inset shows zoom view low field region B) first quadrant of M–H loop showing field dependent transition in low field.

**Figure 3.2.4:** ZFC–FC magnetization curves at various fields for YbMnO<sub>3</sub> nanorods; inset shows zoom view of ZFC magnetization showing peak ~3.2 K due to long range ordering of Yb<sup>+3</sup> moments, ( $M_{FC} - M_{ZFC}$ ) vs. T curve showing Néel temperature ~86 K.

**Figure 3.2.5:** Temperature dependence of A) real and B) imaginary part of the ac-magnetization measured at 5 Oe ac field at various frequencies for YbMnO<sub>3</sub> nanorods. Inset of A) shows zoom view of Yb<sup>+3</sup> moment ordering, line fit is only for guide to eyes.

**Figure 3.2.6:** A comparison between X-ray diffraction patterns of YbMnO<sub>3</sub> nanoplates and reference data from JCPDS card No. 801704 for the hexagonal phase with  $P6_3cm$  symmetry. The X-ray diffraction shows the formation of single phase YbMnO<sub>3</sub> crystal.

**Figure 3.2.7:** A, B, C, D) Transmission electron micrograph of YbMnO<sub>3</sub> nanocrystals at different scales taken from various parts of the same TEM grid E) HRTEM image of nanocrystals F) selected area diffraction pattern of YbMnO<sub>3</sub> nanocrystals.

**Figure 3.2.8:** A) M-H hysteresis loops at various temperatures inset shows zoom view low field region B) first quadrant of M–H loop in low field.

**Figure 3.2.9:** ZFC–FC magnetization curves at various applied fields for YbMnO<sub>3</sub> nanoplates, inset zoom view of ZFC magnetization showing peak ~3.2 K due to long range ordering of Yb<sup>+3</sup> moments, ( $M_{FC} - M_{ZFC}$ ) vs. T curve showing  $T_N$  ~86 K.

**Figure 3.2.10:** Temperature dependence of A) real and B) imaginary part of the ac-magnetization measured at 5 Oe ac-field at various frequencies as indicated in figure for YbMnO<sub>3</sub> nanoplates.

**Figure 3.2.11:** A comparison between X-ray diffraction patterns of YbMnO<sub>3</sub> micron sized particles and reference data from JCPDS card No. 801704 for the hexagonal phase with *P6<sub>3</sub>cm* symmetry. The X-ray diffraction shows the formation of single phase YbMnO<sub>3</sub> crystal.

**Figure 3.2.12:** Scanning electron micrographs of YbMnO<sub>3</sub> ceramic at different scales. SEM images shows irregular micron sized particles of YbMnO<sub>3</sub> crystals.

**Figure 3.2.13:** A) M–H loops at 3 and 100 K B) ZFC–FC magnetization curves at 500 Oe applied field for YbMnO<sub>3</sub> bulk ceramic sample, inset low temperature ZFC–FC magnetization curves showing bifurcation of ZFC and FC curve at ~3.8 K and ( $M_{FC} - M_{ZFC}$ ) vs. T curve showing  $T_N \sim 86$  K.

**Figure 3.2.14:** A) Comparison of ZFC–FC magnetization curves at 500 Oe applied field for YbMnO<sub>3</sub> nanorods, nanoplates and bulk ceramic sample. Bifurcation of ZFC and FC magnetization curves ( $T_N$ ) and B) low temperature anomaly of YbMnO<sub>3</sub> nanorods, nanoplates and bulk ceramic sample.

**Figure 3.3.1:** A comparison between A) powder x-ray diffraction pattern of LuMnO<sub>3</sub> nanocrystals with B) the data from JCPDS Card No. 200650 for orthorhombic phase and (C) JCPDS Card No. 140030 for hexagonal phase. The comparison shows that LuMnO<sub>3</sub> crystallizes in hexagonal phase.

**Figure 3.3.2:** A, B, C) Transmission electron micrograph of LuMnO<sub>3</sub> at different scales taken from various parts of the same TEM grid D) selected area diffraction pattern of LuMnO<sub>3</sub> nanoparticles.

**Figure 3.3.3:** A) Room temperature Raman spectra of nanocrystalline LuMnO<sub>3</sub> B) UV-vis-NIR spectra of LuMnO<sub>3</sub> at room temperature in diffused reflectance mode. Inset shows the zoom view of part of the same curve.

**Figure 3.3.4:** X-ray photoelectron spectroscopy spectra of A) C1s B) O1s C) Mn 2p D) Lu 4d of nanocrystalline LuMnO<sub>3</sub>. The lines represent the deconvoluted peaks.

**Figure 3.3.5:** A) M–H loops for nanocrystalline LuMnO<sub>3</sub> shown at various temperatures B) zoom view of the M–H curves C) initial magnetization curves at different temperature, showing non-linear behavior below 90 K D) variation of coercivity, with temperature, the arrow shows anomalies which were also seen in the M–T curves.

**Figure 3.3.6:** A)  $\chi$  and  $1/\chi$  vs. temperature curves at 100 Oe. Curves show three anomalies at temperature  $T_N$  (deviation of the  $1/\chi$  from linear behavior),  $T_1$  (bifurcation temperature of ZFC-FC curves) and  $T_2$  (sharp peak in ZFC curve) B) ZFC–FC magnetization curves at 50 and 125 Oe applied field C) ZFC–FC magnetization curves at 1000 Oe and 20000 Oe applied field D) the variation of ordering temperature,  $T_1$  with applied field.

**Figure 4.1.1:** XRD patterns of DyMnO<sub>3</sub> from the JCPDS#250330 database (vertical line) and of as-prepared DyMnO<sub>3</sub> nanoparticles annealed at 700 °C.

**Figure 4.1.2:** XRD patterns of GdMnO<sub>3</sub> from the JCPDS#250337 database (vertical line) and of as-prepared DyMnO<sub>3</sub> nanoparticles annealed at 700 °C.

**Figure 4.1.3:** A, B) TEM images, C) HRTEM images shows lattice fringes and d-values calculated from the image correspond to (101) planes of DyMnO<sub>3</sub> D) SAED pattern of as-prepared DyMnO<sub>3</sub>.

**Figure 4.1.4:** A, B) TEM images, C) HRTEM images shows lattice fringes and d-values calculated from the image correspond to (111) planes of GdMnO<sub>3</sub> D) SAED pattern of as-prepared GdMnO<sub>3</sub>.



**Figure 4.1.5:** XPS spectra for Mn 2*p* of as-prepared A) DyMnO<sub>3</sub>, B) GdMnO<sub>3</sub> nanoparticles annealed at 700 °C (scatter curves) and the lines represent the deconvoluted peaks.

**Figure 4.1.6:** Room temperature Raman spectra of nanocrystalline DyMnO<sub>3</sub> and GdMnO<sub>3</sub>.

**Figure 4.1.7:** A) Magnetic hysteresis loops B) expanded plots of hysteresis loops at 3, 5 and 300 K of DyMnO<sub>3</sub> nanoparticles annealed at 700 °C.

**Figure 4.1.8:** A) Magnetic hysteresis loops B) expanded plots of hysteresis loops at 3, 5 and 300 K of GdMnO<sub>3</sub> nanoparticles annealed at 700 °C at indicated temperature values.

**Figure 4.1.9:** A) Temperature dependence ZFC and FC magnetization curves for DyMnO<sub>3</sub> nanoparticles, with an applied field of 200 Oe, inset  $\mu_{\text{eff}}$  shows clear bifurcation of ZFC–FC magnetization curves at  $T_N \sim 43$  K B) expanded plots of ZFC-FC magnetization curves with  $T_N$  at  $\sim 43$  K and ordering temperature of Dy<sup>+3</sup> moments at  $\sim 7$  K.

**Figure 4.1.10:** A) Temperature dependence of the ZFC and FC magnetization curves for GdMnO<sub>3</sub> nanoparticles annealed at 700 °C, with an applied field of 50 and 1000 Oe B) expanded plots of ZFC-FC magnetization curves with  $T_N \sim 42$  K and ordering temperature of Gd<sup>+3</sup> moments at  $\sim 6$  K, inset shows the inverse susceptibility,  $1/\chi$  showing three anomalies at 42, 22 and 6 K.

**Figure 4.1.11:** Temperature dependence of the A) real and B) imaginary part of the ac-magnetization measured in 3 Oe ac field and various frequencies as indicated in figure for DyMnO<sub>3</sub> nanoparticles.

**Figure 4.1.12:** Temperature dependence of the real part of the ac-magnetization measured in 5 Oe ac field and various frequencies as indicated in figure for GdMnO<sub>3</sub> nanoparticles.

**Figure 4.2.1:** X-ray diffraction patterns of EuMnO<sub>3</sub> nanoparticles with the data from JCPDS Card No. 261126 for the orthorhombic phase with Pbnm symmetry. Some peaks are not indexed for maintaining clarity of figure.

**Figure 4.2.2:** A, B) Transmission electron micrograph C) HRTEM image D) SAED pattern of orthorhombic  $\text{EuMnO}_3$  nanocrystals.

**Figure 4.2.3:** ZFC–FC magnetization curves at 500 Oe and 1 T applied fields for orthorhombic  $\text{EuMnO}_3$  nanoparticles.

**Figure 4.2.4:** FC heating and cooling magnetization curves at 500 Oe applied fields for orthorhombic  $\text{EuMnO}_3$  nanoparticles.

**Figure 4.2.5:** ZFC magnetization curves at various applied fields for orthorhombic  $\text{EuMnO}_3$  nanoparticles showing field dependency of transitions.

**Figure 4.2.6:** Temperature dependence of A) real and B) imaginary part of ac magnetisation, measured in 5 Oe field and various frequencies as indicated in figure for orthorhombic  $\text{EuMnO}_3$  nanoparticles.

**Figure 4.2.7:** A) M–H loops for orthorhombic  $\text{EuMnO}_3$  nanoparticles at various temperatures B) temperature dependence of exchange bias.

**Figure 4.2.8:** A) M–H loops of orthorhombic  $\text{EuMnO}_3$  nanoparticles at 3 K at different field cooled conditions B) expanded plot of loop.

**Figure 4.2.9:** Schematic model of an individual orthorhombic  $\text{EuMnO}_3$  nanoparticles.

**Figure 4.3.1:** Comparative XRD patterns of  $\text{TbMnO}_3$  from the JCPDS#250933 database,  $\text{TbMnO}_3$  nanoparticles annealed at 700 and 800 °C respectively.

**Figure 4.3.2:** A, B) TEM images C) HRTEM image D) SAED pattern of  $\text{TbMnO}_3$  nanoparticles annealed at 700 °C.

**Figure 4.3.3:** TEM image of sample annealed at 800 °C where particles form aggregated mass and the particle size goes up in micron range.

**Figure 4.3.4:** Room temperature Raman spectra of as-prepared TbMnO<sub>3</sub> nanoparticles annealed at 700 and 800 °C temperature. Vertical dashed lines are guide to eye.

**Figure 4.3.5:** Room temperature XPS spectra for Mn 2*p* of as-prepared TbMnO<sub>3</sub> nanoparticles annealed at A) 700 °C and at B) 800 °C (scatter curves). The lines represent the deconvoluted peaks.

**Figure 4.3.6:** A) Hysteresis loops of as-prepared TbMnO<sub>3</sub> nanoparticles annealed at 700 °C at indicated temperature B) expanded plots of magnetization in higher magnification.

**Figure 4.3.7:** A) Initial magnetization curves B) coercivity as a function of temperature of d TbMnO<sub>3</sub> nanoparticles annealed at 700 °C.

**Figure 4.3.8:** A) Temperature dependence of the susceptibility in ZFC–FC modes, with an applied field of 50 and 200 Oe for TbMnO<sub>3</sub> nanoparticles. Inset shows the zoom view of ZFC–FC magnetization curves with bifurcation at  $T_N \sim 45$  K and ordering of Tb<sup>+3</sup> moments at  $\sim 10$  K does not depend on applied external field B) inverse susceptibility  $1/\chi$  with straight line behavior above  $T_N$ .

**Figure 4.3.9:** A comparison of M–H hysteresis loops (zoom view) of TbMnO<sub>3</sub> nanoparticles annealed at 700 (black line), 800 °C (blue line) at temperature A) 10 K and B) 50 K.

**Figure 4.3.10:** Temperature dependence of the ZFC–FC susceptibility, with an applied field of 200 Oe for TbMnO<sub>3</sub> nanoparticles annealed at 700 °C (left Y-axis) and 800 °C (right Y-axis). Insets A) and B) show the inverse of susceptibility and their Curie-Weiss fits (red solid line) for TbMnO<sub>3</sub> nanoparticles annealed at 700 and 800 °C, respectively.

**Figure 5.1.1:** XRD pattern of orthorhombic Gd<sub>1-x</sub>Dy<sub>x</sub>MnO<sub>3</sub> (x=0–1).

**Figure 5.1.2:** Room temperature Raman spectra of orthorhombic Gd<sub>1-x</sub>Dy<sub>x</sub>MnO<sub>3</sub> (x=0–1).

**Figure 5.1.3:** Variation of phonon mode frequency with  $x$  in orthorhombic  $\text{Gd}_{1-x}\text{Dy}_x\text{MnO}_3$  ( $x=0-1$ ).

**Figure 5.1.4:** Variation of phonon mode frequency with  $x$  in orthorhombic  $\text{Gd}_{1-x}\text{Dy}_x\text{MnO}_3$  ( $x=0-1$ ).

**Figure 5.1.5:** Variation of phonon mode frequency with  $x$  in orthorhombic  $\text{Gd}_{1-x}\text{Dy}_x\text{MnO}_3$  ( $x=0-1$ ).

**Figure 5.1.6:** Initial magnetization as a function of applied field for orthorhombic  $\text{Gd}_{1-x}\text{Dy}_x\text{MnO}_3$  ( $x=0-1$ ) at A) 3 K, B) 5 K, C) 7 K and D) 10 K.

**Figure 5.1.7:** ZFC magnetization curves for orthorhombic  $\text{Gd}_{1-x}\text{Dy}_x\text{MnO}_3$  ( $x=0-1$ ) at 100 Oe applied field.

**Figure 5.1.8:** Temperature dependence of A) Real part and B) imaginary part of ac magnetization at ac field of 5 Oe and frequency 751 Hz.

**Figure 5.2.1:** Room temperature XRD pattern of orthorhombic  $\text{DyMn}_{1-x}\text{Cr}_x\text{O}_3$  ( $x=0, 0.03, 0.05, 0.1$ ).

**Figure 5.2.2:** Room temperature Raman spectra of  $\text{DyMn}_{1-x}\text{Cr}_x\text{O}_3$  ( $x=0, 0.03, 0.05, 0.1$ ).

**Figure 5.2.3:** Magnetization as a function of applied field for orthorhombic  $\text{DyMn}_{1-x}\text{Cr}_x\text{O}_3$  ( $x=0, 0.03, 0.05, 0.1$ ) at A) 3 K, B) 5 K, C) 10 K and D) 40 K.

**Figure 5.2.4:** ZFC–FC magnetization curves for orthorhombic  $\text{DyMn}_{1-x}\text{Cr}_x\text{O}_3$  ( $x=0, 0.03, 0.05, 0.1$ ) at 200 Oe applied field.

**Figure 5.2.5:** Temperature dependence of A) Real part and B) imaginary part of ac magnetization at ac field of 5 Oe and frequency 751 Hz.

---

## List of tables

---

**Table 1.1:** Types of ferroelectricity on the basis of mechanism of symmetry breaking.

**Table 1.2:** Types of multiferroics on the basis of microscopic sources of ferroelectricity in multiferroic materials.

**Table 3.3.1:** Comparison between the room temperature Raman mode positions ( $\text{cm}^{-1}$ ) from our present study on  $\text{LuMnO}_3$  nanoparticles (figure: 3.3.3 A), reported data on isomorphic structure  $\text{YMnO}_3$  by Iliev *et al.* and calculated data on same symmetric structure (Iliev *et al.*)[65].

---

# Chapter 1. Introduction

---

This chapter is an introduction to the basic concepts of perovskite and magnetic and electric ordering in rare-earth manganites. Fundamentals of multiferroic and magnetoelectric phenomenon in perovskites with example is presented. A summary on crystal structure of rare-earth manganites with rare-earth ionic size and types of distortion is presented. In last section, a review on synthesis of rare-earth manganites in nano dimensions reported in literature and challenges associated with their synthesis are also presented.

---

## 1.1 Perovskite

The perovskite structure comprises a wide range of compounds. Perovskite structure can accommodate a broad variety of ions, which gives diverse physical properties to this class of compounds. Perovskite compounds were studied for their dielectric, magnetic, electrical, optical and catalytic properties. The ideal perovskite structure has an  $ABO_3$  (A, B=cations, O=oxygen) stoichiometry with cubic structure. The A cation is surrounded by 12 O anions in a dodecahedral environment, the B cation is octahedrally coordinated by six O ions, and the O anions are coordinated by two B cations and four A cations. The common description of perovskite structure is a three-dimensional cubic network of corner-sharing  $BO_6$  octahedra. In this description, A cation sits in the center of a cube defined by eight corner-sharing octahedral units [1].

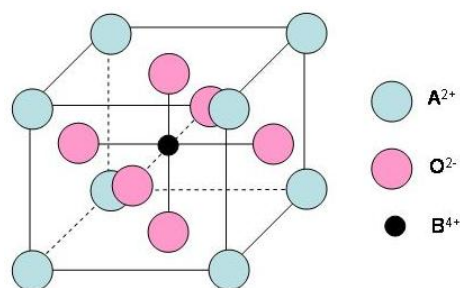


**Figure 1.1:** Ideal cubic perovskite structure.

Ideally, perovskite structure is cubic but several structural distortions are possible which make perovskites rich in its physical properties. Perovskite materials exist in cubic, tetragonal, orthorhombic, rhombohedral, monoclinic, and triclinic crystal structures [1]. Distortions from ideal perovskite structure can arise from three mechanisms: distortions of the octahedra, cation displacements within the octahedra and tilting of the octahedra. Distortions of the octahedra and cation displacements within the octahedra are driven by electronic instabilities of the octahedral metal ion. The examples of electronic instability are

Jahn-Teller distortion in orthorhombic manganites, which leads to octahedral distortions, and ferroelectric displacement of  $Ti^{+4}$  ions in  $BaTiO_3$  leads to cation displacements. The third, octahedral tilting, distortion mechanism is governed by, tilting of rigid  $BO_6$  octahedra while maintaining their corner-sharing connectivity. This type of distortion is typically observed when the A cation is too small for the cubic  $BO_3$  corner sharing octahedral network. This is the lowest energy distortion mode; because the A–O distances can be shortened along with the first coordination sphere about the B cation remains unchanged [2].

## 1.2 Ferroelectricity

A ferroelectric is defined as a material whose intrinsic lattice polarization  $P$  can be reversed by the application of an external electric field  $E$  which is greater than the coercive field  $E_c$ . Ferroelectrics usually have a phase-transition temperature  $T_0$  above which they are paraelectric. All ferroelectric materials are also pyroelectric and all pyroelectric materials are piezoelectric. But pyroelectric materials are not ferroelectric materials e.g. ZnO. Ferroelectric materials have domains and show hysteresis of polarization to the applied field.

	Mechanism of symmetry breaking	Materials
<b>Proper</b>	Covalent bonding between $3d^0$ transition metal (Ti) and oxygen	$BaTiO_3$ , $PbTiO_3$
	Polarizability of $6s^2$ lone pair	$BiFeO_3$ , $BiMnO_3$
<b>Improper</b>	Structural transition	$h$ - $RMnO_3$
	Charge ordering	$LuFe_2O_4$
	Magnetic ordering	$o$ - $RMnO_3$ , $RMn_2O_5$

**Table 1.1:** Types of ferroelectricity on the basis of mechanism of symmetry breaking [3].



Early work on ferroelectrics was mostly focused on rochelle salt,  $\text{KNa}(\text{C}_4\text{H}_4\text{O}_6) \cdot 4\text{H}_2\text{O}$ . Due to their complex structure and large number of cations per unit cell, theoretical study on these materials was very difficult. Today, the most studied ferroelectrics are oxides,  $\text{ABO}_3$ . Below Curie temperature, structural distortion lowers symmetry structure making them ferroelectric [4].

### 1.3 Ferromagnetism

Ferromagnetic materials possess a spontaneous magnetization even in the absence of an applied external field. Ferromagnetic materials usually have a phase-transition temperature  $T_0$  above which they are paramagnetic. Curie-Weiss localized moment theory postulated that an internal molecular field is responsible for parallel alignment of magnetic moment in a ferromagnetic material. The origin of molecular field is the exchange energy, which causes electron with parallel spins to have a lower energy than antiparallel spins [5].

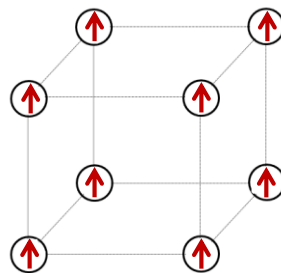


*Figure 1.2: Ferromagnetic ordering in simple cubic structure.*

### 1.4 Antiferromagnetism

In antiferromagnetic materials, spins are ordered but arranged in such a way that they cancel each other leading to no net magnetization. Depending upon the arrangement of spins there

can be a wide variety of antiferromagnetic materials. Some examples of antiferromagnetic ordering that can be seen in simple cubic system are shown in figure 1.3.

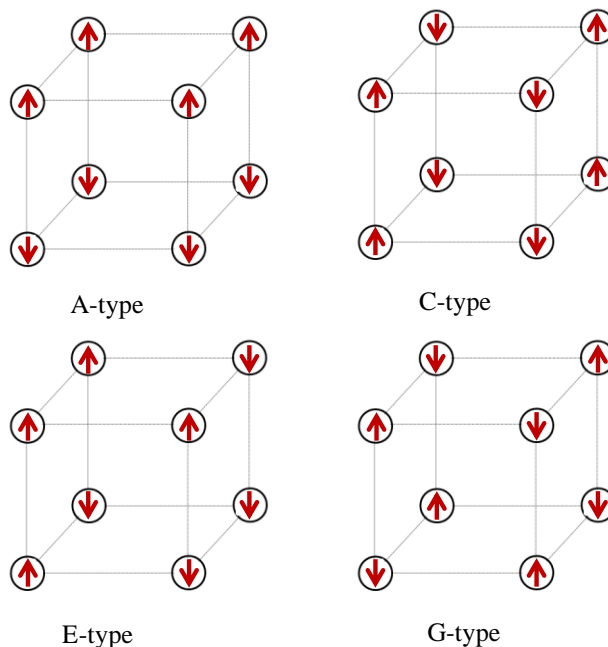


**Figure 1.3:** Types of antiferromagnetic ordering in simple cubic structure [6].

In A-type antiferromagnetic system, ferromagnetic layers are coupled antiferromagnetically whereas, in C-type, ferromagnetic rods are coupled antiferromagnetically [6].

### 1.5 Chemistry between ferroelectric and ferromagnetic ordering

Empty  $d$ -states of transition metal ions like  $Ti^{+4}$  in  $BaTiO_3$ , establish strong covalency with the surrounding oxygen ions. This favors the shift of transition metal ion from the centre of  $MO_6$  octahedra towards one (or three) oxygen, to form a strong covalent bond with this particular oxygen at the expense of weakening the bonds with other oxygen. This off-centre shift of transition metal ion provides the core driving force for ferroelectricity. The

microscopic origin of magnetism is the presence of localized electrons, mostly in the partially filled  $d$  or  $f$  shells of transition-metal or rare-earth ions, which have a corresponding localized spin or magnetic moment. Exchange interactions between the localized moments lead to magnetic ordering. This so called " $d^0$  vs  $d^n$  problem" [7].

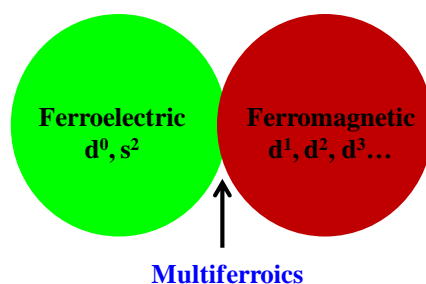


*Figure 1.4: Schematic showing no chemistry between ferroelectricity and ferromagnetism.*

## 1.6 Multiferroism

"Multiferroism" term was coined by Schmid to describe materials in which two or all three of the ferroic properties ferromagnetism, ferroelectricity, ferroelasticity exists in the same phase [8].

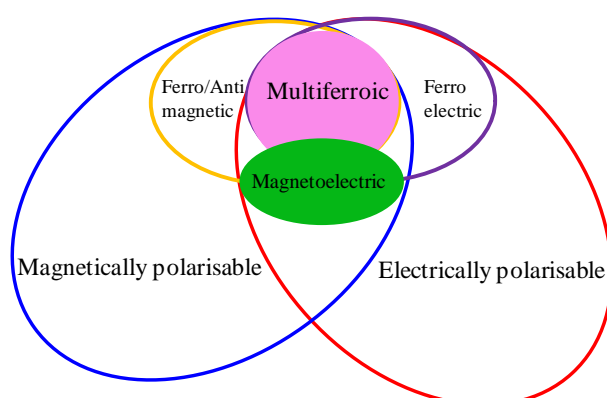


*Figure 1.5: Multiferroic combines both magnetism and ferroelectricity [8].*

Multiferroic materials are interesting class of material, because the microscopic conditions which combine magnetic and ferroelectric properties, are non-trivial as these two phenomenon tend to exclude each other.

### 1.6.1 Types of multiferroics

Despite of bad compatibility of magnetism and ferroelectricity as there is no chemistry between them, there exists many systems in which these properties coexists. Depending on the different microscopic sources of ferroelectricity, multiferroic materials can be classified in two classes: type I and type II [9].

	Mechanism	Description	Examples
<b>Type I</b>	Lone-pair effects	Mixing between the $(ns)^2$ ground state and a low-lying $(ns)^1 (np)^1$ excited state	BiFeO <sub>3</sub> , BiMnO <sub>3</sub>
	Geometric frustration	Buckling of MnO <sub>5</sub> pyramids & displacement of Y	YMnO <sub>3</sub>
	Charge ordering	Certain ‘non-centrosymmetric’ arrangements of ions induce ferroelectricity in magnetic materials	LuFe <sub>2</sub> O <sub>4</sub>
<b>Type II</b>	Magnetic ordering	Ferroelectricity is induced by magnetic long-range order in which the arrangement of magnetic dipoles lacks reflection symmetry	TbMnO <sub>3</sub> , DyMnO <sub>3</sub> , TbMn <sub>2</sub> O <sub>4</sub>

**Table 1.2:** Types of multiferroics on the basis of microscopic sources of ferroelectricity in multiferroic materials [9].

### 1.6.1.1 Type-I multiferroics

The type-I multiferroics, refers to materials in which origin of ferroelectricity and magnetism have different sources (different groups of electrons) and independent of one another, though there is some coupling between them. In this class of materials, ferroelectricity typically appears at higher temperatures than magnetism, and the spontaneous polarization  $\mathbf{P}$  is often large (of order 10–100  $\mu\text{C}/\text{cm}^2$ ). Depending on the mechanism of ferroelectricity we can sub-classify type-I multiferroics:

#### 1.6.1.11 Independent magnetic and ferroelectric system

The simplest way to combine magnetic and ferroelectric properties in a material is to have two separate structural units, noncentrosymmetric unit which will give rise to ferroelectricity and simultaneously contain magnetic ions which can give magnetic order. Example of such class of materials are Ni-I boracite,  $\text{GdFe}_3(\text{BO}_3)_4$  [10].

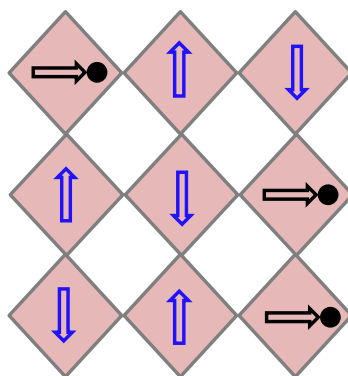


**Figure 1.6:** Mixed perovskites with ferroelectrically active  $d^0$  ions (black circles) and magnetic  $d^n$  ions (blue arrows) [9].

As ferroelectricity and magnetism have different sources of origin, the magnetic-ferroelectric coupling in these systems are very weak. In this class of materials, the challenge

is to increase the coupling between magnetic-ferroelectric ordering, maintaining the high value of magnetic and electric ordering.

### 1.6.1.12 Role of lone pairs

$\text{Bi}^{+3}$  and  $\text{Pb}^{+2}$  have lone pairs, two valence electrons which could have participated in chemical bonds using hybridized states ( $sp^2$  or  $sp^3$ ), but in these systems, they do not participate in such bonds. From the microscopic point of view, the particular orientation of these lone pairs, or dangling bonds may create local electric dipoles, which ultimately can order in a ferroelectric state. Examples of such systems are  $\text{BiFeO}_3$ ,  $\text{BiMnO}_3$ . As electric and magnetic ordering have different sources of origin, there exists very weak magnetic-ferroelectric coupling in these systems.

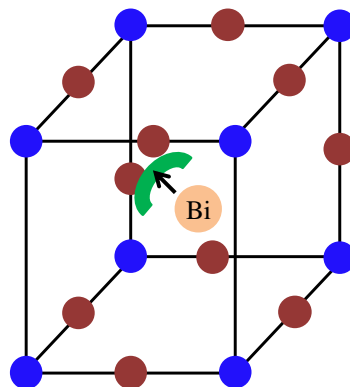


**Figure 1.7:** Ordering of lone pairs (green lobes) of  $\text{Bi}^{+3}$  ions in  $\text{BiFeO}_3$ , direction of the polarization (black arrow) [11].

### 1.6.1.13 Ferroelectricity due to charge ordering

Charge ordering is seen in systems with non integer average valence of transition metals, such as  $\text{Pr}_{0.5}\text{Ca}_{0.5}\text{MnO}_3$ . Let's consider a one dimensional chain with equal charge on each site. Now consider  $\text{Pr}_{0.5}\text{Ca}_{0.5}\text{MnO}_3$ , which contains equal number of  $\text{Mn}^{+3}$  and  $\text{Mn}^{+4}$  ions. At

this moment, we can imagine of a checkerboard with charge ordering with alternate of  $\text{Mn}^{+3}$  and  $\text{Mn}^{+4}$  ions, this is termed as site-centered charge order. This process does not break spatial inversion symmetry, as a result no net dipole moment. Another type of charge ordering where lattice dimerization can take place, where all sites remain equivalent with alternate weak and strong bonds. This bond centered charge ordering is centrosymmetric and hence no net dipole moment. Now if we combine both the type of charge ordering in single system, inversion symmetry is broken, each short bond develops a net dipole moment, and thus the system becomes ferroelectric [12].

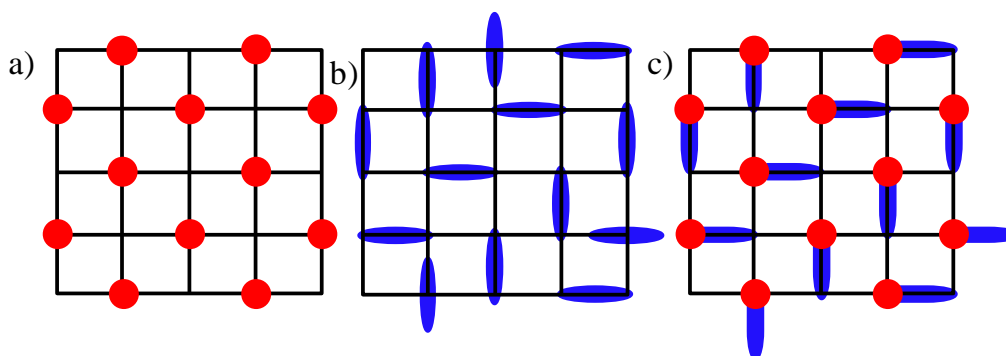


**Figure 1.8:** a) Site-centered charge order b) bond centered charge order and c) a ferroelectric intermediate state. The charge-ordered structure in which c lacks inversion symmetry [13].

#### 1.6.1.14 Geometric ferroelectricity

In hexagonal manganites,  $\text{YMnO}_3$ , to achieve a close packed structure, the  $\text{MnO}_5$  trigonal bipyramids tilts. In  $\text{YMnO}_3$ , such tilting leads to breaking of inversion symmetry, resulting in ferroelectricity with dipole moments mostly coming from Y–O bonds. In this system ferroelectric transition temperature is very high than magnetic ordering temperature and the coupling of magnetic and ferroelectric degrees of freedom is very weak.

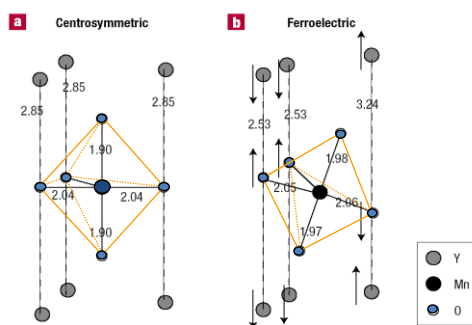


**Figure 1.9:** Schematic of  $MnO_5$  polyhedron, with Y layer above and below in hexagonal  $YMnO_3$ . a) paraelectric phase b) ferroelectric phase after tilting of  $MnO_5$  polyhedron [14].

### 1.6.1.2 Type-II multiferroics

The type-II multiferroics, include materials in which magnetism causes ferroelectricity, imply a strong coupling between ferroelectricity and magnetism. However, the polarization in these materials is usually much smaller (of order  $10^{-2} \mu\text{C}/\text{cm}^2$ ).

#### 1.6.1.21 Ferroelectricity due to magnetic ordering

This type of ferroelectricity can be found in  $TbMnO_3$ ,  $GdMnO_3$ ,  $TbMn_2O_5$ ,  $YMn_2O_5$  etc. In these systems ferroelectricity appears in magnetic phase with spiral or helicoidal magnetic structure. In  $TbMnO_3$ , no electric polarization exists in phase with sinusoidal magnetic structure between 40–30 K, but non zero electric polarization appears below 30 K, with helicoidal structure. In this phase, inversion symmetry breaks and polarization appears. Spin-orbit coupling in the form of Dzyaloshinskii antisymmetric exchange interaction influences magnetic spiral ordering on lattice and charge in these systems to produce ferroelectricity [15, 16].



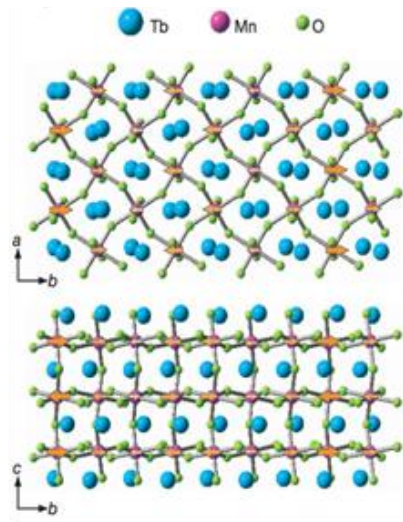


**Figure 1.10:** Schematic of magnetic structure at Mn sites in the above figure paraelectric antiferromagnetic phase and below ferroelectric antiferromagnetic phase of  $TbMnO_3$  [17].

Spiral magnetic structure is the only criteria for ferroelectricity, spin rotation axis  $e$  should not coincide with the wave vector of spiral  $Q$  to observe polarization and is proportional to vector product of  $e$  and  $Q$  by the relation  $P \sim [e \times Q]$ . In these systems, the coupling between magnetic and electric ordering is very strong as ferroelectricity in this system originates from magnetic ordering.

### Inverse Dzyaloshinskii-Moriya (DM) interaction

Consider a cycloidal spin structure where spins rotate in the  $bc$  plane, two nearest neighbor (NN) spins along the  $b$  axis, termed S1 and S2. The DM interaction Hamiltonian between the two spins are written as:

$$H_{DM} = \mathbf{D} \cdot (\mathbf{S}_1 \times \mathbf{S}_2)$$

where  $D$  is the DM vector which is given by  $(\lambda t_{pd}^4 / \Delta E^4)$  with relativistic spin-orbit coupling

$\lambda$ , the electron transfer integral between NN O  $2p$  and transition-metal  $3d$  orbitals,  $t_{pd}$  and energy separation between the ground and excited states,  $\Delta E$ .

Above the spin ordering temperature, it is assumed that there is a reflection symmetry at the center of the bond connecting sites 1 and 2, and the DM vector is zero,  $D=0$ . With decreasing temperature, a cycloidal spin order sets in at a certain temperature due to frustrated exchange interactions, and a vector chirality  $S_1 \times S_2$  becomes finite. Then in order to gain the DM interaction energy, a spontaneous breaking of inversion symmetry along the  $c$  axis is induced and  $D$  becomes finite. This is the inverse process of the usual DM interaction in magnets. There, the DM vector is finite,  $D \neq 0$ , due to the low symmetry crystal structure in all temperature range. Above the magnetic transition temperature, the vector chirality is zero,  $S_1 \times S_2 = 0$ , and below this temperature, a non-collinear spin structure with  $S_1 \times S_2 \neq 0$  is induced in order to gain the DM interaction energy. In such case, polarization  $P$  is given by

$$P \propto d_{12} \times (S_1 \times S_2)$$

where  $d_{12}$  is a vector connecting  $S_1$  and  $S_2$  [18,19].

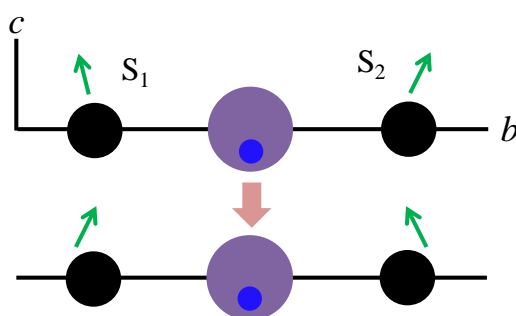


**Figure 1.11:** Inverse Dzyaloshinskii-Moriya (DM) interaction mechanism. A paramagnetic and paraelectric phase (above) and a non-collinear magnetic ordered ferroelectric phase (below). Purple circles represent the oxygen ions and black circles, the B-site ions [20].

The spin current mechanism is the electronic version of inverse DM interaction; the electronic cloud breaks the inversion symmetry in the limit of heavy mass ion.

### 1.6.1.22 Exchange-striction mechanism

The coupling between the electric polarization and spins are caused by the symmetric exchange interaction,

$$J \sum_{\langle ij \rangle} \mathbf{S}_i \cdot \mathbf{S}_j$$

where the exchange constant  $J$  is  $(t_{pd}^4/\Delta E^3)$ .

Consider a chain where the transition-metal ions M and oxygen ions O are aligned alternately, and the exchange interaction (NN) between M ions caused by the super-exchange processes between the two M ions via O ion. In this regard, a commensurate collinear magnetic order, up–up–down–down structure is considered. Favorable bond angles in the M–O–M bonds depend on spin configurations in M ions.

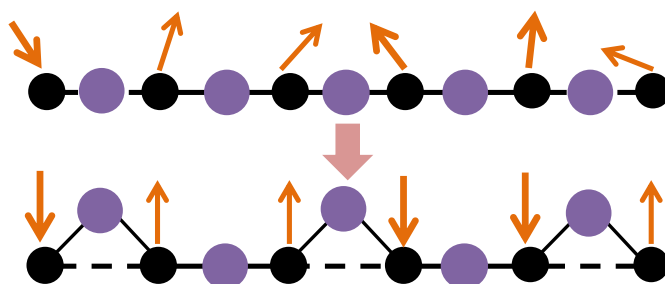


**Figure 1.12:** The magneto-striction mechanism for the up–up–down–down collinear spin ordered phase. Purple and black circles represent oxygen ions and B-site ions, respectively [20].

Here we assume that a large (small) bond angle is favored in the ferromagnetic (antiferromagnetic) spin configuration in order to gain the exchange energy. This is realized in the exchange interaction with the orbital degree of freedom in an M ion. As a result, the O ions between the antiparallel spins are distorted spontaneously, and the inversion symmetry in the system is broken.

### 1.7 Magnetoelectric effect

The conventional linear magnetoelectric materials, there exists a cross-coupling between electric and magnetic field given by the relation,

$$\Delta M = \mu_0 \alpha_{EM} E \text{ and } \Delta E = \alpha_{ME} H$$

in single phase ME materials  $\alpha_{EM} = \alpha_{ME}$ .

Materials can also show higher order magnetoelectric effect.

Linear magnetoelectric effect was first theoretically observed in rhombohedral antiferromagnet,  $\alpha$ -Cr<sub>2</sub>O<sub>3</sub> by Landau and Lifshitz [21]. To observe linear magnetoelectric effect in any material they found that time and spatial inversion symmetry ( $\mathbf{T}$ ,  $\mathbf{I}$ ) have to be broken. This symmetry restriction is followed by 69 magnetic point group out of which 58 allow linear magnetoelectric effect because of other constrains [22].

If the above symmetric conditions are not fulfilled, the material can show higher order magnetoelectric effect. The free energy density can be written as,

$$F(E, H) = F_0 - \frac{1}{2} \epsilon_0 \chi_{ij}^e E_i E_j - \frac{1}{2} \mu_0 \chi_{ij}^m H_i H_j - \alpha_{ij} H_i E_j - \frac{\beta_{ijk}}{2} E_i H_j H_k - \frac{\gamma_{ijk}}{2} H_i E_j E_k - \frac{\delta_{ijkl}}{2} E_i E_j H_k H_l$$

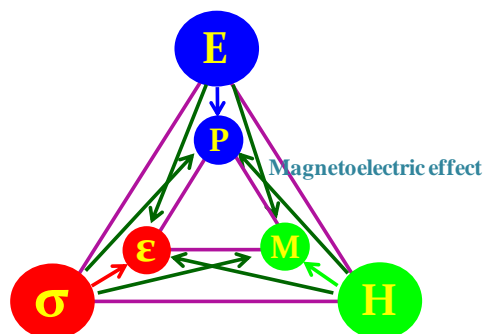


**Figure 1.13:** Coupling of electric, elastic and magnetic degree of freedom in magnetoelastic materials [22].

### 1.8 Why rare-earth manganites?

Manganites are crystals where magnetic, manganese ions are linked to oxygen ions with rare-earth/alkali earth ions sitting in the gap of Mn and O ions. In condense matter physics, manganites are the most famous subset as it shows all the known phenomenons like Jahn-Teller polaron [23, 24], Zener double-exchange [25, 26] etc. Technologically important discoveries like, giant magnetoresistance [27], giant magnetocapacitance, geometric ferroelectricity was observed in manganites. Highest value of magnetoelastic coupling is also reported in manganites [17]. The complex crystal structure and its unrevealed features make these class of materials important to explore.

### 1.9 Rare-earth manganites

Rare-earth manganites come under type-II multiferroics and are of utmost important as all the known physical mechanism involved in type-II multiferroicity exists in this class of materials. The largest polarization value in type-II multiferroics, belongs to manganites. After

the discovery of magnetic field controllable ferroelectricity in  $\text{TbMnO}_3$ , research interest in multiferroicity revived [28].

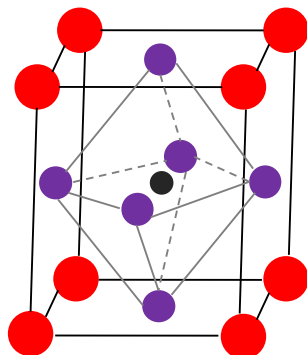


**Figure 1.14:** The perovskite orthorhombic manganite structure. Black circle Mn cation, red circle R cation and violet circle oxygen anion [29].

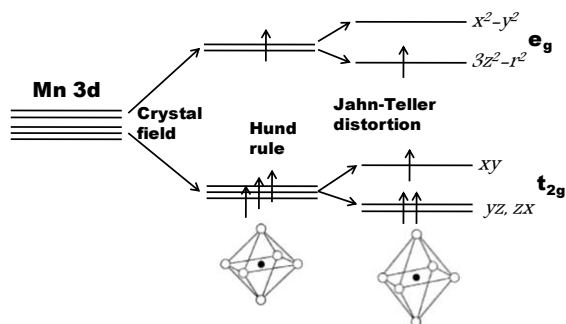


**Figure 1.15:** Schematic of splitting of Mn 3d levels by crystal field and Jahn-Teller distortion.

### 1.9.1 Why there is no Jahn-Teller distortion in hexagonal manganites?

In hexagonal manganites  $Mn^{+3}$  ions are located in five fold coordination in the centre of  $O_5$  trigonal bipyramid and rare-earth ion in 7 fold coordination. In orthorhombic compounds Mn ions in octahedral coordination have triplet  $t_{2g}$  and doublet  $e_g$ . In hexagonal manganites,  $Mn^{+3}$  ions in trigonal bipyramid,  $d$  levels split into two doublets and a upper singlet. Four  $d$  electrons of  $Mn^{+3}$  ions occupy two lowest doublets. As a result no orbital degeneracy is left, so  $Mn^{+3}$  ions is not Jahn-Teller active in hexagonal manganites [30].

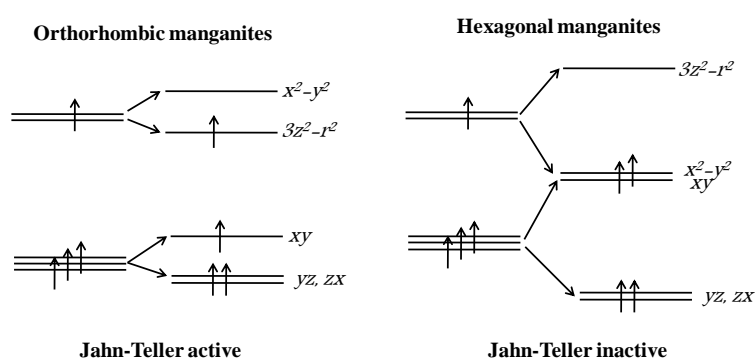


**Figure 1.16:** Crystal field level of  $Mn^{+3}$  in orthorhombic and hexagonal manganites [30].

### 1.9.2 Structural change from orthorhombic to hexagonal with decreasing ionic radius of rare-earth ions

In order to quantify, the ionic size match of the A and B cations to the cubic perovskite, Goldschmidt tolerance factor is defined as

$$\tau = d(A-X)/[2^{1/2}d(B-X)]$$

where,  $d(A-X)$  is the ideal  $(A-X)$  distance and  $d(B-X)$  is the weighted average of the ideal  $(B-X)$  distances [31].

---

Perovskites with a tolerance factor equal to or greater than one exhibit no octahedral tilting. If A cation is too small for the corner-sharing octahedral network, then octahedral-tilting distortion takes place. Cooperative tilting of the undistorted octahedra shorten the A–X bonds and thereby improving the coordination environment and bonding of the A-site cation. Decreasing tolerance factor (increased tilting) leads to a larger distortion of the O–M–O angles. This is pronounced in the  $AMnO_3$  series, as a result of the Jahn-Teller distortion. The  $AMnO_3$  series, with  $Pnma$  (also sometime referred as  $Pbnm$ ) perovskite structure becomes increasingly unstable as the octahedral tilting increases ( $< 0.88$ ), a trend that is exacerbated by the presence of a Jahn-Teller cation on the octahedral site. A hexagonal structure with space group  $P6_3cm$  with manganese in a trigonal-bipyramidal coordination is observed for  $AMnO_3$  compounds when the ionic radius of the A-site cation becomes too small that makes  $\tau < 0.88$ . For  $RFeO_3$  series orthorhombic to hexagonal structure transformation takes place  $\tau = 0.85$  [32].

### 1.9.3 Phase diagram of $RMnO_3$

The most significant effect on the crystal structure by decreasing rare-earth radius,  $r_R$  is an enhancement of the cooperative rotation of the  $MnO_6$  octahedra characterized by the decrease of Mn–O–Mn bond angle. The  $T_{OO}$  monotonically increases with decreasing  $r_R$ , while the magnetic transition occurs from the A-type AF to the E-type one through the incommensurate structure.

With decreasing  $r_R$ ,  $T_{OO}$  is shifted toward higher temperature, with further smaller  $r_R$  than  $r_{Nd}$ , no anomaly was observed up to 1500 K. Thus, the orbital-ordering (OO) state associated with the cooperative JT distortion is extremely stable in  $RMnO_3$  with smaller  $r_R$ .



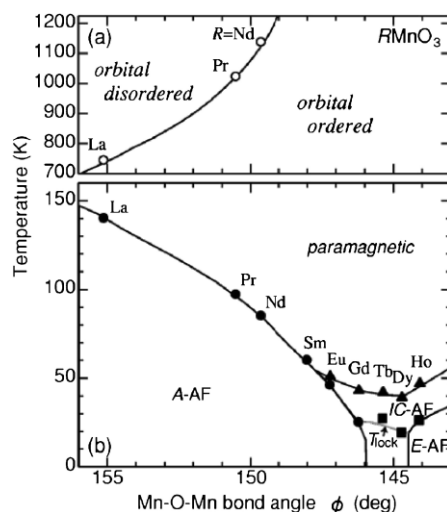


**Figure 1.17:** (a) Orbital and (b) spin ordering temperature of  $RMnO_3$  as a function of the in-plane Mn–O–Mn bond angle [33].

With decreasing  $\phi$ ,  $T_N$  for the A-type AF order monotonically decreases. With the suppression of the A-type AF order, the incommensurate (IC) sinusoidal magnetic structure propagating along the  $b$  axis appears. With further decreasing  $\phi$ , the CM (E-type AF structure) magnetic structure with the wave vector of  $(0, 1/2, 0)$  turns up at the ground state in  $HoMnO_3$ . When R is large (La and Pr) the magnetic ground state is A-type antiferromagnetic phase. When R is very small (Ho and Tm), it becomes E-type antiferromagnetic order. In the middle region (e.g. Tb and Dy) between the A-type and E-type antiferromagnets, the ground state is spiral spin order [33, 34].

#### 1.9.4 Properties of hexagonal manganites

In 1963, Bertaut *et al.* first observed ferroelectricity in single crystals of hexagonal manganites,  $RMnO_3$  (R=Er, Lu, Y) [35]. In the same year Bokov *et al.* showed antiferromagnetic ordering in single crystals of  $RMnO_3$  (R=Yb, Y) [36]. Smolenskii *et al.* first

---

confirmed the presence of ferroelectric and antiferromagnetic ordering of  $\text{Mn}^{+3}$  ions in  $\text{Yb,YMnO}_3$  single crystals [37]. First experimental observation of ferroelectric transition was demonstrated in  $\text{YMnO}_3$  by Ismailzade *et al.* [38].

Single phase multiferroic materials which show both ferroelectricity and magnetism in same phase are of great interest due to its application in memory devices. Such coexistence of electric and magnetic ordering in hexagonal manganites with  $T_c$ , 900–1000 K and  $T_N$ , 80–140 K. Hexagonal manganites undergoes a ferroelectric transition from room temperature non-centrosymmetric phase to high temperature centrosymmetric phase. Recently it is proven that antiferromagnetic and ferroelectric order parameters are coupled in this system [39, 40]. This coupling allow its application in magnetoelectric devices. Multiferroics without lone pair shows low polarization values but hexagonal manganites show saturation polarization of  $\sim 5.5 \mu\text{C}/\text{cm}^2$  [41].

In hexagonal manganites, origin of ferroelectricity in  $\text{YMnO}_3$ , was demonstrated by Kimura *et al.* They showed that tilting of  $\text{MnO}_5$  bipyramids and buckling of R-layer is responsible for non-centrosymmetry in  $\text{YMnO}_3$ .

### 1.9.5 Properties of orthorhombic manganites

Crystal structure of orthorhombic manganites are simple cubic with little deformation. High temperature phase of orthorhombic manganites are pseudo-cubic. At low temperature, combination of small A-site size and Jahn-Teller effect, distorts and rotates the  $\text{MnO}_6$  octahedra. In orthorhombic manganites, Mn–O bond distance and Mn–O–Mn bond angle are important to know as these parameter determines the competition between super-exchange and double-exchange interaction. Two deformations which are generally observed in orthorhombic manganites are  $\text{GdFeO}_3$  rotation, and Jahn-Teller distortion. Due to small size

---

of A-site cation, the  $\text{MnO}_6$  octahedra tilt and buckle to accommodate lanthanide cation. This is  $\text{GdFeO}_3$  rotation in orthorhombic manganites. Simple cubic structure allows only one unique position of O ions, due to  $\text{GdFeO}_3$  rotation there are two inequivalent position of oxygen ion in the unit cell. Due to the degeneracy of  $d^4$  ( $\text{Mn}^{+3}$ ) in an octahedral crystal field, two types of Jahn-Teller distortion are possible. In orthorhombic distortion, in-plane Mn–O bond length changes (shortens or extends), in tetragonal distortion, in-plane Mn–O bond length shortens and out-of-plane bond extends and vice versa [42,43].

### 1.10 Applications

The discovery of giant magneto-resistance (GMR) by Albert Fert and Peter Grünberg for which they got Nobel prize in 2007 gave birth to the field of spintronics, where electron spin was found to be functional in electronics. After the introduction of 3-D storage devices with current controlled read-write heads like MRAM, the heat release became a serious problem. The electric field controlled read-write heads with minimum Joule heating became the frontier research field in electronic industry. Magnetoelectric materials find application in magnetic tunnel junctions which can be controlled by electric fields. In a magnetoelectric RAM, to combine the ultrafast (250 ps) electrical WRITE operation with the non-destructive (no reset) magnetic READ operation, thus in turn combining the best qualities of FeRAM and MRAM. These materials can also be used as four state memory system [44, 45].

### 1.11 Synthesis of nano crystalline rare-earth manganites

Synthesis of perovskite  $\text{RMnO}_3$  (R=rare-earth ions) is challenging due to the fact that, Mn can exist in both +3 and +4 oxidation. Rare-earth manganites have been synthesized by solid state reaction, at high annealing temperature (1400 °C). This annealing is carried out in

appropriate gas environment to get proper stoichiometry [46]. The synthesis of nano sized rare-earth manganites were focused mostly around  $\text{LaMnO}_3$ ,  $\text{La}_x\text{Ca}_{1-x}\text{MnO}_3$  compounds due their wide range of applications. Micron/nano sized manganites were mostly synthesized by hydrothermal, sol-gel, polymer complexation reactions. High temperature annealing was used in all the cases in order to get the single phase. High temperature annealing causes the particles to aggregate leading poor control of size and morphology. There is no report in literature of monodisperse, controlled morphology of rare-earth manganites except some reports on  $\text{LaMnO}_3$ .

Hydrothermal/solvothermal method was used by several researchers to get single phase  $\text{RMnO}_3$  mostly with micron size crystals. Stamper *et al.* synthesized micron sized  $\text{RMnO}_3$  (R = Ho–Lu and Y) using hydrothermal method by dissolving representative oxides in alkaline aqueous solution.

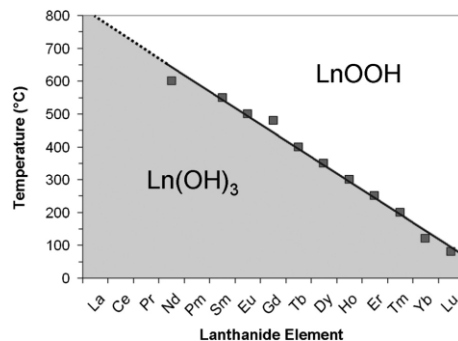


**Figure 1.18:** Temperature boundary that separates the stability ranges of rare-earth trihydroxides from the rare-earth oxide hydroxides in hydrothermal conditions [47].

Nano size orthorhombic  $\text{DyMnO}_3$  was prepared by the sol-gel method. For the reaction stoichiometric amounts of high purity  $\text{Mn}_3\text{O}_4$  and  $\text{Dy}_2\text{O}_3$  oxides were dissolved in acetic acid with hydrogen peroxide. Then urea was added to the solution and mixture was evaporated to

dryness. The dried powder was decomposed at 250–450 °C. Later, the powder was annealed at 800 and 850 °C for 20 h in air. The grain sizes calculated using X-ray data were ~28 and 48 nm respectively for samples annealed at 800 and 850 °C, respectively. In this study, they have shown that crystal structure parameters, the Néel, Curie temperatures and effective magnetic moments do not change with the grain size [48].

In another report, hydrothermal method was used to synthesize two metastable perovskite rare-earth manganites, HoMnO<sub>3</sub> and DyMnO<sub>3</sub>. For the reaction, HNO<sub>3</sub> solution, KMnO<sub>4</sub>, MnCl<sub>2</sub>·4H<sub>2</sub>O were mixed with H<sub>2</sub>O and 20 g KOH. The reaction mixture was placed in the autoclave and heated at 250 °C under the autogenous pressure for 2 days. The formed crystals were pyramidal shape with size 40–50 μm [49]. Similarly RMnO<sub>3</sub> (R=Yb and Lu) nanocrystalline samples were prepared by hydrothermal method using KMnO<sub>4</sub> and Mn(C<sub>2</sub>H<sub>3</sub>O<sub>2</sub>)<sub>2</sub> as the manganese source by Zhu *et al.* [50].

Single-crystalline La<sub>1-x</sub>Ba<sub>x</sub>MnO<sub>3</sub> nanocubes with an adjustable Ba doping was synthesized via hydrothermal method. In a typical synthesis, MnCl<sub>2</sub>·4H<sub>2</sub>O, KMnO<sub>4</sub>, La(NO<sub>3</sub>)<sub>3</sub>·6H<sub>2</sub>O, and Ba(OH)<sub>2</sub>·8H<sub>2</sub>O were mixed in distilled water. The solution was made strongly alkaline by saturating it with KOH. The reaction mixture was placed in hydrothermal cell and kept at 300 °C for 24 h [51].

In another approach, orthorhombic YMnO<sub>3</sub> and HoMnO<sub>3</sub> have been prepared by solution based procedure via complexation by citrates [52]. Alonso *et al.* demonstrated synthesis of rare-earth manganites (R=Pr, Nd, Dy, Tb, Ho, Er, Y) by dissolving R<sub>2</sub>O<sub>3</sub> and MnCO<sub>3</sub> in citric acid by adding concentrated HNO<sub>3</sub> [53].

GdMnO<sub>3</sub> nanoparticles were synthesized by a polymerized complex method. In this reaction, aqueous solution of Mn(NO<sub>3</sub>)<sub>2</sub>, Gd(NO<sub>3</sub>)<sub>3</sub> and citric acid was adjusted to pH 6 by adding dilute ammonia solution. Then, ethylene glycol was added to make gelation. The

---

solution was stirred and heated at 100 °C until a gel was formed. This gel was further dried at 130 °C and grounded. Finally, black precursor powders were calcined 800 °C for 5 h [54].

There is very less understanding on synthesis mechanism of rare-earth manganites. The understanding of synthesis mechanism will open up a new research area, of size and morphology dependent multiferroic properties of rare-earth manganites.

---

**1.12 References**

- [1] Aleksandrov, K. S.; Bartolome, J. *Phase Transitions* **2006**, 74, 255.
- [2] Woodward, P. M. *Acta Cryst. B* **1997**, 53, 32.
- [3] Cheong, S. W.; Mostovoy, M. *Nat. Mater.* **2007**, 6, 13.
- [4] Hill, N. A. *J. Phys. Chem. B* **2000**, 104, 6694.
- [5] Cullity, B. D.; Graham, C. D. *Introduction to magnetic materials*, 2009, John Wiley & Sons Inc.
- [6] Wollan, E. O.; Koehler, W. C. *Phys. Rev.* **1955**, 100, 545.
- [7] Khomskii, D. I. *J. Magn. Magn. Mater.* **2006**, 306, 1.
- [8] Schmid, H. *Ferroelectrics* **1994**, 162, 317.
- [9] Khomskii, D. *Physics* **2009**, 2, 20.
- [10] Ascher, E.; Rieder, H.; Schmid, H.; Stoessel, H. *J Appl. Phys.* **1966**, 37, 1404.
- [11] Wang, J.; Neaton, J. B.; Zheng, H.; Nagarajan, V.; Ogale, S. B.; Liu, B.; Viehland, D.; Vaithyanathan, V.; Schlom, D. G.; Waghmare, U. V.; Spaldin, N. A.; Rabe, K. M.; Wuttig, M.; Ramesh, R. *Science* **2003**, 299, 1719.
- [12] van den Brink, J.; Khomskii, D. I. *J. Phys.: Condens. Matter.* **2008**, 20, 434217.
- [13] Efremov, D. V.; van den Brink, J.; Khomskii, D. I. *Nat. Mater.* **2004**, 3, 853.
- [14] Aken, B. B. V.; Palstra, T. T. M.; Filippetti, A.; Spaldin, N. A. *Nat. Mater.* **2004**, 3, 164.
- [15] Kenzelmann, M.; Harris, A. B.; Jonas, S.; Broholm, C.; Schefer, J.; Kim, S. B.; Zhang, C. L.; Cheong, S.W.; Vajk, O. P.; Lynn, J. W. *Phys. Rev. Lett.* **2005**, 95, 087206.
- [16] Kimura, T. *Annu. Rev. Mater. Res.* **2007**, 37, 387.
- [17] Kimura, T.; Goto, T.; Shintani, H.; Ishizaka, K.; Arima, T.; Tokura, Y. *Nature* **2003**, 426, 55.
- [18] Katsura, H.; Nagaosa, N.; Balatsky, A. V. *Phys. Rev. Lett.* **2005**, 95, 057205.
-

- 
- [19] Mostovoy, M. *Phys. Rev. Lett.* **2006**, *96*, 067601.
- [20] Ishihara, S. *J. Phys. Soc. Jpn.* **2010**, *79*, 011010.
- [21] Landau, L.D.; Lifshitz, E. M. *Electrodynamics of Continuous Media*, **1960**, Pergamon, Cambridge.
- [22] Fiebig, M. *J. Phys. D: Appl. Phys.* **2005**, *38*, R123.
- [23] Pollert, E.; Krupicka, S.; Kuzmicova, E. *J. Phys. Chem. Solids* **1982**, *43*, 1137.
- [24] Zhao, G-M.; Conder, K.; Keller, H.; Müller K. A. *Nature* **1996**, *381*, 676.
- [25] Zener, C. *Phys. Rev.* **1951**, *82*, 403.
- [26] Zener, C. *Phys. Rev.* **1951**, *81*, 440.
- [27] Tokura, Y. *Reports on Progress in Physics* **2006**, *69*, 3.
- [28] Van Aken, B. B.; Palstra, T. T. M.; Filippetti, A.; Spaldin, N. A. *Nat. Mater.* **2004**, *3*, 164.
- [29] Dong, S.; Liu, J. M. *Modern Phys. Lett. B* **2012**, *26*, 1230004.
- [30] Kang, J. S.; Han, S. W.; Park, J. G.; Wi, S. C.; Lee, S. S.; Kim, G.; Song, H. J.; Shin, H. J.; Jo, W.; Min, B. I. *Phys. Rev. B* **2005**, *71*, 092405.
- [31] Goodenough, J. B.; Zhou, J. S. *J. Mater. Chem.* **2007**, *17*, 2394.
- [32] Lufaso, M. W.; Woodward, P. M. *Acta. Cryst. B* **2004**, *60*, 10.
- [33] Goto, T.; Kimura, T.; Lawes, G.; Ramirez, A. P.; Tokura, Y. *Phys. Rev. Lett.* **2004**, *92*, 257201.
- [34] Kimura, T.; Ishihara, S.; Shintani, H.; Arima, T.; Takahashi, K. T.; Ishizaka, K.; Tokura, Y. *Phys. Rev. B* **2003**, *68*, 060403(R).
-



- 
- [35] Bertaut, E. F.; Forrat, E. F.; Pang, P. *C. R. Acad. Sci. Paris* **1963**, 256, 1958.
- [36] Bokov, V. A.; Smolenski, G. A.; Kizhaev, S. A.; Mylnilova, I. E. *Sov. Phys. Solid State* **1964**, 5, 2646.
- [37] Smolenskii, G. A.; Bokov, V. A. *J. Appl. Phys.* **1964**, 35, 915.
- [38] Ismailzade, I. G.; Kizhaev, S. A. *Sov. Phys. Solid State* **1965**, 7, 236.
- [39] Iliev, M. N.; Lee, H.-G. *Phys. Rev. B* **1997**, 56, 2488.
- [40] Fiebig, M.; Lottermoser, T.; Fröhlich, D.; Goltsev, A. V.; Pisarev, R. V. *Nature* **2002**, 419, 818.
- [41] Peuzin, J.-C. *C. R. Acad. Sc. Paris* **1965**, 261, 2195.
- [42] Dabrowski, B.; Xiong, X.; Bukowski, Z.; Dybziński, R.; Klamut, P. W.; Siewenie, J. E.; Chmaissem, O.; Shaffer, J.; Kimball, C. W.; Jorgensen, J. D.; Short, S. *Phys. Rev. B* **1999**, 60, 7006.
- [43] Urushibara, A.; Moritoma, Y.; Arima, T.; Asamitsu, A.; Kido, G.; Tokura, Y. *Phys. Rev. B* **1995**, 51, 14103.
- [44] Eerenstein, W.; Mathur, N. D.; Scott, J. F. *Nature* **2006**, 442, 759.
- [45] Scott, J. F. *J. Mater. Chem.* **2012**, 22, 4567.
- [46] Modeshia, D. R.; Walton, R. I. *Chem. Soc. Rev.* **2010**, 39, 4303.
- [47] Klevtsov, P. V.; Sheina, L. P. *Izv. Akad. Nauk, Neorg. Mater.* **1965**, 1, 912.
- [48] Dyakonov, V.; Szytuła, A.; Baran, S.; Kravchenko, Z.; Zubov, E.; Iessenchuk, O.; Bazela, W.; Dul, M.; Zarzycki, A.; Szymczak, H. *Acta Physica Polonica A* **2010**, 117, 607.
-

- 
- [49] Wang, Y.; Lu, X.; Chen, Y.; Chi, F.; Feng, S.; Liu, X. *J. Solid State Chem.* **2005**, *178*, 1317.
- [50] Zhu, G.; Liu, P.; Liu, Y.; Miao, H.; Zhou, J. *J. Am. Ceram. Soc.* **2008**, *91*, 3423.
- [51] Urban, J. J.; Ouyang, L.; Jo, M.-H.; Wang, D. S.; Park, H. *Nano Lett.* **2004**, *4*, 1547.
- [52] Brinks, H. W.; Fjellvag, H.; Kjekshus, A. *J. Solid State Chem.* **1997**, *129*, 334.
- [53] Alonso, J. A.; Martínez-Lope, M. J.; Casais, M. T. *Inorg. Chem.* **2000**, *39*, 917.
- [54] Wang, X. L.; Li, D.; Cui, T. Y.; Kharel, P.; Liu, W.; Zhang, Z. D. *J. Appl. Phys.* **2010**, *107*, 09B510.

## **Chapter 2. Experimental methods**

---

This chapter describes hydrothermal and solid-state reaction methods used in this thesis for the synthesis of materials used in the study. Different experimental techniques used for characterization and measuring properties of materials were also discussed.

---

---

## 2.1 Methods of synthesis

### 2.1.1 Hydrothermal synthesis

Among low temperature synthesis routes, hydrothermal method is interesting because it is environmental friendly, energy efficient and very versatile method for synthesis of large variety of materials [1–4]. In hydrothermal method, reaction takes place in a sealed heated vessel to achieve condition above atmosphere pressure and temperature. In hydrothermal synthesis, at temperature in the range 100–200 °C superheated water acts as a strongly polarizing agent, provides reaction conditions adequate to enhance solubility, diffusion, and crystallization.

The operating variables in hydrothermal synthesis are

- a) molar ratio of reagents
- b) temperature
- c) pH
- d) reaction time

The molar ratios of reactants play an important role in determining the degree of supersaturation, which influence the rate of crystal-growth. Introducing a complexing agent into the solution, may induce supersaturation. The complexing agent needs to be stable enough and exist in adequate concentration to enhance solubility but not be so stable to form solid phase. Critical growth of crystals directly depends on the temperature. Generation of autogenous pressure within the autoclave highly depends on the temperature of the experiment. In aqueous solution growth, the aim is to supersaturate the solution without causing spontaneous nucleation, which hamper crystalline product. Water promotes density of dissolve materials, a higher diffusivity, a low viscosity facilitating mass transport and high

---

compressibility allows easy changes in density and dissolving power. Water enhances chemical reaction under elevated pressure [5–9].

The advantages of hydrothermal synthesis are high reactivity of reactants, easy control of solution or interface reactions, formation of metastable and unique condensed phases, less air pollution, and lower energy consumption [10].

In a typical reaction, stoichiometric amounts of rare-earth (III) nitrate, magnesium (II) nitrate and an equal amount of citric acid ( $C_6H_8O_7$ ) [(metal/citric acid molar ratio=1/1)] were dissolved in deionized water. The transparent solution was stirred for 6 h followed by drop-wise addition of ammonia solution (28 wt. %) to neutralize the unreacted citric acid as well as to raise the pH value of the solution near 9.2 resulting in sol formation. Further the solution was stirred for 3 h and then transferred into an 80 mL capacity autoclave with the Teflon liner. After the hydrothermal treatment at 200 °C for 20 h, the precipitate was in turn filtered, washed with deionized water and finally dried at 100 °C. Finally, the powder sample was calcined at different temperature and duration.

In our study, we showed the particles formed by above mentioned reaction were having mostly plate-like morphology. We believe that, nitrate and citrate ions are extremely important for morphology. It is known that, apart from other factors such as twinning, stacking faults and so forth, the shape control in wet-chemical synthesis can also be driven by preferential binding of ionic ligands, surfactants to the particular lattice facets due to their variable degree of affinity from one facet to another, which allows the growth of particular facets while restricting the growth of others. In hydrothermal synthesis, the strong affinity of both nitrate and citrate ions with metal ions towards particular crystalline facets might have promoted the formation of negatively charged anisotropic structures much similar to the role of halide ions in the formation of anisotropic gold nanoparticles [11]. However,

experimentally, it is quite difficult to prove the role of preferential binding of ionic ligands on the overall morphologies.

### 2.1.2 Solid-state reaction

The rate at which product is formed in solid-state reaction is governed by diffusion of reactant through product layer, nucleation of the product at active site and growth of nuclei. Solid-state reaction starts at the nucleation site and the product grows at the expense of unreacted reactant. The kinetics of solid-state reaction can be expressed as  $\alpha = f(kT)$  where  $\alpha$ =fractional reaction completed,  $k$ =kinetic rate constant [12]. The activation energy of solid-state reactions are calculated from temperature dependent kinetic rate constant by assuming the reaction to be diffusion controlled [13]. Activation energy of solid-state reaction varies largely depending upon the nature and method of preparing starting materials.

Bulk polycrystalline samples of  $\text{RMnO}_3$  were synthesized by the conventional solid-state reaction method, using stoichiometric mixtures of high purity metal oxide as starting materials. The compounds were ground thoroughly in a mortar and calcined at 850 °C for 24 h. Again, the sample was ground and calcined at 1300 °C for 24 h. Finally, the ground sample was compressed into pellet and was sintered at 1400 °C for 24 h.

## 2.2 Characterization and measurement techniques

### 2.2.1 Powder X-Ray diffraction

Powder X-ray diffraction (PXRD) was used to check the phase formation and determination of structure. The Bragg's law is used to treat diffraction from crystals. The Bragg's law is given as

$$n\lambda = 2d\sin\theta$$

---

where,  $d$  is the spacing between two adjacent lattice planes,  $\lambda$  is the wavelength of the X-ray,  $n$  is an integer and  $\theta$  is the Braggs angle or diffraction angle [14].

The width of the diffraction peak increases when the crystallite size is reduced below a certain limit ( $\leq 100$  nm). So, XRD patterns can be used to measure the average crystallite size. Scherrer formula is used to calculate the crystallite size which is given by

$$t = 0.9 \lambda / \beta \cos\theta$$

where,  $t$  is the crystallite size (in Å),  $\lambda$  is wavelength of the X-ray radiation,  $\beta$  is the FWHM (in radian) and  $\theta$  is the diffraction angle [14].

The width of the FWHM increase with the decrease in crystallite size due to the fact that reducing the particle size, increase the rms atomic displacement and lattice strain in the particle.

In this thesis, PXRD were carried out using a PANalytical X'PERT PRO instrument using iron-filtered Cu-K $\alpha$  radiation ( $\lambda=1.5406$  Å) in the  $2\theta$  range of  $10-80^\circ$  with a step size of  $0.02^\circ$ .

### 2.2.2 Transmission electron microscopy

Transmission electron microscopy (TEM) is an imaging technique whereby a beam of electrons is focused onto a specimen causing an enlarged version to appear on a fluorescent screen or photographic film, or to be detected by a CCD camera. TEM operates on the same basic principles as the light microscope but uses electrons instead of light. TEM is useful for determining size, shape and arrangement of the particles which make up the specimen.

---

Moreover, it is highly useful for determination of the lattice planes and the detection of atomic-scale defects in areas of few nanometers in diameter with the help of selected area electron diffraction (SAED) technique. The  $d$ -spacing between lattice planes of crystalline materials can be calculated from a SAED pattern using the relationship,

$$dr = \lambda L$$

where  $L$  is the distance between the specimen and the photographic plate,  $\lambda L$  is known as the camera constant and  $r$  is the radius of diffracted rings.

It is easy to measure  $r$  directly from the photographic plate, and  $\lambda L$  can be established from the instrument by calibrating it with a standard material (usually Ag), and hence one can easily get  $d$  values. Since each  $d$  value corresponds to a specific lattice plane for a specific crystal structure, a minimum description of the crystal structure of a crystalline specimen can be obtained from a SAED pattern [15].

In the present thesis, we used F30 high resolution transmission electron microscope (HRTEM) equipped with a super twin lens (s-twin) operated at 300 kV accelerating voltage with Schottky field emitter source with maximum beam current ( $> 100$  nA) and small energy spread (0.8 eV or less). The point to point resolution of the microscope is 0.20 nm and line resolution of 0.102 nm with a spherical aberration of 1.2 mm and chromatic aberration of 1.4 mm with 70  $\mu\text{m}$  objective aperture size.

### 2.2.3 Scanning electron microscopy

Scanning electron microscopy (SEM) is a tool which gives information about the 3-dimensional microstructure morphology. Main components of scanning electron microscopy



are electron gun, electromagnetic lenses and detector. Electron gun produces electron beam, electromagnetic lenses focused electron probe and detector detects the signal after the interaction of electron beam with sample. To produce image of a specimen focused electron beam is scanned across a specimen with a scanning coil and point of specimen struck by electron beam emits secondary electrons. The collected secondary electrons are detected and amplified by detector and produce image of the specimen's 3-D morphology [16]. SEM imaging was performed on a FEI Quanta 200 environmental scanning electron microscope.

#### 2.2.4 X-ray photoelectron spectroscopy

X-ray photoelectron spectroscopy (XPS) is a quantitative technique that measures the elemental composition, chemical state of the element that exists in the material. XPS spectra are obtained by irradiating a material with a beam of X-ray while spontaneously measuring the kinetic energy and number of electron that escape from the sample surface. XPS is done under ultra high vacuum condition.

Since the energy of the X-ray used is a known quantity, we can determine the binding energy of the emitted electron by using the equation

$$E_{\text{binding}} = E_{\text{photon}} - E_{\text{kinetic}} - \phi$$

$E_{\text{binding}}$  is the binding energy of the emitted electron,  $E_{\text{photon}}$  is the energy of the X-ray used,  $E_{\text{kinetic}}$  is the kinetic energy of the emitted electron and  $\phi$  is work function of the spectrometer [17, 18].

A typical XPS spectrum is plot of number of electron detected versus the binding energy of the detected electron. Each element has a characteristic binding energy, so it gives directly the information about the element present in the sample [17, 18].

---

In the present thesis, X-ray photoelectron spectroscopy (XPS) was done with an ESCALab spectrometer having Al-K $\alpha$  x-ray source ( $h\nu=1486.6$  eV) operating at 150 W using a Physical Electronics 04-548 dual Mg/Al anode and in a UHV system with a base pressure of  $\leq 5 \times 10^{-9}$  Torr. Both the incident and take off angles are  $55^\circ$  with respect to the surface normal. The analysis depth was around 10 to 15 Å. The spectra were energy-analyzed with an Omicron Nanotechnology EA 125 Hemispherical Energy Analyzer in pulse-count mode with pass energies of 50 eV for broad scan data and 25 eV for specific, narrow-range core-level transitions. We used Shirley algorithm for background correction and chemically distinct species were resolved using a nonlinear least squares fitting procedure. The core level binding energies were aligned with the carbon binding energy of 285 eV.

### 2.2.5 Raman spectroscopy

The phenomenon Raman scattering was discovered in 1928 by Sir Chandrasekhra Venkata Raman, using sunlight as a source, telescope as a collector and his eyes as a detector. When monochromatic radiation of frequency  $\omega_1$  is incident on systems such as dust free, transparent gases and liquids, or optically perfect transparent solids, most of it is transmitted without change but, in addition, some scattering of the radiation occurs. If the frequency content of the scattered radiation is analysed, there will not present only the frequency  $\omega_1$  associated with the incident radiation but also, in general, pairs of new frequencies of the type  $\omega_1 \pm \omega_M$ . In molecular systems, the frequencies  $\omega_M$  are found to lie principally in the ranges associated with transitions between rotational, vibrational and electronic levels. The scattered radiation usually has polarization characteristics different from those of the incident radiation. The scattering occurs over all directions and both the intensity and polarization of the scattered radiation depend on the direction of observation.

The scattering without change of frequency is called Rayleigh scattering, and that with change of frequency is called Raman scattering. Raman bands at frequencies less than the incident frequency (i.e. of the type  $\omega_1 - \omega_M$ ) are called Stokes bands and those at frequencies greater than the incident frequency (i.e. of the type  $\omega_1 + \omega_M$ ) as anti-Stokes bands. Raman scattering is inherently incoherent and as a result the intensity of scattering from a material system of  $N$  non-interacting molecules is simply  $N$  times that from one molecule [19, 20].

Raman spectroscopy measurements were recorded at room temperature on an HR 800 Raman spectrophotometer (Jobin Yvon, Horiba, France) using monochromatic radiation (achromatic Czerny-Turner type monochromator with silver treated mirrors) emitted by a He-Ne laser (633 nm), operating at 20 mW and with accuracy in the range between 450 nm and 850 nm  $\pm$  1 cm<sup>-1</sup>, equipped with thermoelectrically cooled (with Peltier junctions), multi-channel, spectroscopic grade charge coupled detector (1024 $\times$ 256 pixels of 26 microns) with dark current lower than 0.002 electrons pixel<sup>-1</sup>s<sup>-1</sup>. An objective of x50 magnification was used both to focus and collect the scattered light from the sample, dispersed on a glass slide.

### 2.2.6 UV-vis-NIR spectroscopy

UV-vis spectroscopy is a technique to measure intensity of absorption of ultra-violet and visible light by sample. UV-vis-NIR light excite an electron from outer orbital to higher energy state. So, UV-vis-NIR spectroscopy is used determine optical band-gap of materials.

In the present thesis, UV-vis-NIR spectroscopy was carried out on a Jasco UV-vis-NIR spectrometer (model V570 UV/vis/NIR) dual-beam spectrometer operated at a resolution of 2 nm.

### 2.2.7 Vibrating sample magnetometer (VSM)

The basic principle of operation of VSM is changing of magnetic flux will produce a voltage in the pickup coil. The time dependent voltage induced can be written as,

$$\begin{aligned} V_{\text{coil}} &= d\phi/dt, \\ &= (d\phi/dz) (dz/dt) \end{aligned}$$

where,  $\phi$  is the magnetic flux,  $z$  is the vertical position of the coil with respect to the coil and  $t$  is the time [21].

For sinusoidal oscillating sample position the induced voltage can be written as,

$$V_{\text{coil}} = 2\pi f C m A \sin(2\pi f t)$$

where,  $C$  is coupling constant,  $m$  is DC magnetic moment of sample,  $A$  is amplitude of oscillation,  $f$  is frequency of oscillation.

The measurement is done by oscillating the sample near a pickup coil (detection coil) and synchronously detecting the voltage induced. Quantum Design uses a gradiometer pickup coil which operates at large oscillating amplitude of 1–3 mm (peak to peak) and 40 Hz frequency, the system is able to resolve magnetization change of  $10^{-6}$  emu at a data rate of 1 Hz.

DC magnetization versus temperature and magnetic field versus magnetization measurements were done using a Physical Property Measurement System (PPMS) from Quantum Design Inc., San Diego, CA., equipped with a 9 T superconducting magnet and a vibrating sample magnetometer operating at 40 Hz. Temperature dependent  $M-H$  loops were collected in a field sweep from  $-50$  to  $+50$  kOe at different scan rate by first demagnetizing the sample by heating it at 300 K in zero field before cooling it to the desired temperature. Magnetization versus temperature measurements in various field conditions in a broad

temperature range from 3 to 300 K with cooling and heating rates of 2 K/min were recorded. For the field cooled measurements (FC), at first, the desired field was applied at 300 K and sample was cooled down to 3 K, for the zero field cooled measurements (ZFC), the sample was cooled without applying any external field and the desired field was turned-on at 3 K and the magnetic signal was picked-up while heating the sample in both ZFC and FC mode.

### 2.2.8 AC measurement system (ACMS)

The ACMS option of PPMS can serve as both DC magnetometer and AC susceptometer. It consists of drive and detection coil, thermometer and electronics. AC drive coil set provides an alternating excitation field and the detection coil inductively measures the sample moment and excitation field [22]. Drive coil can generate alternating field of  $\pm 10$  Oe and frequency in range of 10 Hz to 10 kHz. The ac magnetic measurements were performed using an AC Susceptibility & DC Magnetization Option (ACMS) from Quantum Design Inc., San Diego, CA.

### 2.2.9 Impedance spectroscopy

For impedance measurements, a voltage  $U_o$  with a fixed frequency  $\omega/2\pi$  is applied to a sample in a capacitive arrangement.  $U_o$  causes a current  $I_o$  in the sample with same frequency with a phase shift between current and voltage, with phase angle  $\phi$ . The ratio of  $U_o/I_o$  and phase angle  $\phi$  is dependent on sample geometry and sample material [23].

For a sample with linear electromagnetic response,

$$Z = Z' + i Z'' = U^*/I^*$$

This connected to dielectric function of materials as,

$$\begin{aligned}\varepsilon^*(\omega) &= \varepsilon' - i\varepsilon'' \\ &= [-i/\omega Z^*(\omega)][1/C_o]\end{aligned}$$

$C_o$  is the empty cell capacitor.

$$\text{Loss factor, } \tan(\delta) = \varepsilon''/\varepsilon'.$$

For impedance measurements, we used Novocontrol beta impedance analyzer with a home-built sample holder to couple with a Janis Inc. helium closed cycle refrigerator in a frequency range from 0.1 Hz to  $1 \times 10^6$  Hz at 1 V (rms) and with no dc bias. The data were taken in a temperature range from 15–325 K at each 2 K step size. A compressed circular pallet, with 13 mm diameter, was kept in a custom designed sample holder to form a circular parallel plate capacitor geometry.

---

### 2.3 References

- [1] Spooren, J.; Ruplecker, A.; Millange, F.; Walton, R. I. *Chem. Mater.* **2003**, *15*, 1401.
- [2] Feng, S.; Wang, D.; Yu, R.; Na, L. *Proceedings of the International Symposium on Solvo-Hydro-Thermal Processes* **1997**, 12.
- [3] Feng, S.; Li, G.; Zhao, C.; Wang, G.; Wang, D.; Mao, Y. *Proc. 2nd Int. Conf. Solvothermal Reactions; Org. Comm. Solvothermal Tech. Res.: Takamatsu, Japan* **1996**, 101.
- [4] Hagrman, P. J.; Hagrman, D.; Zubieta, J. *Angew. Chem., Int. Ed.* **1999**, *38*, 2638.
- [5] Batten, S. R.; Robson, R. *Angew. Chem., Int. Ed.* **1998**, *37*, 1460.
- [25] Yaghi, O. M.; Li, H.; Davis, C.; Richardson, D.; Groy, T. L. *Acc. Chem. Res.* **1998**, *31*, 474.
- [6] Janiak, C. *Angew. Chem., Int. Ed. Engl.* **1997**, *36*, 1431.
- [7] West, A.R. *Solid State Chemistry* **1984**, John Wiley & Sons USA
- [8] Laudise, R.A. *The growth of single crystals* **1970**, Prentice Hall USA.
- [9] Wu, N. C.; Shi, E. W.; Zheng Y. Q.; Li, W. J. *J. Amer. Cer. Soc.* **2002**, *85*, 2462.
- [10] Henisch, H.K. *Crystal in Gels and Liesegang Rings* **1988**, CUP. Britain.
- [11] Younan, X.; Yujie, X.; Byungkwon, L.; Sara, E. S. *Angew. Chem. Int. Ed.* **2009**, *48*, 60.
- [12] Akhtar, N.; Janes, R.; Parker, M. J. *J. Mater. Sci.* **1996**, *31*, 3053.
- [13] El-Bellihi, A. A.; Abdel-Badei, A. M.; Diefallah, El-H. M. *Thermochimica Acta* **1990**, *165*, 147.
- [14] Cullity, B.D. *Elements of X-ray diffraction* **1959**, Addison-Wesley, London.
- [15] Williams D. B.; Carter, C. B. *Transmission Electron Microscopy: A Textbook for Materials Science* Vol. I-IV, **1996**, Plenum Press, New York.
- [16] Lawes, G. *Scanning electron microscopy and X-ray microanalysis: Analytical chemistry by open learning* John wiley & sons.

- 
- [17] Carlson, T. A. *Photoelectron and Auger spectroscopy* Plenum Press, New York and London.
- [18] Wagner, C. D.; Riggs, W. M.; Devis, L. E.; Mouldev, J. F.; Muilenberg, G. E. *Handbook of X-Ray Photoelectron Spectroscopy* **1979**, Eden Praivie, Minnesota 55344.
- [19] Derek, A. *Long Raman effect A unified treatment of the theory of Raman scattering by molecules* John Willey & Sons, Ltd. Baffins Lane, Chichester West Sussex PO19 1UD, England.
- [20] Amer, M. S. *Raman spectroscopy for soft matter applications* Wiley A John Willey & Sons, Inc., Publication Hoboken, New Jersey.
- [21] *Vibrating Sample Magnetometer (VSM) Option*, User's Manual Quantum Design, 6325 Lusk Boulevard San Diego, CA 92121 USA.
- [22] *AC Measurement System (ACMS) Option*, User's Manual Quantum Design 11578 Sorrento Valley Rd. San Diego, CA 92121-1311 USA.
- [23] *Alpha and beta dielectric, conductivity, impedance and gain phase analyser*, User's manual, Novacontrol Technologies.



# Chapter 3. Hexagonal rare-earth manganites

## (RMnO<sub>3</sub>)

---

Hexagonal rare-earth manganites have fascinated material-scientists due to their rich interplay between spin, charge, and orbital ordering. Depending upon the size of the rare-earth ions, manganites crystallize in both orthorhombic (R=La, Ce–Dy) and hexagonal (R=Ho–Lu, Y, Sc) structure. Hexagonal manganites are improper ferroelectrics, which exhibit ferroelectric transition,  $T_{FE}$  900–1000 K and Néel transition,  $T_N$  80–140 K.

In this chapter, we discuss the synthesis of nano-sized hexagonal RMnO<sub>3</sub> (R=Er, Y, Yb, Lu) by modified hydrothermal method. Magnetic measurements on ErMnO<sub>3</sub> nanoparticles reveal that triggering of Er<sup>+3</sup> (4b) spin ordering by Mn<sup>+3</sup> spins at  $T_N$  can be suppressed by external field  $\geq 1500$  Oe. The bifurcation of ZFC–FC magnetization curves below  $\sim 40$  and  $\sim 20$  K for ErMnO<sub>3</sub> and YMnO<sub>3</sub> nanoparticles, respectively were attributed to SR of Mn<sup>+3</sup> spins due to DM interactions. Single-crystalline 1D- and 2D-YbMnO<sub>3</sub> nanocrystallites were synthesized by a complete ionic control, without the use of surfactant or template. Magnetic study of 1D, 2D, and bulk YbMnO<sub>3</sub> showed an influence of morphology. Two unique and field-dependent magnetic anomalies that were predicted earlier but never reported experimentally were shown in LuMnO<sub>3</sub> nanoparticles. The first anomaly was observed as a sharp bifurcation in the ZFC–FC magnetization curves below 44 K at 100 Oe applied field, was attributed to the reorientation of the Mn<sup>+3</sup> ions due to the DM interaction. A second transition, observed  $\sim 12$  K as a peak in the ZFC magnetization curves, can be explained by weak AFM coupling between Mn–O–Mn in the *ab* plane, which become dominant at lower temperature.

---

---

## Section 3.1 $R^{+3}$ and $Mn^{+3}$ spin interaction: $Er/YMnO_3$

---

This section presents magnetic and dielectric properties of hexagonal  $ErMnO_3$  and  $YMnO_3$  fine particles. Magnetic measurements revealed that triggering of  $Er^{+3}$  (4b) spin ordering by  $Mn^{+3}$  spins at  $T_N$  can be suppressed by an external field  $\geq 1500$  Oe. The bifurcation of ZFC–FC magnetization curves below  $\sim 40$  and  $\sim 20$  K for  $ErMnO_3$  and  $YMnO_3$  nanoparticles respectively were attributed to SR of  $Mn^{+3}$  spins due to DM interactions. The hump at  $\sim 8$  and  $\sim 10$  K in ZFC–FC magnetization curves and real part of ac magnetization curves, respectively for  $YMnO_3$  nanoparticles could be due to AFM ordering of  $Mn^{+3}$  spins in  $ab$ -plane. Temperature dependent dielectric spectroscopy showed anomaly in the vicinity of  $T_N$  for both  $ErMnO_3$  and  $YMnO_3$  nanocrystals indicating presence of ME coupling.

---

### 3.1.1 Introduction

Rare-earth manganites with general formula  $\text{RMnO}_3$  (R=rare-earth element) have always fascinated materials scientists, physicists and chemists due to their rich interplay between spin, charge and orbital ordering [1, 2]. Depending upon the size of the rare-earth ions, manganites crystallize in both orthorhombic (R=La–Dy) and hexagonal (R=Ho–Lu, Y, Sc) structures [3–6].  $\text{ErMnO}_3$  and  $\text{YMnO}_3$ , under normal conditions, crystallize in hexagonal phase. In hexagonal  $\text{RMnO}_3$ , the origin of ferroelectricity is not well understood, and they show large ferroelectric polarization ( $10\text{--}100 \mu\text{C}/\text{cm}^2$ ) at room temperature. Hexagonal manganites are improper ferroelectrics, which exhibit,  $T_{\text{FE}} 900\text{--}1000 \text{ K}$  and  $T_{\text{N}}, 80\text{--}140 \text{ K}$  [7–11]. Hexagonal  $\text{YMnO}_3$  undergoes an isostructural transition below  $T_{\text{N}}$  with an increase of  $c$ -parameter, and a decrease of  $a$ -parameter with unusual atomic displacements of the order of  $0.05\text{--}0.09 \text{ \AA}$  [12].  $\text{YMnO}_3$  comes under the category of geometric ferroelectrics, where opposing dipoles caused by opposite but unequal displacements of the two yttrium sites and the associated tilting and distortion of the  $\text{MnO}_5$  bipyramids result into ferroelectric ordering. This ferroelectricity solely depends on ionic size of rare-earth ions [13, 7]. Below  $T_{\text{N}}$  ( $\sim 75 \text{ K}$ ), bulk  $\text{YMnO}_3$  shows frustrated AFM in  $ab$ -plane due to triangular lattice arrangement.

In hexagonal  $\text{ErMnO}_3$ , magnetic ordering of  $\text{Mn}^{+3}$  sublattice is dominated by antiferromagnetic in-plane Mn–O–Mn SE-interaction and is supplemented by a weaker interplane Mn–O–O–Mn exchange interaction in the triangular lattice. Below  $T_{\text{N}}$ , a  $120^\circ$  spin arrangement of  $\text{Mn}^{+3}$  spins in the basal plane breaks the triangular frustration and  $\text{Mn}^{+3}$  spins orient along the crystallographic  $y$ -axis [14–17]. At  $T_{\text{N}}$ , the AFM,  $\text{Mn}^{+3}$  spins trigger ordering of  $\text{Er}^{+3}$  (4b) spins by a biquadratic coupling, whereas the  $\text{Er}^{+3}$  (2a) sites remain disordered. At temperature below  $\sim 10 \text{ K}$ , the ordering of  $\text{Er}^{+3}$  (2a) sublattice starts, inducing ordering of  $\text{Er}^{+3}$

(4b) site ( $\sim 7$  K) followed ordering of  $\text{Mn}^{+3}$  site  $\sim 2.5$  K. This inducing, ordering of  $\text{Er}^{+3}$  (4b) by  $\text{Er}^{+3}$  (2a) site is a linear coupling mechanism [18].

Nano-size effects on both magnetic and ferroelectric properties of various materials are well studied due to their potential application in various devices. Chemically synthesized  $\text{Fe}_3\text{O}_4$  nanoparticles (6–8 nm) show Verwey transition  $\sim 90$  K as compared to 120 K of bulk phase [19]. Similarly, FE–PE transition was observed in  $\text{BaTiO}_3$  nanoparticles (5–6 nm) [20]. These reports, drew attention for the investigation of physical properties of multiferroic materials at nanosize. There are very few reports on the multiferroic property of materials with crystallite size  $< 100$  nm, due to challenges associated with the synthetic chemistry, as high temperature calcination is required to form these phases.  $\text{RMnO}_3$  are mostly studied in bulk single crystalline, thin film and ceramic forms. However, recent reports on their nano-dimensional physical properties indicated interesting change in its behavior [21]. The effect of reduced crystallite size on ordering of  $\text{Mn}^{+3}$  and rare-earth ions is not well understood in literature. Nano-dimensional property of  $\text{ErMnO}_3$  is studied in particles prepared by sol-gel method, which showed  $T_N$  at 65 K [22, 23].

In this section, we have showed effect of reduced particle size on magnetic and electric properties of  $\text{ErMnO}_3$  and  $\text{YMnO}_3$  nanoparticles.

### 3.1.2 Synthesis

$\text{ErMnO}_3$  and  $\text{YMnO}_3$  nanoparticles were synthesized by modified hydrothermal method [24]. In a typical reaction, stoichiometric amounts of erbium (III) nitrate pentahydrate ( $\text{Er}(\text{NO}_3)_3 \cdot 5\text{H}_2\text{O}$ , Sigma Aldrich, 99.9% purity) or yttrium (III) nitrate pentahydrate ( $\text{Y}(\text{NO}_3)_3 \cdot 5\text{H}_2\text{O}$ , Sigma Aldrich, 99.9% purity) and manganese (II) nitrate  $x$  hydrate ( $\text{Mn}(\text{NO}_3)_2 \cdot x\text{H}_2\text{O}$ , Sigma Aldrich, 99.9% purity) and an equal molar ratio of citric acid

( $C_6H_8O_7$ , Merck, 99.5% purity) were dissolved in deionized water. To this, ammonia solution (28 wt %) was added drop-wise till the solution pH raised up to  $\sim 9.2$ . Further, sol was stirred for 3 h and transferred into a 80 mL capacity autoclave with a Teflon liner. After the hydrothermal treatment at 180 °C for 48 h, the precipitate was filtered, washed with deionized water and was dried in vacuum oven. Finally, the powder sample were calcined at 700 °C for 6 h and used for further study.

### 3.1.3 Structure and morphology

The X-ray diffraction pattern of synthesized powder matches with the reference data from hexagonal (PDF#140689 and PDF#251079) phase of bulk  $ErMnO_3$  and  $YMnO_3$  respectively (Figure 3.1.1, 3.1.2) with  $P6_3cm$  symmetry.

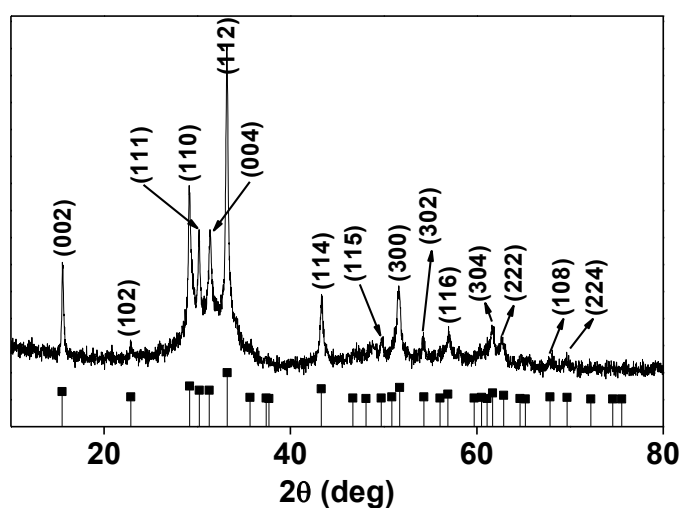


**Figure 3.1.1:** Room temperature powder XRD pattern of  $ErMnO_3$  from the JCPDS#140689 database (vertical line) and of as-prepared  $ErMnO_3$  nanoparticles annealed at 700 °C.

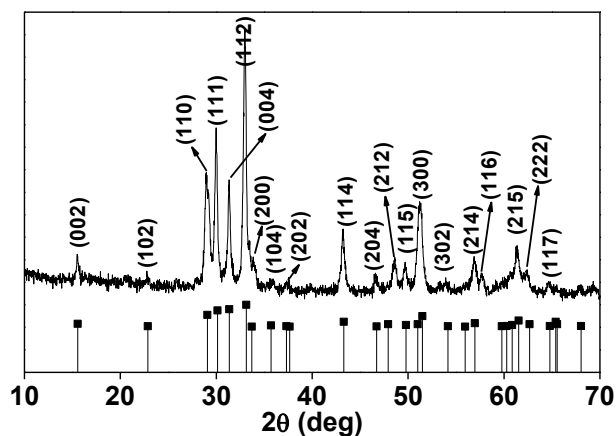
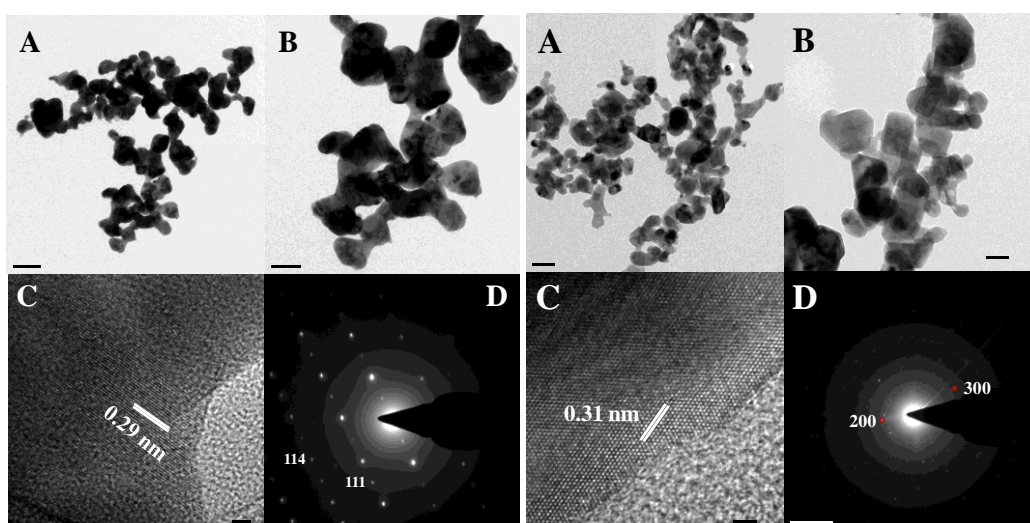


**Figure 3.1.2:** Room temperature powder XRD pattern of  $YMnO_3$  from the JCPDS#251709 database (vertical line) and of as-prepared  $YMnO_3$  nanoparticles annealed at 700 °C.

Variation in the relative peak intensity could be due to shape anisotropy of samples. The crystallite size calculated from Scherrer equation were ~50 and ~40 nm for  $ErMnO_3$  and  $YMnO_3$ , respectively.

The TEM images (figures 3.1.3, 3.1.4) suggest that particles have plate-like morphology with average particles size ~65 and ~50 nm for  $ErMnO_3$  and  $YMnO_3$ , respectively.



---

**Figure 3.1.3:** A, B) TEM images, C) HRTEM image of nanoparticle showing lattice fringes, D) SAED pattern of as-prepared  $\text{ErMnO}_3$ , shows that the particles are single-crystalline. **Figure 3.1.4:** A, B) TEM images, C) HRTEM image of nanoparticle showing lattice fringes, D) SAED pattern of as-prepared  $\text{YMnO}_3$ .

$\text{YMnO}_3$  nanoparticles have more regular shape than  $\text{ErMnO}_3$  nanoparticles (figures 3.1.3 A, B and 3.1.4 A, B). In figures 3.1.1 C and 3.1.4 we have shown the HRTEM images where we could see pronounced lattice fringes indicating good level of crystallinity. The  $d$ -values calculated from these images correspond to (111) and (110) planes of hexagonal  $\text{ErMnO}_3$  and  $\text{YMnO}_3$ , respectively. SAED patterns (figures 3.1.3 D and 3.1.4 D) show that  $\text{ErMnO}_3$  nanocrystallites are single crystalline whereas  $\text{YMnO}_3$  nanocrystallites are polycrystalline in nature.

### 3.1.4 Magnetic study

The M–H curves for both the samples (figures 3.1.5, 3.1.6) show no saturation in the measured temperature range as expected for AFM compounds.  $\text{ErMnO}_3$  nanoparticles show linear curves at  $\sim 30$  and  $\sim 50$  K (figure 3.1.5), whereas, at  $\sim 2$  and  $\sim 4$  K, it shows non-linear behavior.  $\text{YMnO}_3$  nanoparticles show coercivity of  $\sim 600$  Oe at  $\sim 2$  K whereas  $\text{ErMnO}_3$  nanoparticles show coercivity of  $\sim 260$ ,  $\sim 120$  Oe at  $\sim 2$  and  $\sim 4$  K, respectively (figures 3.1.5, 3.1.6). The high coercivity value for  $\text{YMnO}_3$  as compared to  $\text{ErMnO}_3$  nanoparticles at  $\sim 2$  K, could be due to less-agglomeration and small particle size of  $\text{YMnO}_3$ . Coercivity in nanoparticles might originate from the surface anisotropy which at low temperature become prominent due to low  $k_B T$  ( $k_B$ =Boltzmann constant, T=temperature).

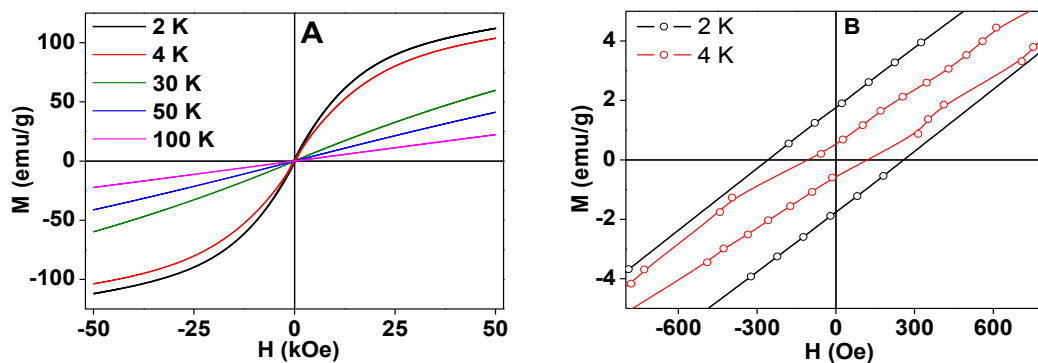


**Figure 3.1.5:** A) Magnetic hysteresis loops of  $\text{ErMnO}_3$  nanoparticles B) zoom view of  $M$ - $H$  loops at  $\sim 2$  and  $\sim 4$  K.

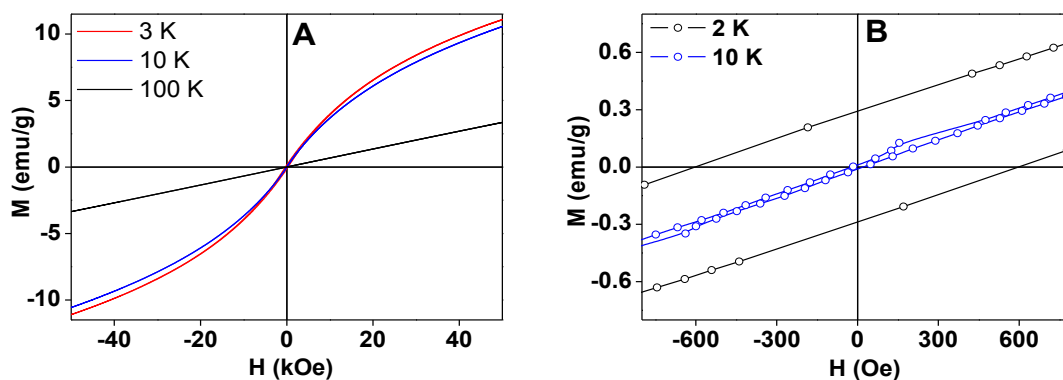


**Figure 3.1.6:** A) Magnetic hysteresis loops of  $\text{YMnO}_3$  nanoparticles B) zoom view of  $M$ - $H$  loops at 2 and 10 K.

The ZFC–FC magnetization curves do not show signature of  $T_N$  for both  $\text{ErMnO}_3$  and  $\text{YMnO}_3$  nanoparticle systems (figure 3.1.6). At  $\sim T_N$ , hexagonal  $\text{ErMnO}_3$  undergoes a phase transition from high temperature paramagnetic to E-type AFM state, which is a second order phase transition. At  $T_N$ , AFM  $\text{Mn}^{+3}$  spins trigger the ordering of  $\text{Er}^{+3}$  (4b) spins [18]. The absence of anomaly in  $T_N$  could be due to the second-order nature of the transition, which is very weak, and perturbation from applied field can suppress this transition.



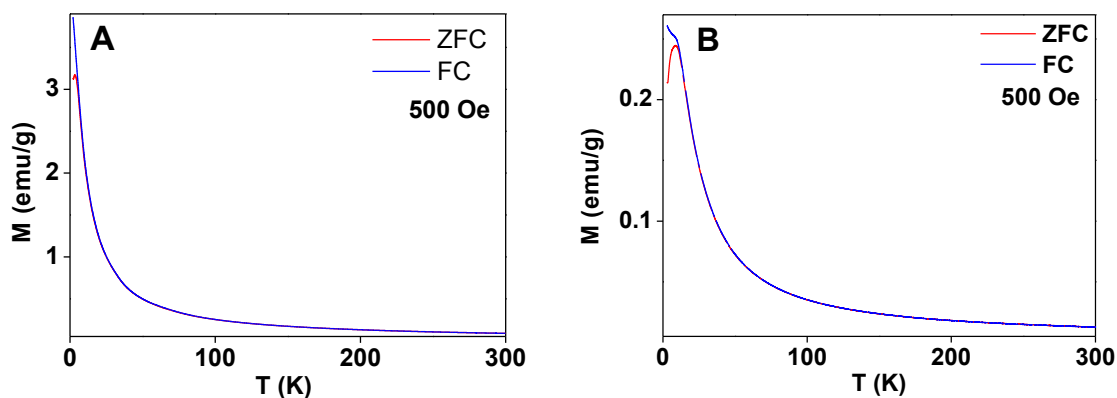


**Figure 3.1.7:** Temperature dependence of ZFC–FC magnetization curves at an applied field of 500 Oe for A)  $\text{ErMnO}_3$  nanoparticles B)  $\text{YMnO}_3$  nanoparticles.

ZFC–FC magnetization curves show bifurcation below  $\sim 40$  and  $\sim 20$  K for  $\text{ErMnO}_3$  and  $\text{YMnO}_3$  nanoparticles, respectively (figure 3.1.7). Yen *et al.* attributed this bifurcation of ZFC–FC magnetization curves for  $\text{ErMnO}_3$  below  $T_N$  due to rotation of rare-earth spin moment along  $c$ -axis due the influence of  $\text{Mn}^{+3}$  spins. Below  $T_N$ , as the  $\text{Mn}^{+3}$  spins form AFM domain, this influences the  $\text{R}^{+3}$  spins to form AFM ordering along  $c$ -axis. This effect is not prominent just  $< T_N$ , as, the  $\text{Mn}^{+3}$  moment is not prominent around that temperature [25]. As the temperature decreases, the coupling between  $\text{Mn}^{+3}$  and rare-earth ions become prominent and bifurcation of ZFC–FC magnetization curves occurs at low temperature [25].

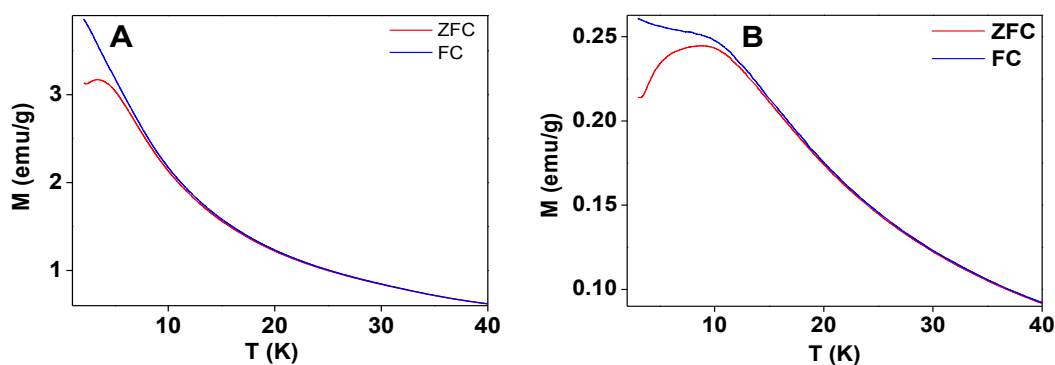


**Figure 3.1.8:** Expanded plots ZFC–FC magnetization curves showing the splitting below  $\sim 40$  and  $\sim 20$  K, respectively for A)  $\text{ErMnO}_3$  and B)  $\text{YMnO}_3$  nanoparticles.

From neutron diffraction-data, Meier *et al.* showed, ordering of  $\text{Er}^{+3}$  (4b) sublattice at  $\sim 80$  K and which increases with decreasing temperature [18]. If the above explanation of Yen *et al.* is the reason for bifurcation of ZFC–FC magnetization curves,  $\text{YMnO}_3$  should not show such bifurcation as  $\text{Y}^{+3}$  ions have  $f^0$  electronic configuration [25].

The field dependent ZFC–FC magnetization curves for  $\text{ErMnO}_3$  showed no change of bifurcation temperature from applied field of  $\sim 50$  to  $\sim 1000$  Oe (figure 3.1.9).

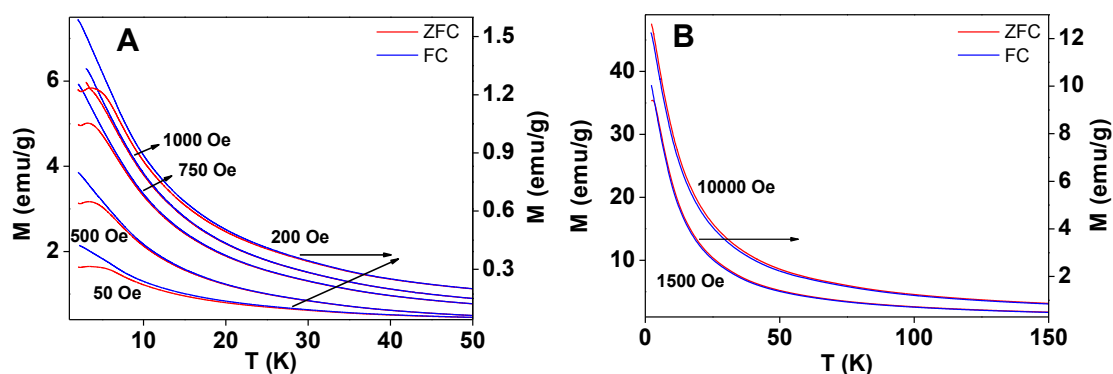


**Figure 3.1.9:** A, B) Temperature dependence of ZFC–FC magnetization curves for  $\text{ErMnO}_3$  with different applied field.

However, at higher applied field ( $\sim 1500$  Oe and  $\sim 1$  T), the bifurcation of ZFC–FC magnetization curves shift to higher temperature (figure 3.1.9 B). At field  $\sim 1500$  and  $\sim 10,000$  Oe the magnetization value of ZFC is greater than FC magnetization (figure 3.1.9 B). This might be due to the fact that, at higher applied field the triggering of  $\text{Er}^{+3}$ (4b) ordering by AFM  $\text{Mn}^{+3}$  spins is disturbed, so contribution of  $\text{Er}^{+3}$  (4b) moments in FC magnetization is

absent. The bifurcation of ZFC–FC magnetization curves can be attributed to SR of  $\text{Mn}^{+3}$  spins due to DM interactions.

The ZFC magnetization curves for  $\text{ErMnO}_3$  show increasing trend below bifurcation temperature and a hump  $\sim 4$  K. The hump  $\sim 4$  K in ZFC magnetization curves are due to the

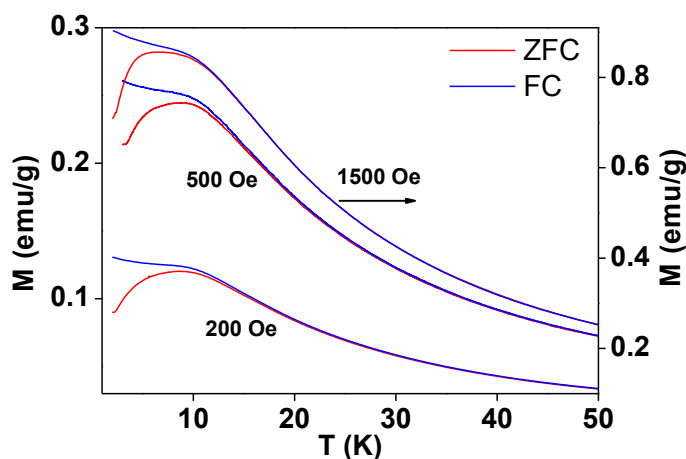


**Figure 3.1.10:** Temperature dependence of ZFC–FC magnetization curves for  $\text{YMnO}_3$  with different applied field.

ferrimagnetic ordering of  $\text{Er}^{+3}$  spins. Yen *et al.* showed the ordering of  $\text{Er}^{+3}$  moments at 2.5 K. Till an applied field of 1500 Oe, the ordering of  $\text{Er}^{+3}$  spins does not show any change. At applied field of 1500 Oe, the  $\text{Er}^{+3}$  (2a) ordering is not disturbed but  $\text{Er}^{+3}$  (4b) ordering is disturbed.

For  $\text{YMnO}_3$  nanoparticles ZFC–FC magnetization curves show hump  $\sim 8$  K (figure 3.1.10), the reason for this is discussed later. The field dependent magnetization does not show any change up to an applied field of  $\sim 1500$  Oe. At  $\sim 1500$  Oe, bifurcation of ZFC–FC magnetization curves shift to lower temperature compared to  $\sim 200$  Oe but the hump  $\sim 8$  K does not change.

The real part of ac magnetization shows peak at  $\sim 4.5$  and  $\sim 10$  K for  $\text{ErMnO}_3$  and  $\text{YMnO}_3$ , respectively (figure 3.1.11).

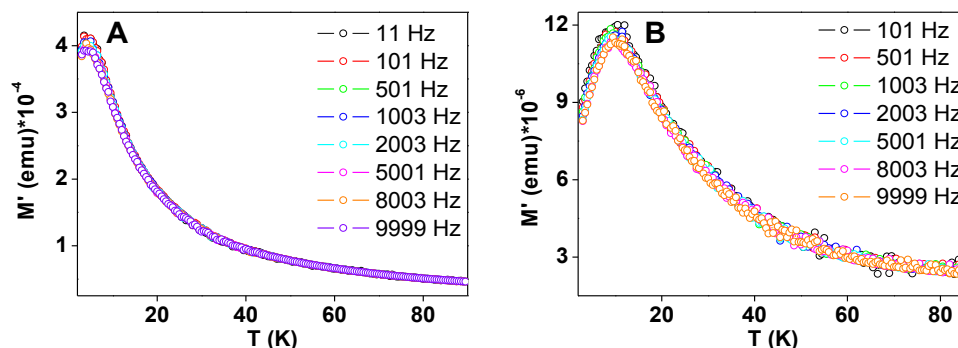


**Figure 3.1.11:** Temperature dependence of the real part of the ac magnetization for A)  $\text{ErMnO}_3$ , B)  $\text{YMnO}_3$  nanoparticles measured in  $\sim 5$  Oe ac field and various frequencies as indicated in figure.

whereas, the imaginary part of  $\text{ErMnO}_3$  shows peak at  $\sim 4.5$  K and a hump  $\sim 40$  K (figure 3.1.12).

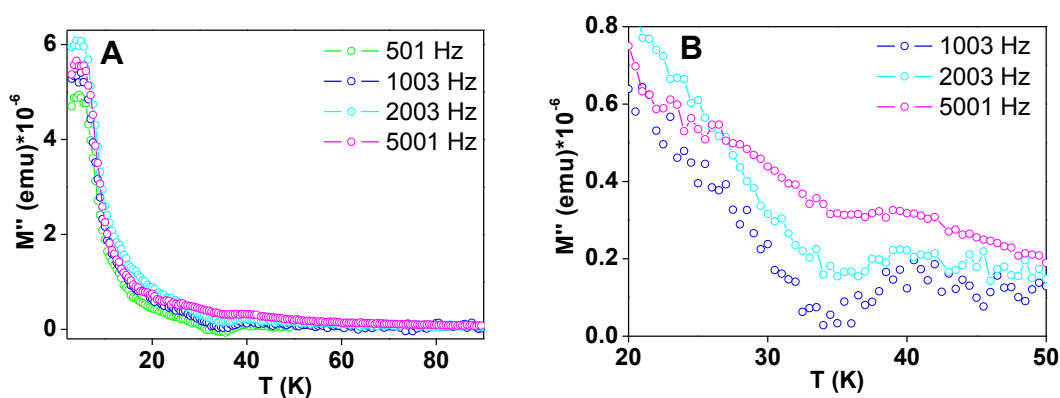


**Figure 3.1.12:** A) Temperature dependence of imaginary part of the ac magnetization measured at 5 Oe ac field for  $\text{ErMnO}_3$  B) showing anomaly  $\sim 40$  K.

The derivative of real part of ac magnetization curves shows a sharp peak  $\sim 69$  and  $\sim 82$  K for  $\text{ErMnO}_3$  and  $\text{YMnO}_3$  nanocrystals, respectively (figure 3.1.13), which indicates the signature of  $T_N$ .

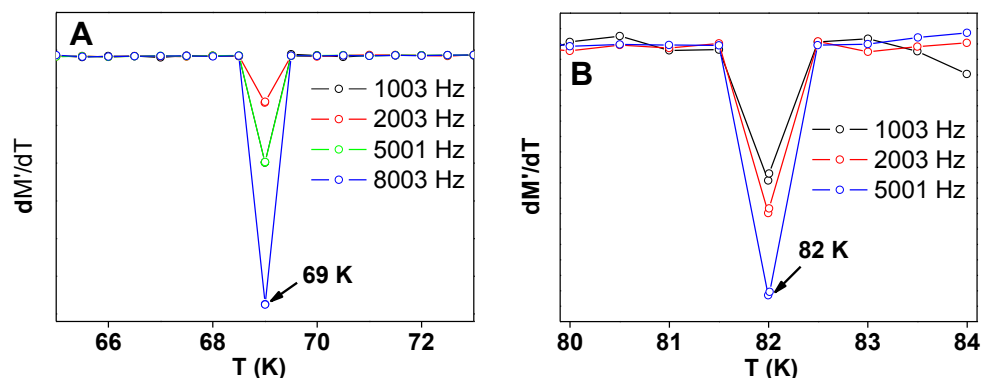


**Figure 3.1.13:** Temperature derivative of real part of ac magnetization,  $dM'/dT$  for A)  $\text{ErMnO}_3$ , B)  $\text{YMnO}_3$  nanoparticles showing  $T_N$  at  $\sim 69$  and  $\sim 82$  K respectively.

In literature, it is reported that  $T_N$  of  $\text{YMnO}_3$  decreases with particles size [26], but our results clearly showed no change of  $T_N$  of hexagonal  $\text{ErMnO}_3$  and  $\text{YMnO}_3$  with particles size. In our other studies, we showed no change of  $T_N$  with particle size in  $\text{LuMnO}_3$ ,  $\text{DyMnO}_3$ ,  $\text{GdMnO}_3$ . Overton *et al.* reported the decrease of  $T_N$  from  $\sim 70$  to  $\sim 65$  K in  $\text{YMnO}_{2.95}$  compared to  $\text{YMnO}_3$  [27]. In our case, the  $T_N$  value is almost equal to reported values for bulk ceramic and single crystal. This indirectly proves the stoichiometric oxygen content of the sample. The hump at  $\sim 40$  K in imaginary part of ac susceptibility for  $\text{ErMnO}_3$  (figure 3.1.12), where bifurcation temperature of ZFC–FC magnetization curves was observed, can be attributed to SR transition of  $\text{Mn}^{+3}$  spins due to DM interaction. This transition was also observed in hexagonal  $\text{LuMnO}_3$  by us. The peak at  $\sim 4.5$  K in both real and imaginary part of ac-magnetization for  $\text{ErMnO}_3$ , is due to ferrimagnetic ordering of  $\text{Er}^{+3}$  spins. The peak at  $\sim 10$  K in real part of ac-magnetization curve in  $\text{YMnO}_3$  cannot be due to ordering of  $\text{Y}^{+3}$  moments

as  $Y^{+3}$  is non-magnetic. Munoz *et al.* observed anomaly at  $\sim 11$  K in real part of ac-magnetization in orthorhombic  $YMnO_3$  and assigned it to freezing temperature associated with partial spin glass nature [28]. They also discussed, anomaly at  $\sim 11$  K, is associated with disorder of the lattice due to presence of  $Mn^{+4}$  ions, which is necessary for the stabilization of the orthorhombic phase [28]. The peak at  $\sim 10$  K in real part of ac-magnetization does not show any frequency dependency, which rules-out the possibility of spin glass behavior. The hump at  $\sim 8$  and  $\sim 10$  K in ZFC-FC magnetization curves and real part of ac-magnetization, respectively for  $YMnO_3$  nanoparticles could be due to AFM ordering of  $Mn^{+3}$  spins in *ab* plane, this type of anomaly was observed in  $LuMnO_3$  having same structure.

### 3.1.5 Dielectric spectroscopy

Temperature dependent dielectric spectroscopy for both the samples showed anomaly near  $T_N$ . Real part of permittivity for  $ErMnO_3$  nanocrystals showed anomaly at  $\sim 70$  K (figure 3.1.14), near the  $T_N$  as observed from ac-magnetization measurement.

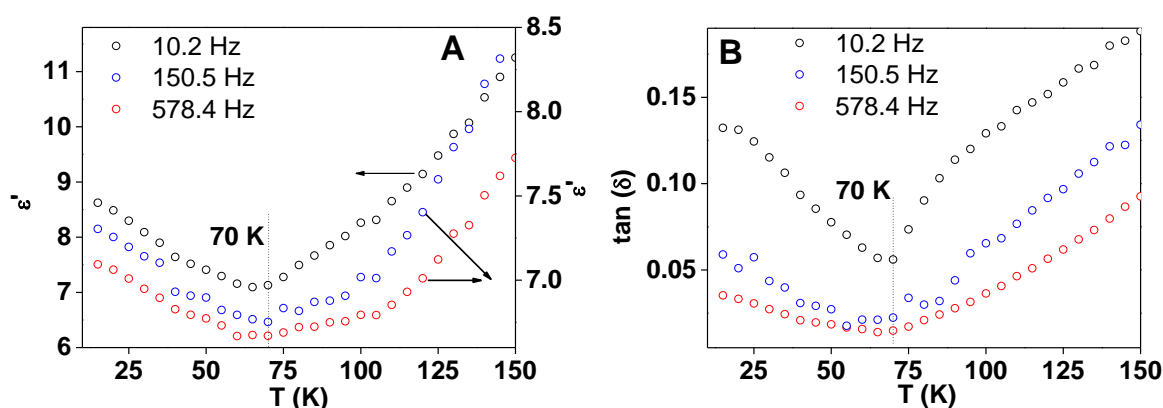


**Figure 3.1.14:** Temperature dependent variation of A) real part of permittivity ( $\epsilon'$ ) and B) loss factor ( $\tan \delta$ ) of  $ErMnO_3$  nanocrystals. Both real part of permittivity ( $\epsilon'$ ) and loss factor ( $\tan \delta$ ) showing anomaly at  $\sim 70$  K,  $T_N$  of  $ErMnO_3$  nanocrystals.

Loss  $\tan(\delta)$  of  $\text{ErMnO}_3$  nanocrystals also shows anomaly  $\sim 70$  K (figure 3.1.14 B). Temperature dependent real part of permittivity for  $\text{YMnO}_3$  nanocrystals showed anomaly at 85 K (figure 3.1.15), close to  $T_N$  as observed from ac susceptibility measurement.

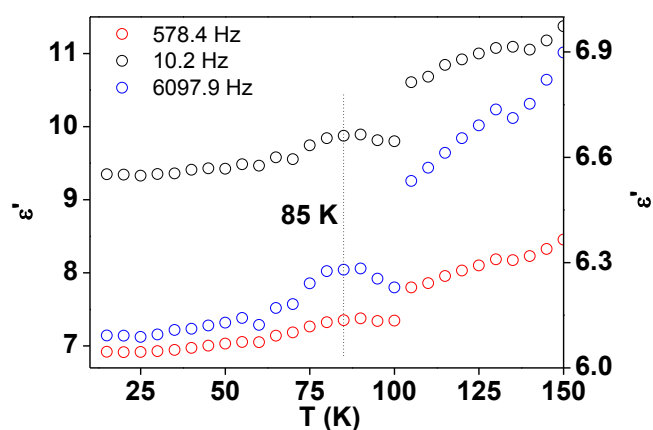


**Figure 3.1.15:** Temperature dependent variation of real part of permittivity ( $\epsilon'$ ) of  $\text{YMnO}_3$  nanocrystals showing anomaly at  $\sim 85$  K ( $\sim T_N$ ).

The presence of anomaly near  $T_N$  in dielectric measurement shows the signature of spin-lattice and ME coupling in nanocrystalline  $\text{ErMnO}_3$  and  $\text{YMnO}_3$  nanocrystals.

### 3.1.6 Conclusion

In conclusion, we have synthesized plate shaped nanocrystallites of hexagonal phase  $\text{ErMnO}_3$  and  $\text{YMnO}_3$  with average particles size  $\sim 65$  and  $\sim 50$  nm respectively. DC magnetization showed no signature of  $T_N$  but derivative of real part of magnetization showed sharp anomalies at  $\sim 69$  and  $\sim 82$  K for  $\text{ErMnO}_3$  and  $\text{YMnO}_3$ , respectively. Bifurcation of ZFC–FC magnetization curves below  $\sim 40$  and  $\sim 20$  K for  $\text{ErMnO}_3$  and  $\text{YMnO}_3$  nanoparticles

---

respectively, could be due to SR of  $\text{Mn}^{+3}$  spins due to DM interactions. Field dependent DC magnetic measurements revealed that triggering of  $\text{Er}^{+3}$  (4b) spins ordering by  $\text{Mn}^{+3}$  spins at  $\sim T_N$  can be suppressed by external field of  $\sim 1500$  Oe. Dielectric measurement showed signature of ME coupling in nanocrystalline  $\text{ErMnO}_3$  and  $\text{YMnO}_3$ .



---

## **Section 3.2 Ionic chemistry and morphology dependent magnetic properties: YbMnO<sub>3</sub>**

---

In this section, we showed the synthesis of multiferroic, single crystalline 1D YbMnO<sub>3</sub> in nanoregime. By using ionic chemistry without the use of surfactant or template, we demonstrated control synthesis of one- and two-dimensional nanoparticles of YbMnO<sub>3</sub>. Magnetic properties of YbMnO<sub>3</sub> nanoparticles show influence of morphology. Detailed ac and dc magnetic study shows FM interaction of Mn<sup>+3</sup> and Yb<sup>+3</sup> moments in nanorods of YbMnO<sub>3</sub> below ~35 K.

---

---

### 3.2.1. Introduction

Manganites, ferrites and chromites have always fascinated solid-state science due to their rich interplay between spin, charge, and orbital ordering. Rare-earth manganites with general formula  $\text{RMnO}_3$  (R=rare-earth element) have shown a renewed interest recently due to its potential application in spin-polarized conduction, magnetic storage, colossal magnetoresistance, metal to insulator transition, magnetocaloric effect, and so forth [29–32]. In contrast to rare-earth ferrites and chromites, which largely crystallize in orthorhombic structure (distorted perovskites) with  $Pbnm$  space group, manganites are relatively more diverse in their structure as well as magnetic and dielectric properties. For R=La–Dy, manganites crystallize in distorted orthorhombic perovskite structure whereas for R=Ho–Lu, Y, Sc a hexagonal structure is formed [3–6]. Most of the hexagonal manganites are ferroelectric below  $T_C$ , 900–1000 K and order antiferromagnetically below  $T_N$ , 80–140 K. In hexagonal  $\text{RMnO}_3$ , each  $\text{Mn}^{+3}$  ion is surrounded by three in-plane and two apical oxygen ions, so it is subjected to a trigonal crystal field. These  $\text{MnO}_5$  blocks are mutually connected two dimensionally at their corners therefore a triangular lattice of  $\text{Mn}^{+3}$  ions is formed [5].

$\text{RMnO}_3$  are mostly studied in bulk single crystalline, thin film and ceramics [33]. However, recent reports on their nano-dimensional physical properties indicated interesting change in its behavior. However, because of challenges associated with the synthetic chemistry, most of these studies are limited to the particles of arbitrary shapes, plate-like or quasi-spherical nanostructures. Surprisingly, despite of immense importance, there are very few reports on synthesis of one-dimensional (1D)  $\text{RMnO}_3$  which has prevented detailed experimental investigations on the morphology and size dependent properties. It is well known that the physical and chemical properties of certain materials depend heavily upon dimensionality of electronic confinement [34–36]. The induced shape anisotropy also

---

greatly influence the magnetic properties of these materials [37]. The charge and spin transport in these material along 1D materials is extremely promising for device applications.

Fontcuberta *et al.* showed the anisotropic magnetic response of *h*-YbMnO<sub>3</sub> single crystal in ac and dc magnetic fields [38]. Therefore, it is important to study the morphology dependent magnetic properties. So far, there is only one report on the synthesis of arbitrary-shaped YbMnO<sub>3</sub> nanoparticles and unfortunately this study did not report the magnetic properties [39]. Till date, most synthesis efforts for 1D nanostructures have been given to carbon nanotubes, metals, transition metal oxides, chalcogenides, and so forth. Urban *et al.*, for the first time, demonstrated solution-based synthesis of cubic phase BaTiO<sub>3</sub> and SrTiO<sub>3</sub> nanorods [40]. In this report, they used bimetallic alkoxides precursors, which are difficult to synthesize in some cases, and quite expensive. On the other hand, Han *et al.* demonstrated selective synthesis of multiferroic TbMn<sub>2</sub>O<sub>5</sub> nanorods and TbMnO<sub>3</sub> micrometer crystals by changing the molar ratio of MnCl<sub>2</sub>.4H<sub>2</sub>O and KMnO<sub>4</sub>. However, they could not control the morphology of same phase [41]. Liu *et al.* showed the synthesis of BiFeO<sub>3</sub> nanowires and they concluded that initial morphology of the precursors and the concentration of sodium hydroxide used were responsible for wire formation [42]. One-dimensional ternary perovskite oxides have also been synthesized using sol-gel template method [43]. Ha *et al.* showed that halide ions inhibit the growth of {111} facets in case of gold and silver nanocrystals, thereby helping in forming anisotropic nanoparticles [44].

In this section, we have used chloride ion chemistry to control the morphology of *h*-YbMnO<sub>3</sub> nanoparticles. We used different manganese precursors to synthesize nanorods and nanoplates of YbMnO<sub>3</sub>. For the first time we have shown morphology dependent magnetic property of YbMnO<sub>3</sub> nanocrystallites and compared with the bulk phase.

### 3.2.2 Chemicals

The chemicals, ytterbium (III) nitrate pentahydrate ( $\text{Yb}(\text{NO}_3)_3 \cdot 5\text{H}_2\text{O}$ , Sigma Aldrich, 99.9% purity), manganese (II) chloride tetra hydrate ( $\text{MnCl}_2 \cdot 4\text{H}_2\text{O}$ , Sigma Aldrich, 98% purity), manganese (II) nitrate  $x$  hydrate ( $\text{Mn}(\text{NO}_3)_2 \cdot x\text{H}_2\text{O}$ , Sigma Aldrich, 99.9% purity), ytterbium(III) oxide ( $\text{Yb}_2\text{O}_3$ , Sigma Aldrich, 99.9% trace metals basis), manganese (III) oxide ( $\text{Mn}_2\text{O}_3$ , Sigma Aldrich, 99.99% trace metals basis), sodium hydroxide pellets (NaOH, Merck, 99.5% purity) and ammonia solution (28 wt %) were purchased from above listed companies and used without further purification.

### 3.2.3 Synthesis of $\text{YbMnO}_3$ nanorods

In the standard chemical reaction, 200 mL aqueous solution containing 1 mmol ytterbium (III) nitrate pentahydrate and 1 mmol manganese (II) chloride tetrahydrate was stirred at room temperature for 1 h. Ammonia solution was added drop-wise to form metal hydroxide and precipitation of the hydroxide took place when the solution pH reached ~11. The precipitate was centrifuged-out at 6000 rpm and washed with water several times until the solution became neutral. The precipitate was redispersed in 50 ml of 5 M NaOH and stirred at room temperature for 6 h to ensure uniform dispersion of the precipitate. Then the solution was transferred to a sealed, Teflon-lined steel autoclave of 70 mL capacity and heated at 200 °C for 120 h. The precipitate obtained was filtered and washed with distilled water until the pH became neutral. Then precipitate was dried at 120 °C in vacuum oven. The dried powder was calcined in air at 750 °C for 8 h. This resultant black color powder was characterized further.

### 3.2.4 Structure and morphology

Room temperature XRD pattern of YbMnO<sub>3</sub> nanorods is shown in figure 3.2.1.

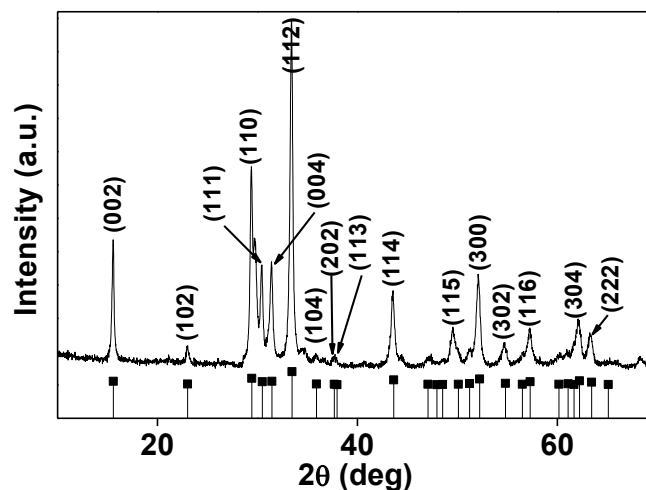


**Figure 3.2.1:** X-ray diffraction patterns of YbMnO<sub>3</sub> nanorods and the reference data from JCPDS card No. 801704 for the hexagonal phase with  $P6_3cm$  symmetry. X-ray diffraction shows the formation of single phase YbMnO<sub>3</sub> crystallites.

All the diffraction peaks are indexed to the hexagonal YbMnO<sub>3</sub> phase (PDF#801704) with space group  $P6_3cm$ . The diffraction peaks are quite broad indicating the formation of small crystallites. Average crystallite size calculated from Scherrer equation for *h*-YbMnO<sub>3</sub> nanorods is found to be ~40 nm.

The TEM images (figure 3.2.2) show that the sample consists of nanorods of YbMnO<sub>3</sub>. Individual YbMnO<sub>3</sub> nanorod has diameter ranging from 20 to 40 nm and a length from few hundreds of nm to micron. HRTEM images show, all nanorods are not grown along same direction. Figure 3.2.2 D shows, the growth of one rod in (110) plane and other in (104) plane. The SAED pattern (figure 3.2.2 F) shows that the nanorods are single-crystalline.

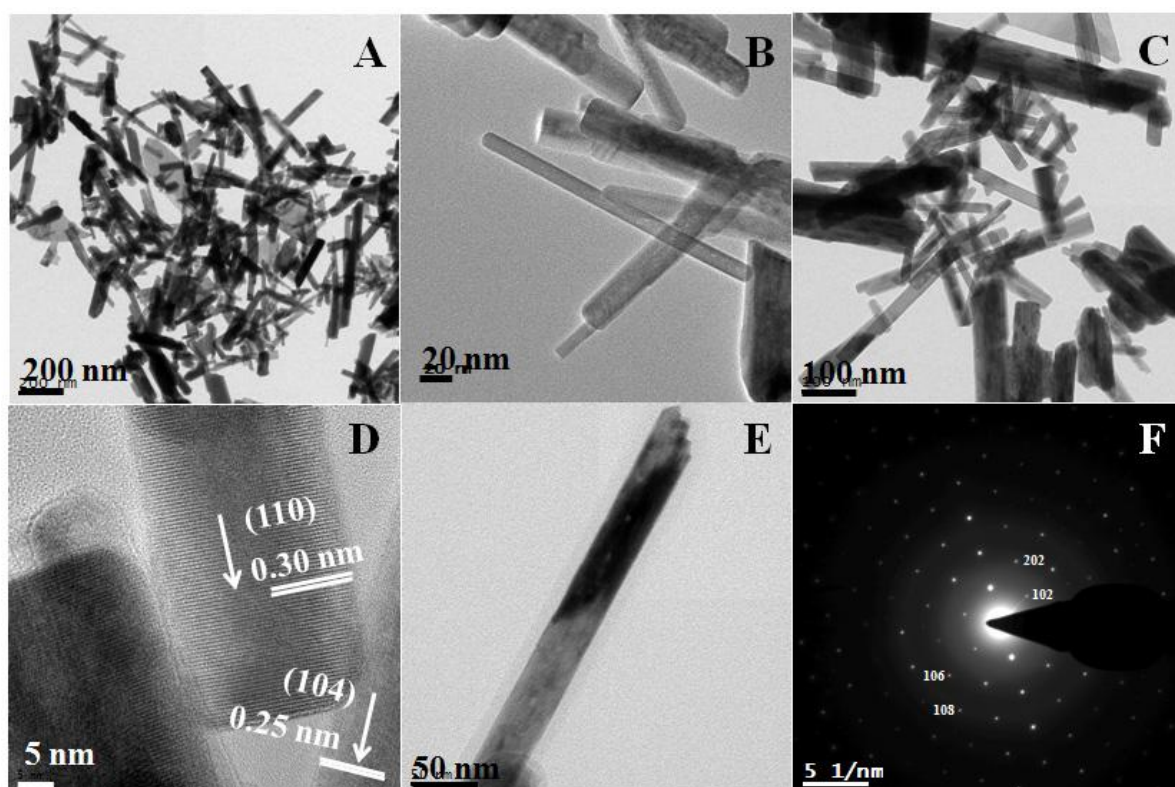


**Figure 3.2.2:** A, B, C) Transmission electron micrograph of  $\text{YbMnO}_3$  nanocrystals at different scales taken from various parts of the same TEM grid D) HRTEM image of nanocrystals F) SAED pattern of  $\text{YbMnO}_3$  nanocrystals E) corresponding TEM image of SAED pattern.

### 2.3.5 Magnetic properties of $\text{YbMnO}_3$ nanorods

It was noticed that the M–H loops of  $\text{YbMnO}_3$  nanorods showed no saturation (until 50 kOe) (figure 3.2.3). The M–H loops below  $\sim 35$  K showed increasing non-linearity which indicates weak ferromagnetic-type ordering.

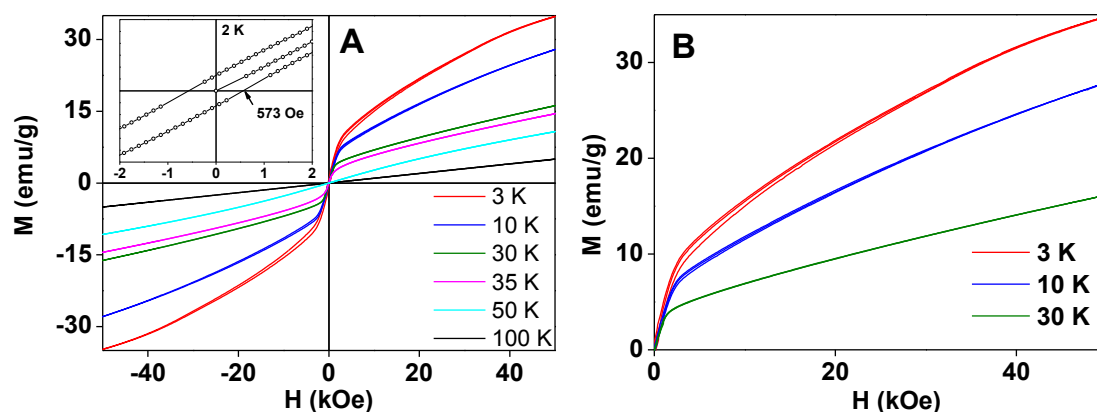


**Figure 3.2.3:** A)  $M$ - $H$  loops at various temperatures, inset shows zoom view in the low field region B) first quadrant of  $M$ - $H$  loop showing field dependent transition in low field.

To probe external magnetic field dependent magnetic transitions in  $\text{YbMnO}_3$  nanorods,  $M$ - $T$  measurements were done at 200 Oe, 500 Oe, 1 kOe, and 10 kOe applied field in both ZFC-FC modes (figure 3.2.4).

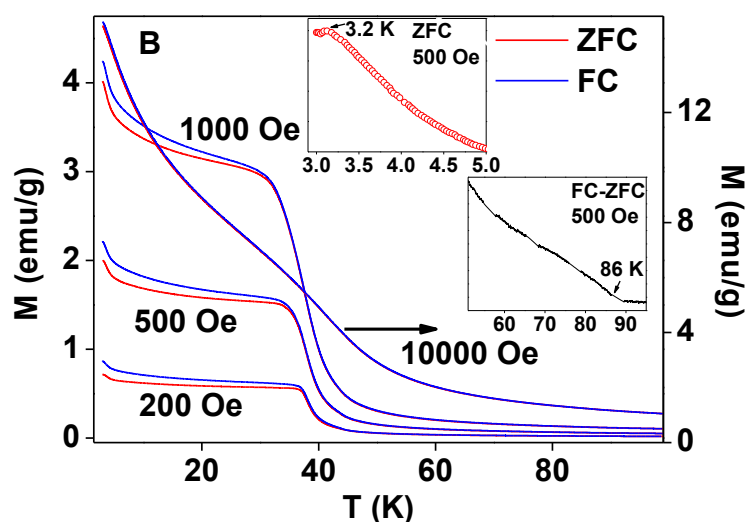


**Figure 3.2.4:** ZFC-FC magnetization curves at various fields for  $\text{YbMnO}_3$  nanorods; inset ZFC magnetization showing peak  $\sim 3.2$  K due to long range ordering of  $\text{Yb}^{+3}$  moments,  $(M_{FC} - M_{ZFC})$  vs.  $T$  curve showing  $T_N \sim 86$  K.

The ZFC–FC magnetization curves showed bifurcation  $\sim 86$  K (lower inset of figure 3.2.4) which is close to the  $T_N$  temperature reported in literature for  $\text{YbMnO}_3$  bulk single crystals [45].

The external field dependent ZFC–FC magnetization curves indicated that, for  $\text{YbMnO}_3$  nanorods,  $T_N$  is quite robust and does not change with increasing field up to  $\sim 10$  kOe; probably, due to relatively stronger AFM exchange forces between  $\text{Mn}^{+3}$  ions. Similar result was also observed in hexagonal  $\text{LuMnO}_3$  nanoparticles. Field dependent ZFC–FC magnetization curves showed a sharp knee along with an abrupt increase in the bifurcation of ZFC–FC magnetization curves up to an applied field of  $\sim 1000$  Oe. But, at  $\sim 10\,000$  Oe field, this transition was not very pronounced. Unlike  $T_N$  of  $\text{YbMnO}_3$ , which does not show field dependency, the anomaly at  $\sim 35$  K shows field dependency, where knee shifts to lower temperature with an increase in field. At 10 kOe applied field, the bifurcation of ZFC–FC magnetization curves almost disappears and instead of a sharp knee, a broad hump was seen. This type of anomaly was also reported earlier in  $\text{LuMnO}_3$ ,  $\text{InMnO}_3$ , and  $\text{ScMnO}_3$   $\sim 43$  K which have the same  $P6_3cm$  symmetry [46]. In contrast to  $\text{YbMnO}_3$ , in these materials, a sharp cusp in ZFC–FC magnetization curves were observed below  $\sim 43$  K. Normally, the cusp is observed in the susceptibility measured in  $c$  axis while  $ab$ -plane a broad peak [47]. In  $\text{LuMnO}_3$ , the bifurcation observed at  $\sim 43$  K was attributed to reorientation transition of  $\text{Mn}^{+3}$  spins as  $\text{Lu}^{+3}$  has zero spin. Han *et al.* showed that for  $\text{YMnO}_3$ , with increasing grain size from  $\sim 25$  to 200 nm, the AFM transition temperature increases from  $\sim 52$  to  $\sim 74$  K [48]. The weak ferromagnetism in small size crystal was attributed to nano-sized effect [48]. In  $\text{YbMnO}_3$  nanorods, we did not observe any change in  $T_N$  in comparison to the bulk  $T_N$ . In  $\text{YbMnO}_3$ , the  $\text{Yb}^{+3}$  ions have four unpaired electrons other than  $\text{Mn}^{+3}$  spins which contribute to the net magnetization. Therefore, the transition at  $\sim 35$  K (at  $\sim 500$  Oe) can be due to the interaction between  $\text{Yb}^{+3}$  and  $\text{Mn}^{+3}$  spin sublattices. At this temperature,  $\text{Yb}^{+3}$  moments try to



align along the  $c$ -direction while  $\text{Mn}^{+3}$  moments order antiferromagnetically in  $ab$  plane. The anomaly in ZFC–FC magnetization curves  $\sim 35$  K, could be due to  $\text{Yb}^{+3}$  and  $\text{Mn}^{+3}$  moments interaction. At higher temperature, AFM ordering of  $\text{Mn}^{+3}$  moment dominates over ferromagnetic alignment of  $\text{Yb}^{+3}$  moment and at low temperature  $\text{Yb}^{+3}$  ferromagnetic alignment dominates over  $\text{Mn}^{+3}$  AFM order. At intermediate temperatures, interaction of both  $\text{Yb}^{+3}$  and  $\text{Mn}^{+3}$  moments give rise to a FM-like interaction. This type of interaction of A and B site moments at intermediate temperature was also observed in  $\text{GdCrO}_3$ .

At temperatures below the knee, the slope of ZFC–FC magnetization curves is reduced significantly, and further below  $\sim 4$  K, the slope increases sharply. Around 3.2 K, ZFC–FC magnetization curves show a peak (upper inset of figure 3.2.4), which is due to long range ordering of  $\text{Yb}^{+3}$  moments. This transition was also observed in single crystal of  $\text{YbMnO}_3$  around the same temperature [49]. Sugie *et al.* showed the presence of ferromagnetism in  $\text{YbMnO}_3$  bulk single crystals below  $\sim 3$  K, where, they reported an opening of hysteresis loop at low field [49]. They showed a field dependent transition in M–H loop below  $\sim 3$  K, as a step increase in magnetization value at low field. Similar field dependent transition in initial magnetization value was also observed in  $\text{YbMnO}_3$  nanorods below  $\sim 35$  K but with no coercivity (inset of figure 3.2.3). In  $\text{YbMnO}_3$  nanorods, till a critical field, the initial magnetization increases sharply (inset of figure 3.2.3 B) like ferrimagnetic/ferromagnetic sample, after that magnetization increases gradually. The critical field required for field dependent transition increases as the temperature decreases. Above  $\sim 35$  K, no field dependent transition was observed.

The real and imaginary part of ac-magnetization doesn't show any anomaly near  $T_N$  in the measured frequency range (figure 3.2.5). This type of behavior was also observed in  $\alpha$ - $\text{DyMnO}_3$  single crystal and nanoparticles previously [50]. The  $M'$  values show a sudden

increase below  $\sim 42$  K with a knee at  $\sim 36$  K which is closer to the similar behavior observed in dc-magnetic measurements.

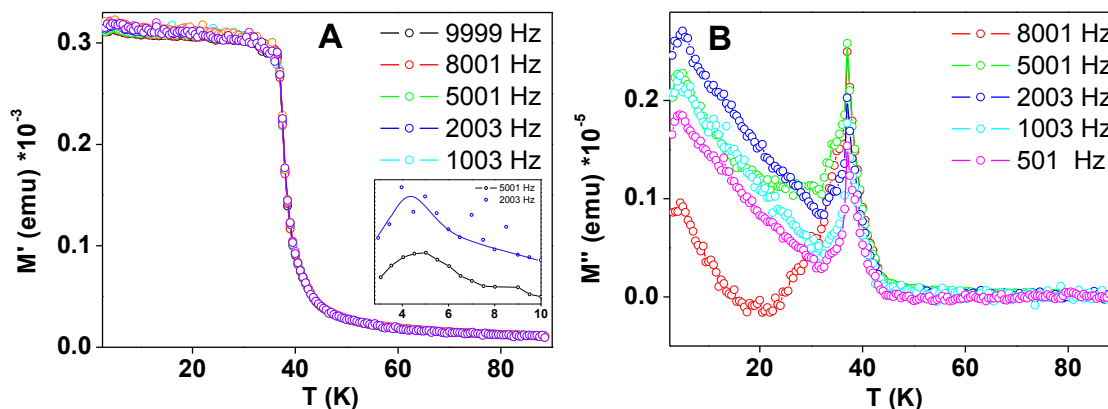


**Figure 3.2.5:** Temperature dependence of A) real and B) imaginary part of the ac-magnetization measured at 5 Oe ac field at various frequencies for YbMnO<sub>3</sub> nanorods. Inset of A) shows zoom view of Yb<sup>+3</sup> moment ordering, line fit is only for guide to eyes.

The origin of this magnetic anomaly was discussed earlier section. Below this temperature, the slope of the  $M'$ - $T$  curves remains almost flat down to the lowest measured temperature. However, a careful zoom view revealed a small hump centered at  $\sim 5$  K (shown in the inset of figure 3.2.5 A) which is due to the ordering of Yb<sup>+3</sup> moments. These observations are consistent with the dc-magnetization data. In contrast, the  $M''$ - $T$  curves show two peaks below the  $T_N$ . The peaks at  $\sim 38$  and  $\sim 5$  K can be attributed to Yb<sup>+3</sup>-Mn<sup>+3</sup> spin interactions and long range ordering of Yb<sup>+3</sup> moments respectively. No significant frequency dependency was observed any anomaly in real and imaginary part of ac-magnetization.

### 3.2.6 Synthesis of YbMnO<sub>3</sub> nanoplates

For the synthesis of YbMnO<sub>3</sub> nanoplates, a reaction procedure similar to YbMnO<sub>3</sub> nanorods was used except that for manganese (II) chloride tetra hydrate, manganese (II) nitrate  $x$  hydrate was used.

### 3.2.7 Structure and morphology

In figure 3.2.6, shows the powder X-ray diffraction pattern (PXRD) of nanoplates (sample 2). All the diffraction peaks are indexed to the hexagonal YbMnO<sub>3</sub> phase (PDF#801704) with space group  $P6_3cm$ . It can be noted that the PXRD patterns do not follow relative peak intensity profile of PDF#801704. This can be due to sample orientation effect or shape anisotropy of the particles (as evident from TEM results).

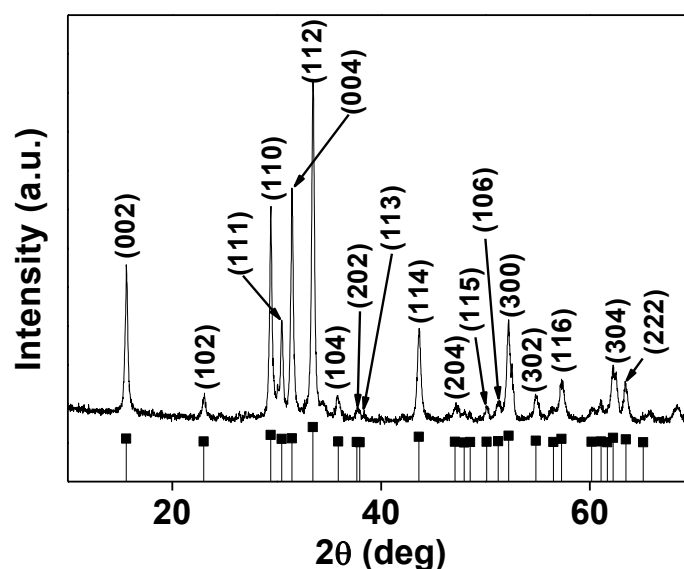


**Figure 3.2.6:** A comparison between X-ray diffraction patterns of YbMnO<sub>3</sub> nanoplates and reference data from JCPDS card No. 801704 for the hexagonal phase with  $P6_3cm$  symmetry. The X-ray diffraction shows the formation of single phase YbMnO<sub>3</sub> crystal.

TEM images show a plate-like structure (figure 3.2.7) with the individual particle having size between  $\sim 65$  to  $75$  nm. We also observed that some of the nanoplates fuse together to form clumps.

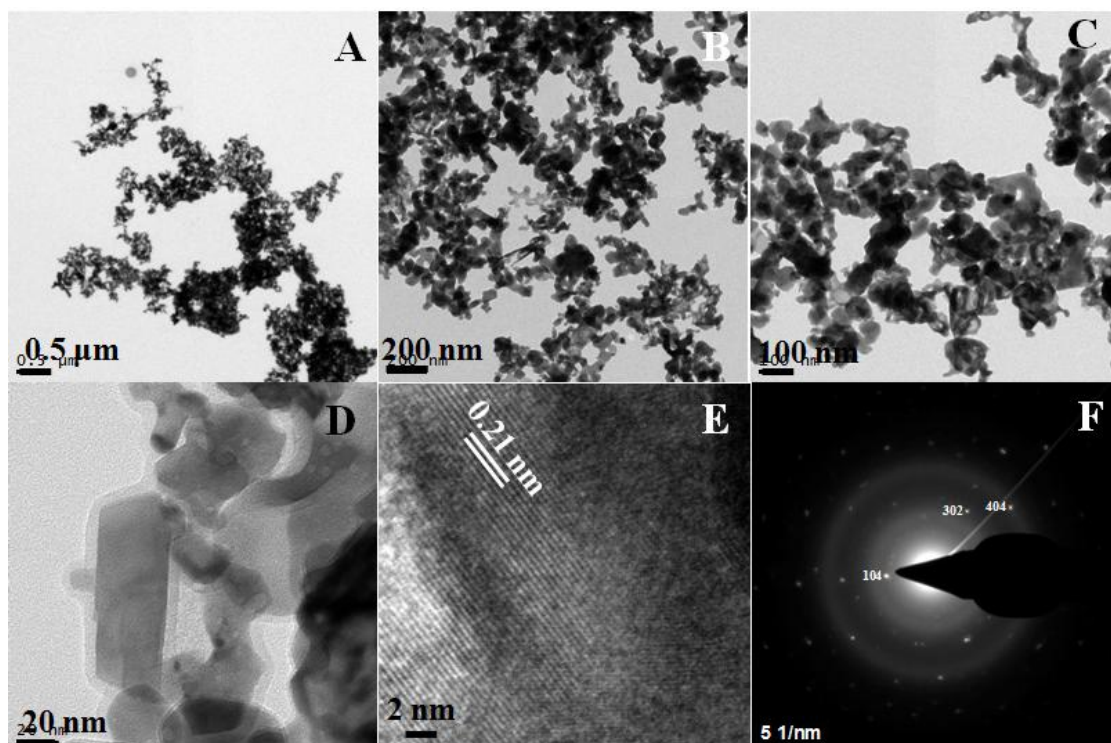


**Figure 3.2.7:** A, B, C, D) Transmission electron micrograph of YbMnO<sub>3</sub> nanocrystals at different scales taken from various parts of the same TEM grid E) HRTEM image of nanocrystals F) SAED pattern of YbMnO<sub>3</sub> nanocrystals.

### 3.2.8 Magnetic properties of YbMnO<sub>3</sub> nanoplates

In figure 3.2.8 (A), the M–H loops for 2D-YbMnO<sub>3</sub> nanostructures showed nonlinear behavior for temperatures  $\leq 50$  K. At  $\sim 3$  K, the M–H loop showed a coercivity of  $\sim 200$  Oe (inset figure 3.2.8A).

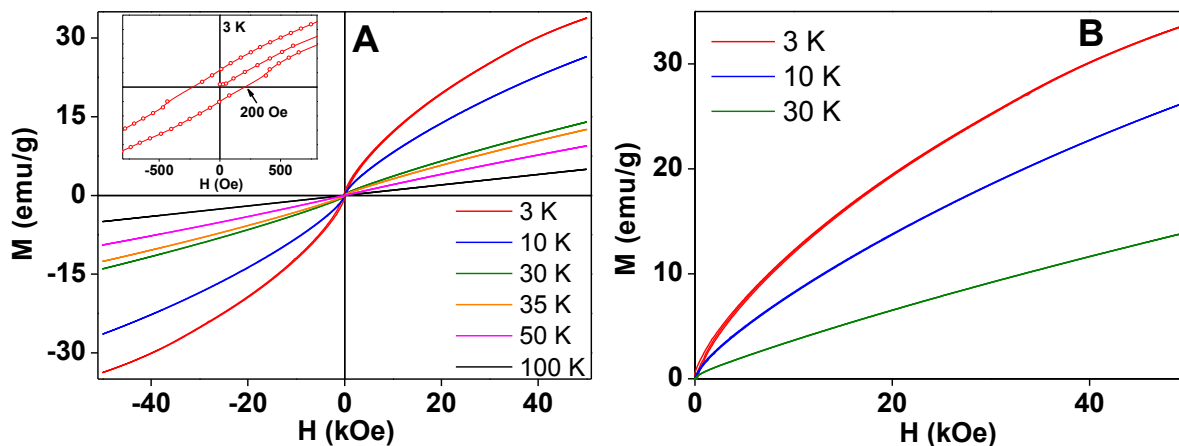


**Figure 3.2.8:** A)  $M$ - $H$  hysteresis loops at various temperatures inset shows zoom view at low field region B) first quadrant of  $M$ - $H$  loop in low field.

To probe the temperature dependent magnetic transition of 2D- $\text{YbMnO}_3$  nanostructures,  $M$ - $T$  measurements were performed at various applied field. The bifurcation of ZFC-FC magnetization curves was observed at  $\sim 86$  K (inset figure 3.2.9) which is the reported  $T_N$  of  $\text{YbMnO}_3$  in bulk single crystal ( $T_N$ )  $\sim 86$  K.

Similar to  $\text{YbMnO}_3$  nanorods, the AFM  $T_N$  at 86 K does not depend on the applied external field up to the highest applied field of 10 kOe. Further, it can be noticed that in comparison to  $\text{YbMnO}_3$  nanorods, the low temperature ZFC-FC magnetization behavior of  $\text{YbMnO}_3$  nanoplates is quite different, as shown in figure 3.2.9.

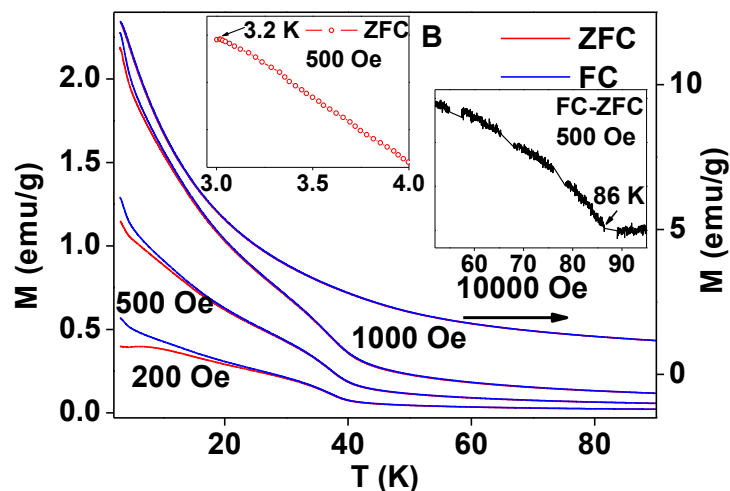


**Figure 3.2.9:** ZFC–FC magnetization curves at various applied fields for  $\text{YbMnO}_3$  nanoplates, inset zoom view of ZFC magnetization showing peak  $\sim 3.2$  K due to long range ordering of  $\text{Yb}^{+3}$  moments,  $(M_{FC} - M_{ZFC})$  vs.  $T$  curve showing  $T_N \sim 86$  K.

Both ZFC–FC magnetization curves showed similar trend below an applied field 1000 Oe and whereas, at 10,000 Oe field, curves showed different nature. ZFC–FC magnetization increases sharply below 45 K and a magnetic anomaly was observed at 30 K as further bifurcation of ZFC–FC magnetization curves. In comparison to nanorods, for nanoplates this transition was quite broad. Unlike  $\text{YbMnO}_3$  nanorods, where the slope of ZFC–FC magnetization curves increases sharply below  $T_N$  and remain approximately flat in temperature range 35–7 K, for  $\text{YbMnO}_3$  nanoplates, the ZFC–FC magnetization values show a continuous increase below this transition temperature. It can be noted that both ZFC–FC magnetization curves do not show any drop in magnetization followed by hump. However, similar to the  $\text{YbMnO}_3$  nanorods, the anomaly at  $\sim 30$  K in  $\text{YbMnO}_3$  nanoplates also shows field dependency. As the applied field increases the bifurcation and hump in the ZFC–FC magnetization curves shift to lower temperature values. At 1000 Oe applied field, the bifurcation of ZFC–FC magnetization curves for  $\text{YbMnO}_3$  nanoplates is almost negligible and

the hump also decreases in its appearance. At 10 kOe, there was no anomaly in ZFC–FC magnetization curves (no significant change in slope). At  $\sim 3.2$  K, ZFC–FC curves show a peak (inset figure 3.2.9) which is due to long range ordering of  $\text{Yb}^{+3}$  moments.

Similar to the  $\text{YbMnO}_3$  nanorods, the real part of magnetization ( $M'$ ) for  $\text{YbMnO}_3$  nanoplates showed no anomaly near  $T_N$  (figure 3.2.10).

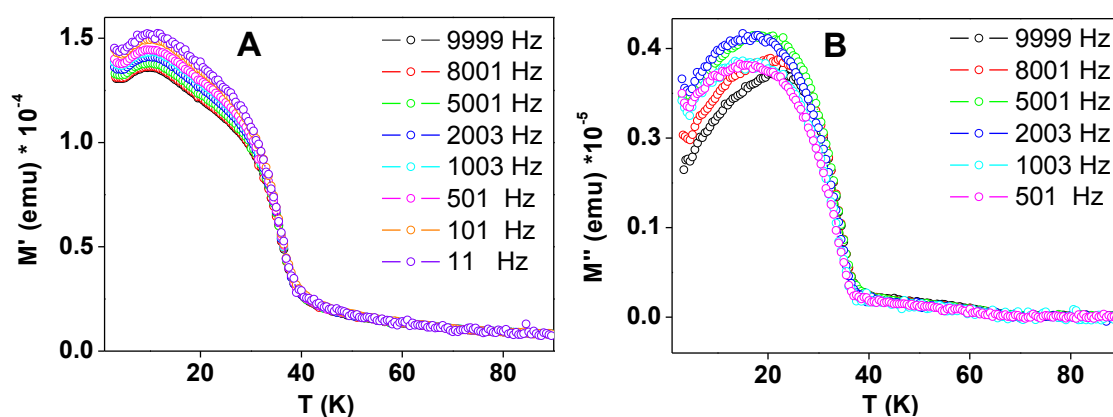


**Figure 3.2.10:** Temperature dependence of A) real and B) imaginary part of the ac-magnetization measured at 5 Oe ac-field at various frequencies as indicated in figure for  $\text{YbMnO}_3$  nanoplates.

The  $M'$ - $T$  curve showed a sudden increase in magnetization value below  $\sim 40$  K but the sharp knee which was observed in  $\text{YbMnO}_3$  nanorods (figure 3.2.10A) has now become a broad hump, similar to dc data (figure 3.2.10 B). The imaginary part of magnetization ( $M''$ ) shows a broad hump unlike a sharp peak for  $\text{YbMnO}_3$  nanorods.

### 3.2.9 Synthesis of YbMnO<sub>3</sub> micron sized particles

Bulk polycrystalline samples of YbMnO<sub>3</sub> were synthesized by the conventional solid-state reaction method, using stoichiometric mixtures of Yb<sub>2</sub>O<sub>3</sub> and Mn<sub>2</sub>O<sub>3</sub> as starting materials. The compounds were ground thoroughly in a mortar and calcined at 850 °C for 24 h. Again the sample was ground and calcined at 1300 °C for 24 h. Finally, the ground sample was compressed into pellet and sintered at 1400 °C for 24 h.

### 3.2.10 Structure and morphology

In figure 3.2.11, show powder X-ray diffraction (PXRD) of YbMnO<sub>3</sub> bulk micron sized particles. All the diffraction peaks are indexed to the hexagonal YbMnO<sub>3</sub> phase (PDF#801704) with space group  $P6_3cm$ .

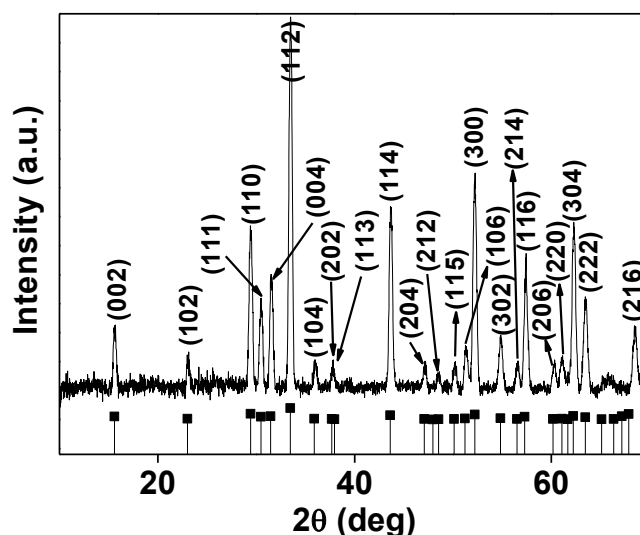


**Figure 3.2.11:** A comparison between X-ray diffraction patterns of YbMnO<sub>3</sub> micron sized particles and reference data from JCPDS card No. 801704 for the hexagonal phase with  $P6_3cm$  symmetry. The X-ray diffraction shows the formation of single phase YbMnO<sub>3</sub> crystal.



The SEM images (figure 3.2.12) of  $\text{YbMnO}_3$  micron particles show that the particles are irregular in shape and have size in micron range.

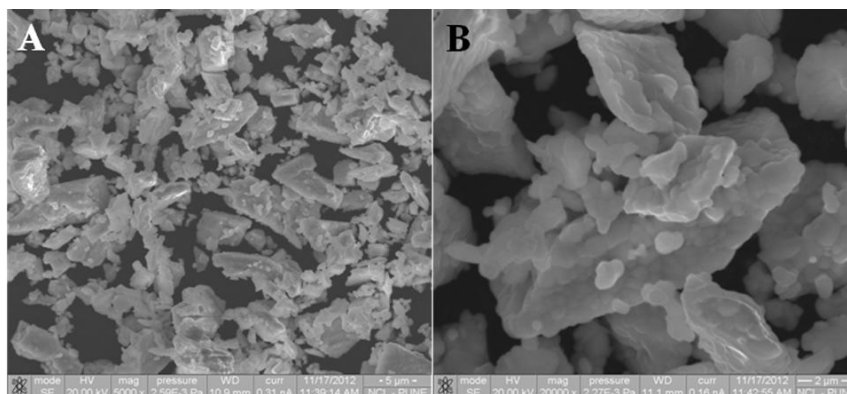


**Figure 3.2.12:** Scanning electron micrographs of  $\text{YbMnO}_3$  ceramic at different scales. SEM images show irregular micron sized particles of  $\text{YbMnO}_3$  crystals.

### 3.2.11 Magnetic properties of bulk $\text{YbMnO}_3$

In figure 3.2.13 (A), the M–H loop for bulk sample at 3 K shows a behavior similar to sample 2 and showed a notable coercivity of 230 Oe which is larger than coercivity observed for nanoplates (200 Oe).

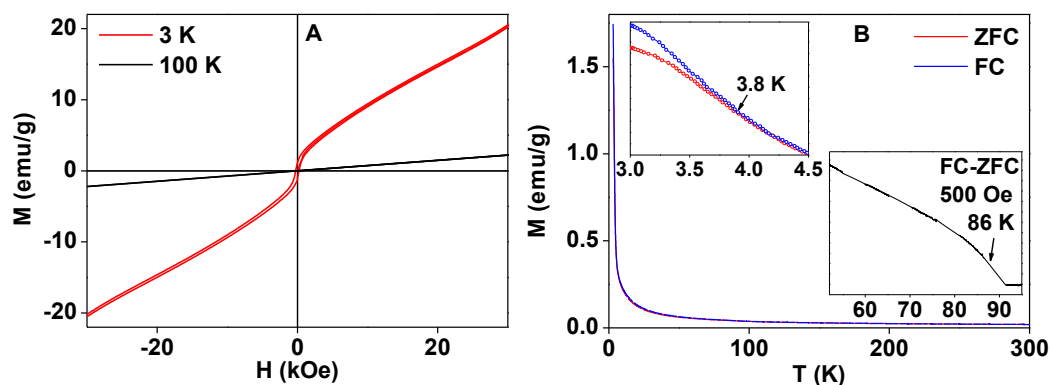


**Figure 3.2.13:** A)  $M$ – $H$  loops at 3 and 100 K B) ZFC–FC magnetization curves at 500 Oe applied field for  $\text{YbMnO}_3$  bulk ceramic sample, inset low temperature ZFC–FC magnetization curves showing bifurcation of ZFC–FC magnetization curves at  $\sim 3.8$  K and  $(M_{FC} - M_{ZFC})$  vs.  $T$  curve showing  $T_N \sim 86$  K.

At 100 K and above, the  $M$ – $H$  curve shows complete paramagnetic nature. In figure 3.2.13 (B), ZFC–FC magnetization curves at 500 Oe applied field is shown where the bifurcation of curves was observed at  $\sim 86$  K (inset figure 3.2.13 B) which is in the proximity of the reported  $T_N$  of  $\text{YbMnO}_3$  in bulk single crystal ( $T_N$ )  $\sim 86$  K. The ZFC–FC magnetization curves for bulk polycrystalline  $\text{YbMnO}_3$  sample show a sharp change in slope below  $\sim 20$  K with an increased amount of bifurcation in ZFC–FC magnetization curves at  $\sim 3.8$  K. The bifurcation of ZFC–FC magnetization curves  $\sim 3.8$  K can be due to the ordering of  $\text{Yb}^{+3}$  ions as discussed earlier.

### 3.2.12 Mechanism of synthesis

#### Ionic control on the morphology of $\text{YbMnO}_3$ nanoparticles

In the hydrothermal process, competition between crystal nucleation and growth determines the size and the morphology of the product. The nucleation and growth is controlled by crystal structure and precursor used [51]. During the growth process, local reaction environment is controlled by facet-selective electrostatic interactions between different ions to growing nuclei, which in turn control final morphology of particles. In the synthesis of  $\text{YbMnO}_3$ , the role of manganese (II) chloride tetrahydrate and manganese (II) nitrate  $x$  hydrate was key for the formation of different morphology. In both the cases, the reaction parameters were similar except the manganese precursor. In the reaction, where manganese (II) chloride tetra hydrate was used as a precursor, crystalline nanorods whereas

---

when manganese (II) nitrate  $x$  hydrate was used, nanoplates of  $\text{YbMnO}_3$  were grown. These experimental evidences show the role of chloride and nitrate ions in determining the crystal growth of  $h$ - $\text{YbMnO}_3$ . In our previous studies on  $\text{DyFeO}_3$ ,  $\text{BiFeO}_3$ ,  $\text{GdCrO}_3$ ,  $\text{LuMnO}_3$  (hexagonal),  $\text{TbMnO}_3$ ,  $\text{DyMnO}_3$ ,  $\text{GdMnO}_3$ , it was shown that nanocrystalline plates are formed with nitrate precursors and we had identified the important role of nitrate and citrate ions in the formation of nanoplates. The shape control in wet-chemical synthesis can also be driven by the preferential binding of ionic ligands, surfactants to different lattice facets due to their variable degree of affinity, which results in the growth of particular facet. In the above cases, strong affinity of nitrate ions with metal ions at particular crystalline facets promoted the formation of plate like morphology. It is known in literature that halide ions play an important role in formation of anisotropic gold nanoparticles [52,53]. Similar analogy can also be used to describe the formation of nanorods of  $\text{YbMnO}_3$  when chloride precursor was used. Using same method Liu *et al.* showed the formation of  $\text{BiFeO}_3$  nanowires but they concluded that it was the initial morphology of the precursors and the concentration of sodium hydroxide used, was primarily responsible for nanowire formation [42]. However, in our method, the change in type of manganese precursor alone resulted into the formation of different particle morphologies.

### 3.2.13 Comparison between $\text{YbMnO}_3$ nanorods, plates and bulk

In figure 3.2.14 A and B, we have shown 500 Oe ZFC–FC magnetization curves for all three samples, in two different temperature regions: (50 to 100 K) and (3 to 50 K).

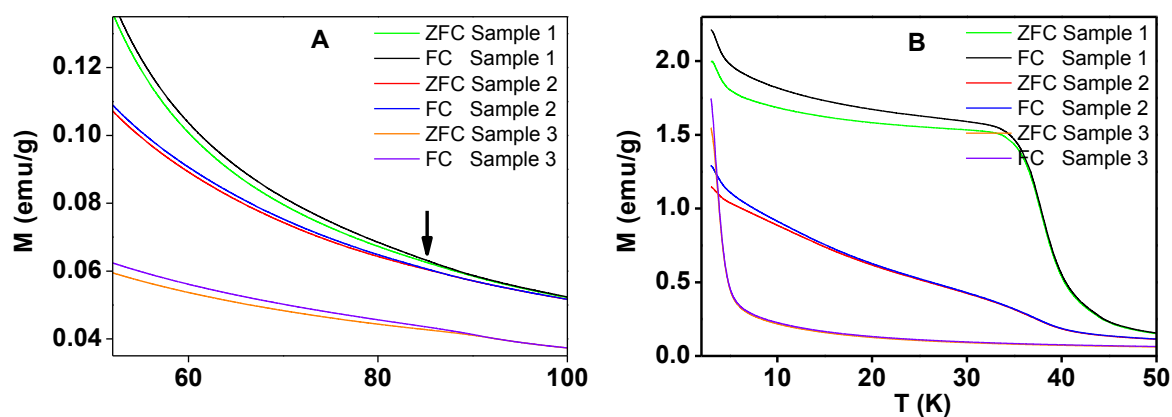


**Figure 3.2.14:** A) Comparison of ZFC–FC magnetization curves at 500 Oe applied field for YbMnO<sub>3</sub> nanorods (sample 1), nanoplates (sample 2), and bulk ceramic (sample 3) sample. Bifurcation of ZFC–FC magnetization curves ( $T_N$ ) and B) low temperature anomaly of YbMnO<sub>3</sub> nanorods, nanoplates and bulk ceramic sample.

As expected, the  $T_N$ , as bifurcation of ZFC–FC magnetization curves of YbMnO<sub>3</sub> was observed at  $\sim 86$  K for all the samples. The ZFC–FC magnetization curves for bulk ceramic powder of YbMnO<sub>3</sub> shows a sharp increase in slope below  $\sim 20$  K while for YbMnO<sub>3</sub> nanorods and plates, it is seen below  $\sim 45$ ,  $40$  K, respectively. YbMnO<sub>3</sub> nanorods and plates showed signature of long range ordering of Yb<sup>+3</sup> moments  $\sim 3.2$  K, as peak in ZFC–FC magnetization curves. Whereas, bulk ceramic powder of YbMnO<sub>3</sub> shows a broad hump and bifurcation of ZFC–FC magnetization curves  $\sim 3.8$  K. The ZFC–FC magnetization curves for YbMnO<sub>3</sub> nanorods show a hump  $\sim 35$  K and bifurcation. ZFC–FC magnetization curves of YbMnO<sub>3</sub> nanoplates shows a broad hump centered  $\sim 30$  K and bifurcation of ZFC–FC magnetization curves below 30 K. As explained earlier anomaly  $\sim 35$  K is due to the Yb<sup>+3</sup> and Mn<sup>+3</sup> moments interaction. In YbMnO<sub>3</sub> nanorods, the surface contributions are less in compared to YbMnO<sub>3</sub> nanoplates, so the anomaly is prominently observed. But, in YbMnO<sub>3</sub> nanoplates, this anomaly is weakened and masked by surface contributions. The shifting of

---

anomaly to low temperature in YbMnO<sub>3</sub> nanoplates compared to YbMnO<sub>3</sub> nanorods can be due to the dimensionality of samples. At low temperature, Yb<sup>+3</sup> moments align ferromagnetically along *c*-axis, in hexagonal YbMnO<sub>3</sub>, it is probable that rods are align more in *c*-axis than in plates so the interaction of Yb<sup>+3</sup> and Mn<sup>+3</sup> moments are more prominent in YbMnO<sub>3</sub> nanorods. YbMnO<sub>3</sub> nanorods show no opening of hysteresis loop till 3 K, whereas YbMnO<sub>3</sub> nanoplates showed notable coercivity at 3 K. In YbMnO<sub>3</sub> nanorods ferromagnetic nature is probably coming from dimensionality of samples, where it is likely that more number of particles will align along *c*-axis which gives ferromagnetic character. Whereas, in YbMnO<sub>3</sub> nanoplates, surface effects are more prominent which results in opening of hysteresis loop at low temperature. These features show the morphology dependent magnetic property of YbMnO<sub>3</sub> nanoparticles.

### 3.2.14 Conclusion

We have synthesized single-crystalline hexagonal YbMnO<sub>3</sub> nanorods and nanoplates by modified hydrothermal process. It was found that nitrate and chloride ions are structural directing agent for the formation of YbMnO<sub>3</sub> nanorods and nanoplates. The preferential binding of nitrate and chloride ions to growing YbMnO<sub>3</sub> seeds during synthesis is not understood yet and can be subject of further study. Detailed ac and dc magnetic study shows ferromagnetic interaction of Mn<sup>+3</sup> and Yb<sup>+3</sup> moments in nanorods of ytterbium manganese oxide below ~35 K.

---

## Section 3.3 Effect of $R^{+3}$ ( $S=0$ ) on magnetic properties: $\text{LuMnO}_3$

---

In this section, synthesis of nanocrystalline  $\text{LuMnO}_3$  and investigation of its optical and magnetic properties is presented. The UV-vis-NIR spectra at room temperature showed electronic transitions at 1.7 eV (729 nm), 2.3 eV (539 nm) and 5 eV (258 nm). We observed two new anomalies in the ZFC–FC magnetization curves at lower applied field which were not seen previously. The first transition was observed as a sharp bifurcation below 44 K (at 100 Oe) and second transition was observed at 12 K in form of a peak in the ZFC magnetization curves. We attribute the transition at 44 K to the reorientation of the  $\text{Mn}^{+3}$  ions in the sublattice due to the DM interaction. The transition at 12 K is attributed to the weak AFM coupling between Mn–O–Mn in the *ab* plane which become dominant at lower temperature.

---

### 3.3.1 Introduction

Several compounds from  $\text{RMnO}_3$  (R=rare-earth) family show multiferroic properties and adopt two types of structures depending upon the size of rare-earth atom, synthesis conditions etc [54]. In the case of R=La, Ce–Dy, the  $\text{RMnO}_3$  compounds crystallize in the distorted orthorhombic perovskite structure where  $\text{Mn}^{+3}$  ions are octahedrally coordinated by  $\text{O}^{2-}$  ions and form a three-dimensional network by sharing a corner [3-6, 10]. On the other hand, when R=Ho–Lu, Y, Sc, these materials form hexagonal structure, where  $\text{Mn}^{+3}$  ions are coordinated in trigonal bipyramid geometry to the surrounding  $\text{O}^{2-}$  ions and form a pseudo-layered structure by corner sharing of the trigonal basal plane  $\text{O}^{2-}$  ions [54]. These  $\text{MnO}_5$  bipyramids tilt and shift with respect to the  $\text{R}^{+3}$  cations to form noncentrosymmetric structure, resulting in the ferroelectric polarization along *c*-axis [55]. For example, in  $\text{YMnO}_3$ , anomalies in dielectric constant values were observed near the  $T_N$  showing the signature of ME coupling [56]. It is also possible to crystallize these materials in orthorhombic phase (for R=Ho–Lu, Y) either at very high pressure [57, 58] or by using special low temperature soft chemistry synthesis routes and epitaxial thin film growth processes [59]. It is reported that this structural transition from hexagonal to orthorhombic phase in  $\text{RMnO}_3$  compounds (R=Ho–Lu) is associated with a remarkable change in Néel and Weiss temperature. For the hexagonal  $\text{LuMnO}_3$ , Néel and Weiss temperatures are located at around 88 and -600 K respectively [54, 60] but for the orthorhombic phase; these temperatures are shifted to 40 and -70 K, respectively [54].

The spin arrangement for  $\text{RMnO}_3$  is known to be AFM A-type for (R=La, Pr, Nd) and metamagnetic for (R=Gd, Tb, Dy, Ho). The  $T_N$  due to  $\text{Mn}^{+3}$  spin ordering is highly dependent on the ionic radius of rare-earth ions and decreases from 141 K for  $\text{LaMnO}_3$  to 40 K for  $\text{TbMnO}_3$  [61]. For the orthorhombic phases of  $\text{HoMnO}_3$ ,  $\text{DyMnO}_3$ ,  $\text{YbMnO}_3$ ,  $\text{ErMnO}_3$ ,  $\text{TmMnO}_3$  and  $\text{YMnO}_3$ , the AFM ordering of the manganese moments is reported to occur at

38, 39, 43, 42, 43, and 43 K, respectively [54]. For orthorhombic  $\text{RMnO}_3$  structure, it was observed that the decrease in ionic radius of R is accompanied with an increasing deformation from the ideal perovskite structure [61]. In hexagonal rare-earth manganites, magnetic interaction between  $\text{Mn}^{+3}$  ions is more prominent in-plane in comparison to the adjacent triangular planes via Mn–O–Mn AFM SE interaction. This is due to the fact that in-plane Mn–Mn distance is 3.5 Å whereas in the adjacent planes it is around 6 Å. The overall magnetic interaction in the in-plane  $\text{Mn}^{+3}$  ions is decided by the size and magnetic property of the rare-earth ions present in the non-coplanar layer which is present in between the two adjacent plane [62]. In addition to the ordering of  $\text{Mn}^{+3}$  spins, some of these rare-earth manganites show an additional AFM ordering transition at much lower temperature. This second AFM ordering is due to the SE interactions between rare-earth spins which occurs at lower temperatures due to relatively weaker SE interaction between rare-earth spins. For example, the rare-earth spins get antiferromagnetically ordered below 1.5 K for  $\text{PrMnO}_3$  and  $\text{NdMnO}_3$  [61]. The Ho and Dy spins get ordered in  $o$ - $\text{HoMnO}_3$  [61],  $o$ - $\text{DyMnO}_3$  [63] at 6 K and 10 K respectively. In  $\text{TbMnO}_3$ , the  $\text{Tb}^{+3}$  spins get ordered at 7 K [61].

In addition to the  $T_N$  discussed above, the rare-earth manganites also show some other interesting features. Both  $\text{LuMnO}_3$  and  $\text{YMnO}_3$  show magnetic as well as ferroelectric dipole coupling simultaneously below  $T_N$  where the triangular lattice arrangement might lead to the spin reorientation transition at lower temperatures (far below their respective  $T_N$ ) due to the geometrical frustration of  $\text{Mn}^{+3}$  spins [64]. Such type of spin reorientation transition does not only depend upon the temperature and magnetic field but also on the factors such as size of rare-earth ions, interatomic distance, and angles between the bonds in the structure [62]. Smaller rare-earth ions leads to more than one spin reorientation transitions as smaller ions enhance geometrical frustration in the lattice compare to the bigger ions. As the size of the rare-earth ion decreases, the oxygen atoms re-adjust to maintain the connectivity with rare-



earth ions and manganese ions. The displacement of oxygen in the lattice leads to the overall tilting of  $\text{MnO}_5$  planes. As the temperature goes below the  $T_N$  distortion in the lattice increases, such an enhanced geometrical frustration in  $\text{LuMnO}_3$  at low temperature arises because of trimerization of  $\text{Mn}^{+3}$  ions which leads to the displacement of various atoms resulting in the tilting of the  $\text{MnO}_5$  bi-pyramid. This is the reason that manganites with smaller rare-earth ions such as  $\text{LuMnO}_3$  were predicted to show magnetic ordering at much lower temperatures where as  $\text{YMnO}_3$  doesn't show such magnetic ordering at low temperature [62]. The spin reorientation transition as well as ordering at further lower temperature for  $\text{LuMnO}_3$  was predicted but never reported experimentally so far.

Here, we have revisited this interesting material by synthesizing it using simple wet-chemical technique to explore the field and temperature dependent magnetic behavior. Below, we have presented our results on the magnetic and optical behavior of nanocrystalline  $h\text{-LuMnO}_3$ .

### 3.3.2 Synthesis

We prepared nanocrystalline, hexagonal phase  $\text{LuMnO}_3$  using a modified hydrothermal process followed by annealing at  $750\text{ }^\circ\text{C}$ . Here, the pressure plays an important role in stabilizing the required phase of the  $\text{LuMnO}_3$ . For this purpose, stoichiometric amounts of lutetium (III) nitrate hydrate,  $(\text{Lu}(\text{NO}_3)_3 \cdot x\text{H}_2\text{O})$  (Aldrich, 99.9% purity), magnesium(II) nitrate x hydrate  $(\text{Mn}(\text{NO}_3)_2 \cdot x\text{H}_2\text{O})$  (Aldrich, 99.9% purity) and an equal amount of citric acid ( $\text{C}_6\text{H}_8\text{O}_7$ ) [(metal/citric acid molar ratio=1/1)] (Merck, 99.5% purity) were dissolved in the deionized water. The transparent solution was stirred for 6 h followed by drop-wise addition of ammonia solution (28 wt. %) to neutralize the unreacted citric acid as well as to raise the pH value of the solution near 9.2 resulting in sol formation. Further stirring for 3 h resulted in to a brick red solution which was transferred into an 80 mL capacity autoclave

with the Teflon liner. After the hydrothermal treatment at 150 °C for 20 h, the precipitate was in turn filtered, washed with deionized water and finally dried at 100 °C. Finally, the powder sample was calcined at 750 °C for 6 h and used for further study.

### 3.3.3 Structure and morphology

In figure 3.3.1, we have shown the room temperature x-ray diffraction pattern (XRD) of  $\text{LuMnO}_3$ .

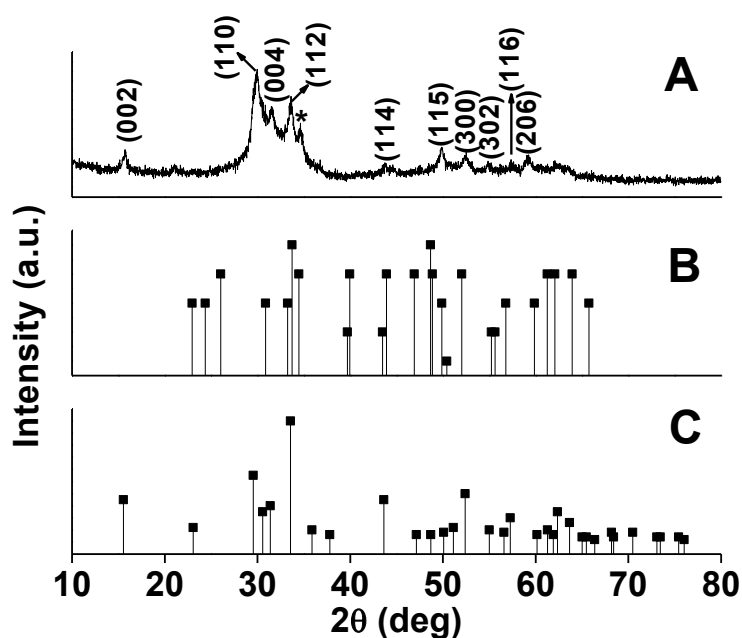


**Figure 3.3.1:** A comparison between A) powder x-ray diffraction pattern of  $\text{LuMnO}_3$  nanocrystals with B) the data from JCPDS Card No. 200650 for orthorhombic phase and C) JCPDS Card No. 140030 for hexagonal phase. The comparison shows that  $\text{LuMnO}_3$  crystallizes in hexagonal phase.

In figure 3.3.1, we have compared the experimental data with the reference data for both hexagonal (JCPDS file no. 140030) and orthorhombic (JCPDS file no. 200650) phases of bulk  $\text{LuMnO}_3$ . It can be noticed that the XRD pattern is matching with the hexagonal form

of  $\text{LuMnO}_3$ . The diffraction peaks are quite broad showing the formation of  $\text{LuMnO}_3$  nanocrystallites. The mean crystallite size calculated by means of Debye-Scherrer formula based on FWHM of different diffraction peaks was found to be approximately 32 nm which confirms the nanocrystalline nature of material.

To further investigate the microstructure and morphology of the as-synthesized material, we used HRTEM to image the  $\text{LuMnO}_3$  nanocrystals on carbon-coated copper TEM grids. The TEM images of  $\text{LuMnO}_3$  nanoparticles with different magnification is shown in figures 3.3.2 A–C, suggests that particles are with plate like morphology and nanocrystalline in nature despite of sintering, required to get the desired hexagonal phase.

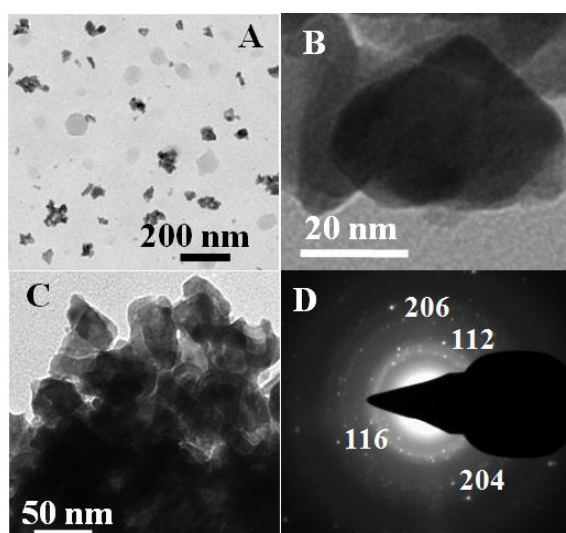


**Figure 3.3.2:** A, B, C) Transmission electron micrograph of  $\text{LuMnO}_3$  at different scales taken from various parts of the same TEM grid D) SAED pattern of  $\text{LuMnO}_3$  nanoparticles.

In panel 3.3.2 D, we have shown the SAED patterns which again confirms the formation of hexagonal phase consistent with the powder XRD profile.

### 3.3.4 Raman spectroscopy

Raman spectroscopy is a very sensitive technique which can be effectively used to study the changes of symmetry and structure of compounds. Figure 3.3.3 A, shows Raman spectra of  $\text{LuMnO}_3$  in nanocrystalline form. In the absence of any previous report on the room temperature Raman spectra on  $\text{LuMnO}_3$  in detail, we compared our results with another closely related structure  $\text{YMnO}_3$  [65] which also crystallizes in similar  $P6_3cm$  space group symmetry. From the group-theoretical analysis for the  $\Gamma$ -point phonon modes of hexagonal  $\text{RMnO}_3$ , 38 ( $9A_1 + 14E_1 + 15E_2$ ) modes are Raman active. In table 1, we have compared our results, with the reported values on  $\text{YMnO}_3$  and calculated value for  $P6_3cm$ . The experimental values are in reasonable agreement with the calculated values.

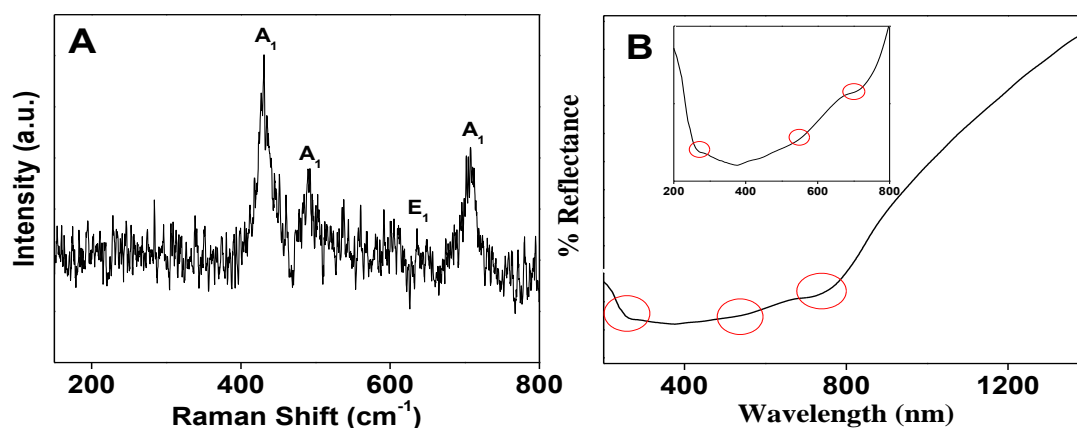


**Figure 3.3.3:** A) Room temperature Raman spectra of nanocrystalline  $\text{LuMnO}_3$  B) UV-vis-NIR spectra of  $\text{LuMnO}_3$  at room temperature in diffused reflectance mode. Inset shows the zoom view of part of the same curve.

**Table 3.3.1:** Comparison between the room temperature Raman mode positions ( $\text{cm}^{-1}$ ) from our present study on  $\text{LuMnO}_3$  nanoparticles (figure: 3.3.3 A), reported data on isomorphic structure  $\text{YMnO}_3$  by Iliev *et al.* and calculated data on same symmetric structure (Iliev *et al.*)[65].

Raman modes	Our study	Iliev <i>et al.</i>	Calculated
$A_1$	146	148	147
$A_1$	192	190	204
$A_1$	257	257	222
$A_1$	297	297	299
$A_1$			388
$A_1$	229	433	423
$A_1$	490	459	492
$A_1$			588
$A_1$	685	681	662
$E_1$	114		117
$E_1$			147
$E_1$	159		158
$E_1$			212
$E_1$			233
$E_1$			250
$E_1$			353
$E_1$	389	376	390
$E_1$	412	408	410
$E_1$			459
$E_1$	559		492
$E_1$			559

---

E <sub>1</sub>	636	632	586
			635
E <sub>2</sub>	72		
E <sub>2</sub>	105		71
E <sub>2</sub>	136	135	108
E <sub>2</sub>	173		136
E <sub>2</sub>	215	215	161
E <sub>2</sub>	233		212
E <sub>2</sub>	245		241
E <sub>2</sub>	338	302	245
E <sub>2</sub>	375		336
E <sub>2</sub>			382
E <sub>2</sub>	514		407
E <sub>2</sub>			458
E <sub>2</sub>	581		515
E <sub>2</sub>			557
			580
			638

---

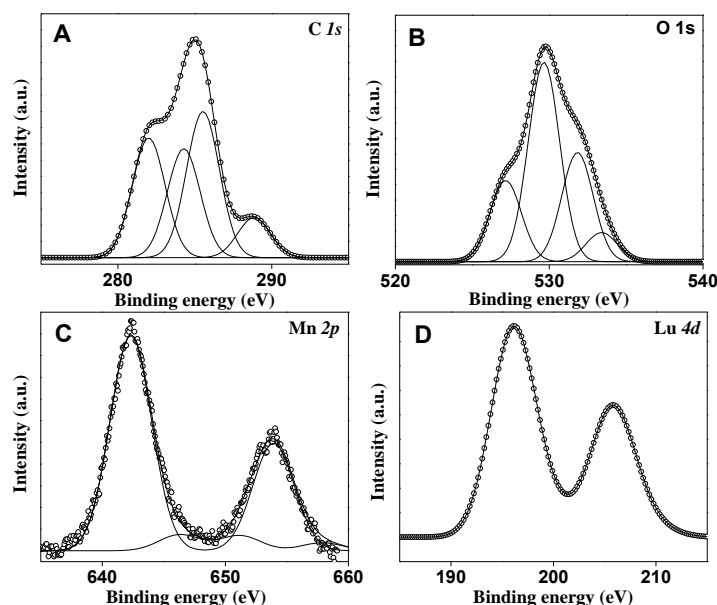
### 3.3.5 UV-vis-NIR spectroscopy

Figure 3.3.3 B shows the UV-vis-NIR spectra of dried LuMnO<sub>3</sub> in diffuse reflectance mode at room temperature. We observed three peaks situated at around 1.7 eV (729 nm), 2.3 eV (539 nm) and 5 eV (248 nm) for the hexagonal phase of LuMnO<sub>3</sub>. The peak situated around 729 nm is attributed to the inter-site optical transition from the hybrid occupied state with  $d_{xy}/d_x^2-d_y^2$  orbital symmetry to unoccupied Mn  $d_{3z^2-r^2}$  state and the peak around 539 nm is attributed to the inter-site optical transition from the hybrid occupied state with  $d_{yz}/d_{zx}$  orbital

symmetry to unoccupied Mn  $d_{3z^2-r^2}$  state [66]. The 248 nm peak is due to the charge transfer transition from hybridized oxygen 2p level to Mn  $d_{3z^2-r^2}$  level [66]. It should be noticed that these peaks are only observed for the hexagonal phase of RMnO<sub>3</sub> compounds. On the other hand, for the orthorhombic phase, these peaks are either very weak in intensity or entirely absent which is in accordance to the selection rules for the on-site Mn  $d-d$  transitions in the hexagonal and (near) cubic symmetry [66]. The electronic transition spectra, therefore, is consistent with the powder XRD observations.

### 3.3.6 X-ray photoelectron spectroscopy (XPS)

In figure 3.3.4, we have shown the room temperature XPS results. The XPS spectrum of Mn<sup>+3</sup> 2p is shown in figure 3.3.4 C. Mn<sup>+3</sup> 2p spectrum shows two prominent peaks at 642.3 eV ( $2p^{3/2}$ ) and 654.2 eV ( $2p^{1/2}$ ).



**Figure 3.3.4:** X-ray photoelectron spectroscopy spectra of A) C 1s B) O 1s C) Mn 2p D) Lu 4d of nanocrystalline LuMnO<sub>3</sub>. The lines represent the deconvoluted peaks.

The slight hump centered at  $\sim 646.4$  eV is quite weak in intensity and can be considered as a satellite peak due to shake-up process [67]. The  $\text{Mn}^{+3}$  cations in  $\alpha\text{-Mn}_2\text{O}_3$  show peaks at 641.9 and 653.5 eV (within the error of 0.2 eV) [68]. In our case, the shift in  $\text{Mn}^{+3}$  peaks by 0.4 eV is probably due to the change in the crystal field environment in comparison to  $\alpha\text{-Mn}_2\text{O}_3$ . The XPS spectrum of  $\text{Lu}^{+3}$  ions is shown in figure 3.3.4 (D) where we see the characteristic peaks situated at 196.2 and 205.8 eV indicating the presence of  $\text{Lu}^{+3}$  ions [69].

### 3.3.7 Magnetic study

To check the possibility of predicted magnetic transition in  $h\text{-LuMnO}_3$  below its  $T_N$ , we performed a detailed DC magnetic susceptibility vs. temperature measurements as well as M–H hysteresis measurements in various conditions on  $\text{LuMnO}_3$ . Figure 3.3.5 A shows that M–H curves at higher temperatures (70, 90, 250 K) are almost linear indicating the existence of paramagnetic phase, however below 90 K we observed the onset of small non-linear behavior. In the figure 3.3.5 C, we have shown the initial magnetization vs. applied magnetic field at various temperatures. It is clear that just above 90 K, the initial M–H curves are linear and below that, at 85 K, the curve starts getting a small curvature which indicates that the  $T_N$  is somewhere in between these temperature range. In figure 3.3.5 D, we have shown the zoom view of M–H loops. The non-linear behavior is followed by a sharp increase in the coercivity value below  $\sim 45$  K which opens-up further at lower temperatures along with increasing nonlinear behavior.



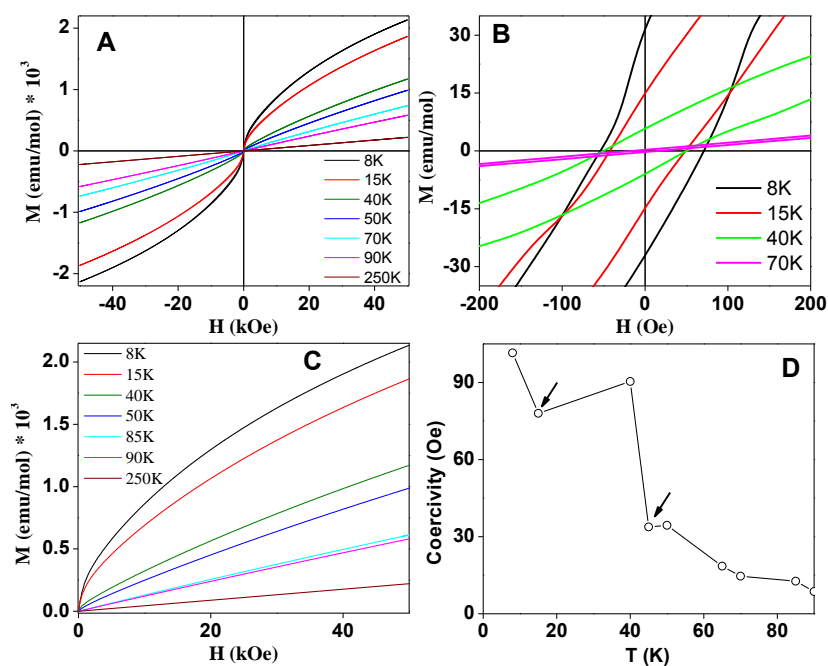


**Figure 3.3.5:** A)  $M$ – $H$  loops for nanocrystalline  $\text{LuMnO}_3$  shown at various temperatures B) zoom view of the  $M$ – $H$  curves C) initial magnetization curves at different temperature, showing non-linear behavior below 90 K D) variation of coercivity, with temperature, the arrow shows anomalies which were also seen in the  $M$ – $T$  curves.

At 14 K, the  $M$ – $H$  loop showed a dip in the coercivity from 90 Oe at 45 K to 78 Oe at 15 K. Below 14 K, the coercivity again shows an increasing trend. The origin of these anomalies will be discussed later. It can also be noticed that at any of the measured temperatures, the magnetization does not saturate up to 50 kOe magnetic field due to PM or AFM character of the material.

In figure 3.3.6, we have shown the magnetic susceptibility ( $\chi$ ) and the inverse of magnetic susceptibility ( $1/\chi$ ) versus temperature for  $\text{LuMnO}_3$  nanocrystals at 100 Oe applied field. Here, an anomaly was observed below 89 K (shown as  $T_N$ ), which is in the close proximity to the  $T_N$  observed for bulk  $\text{LuMnO}_3$  [60]. Below this temperature, the magnetic

susceptibility curves deviated from the ideal Curie-Weiss behavior as  $\text{Mn}^{+3}$  sublattice AFM ordering starts to set-in through the SE interaction. Above this transition temperature, both ZFC–FC magnetization curves follow the Curie-Weiss law (as shown by the straight line). Below the  $T_N$ , we see two more sharp magnetic anomalies marked by  $T_1$  and  $T_2$  in figure 3.3.6 A. The anomaly at  $T_1=44$  K is witnessed by a sharp bifurcation between ZFC–FC magnetization curves and a sudden rise in the magnetization with decreasing temperature. Another anomaly situated at  $T_2=12$  K is observed in form of a peak in ZFC magnetization curves.

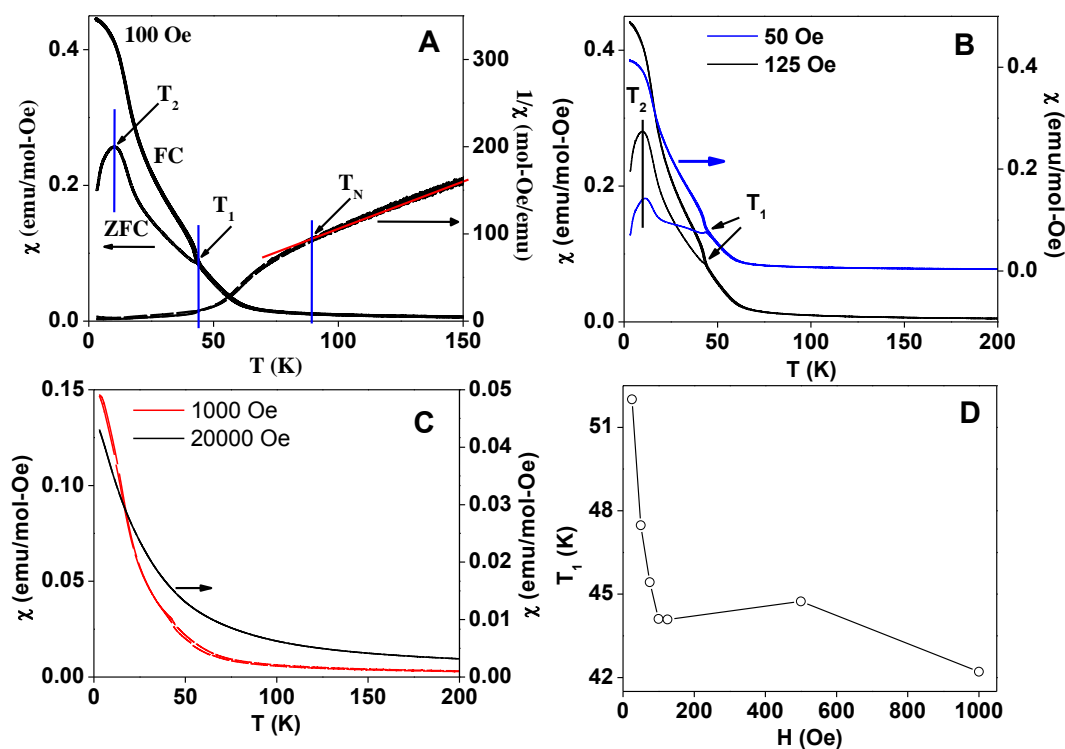


**Figure 3.3.6:** A)  $\chi$  and  $1/\chi$  vs. temperature curves at 100 Oe. Curves show three anomalies at temperature  $T_N$  (deviation of the  $1/\chi$  from linear behavior),  $T_1$  (bifurcation temperature of ZFC–FC curves) and  $T_2$  (sharp peak in ZFC curve) B) ZFC–FC magnetization curves at 50 and 125 Oe applied field C) ZFC–FC magnetization curves at 1000 Oe and 20000 Oe applied field D) the variation of ordering temperature,  $T_1$  with applied field.

To see the field dependent response of these curves we measured the ZFC–FC magnetization curves at various field values from 100 Oe to 20 kOe (shown in figure 3.3.6 B, C). Here, we observe that the AFM transition at ~89 K does not depend on the applied external field up to the highest applied field of 20 kOe, probably due to the relatively strong AFM exchange forces between  $\text{Mn}^{+3}$  ions. It is worth pointing out here that, these anomalies at 44 K and 12 K observed in our coercivity vs. temperature (figure 3.3.5 D) and M–T curves were theoretically predicted but never reported experimentally in previous works [64]. The earlier research efforts, the ZFC–FC magnetization measurements were done at much higher applied field showed only the  $T_N$  in form of deviation in ZFC–FC magnetization curves below 90 K [54, 60]. We believe that higher applied magnetic field might have masked these relatively weaker magnetic anomalies as seen by us in coercivity and magnetization. Earlier reports on *h*-LuMnO<sub>3</sub> did not attempt to check the coercivity variation with temperature. We attributed the bifurcation observed at 44 K to reorientation transition of  $\text{Mn}^{+3}$  spins resulting into a sharp jump in the coercivity and net magnetization. This type of spin reorientation transition was experimentally observed in many other compounds including YMnO<sub>3</sub>. For InMnO<sub>3</sub>, ScMnO<sub>3</sub>, which have the same  $P6_3cm$  symmetry, this type of transition was observed at around 43 K [64]. Our field dependent ZFC–FC magnetization studies revealed that this anomaly  $T_1$  is highly field dependent and shifts from 42 K to 52 K as the field value decreases from 1000 to 25 Oe and disappears completely at 20 kOe (shown in figure 3.3.6 C).

The origin of the spin-reorientation can be explained by the onset of DM with decreasing temperature [70]. The canting/reorientation of spins due to DM interaction results in the rise in the coercivity and magnetization below  $T_1$ .  $\text{Lu}^{+3}$  ion have  $4f^{14}$  outer most electronic configuration which doesn't have local magnetic moment so it does not have any direct exchange field interaction on the  $\text{Mn}^{+3}$  spins but its size evidently plays an important

role in lattice (in deciding the atomic arrangement) thereby affecting the magnetic properties significantly. Unlike LuMnO<sub>3</sub>, the rare-earth manganites with larger ionic radius of rare-earth ions do not show any further long range magnetic ordering below the T<sub>N</sub> [64]. The AFM ordering in LuMnO<sub>3</sub> results into a large atomic displacement around T<sub>N</sub>, where the lattice constant values change in such a way that overall symmetry of the structure remains unchanged. Such kind of isostructural transitions (which are rarely observed) are also the driving force for the gigantic magnetoelastic coupling in manganites as seen in YMnO<sub>3</sub> [71]. Lee *et al.* have reported that in YMnO<sub>3</sub>, below the T<sub>N</sub>, the positions of Mn<sup>+3</sup> ions drastically change to make an ordered triangular arrangement in the *ab* plane [71]. Such an abnormal large shift in the Mn<sup>+3</sup> position starts from 40–50 K to T<sub>N</sub>, 89 K [71]. This large atomic displacement produce a coupling between the electric and magnetic dipole throughout all temperature range from 40 to 89 K. They commented that such coupling is observed at T<sub>N</sub> only but had not mentioned that this magnetoelastic coupling is starting from 40–50 K where magnetic reorientation transition is coming from the DM interaction.

Now, we discuss the new transition seen around 12 K (marked as T<sub>2</sub>) which was observed by us in form of a sharp peak. This transition is also not reported previously [54]. This transition is AFM in nature and accompanied by a decrease in the coercivity at 12 K. Unlike the T<sub>N</sub> seen ~90 K, this rather weak AFM coupling (T<sub>2</sub>) between Mn–O–Mn in the *ab* plane depends highly on magnetic field and disappears at 2 kOe. In hexagonal manganites such as LuMnO<sub>3</sub>, the in-plane Mn<sup>+3</sup> ions interact much strongly (through AFM Mn–O–Mn SE interaction) in comparison to the Mn<sup>+3</sup> ions situated in adjacent triangular planes. The reason being relatively shorter distance of in-plane Mn–Mn ions (3.5 Å) in comparison to the distance between Mn<sup>+3</sup> ions situated in the adjacent planes (~6 Å) [62]. The geometrical distortion which is coming due to the size of the rare-earth ions creates difference in the bond

---

length and bond angle of the Mn–O–Mn in the *ab* plane which leads to the appearance of various triangular ordered AFM arrangement in LuMnO<sub>3</sub> at low temperature.

### 3.3.8 Conclusion

We have synthesized *h*-LuMnO<sub>3</sub> nanoparticles using the hydrothermal method. The XRD, UV-vis and Raman spectra confirm hexagonal phase with *P6<sub>3</sub>cm* symmetry. The magnetic measurements revealed two new field dependent transitions at 44 and 12 K. These transitions are attributed to Mn<sup>+3</sup> ion reorientation and weak AFM coupling between Mn–O–Mn in the *ab* plane, respectively.

---

### 3.4 References

- [1] Rao, C. N. R.; Serrao, C. R. *J. Mater. Chem.* **2007**, *17*, 4931.
- [2] Sahu, J. R.; Ghosh, A.; Sundaresan, A.; Rao, C. N. R. *Mater. Res. Bull.* **2009**, *44*, 2123.
- [3] Uusi-Esko, K.; Malm, J.; Imamura, N.; Yamauchi, H.; Karppinen, M. *Mater. Chem. Phys.* **2008**, *112*, 1029.
- [4] van Aken, B. B.; Palstra, T. T. M. *Phys. Rev. B* **2004**, *69*, 134113.
- [5] van Aken, B. B.; Meetsma, A.; Palstra, T. T. M. *Acta Crystallogr. Sect. C: Cryst. Struct. Commun.* **2001**, *57*, 230.
- [6] Singh, A. K.; Patnaik, S.; Kaushik, S. D.; Siruguri, V. *Phys. Rev. B* **2010**, *81*, 184406.
- [7] van Aken B.; Palstra, T. T. M.; Filippetti, A; Spaldin, N. A. *Nat. Mater.* **2004**, *3*, 164.
- [8] Huang, Z. J.; Cao, Y.; Sun, Y. Y.; Xue, Y. Y.; Chu, C. W. *Phys. Rev. B* **1997**, *56*, 2623.
- [9] Iliev, M. N.; Lee H-G *Phys. Rev. B* **1997**, *56*, 2488.
- [10] Fiebig, M.; Lottermoser, T.; Fröhlich, D.; Goltsev, A. V.; Pisarev, R. V. *Nature* **2002**, *419*, 818.
- [11] Lorenz, B.; Litvinchuk, A. P.; Gospodinov, M. M.; Chu, C. W. *Phys. Rev. Lett.* **2004**, *92*, 87204.
- [12] Lee, S.; Pirogov, A.; Kang, M.; Jang, K. H.; Yonemura, M.; Kamiyama, T.; Cheong, S. W.; Gozzo, F.; Shin, N.; Kimura, H.; Noda, Y.; Park, J. G. *Nature* **2008**, *451*, 805.
- [13] Fennie, C. J.; Rabe, K. M. *Phys. Rev. B* **2005**, *72*, 100103.
- [14] Fiebig, M.; Degenhardt, C.; Pisarev, R.V. *Phys. Rev. Lett.* **2002**, *88*, 027203.

- 
- [15] Koehler, W. C.; Yakel, H. L.; Wollan, E. O.; Cable, J. W. *Proceedings of the 4th Conference on Rare-Earth Research, Phoenix, Arizona, 1964* (Gordon and Breach, New York, 1965), p. 63; *Phys. Lett.* **1964**, *9*, 93.
- [16] Fiebig, M.; Fröhlich, D.; Kohn, K.; Leute, St.; Lottermoser, Th.; Pavlov, V. V.; R. Pisarev, V. *Phys. Rev. Lett.* **2000**, *84*, 5620.
- [17] Bertaut, E. F.; Mercier, M.; Pauthenet, R. *Phys. Lett.* **1963**, *5*, 27.
- [18] Meier, D.; Ryll, H.; Kiefer, K.; Klemke, B.; Hoffmann, J. U.; Ramesh, R.; Fiebig, M. *Phys. Rev. B* **2012**, *86*, 184415.
- [19] Poddar, P.; Fried, T.; Markovich, G. *Phys. Rev. B* **2002**, *65*, 172405.
- [20] Bansal, V.; Poddar, P.; Ahmad, A.; Sastry, M. *J. Am. Chem. Soc.* **2006**, *128*, 11958.
- [21] Park, T. -J.; Papaefthymiou, G. C.; , Viescas, A. J.; , Moodenbaugh, A. R.; Wong, S. S. *Nano Lett.* **2007**, *7*, 766.
- [22] Raneesh, B.; Saha, A.; Das, D.; Kalarikkal, N. *J. Alloys Compd* **2013**, *551*, 654.
- [23] Raneesh, B.; Soumya, H.; Philip, J.; Kalarikkal, N. *J. Alloys Compd* **2013**, *579*, 243.
- [24] Jaiswal, A.; Das, R.; Vivekanand, K.; Abraham, P. M.; Adyanthaya, S.; Poddar, P. *J. Phys. Chem. C* **2010**, *114*, 2108.
- [25] Yen, F.; Cruz, dela C.; Lorenz, B.; Galstyan, E.; Sun, Y.Y.; Gospodinov, M.; Chu, C.W. *J. Mater. Res.* **2007**, *22*, 2163.
- [26] Han, T. -C.; Hsu, W. -L.; Lee, W. -D. *Nanoscale Res. Lett.* **2011**, *6*, 201.
- [27] Overton, A. J.; Best, J. L.; Saratovsky, I. Hayward, M. A. *Chem. Mater.* **2009**, *21*, 4940.
-

- 
- [28] Munôoz, A.; Alonso, J. A.; Casais, M. T.; Martínez-Lope, M. J.; Martínezand, J. L.; Fernández-Díaz, M. T. *J. Phys.: Condens. Matter* **2002**, *14*, 3285.
- [29] Edelstein, V. M. *Solid State Commun.* **1990**, *73*, 233.
- [30] Meservey, R.; Tedrow, P. M. *Phys. Rep.* **1994**, *238*, 173.
- [31] Moodera, J. S.; Nowak, J.; van de Veerdonk, R. J. M. *Phys. Rev. Lett.* **1998**, *80*, 2941.
- [32] Verwey, E. J. W. *Nature* **1939**, *144*, 327.
- [33] Fujimura, N.; Takahashi, T.; Yoshimura, T.; Ashida, A. *J. Appl. Phys.* **2007**, *101*, 09M107.
- [34] Alivisatos, P. *Science* **1996**, *271*, 933.
- [35] Hu, J. T.; Odom, T. W.; Lieber, C. M. *Acc. Chem. Res.* **1999**, *32*, 435.
- [36] Goldberger, J.; Fan, R.; Yang, P. D. *Acc. Chem. Res.* **2006**, *39*, 239.
- [37] Aravamudhan, S.; Luongo, K.; Poddar, P.; Srikanth, H.; Bhansali, S. *Appl. Phys. A* **2007**, *87*, 773.
- [38] Fontcuberta, J.; Gospodinov, M.; Skumryev, V. *J. Appl. Phys.* **2008**, *103*, 07B722.
- [39] Zhu, G.; Liu, P.; Liu, Y.; Miao, H.; Zhou, J. *J. Am. Ceram. Soc.* **2008**, *91*, 3423.
- [40] Urban, J. J.; Yun, W. S.; Gu, Q.; Park, H. *J. Am. Chem. Soc.* **2002**, *124*, 1186.
- [41] Han, J. T.; Huang, Y. H.; Huang, W.; Goodenough, J. B. *J. Am. Chem. Soc.* **2006**, *128*, 14454.
- [42] Liu, B.; Hu, B.; Du, Z. *Chem. Commun.* **2011**, *47*, 8166.
- [43] Zhang, X. Y.; Lai, C. W.; Zhao, X.; Wang, D. Y.; Dai, J. Y. *Appl. Phys. Lett.* **2005**, *87*, 143102.



- 
- [44] Ha, T. H.; Koo, H. J.; Chung, B. H. *J. Phys. Chem. C* **2007**, *111*, 1123.
- [45] Fabrèges, X.; Mirebeau, I.; Bonville, P.; Petit, S.; Lebras-Jasmin, G.; Forget, A.; André, G.; Pailhès, S. *Phys. Rev. B* **2008**, *78*, 214412.
- [46] Greedan, J. E.; Bieringer, M.; Britten, J. F.; Giaquinta, D. M.; and Zurloye, H. C. *J. Solid State Chem.* **1995**, *116*, 118.
- [47] Katsufuji, T.; Mori, S.; Masaki, M.; Moritomo, Y.; Yamamoto, N.; Takagi, H. *Phys. Rev. B* **2001**, *64*, 104419.
- [48] Han, T. C.; Hsu, W. L.; Lee, W. D. *Nanoscale Res. Lett.* **2011**, *6*, 201.
- [49] Sugie, H.; Iwata, N.; Kohn, K. *J. Phys. Soc. Jpn.* **2002**, *71*, 1558.
- [50] Harikrishnan, S.; Rößler, S.; Kumar, C. M. N.; Bhat, H. L.; Rößler, U. K.; Wirth, S.; Steglich, F.; Elizabeth, S. *J. Phys.: Condens. Matter* **2009**, *21*, 096002.
- [51] Han, J. T.; Huang, Y. H.; Huang, W.; Goodenough, J. B. *J. Am. Chem. Soc.* **2006**, *128*, 14454.
- [52] Jagannathan, R.; Poddar, P.; Prabhune, A. *J. Phys. Chem. C* **2007**, *111*, 6933.
- [53] Langille, M. R.; Personick, M. L.; Zhang, J.; Mirkin, C. A. *J. Am. Chem. Soc.* **2012**, *134*, 14542.
- [54] Uusi-Esko, K.; Malm, J.; Imamura, N.; Yamauchi, H.; Karppinen, M. *Mater. Chem. Phys.* **2008**, *112*, 1029.
- [55] Kimura, T.; Goto, T.; Shintani, H.; Ishizaka, K.; Arima, T.; Tokura, Y. *Nature* **2003**, *426*, 55.
- [56] Tomuta, D. G.; Ramakrishnan, S.; Nieuwenhuys, G. J.; Mydosh, J. A. *J. Phys.: Condens. Matter* **2001**, *13*, 4543.
-

- 
- [57] Waintal, A.; Capponi, J. J.; Bertaut, E.F.; Contré, M.; François, D. *Solid State Commun.* **1966**, *4*, 125.
- [58] Waintal, A.; Chenavas, J. *Mater. Res. Bull.* **1967**, *2*, 819.
- [59] Salvador, P. A.; Doan, T. D.; Mercey, B.; Raveau, B. *Chem. Mater.* **1998**, *10*, 2592.
- [60] Yoshii, K.; Abe, H. *J. Solid State Chem.* **2002**, *165*, 131.
- [61] Brinks, H. W.; Rodriguez-Carvajal, J.; Fjellvag, H.; Kjekshus, A.; Hauback, B. C. *Phys. Rev. B* **2001**, *63*, 09441.
- [62] Kozlenko, D. P.; Kichanov, S. E.; Lee, S.; Park, J. G.; Savenko, B. N. *J. Phys.: Condens. Matter* **2007**, *19*, 156228.
- [63] Mouallem-Bahout, M.; Pena, O.; Gutierrez, D.; Duran, P.; Moure, C. *Solid State Commun.* **2002**, *122*, 561.
- [64] Greedan, J. E.; Bieringer, M.; Britten, J. F.; Giaquinta, D. M.; Zurloye, H. C. *J. Solid State Chem.* **1995**, *116*, 118.
- [65] Iliev, M. N.; Lee, H. G.; Popov, V. N.; Abrashev, M. V.; Hamed, A.; Meng, R. L.; Chu, C. W. *Phys. Rev. B* **1997**, *56*, 2488.
- [66] Souchkov, A. B.; Simpson, J. R.; Quijada, M.; Ishibashi, H.; Hur, N.; Ahn, J. S.; Cheong, S. W.; Millis, A. J.; Drew, H. D. *Phys. Rev. Lett.* **2003**, *91*, 027203.
- [67] Silipigni, L.; Luca, G. D.; Quattrone, Q.; Scolaro, L. M.; Salvato, G.; Grasso, V. *J. Phys.: Condens. Matter* **2006**, *18*, 5759.
- [68] Oku, M.; Hirokawa, K.; Ikeda, S. *J. Electron. Spectros. Relat. Phenom.* **1975**, *7*, 465.
- [69] Nefedov, V. I.; Gati, D.; Dzhurinskii, B. F.; Sergushin, N. P.; Salyn, Y. V. *Zh. Neorg. Khimii* **1975**, *20*, 2307.
- [70] Munoz, A.; Alonso, J. A.; Martinez-Lope, M. J.; Casais, M. T.; Martinez, J. L.; Fernandez-Diaz, M. T. *Phys. Rev. B* **2000**, *62*, 9498.
-

---

[71] Lee, S.; Pirogov, A.; Kang, M.; Jang, K.-H.; Yonemura, M.; Kamiyama, T.; Cheong, S.-W.; Gozzo, F.; Shin, N.; Kimura, H.; Noda Y.; Park, J.-G. *Nature* **2008**, *451*, 805.

# Chapter 4. Orthorhombic rare-earth manganites ( $\text{RMnO}_3$ )

---

Orthorhombic rare-earth manganites,  $\text{RMnO}_3$  (R=Nd, Sm, Eu, Gd, Tb and Dy) are interesting because changing the ionic radius of rare-earth ions can tune  $\text{Mn}^{+3}$  magnetic structure which in turn control its ME coupling. In orthorhombic  $\text{RMnO}_3$  multiferroics, ferroelectricity is attributed to a complex spiral spin order that breaks the inversion symmetry.

Objective of this chapter is to develop a synthesis method, which can be used for the synthesis of orthorhombic  $\text{RMnO}_3$  (R=Gd, Dy, Eu and Tb) particles in nano dimension. Ferromagnetism is observed in nanoparticles of  $\text{GdMnO}_3$  due to surface uncompensated spins. Particle size dependent magnetic property of spiral magnet,  $\text{Gd/DyMnO}_3$  showed that nanoparticles of  $\text{Gd/DyMnO}_3$  retain the multiferroic property of its bulk phase. Large exchange bias was observed below incommensurate antiferromagnetic (ICAFM) to canted A-type antiferromagnetic (cAAFM) (~43 K) transition which was attributed to core-shell nature of antiferromagnetic core and ferromagnetic-like surface layer of  $\text{EuMnO}_3$  nanoparticles. In  $\text{TbMnO}_3$  nanoparticles, lock-in transition was suppressed in 25 nm particles due to intrinsic strain of nanoparticles. The increased value of magnetization in the 2–3  $\mu\text{m}$  particles of  $\text{TbMnO}_3$  was attributed to double exchange interactions between  $\text{Mn}^{+3}$  and  $\text{Mn}^{+4}$  spins.

---

---

**Section 4.1 Study of manganites with spiral spin structure:****Gd/DyMnO<sub>3</sub>**

---

Single-phase orthorhombic DyMnO<sub>3</sub> and GdMnO<sub>3</sub> nanoparticles in the size range 60–70 and 35–45 nm were synthesized using a modified hydrothermal method. No anomaly near T<sub>N</sub> of the Mn<sup>+3</sup> moments for both DyMnO<sub>3</sub> and GdMnO<sub>3</sub> nanoparticles were observed in ac magnetization which were observed in dc magnetization. The room temperature Raman spectra of DyMnO<sub>3</sub> showed two most intense Raman modes at 480 and 609 cm<sup>-1</sup> which can be assigned to symmetric and anti-symmetric or Jahn-Teller stretching mode involving Mn–O bond stretching.

---

### 4.1.1 Introduction

The strong coupling between ferroelectricity and magnetism in modern multiferroics has offered a new paradigm of ME materials. The ability to control FE polarization ( $\mathbf{P}$ ) with an applied magnetic field and vice versa in manganite perovskites allow its potential applications in data-storage, transducers, actuators, four-stage non-volatile memory, gate FE in field-effect transistors, and possibly in spintronics [1, 2]. Previously, it was believed that, two phenomenon, which are essential to show multiferroic property, are mutually exclusive because the FE in  $ABO_3$  requires the off-centering of  $d^0$  cation on the B-site and this is incompatible with magnetic ordering which requires unpaired spins [3]. However, now, it is known that there are four main possible mechanisms behind the origin of ferroelectricity in magnetic materials: lone-pair effects, geometric frustration, charge ordering, and magnetic ordering [4].

Recently, Goto *et al.* showed giant magnetocapacitance in  $DyMnO_3$ . In  $DyMnO_3$ , the spiral magnetic ordering is stabilized by competing exchange interactions, which forces oppositely charged ions to shift in opposite directions, can be easily influenced by applied magnetic fields [5]. In the orthorhombic rare-earth manganites  $RMnO_3$  ( $R=Gd, Tb, \text{ and } Dy$ ), which crystallize in a distorted perovskite structure, ferroelectricity has been shown to originate from a spiral magnetic structure [6, 7]. In  $DyMnO_3$ , the magnetic ordering of the  $Mn^{+3}$  moments with incommensurate propagation vector  $q_m^{Mn} \mathbf{b}^*$  is associated with a second-harmonic lattice modulation  $q_l^{Mn} = 2q_m^{Mn}$ , *i.e.*, with a quadratic magnetoelastic coupling [8, 9]. On cooling below  $T_N \sim 39$  K, the incommensurate values of  $q^{Mn}$  vary with temperature and below a characteristic temperature  $T_f \sim 18$  K, a spontaneous electric polarization is observed in zero applied magnetic field [10]. In  $DyMnO_3$ ,  $Mn^{+3}$  magnetic structure was inferred from synchrotron x-ray diffraction data which show the presence of an incommensurate lattice modulation with  $q_l^{Mn}$  varying between 0.72 and 0.77 below  $T_N = 39$  K [1]. From synchrotron

---

X-ray diffraction and resonant magnetic scattering experiments,  $\text{Dy}^{+3}$  magnetic structure was calculated along with  $\text{Mn}^{+3}$  in 4–40 K and it was shown that there is a strong interference of  $\text{Mn}^{+3}$  and  $\text{Dy}^{+3}$  induced structural distortions in  $\text{DyMnO}_3$  [11]. The  $\text{Dy}^{+3}$  ordering causes significant anomalies in the dielectric constant and the electric polarization. Therefore, the coupling between the  $\text{Dy}^{+3}$  and  $\text{Mn}^{+3}$  appears to be more important in  $\text{DyMnO}_3$  than other manganite perovskites of the same class.

$\text{Gd/DyMnO}_3$  is the multiferroic rare-earth manganites from the family of  $\text{RMnO}_3$  with  $\text{R}=\text{Gd}$ ,  $\text{Tb}$ , and  $\text{Dy}$  where magnetic and ferroelectric order coexist [12]. For  $\text{R}=\text{Tb}$  and  $\text{Dy}$ , the multiferroic behavior is already present in zero magnetic field, while a finite magnetic field along the  $b$ -axis is necessary to induce multiferroicity in  $\text{GdMnO}_3$  [13, 14]. At room temperature,  $\text{GdMnO}_3$  is PE and PM with a distorted perovskite structure of orthorhombic symmetry with space group  $Pbnm$  [15,16]. At zero magnetic field,  $\text{GdMnO}_3$  remains PE. At 42 K,  $T_N$ ,  $\text{GdMnO}_3$  undergoes a phase transition from PM to an ICAFM phase, with a modulation wave vector directed along the  $b$  axis [12, 13, 17]. This modulation corresponds to a collinear arrangement of the  $\text{Mn}^{+3}$  spins, is a consequence of competing exchange interactions between successive neighbor spins, which lead to a frustrated magnetic system. The modulated magnetic order below  $T_N$  remains collinear until the system enters into an  $A$ -type AFM phase at  $\sim 27$  K [14]. Around 22 K, it under goes further transition from ICAFM into a  $c$ AAFM of the  $\text{Mn}^{+3}$  spins along the  $c$  axis [12, 18]. Below this transition, the polarization of the  $\text{Gd } 4f$  spins by the spin canting of  $\text{Mn}^{+3}$  moments results weak ferromagnetism. At low temperature around 6 K, the long-range ordering of  $\text{Gd}^{+3}$  moments occurs [16]. Below this temperature there is a resultant configuration of net moment of canted  $\text{Gd}$  spins antiparallel to that of canted  $\text{Mn}^{+3}$  spins. The application of a strong magnetic field,  $H \geq 5$  T along the  $a$ -axis induces a FE phase with a polarization oriented along the  $c$ -axis

---

[14]. Structural studies showed that this magnetically induced FE phase is accompanied by a commensurate modulation of the  $\text{Mn}^{+3}$  moments [15].

It is interesting to explore whether the unique properties of intrinsic multiferroics are retained in their nanoparticle form with possible modifications/enhancements, so that multiferroics themselves can be integrated into nano electronics and other applications with potential benefits. Nanoparticle exhibits significant property differences from their bulk counterparts due to their large surface to volume ratio and related changes in elementary excitations and defect states. So it is interesting to explore the corresponding effects in multiferroic properties in nanoparticle form. There are very few reports in the size dependent properties of multiferroic oxide because the synthesis of these materials in nano size with proper crystallinity and phase is non-trivial. Recently, Wang *et al.* had published magnetic and optical properties of  $\text{GdMnO}_3$  nanoparticles, where they used sol-gel method to prepare ~ 52 nm particles [19]. As seen from SEM images particles were agglomerated [19].

In this section, we have synthesized nano-sized  $\text{DyMnO}_3$  and  $\text{GdMnO}_3$  particle. Anomalies near  $T_N$  of the  $\text{Mn}^{+3}$  moments for both  $\text{DyMnO}_3$  and  $\text{GdMnO}_3$  which were observed in dc-magnetization were not observed in ac-magnetization. We showed that the nanoparticles of  $\text{DyMnO}_3$  and  $\text{GdMnO}_3$  synthesized by hydrothermal method retain the interesting magnetic properties of their bulk counterpart.

#### 4.1.2 Synthesis

Dysprosium and gadolinium orthomanganite nanoparticles were synthesized using a hydrothermal process followed by annealing at 700 °C. For this purpose, stoichiometric amounts of dysprosium (III) nitrate hydrate,  $(\text{Dy}(\text{NO}_3)_3 \cdot x\text{H}_2\text{O})$ , Aldrich, 99.9%) and gadolinium (III) nitrate hexahydrate,  $(\text{Gd}(\text{NO}_3)_3 \cdot 6\text{H}_2\text{O})$ , Aldrich, 99.9%), magnesium(II) nitrate x hydrate  $(\text{Mn}(\text{NO}_3)_2 \cdot x\text{H}_2\text{O})$ , Aldrich, 99.9%) and an equal amount of citric acid



( $C_6H_8O_7$ ) (metal/citric acid molar ratio=1/1)] (Merck, 99.5% ) were dissolve in deionized water. Ethylene glycol (Merck, 99.5 %) was added to enhance the gelation, since it reduces the diffusion path of the metal precursors, and so the metal ions can form uniform complexes. The transparent solution was stirred for 6 h followed by drop-wise addition of ammonia solution (28 wt. %) to raise the pH value of the solution near 9.2 resulting in sol formation and further the sol was stirred for 3 h. The final solution was transferred to an 80 mL capacity autoclave with the Teflon liner and heated at 200 °C under the autogenous pressure for 24 h. After completion of the reaction, the precipitate was filtered and washed with de-ionized water to remove all unreacted precursors and then dried in air at 120 °C. After that the powder sample was annealed at 700 °C for 6 h. The annealed sample was used for further characterization.

#### 4.1.3 Structure and morphology

Figure 4.1.1 and 4.1.2 shows the XRD patterns of as-prepared  $DyMnO_3$  and  $GdMnO_3$  nanoparticles annealed at 700 °C. The XRD patterns were indexed with the orthorhombically distorted perovskite structure with space group  $Pbnm$  of  $DyMnO_3$  and  $GdMnO_3$  nanoparticles according to JCPDS file no. 250330 and 250337 respectively. The diffraction peaks in XRD patterns were quite broad showing the formation of nanocrystallites. Additionally, XRD results did not find any signature of  $Mn_3O_4$  or any other impurity phase of hexagonal  $RMnO_3$  or bilayer manganite ( $RMn_2O_5$ ).

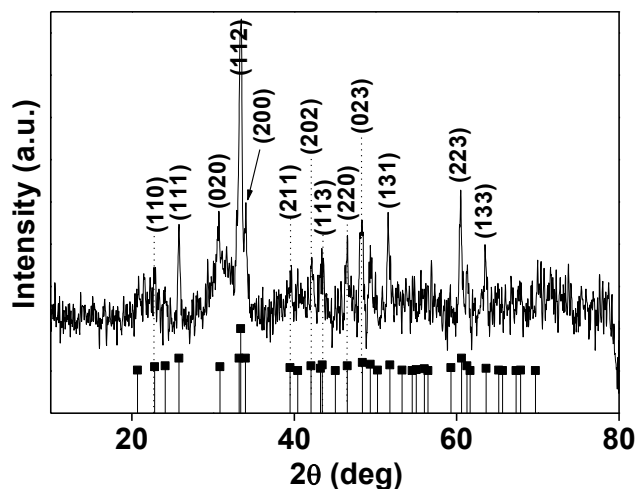


**Figure 4.1.1:** XRD patterns of  $\text{DyMnO}_3$  from JCPDS#250330 database (vertical line) and of as-prepared  $\text{DyMnO}_3$  nanoparticles annealed at  $700^\circ\text{C}$ .

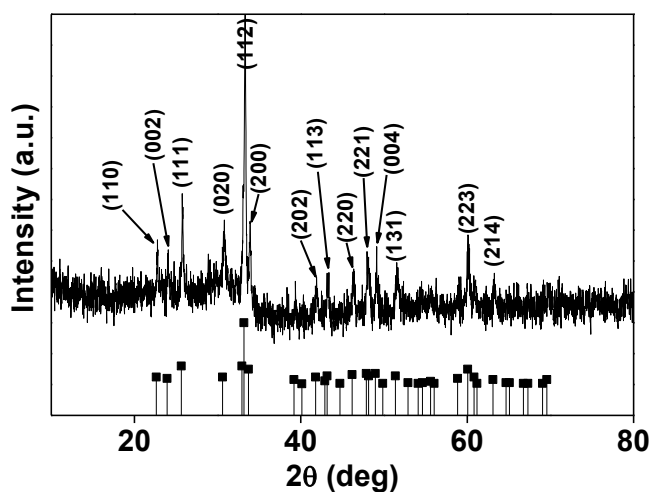


**Figure 4.1.2:** XRD patterns of  $\text{GdMnO}_3$  from JCPDS#250337 database (vertical line) and of as-prepared  $\text{DyMnO}_3$  nanoparticles annealed at  $700^\circ\text{C}$ .

To further investigate the microstructure and morphology of the as-synthesized material, we used the FEI (model Tecnai F30) HRTEM equipped with field emission source operating at 300 kV to image the nanocrystals on carbon-coated copper TEM grid. Analysis of the images (figure 4.1.3 and 4.1.4 A, B) revealed that the size of the nanoparticles range

between 60–75 and 35–45 nm for  $\text{DyMnO}_3$  and  $\text{GdMnO}_3$ , respectively. Figure 4.1.3 C and 4.1.4 C clearly show the presence of pronounced lattice fringes indicating good level of crystallinity.

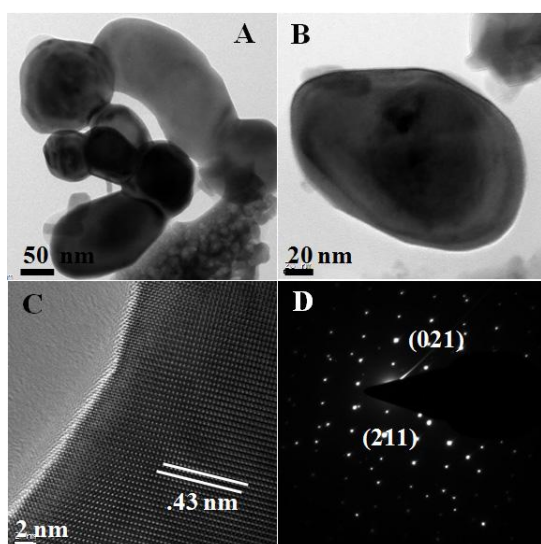


**Figure 4.1.3:** A, B) TEM images, C) HRTEM images shows lattice fringes and  $d$ -values calculated from the image correspond to (101) planes of  $\text{DyMnO}_3$  D) SAED pattern of as-prepared  $\text{DyMnO}_3$ .

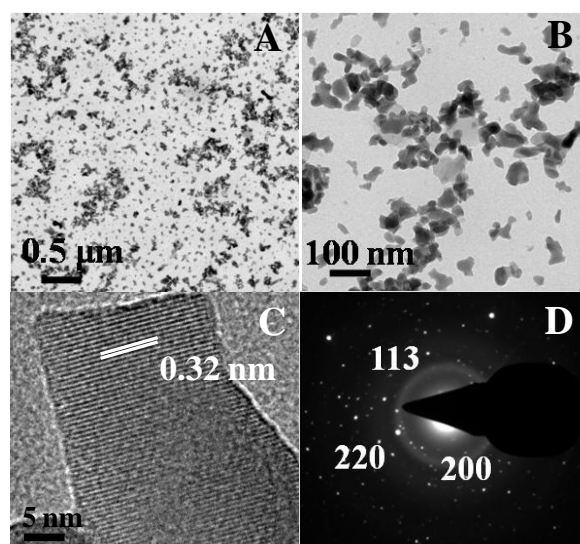


**Figure 4.1.4:** A, B) TEM images, C) HRTEM images shows lattice fringes and  $d$ -values calculated from the image correspond to (111) planes of  $\text{GdMnO}_3$  D) SAED pattern of as-prepared  $\text{GdMnO}_3$ .

The edges of the nanoparticles do not show any defects, which proves that particles surface remains defect-free even after annealing at 700 °C. The  $d$ -values calculated from these images correspond to (101) and (111) planes of  $\text{DyMnO}_3$  and  $\text{GdMnO}_3$ , respectively, matching with those obtained from powder XRD.

#### 4.1.4 X-ray photoelectron spectroscopy (XPS)

Room temperature XPS was used to confirm the oxidation state of  $\text{Mn}^{+3}$  to validate the formation of the pure phase. We used Shirley-algorithm for background correction and chemically distinct species were resolved using a nonlinear least squares fitting procedure. The core-level binding energies were aligned with the carbon binding energy of 285 eV. The  $\text{Mn}^{+3}$   $2p$  core level electron binding XPS spectra of  $\text{DyMnO}_3$  and  $\text{GdMnO}_3$  are given in figure 4.1.5, which shows peaks at 642.8 and 641.9 eV for  $\text{DyMnO}_3$  and  $\text{GdMnO}_3$  respectively, characteristic of  $\text{Mn}^{+3}$   $2p_{3/2}$  [20]. XPS results don't show signature of Mn ions in any other oxidation states (+2 or +4). This also indicated the absence of  $\text{RMn}_2\text{O}_5$  phase.

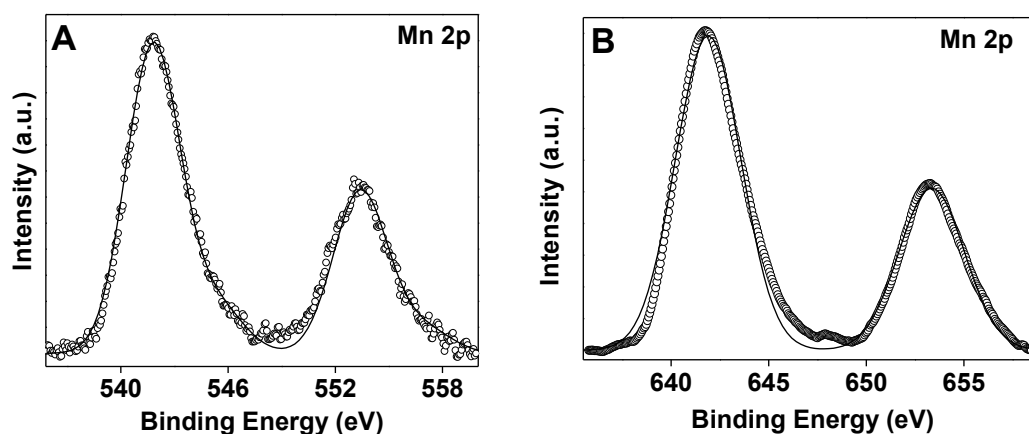
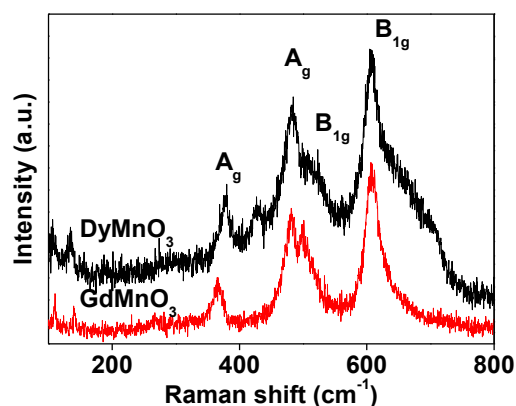


**Figure 4.1.5:** XPS spectra for Mn 2p of as-prepared (A)  $\text{DyMnO}_3$ , (B)  $\text{GdMnO}_3$  nanoparticles annealed at 700 °C (scatter curves) and the lines represent the deconvoluted peaks.

#### 4.1.5 Raman spectroscopy

Raman spectroscopy is a very sensitive technique which can be effectively used to study the changes of symmetry and structure of compounds. Experimentally observed Raman peaks  $A_g$

and  $B_{1g}$  of  $DyMnO_3$  and  $GdMnO_3$  are shown in figure 4.1.6. The Raman active modes in orthorhombic  $DyMnO_3$  and  $GdMnO_3$  with  $Pbnm$  structure are  $7A_g+7B_{1g}+5B_{2g}+5B_{3g}$  [21]. These Raman modes are active due to the deviation of the structure from ideal perovskite structure. Two



most intense Raman modes at 480 and 609  $cm^{-1}$  can be assigned to an antisymmetric Jahn-Teller stretching mode and a symmetric or breathing

stretching mode respectively. Two modes at 508 and 525  $cm^{-1}$  are assigned to bending modes of  $MnO_6$  around y- and x-axis respectively [21]. The peak at 380  $cm^{-1}$  is assigned to the tilt of  $MnO_6$ . Raman shift at 426  $cm^{-1}$  in  $DyMnO_3$  Raman spectra is assigned to the out-of-phase bending of  $MnO_6$  [21]. Raman shift at 426  $cm^{-1}$  was not observed in  $GdMnO_3$ . However, in case of  $TbMnO_3$ , we observed out-of-phase bending of  $MnO_6$   $\sim 426$   $cm^{-1}$  [21].

**Figure 4.1.6:** Room temperature Raman spectra of nanocrystalline  $DyMnO_3$  and  $GdMnO_3$ .

#### 4.1.6 Magnetic study

M–H curves for  $DyMnO_3$  nanoparticles above 50 K shows linear behavior (figure 4.1.7 A) thereby indicating the presence of paramagnetic behavior around this temperature. The coercivity values at 3 and 5 K are 473 and 185 Oe, respectively (figure 4.1.7 B). The large coercivity at low temperature might be due the uncompensated surface spins and weak FM frequently noticed in nano-sized particles [22].

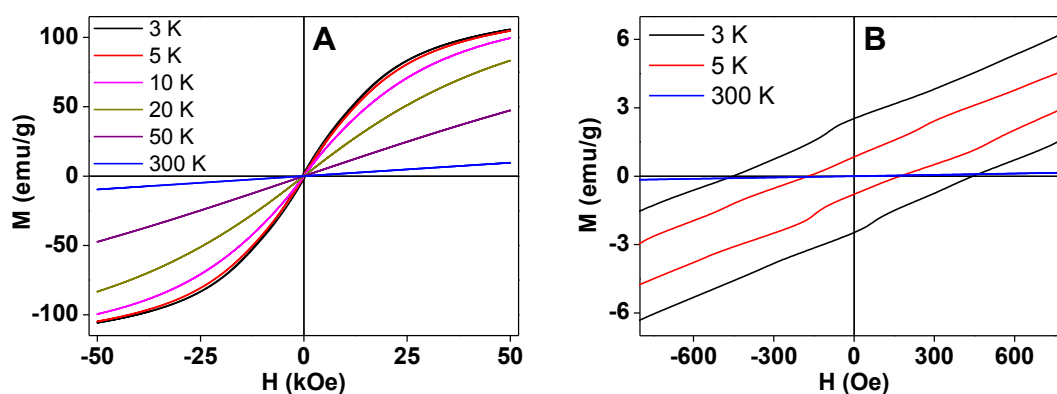


**Figure 4.1.7:** A) Magnetic hysteresis loops B) expanded plots of hysteresis loops at 3, 5 and 300 K of  $\text{DyMnO}_3$  nanoparticles annealed at  $700^\circ\text{C}$ .

Figure 4.1.8 (B) shows zoomed view of M–H loops at representative temperatures for  $\text{GdMnO}_3$  nanoparticles. The M–H curves at 200 K ( $T > T_N$ ) show linear behavior similar to the PM phase (figure 4.1.8 A), however, below  $T_N$ , we observed an increasingly non-linear behavior and opening-up of hysteresis loop.

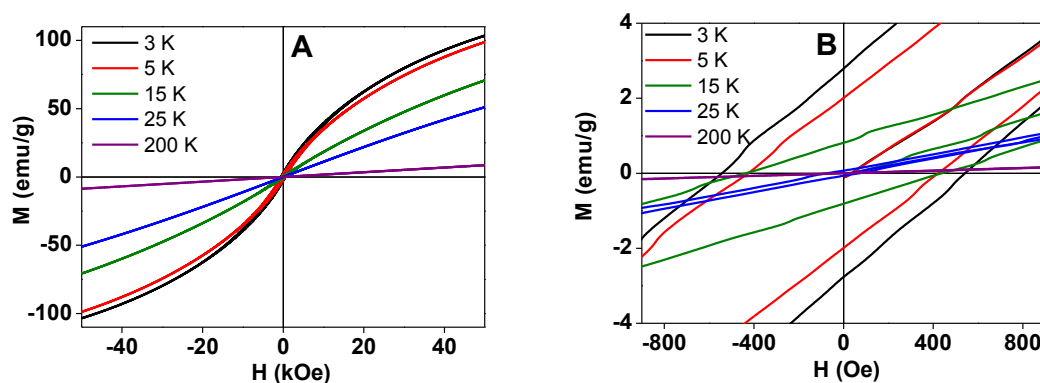


**Figure 4.1.8:** A) Magnetic hysteresis loops B) zoom view of hysteresis loops of  $\text{GdMnO}_3$  nanoparticles annealed at  $700^\circ\text{C}$  at indicated temperature values.

Unlike the previous report by Wang *et al.* on 52 nm nanoparticles, where authors observed the opening of hysteresis loop below 10 K, we observed opening of hysteresis loop  $\sim 40$  K (with coercivity of  $\sim 50$  Oe) [19]. However, Wang *et al.* did not report the value of coercivity for GdMnO<sub>3</sub>. With further decrease in temperature, the coercivity increases showing a maximum value at 3 K (540 Oe) [19]. The opening-up of hysteresis loop indicates the onset of weak-ferromagnetic behavior. The weak FM above the transition from ICAFM into a *c*AAFM ordering can be due to the small canting of Mn<sup>+3</sup> spins which starts to occur below T<sub>N</sub> and surface uncompensated spins [19]. The large coercivity at 3 K is from the Gd<sup>+3</sup> spins which align in the external magnetic field. The higher value of coercivity compared to the reported values for 52 nm sized nanoparticles may be due the uncompensated surface spins which may contribute to weak FM in small particle size (35 nm to 45 nm) [22]. In nano-sized particles, due to enhanced contribution from surface uncompensated spins, the coercivity increases when compared to its bulk counterpart [23]. Due to the surface to volume ratio, magnetization follows  $1/d$  ( $d$  is diameter of the particle) for AFM particles [22, 23].

We also performed the dc M–T measurements at various applied field in a broad temperature range from 3 K to 300 K. For all these measurements, the cooling and heating rate was kept at 2 K per min. For the FC, at first, the desired field was applied at 300 K and sample was cooled down to 3 K, for the ZFC, the sample was cooled without applying any external field and the desired field was turned-on at 3 K and the magnetic signal was measured while heating the sample in both ZFC–FC modes. The effective paramagnetic moment for Dy<sup>+3</sup> is  $10.7 \mu_B$  at 300 K which is slightly less than the theoretical value  $11.7 \mu_B$  for DyMnO<sub>3</sub> and closer to the value reported ( $11.3 \mu_B$ ) for nano-sized DyMnO<sub>3</sub> [24, 25]. The anomaly at 43 K (bifurcation of ZFC–FC magnetization curves) and 7 K (peak in ZFC curves) in the M–T curves can be attributed to the ordering of Mn<sup>+3</sup> spins and AFM interaction between the Dy<sup>+3</sup> spins respectively (figure 4.1.9 a) [26, 27].

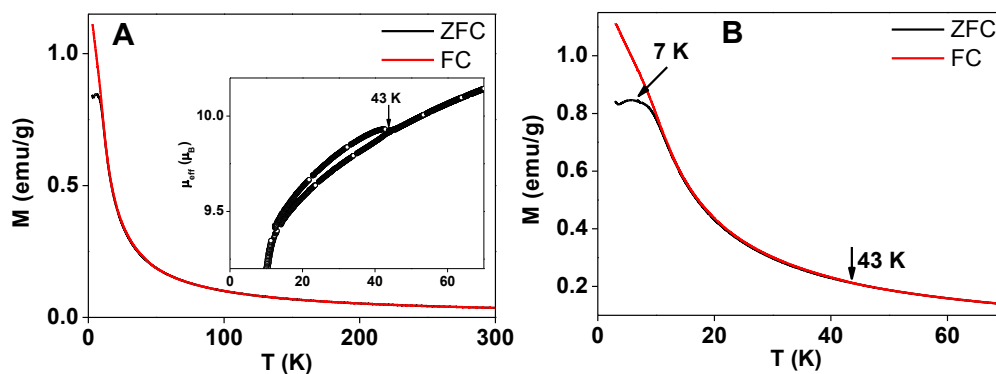


**Figure 4.1.9:** A) Temperature dependence ZFC and FC magnetization curves for  $\text{DyMnO}_3$  nanoparticles, with an applied field of 200 Oe, inset  $\mu_{\text{eff}}$  shows clear bifurcation of ZFC–FC magnetization curves at  $T_N \sim 43$  K B) expanded plots of ZFC–FC magnetization curves with  $T_N$  at  $\sim 43$  K and ordering temperature of  $\text{Dy}^{+3}$  moments at  $\sim 7$  K.

The divergence of ZFC–FC magnetization curves below 43 K ( $T_N$ ) shows the presence of overall weak FM ordering due to spin-canting.

In figure 4.1.10, we have shown the M–T curves for  $\text{GdMnO}_3$  nanoparticles at 50 Oe and 1000 Oe applied field values. The temperatures of the anomalies were determined from the  $1/\chi$ –T plot (inset of Fig. 4.1.10 B). In ZFC–FC magnetization curves, we observed first anomaly at  $\sim 42$  K, which is the  $T_N$  of  $\text{GdMnO}_3$  [6].

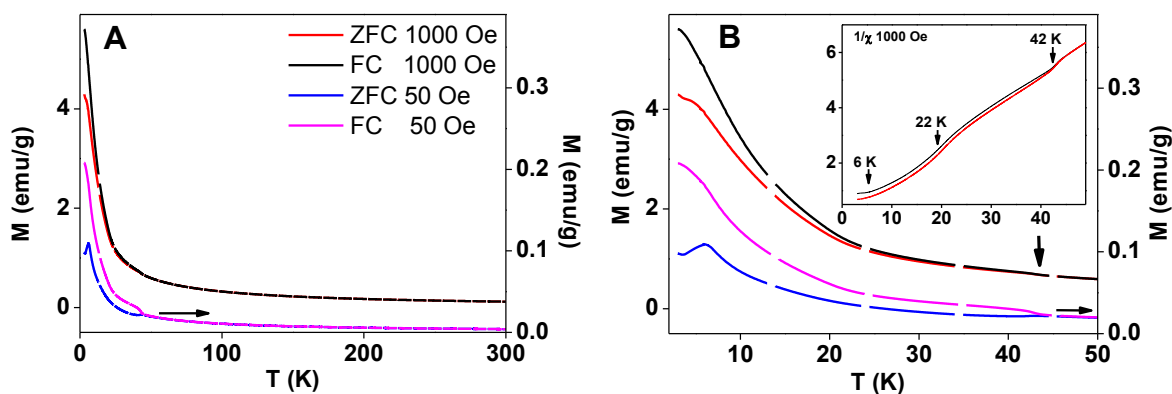




**Figure 4.1.10:** A) Temperature dependence of the ZFC and FC magnetization curves for  $\text{GdMnO}_3$  nanoparticles annealed at  $700^\circ\text{C}$ , with an applied field of 50 and 1000 Oe B) expanded plots of ZFC–FC magnetization curves with  $T_N \sim 42\text{ K}$  and ordering temperature of  $\text{Gd}^{+3}$  moments at  $\sim 6\text{ K}$ , inset shows the inverse susceptibility,  $1/\chi$  showing three anomalies at 42, 22 and 6 K.

At this temperature,  $\text{GdMnO}_3$  nanoparticles undergo a phase transition from paramagnetic to an ICAFm, with a modulation wave vector directed along  $b$ -axis. This modulation, which corresponds to a collinear arrangement of the  $\text{Mn}^{+3}$  spins, is a consequence of competing exchange interactions between successive neighboring spins, which lead to a frustrated magnetic system. Note that, at this temperature, the polarization of  $\text{Gd}^{+3}$  sites doesn't take place and hence the  $\text{Gd}^{+3}$  spins still behave paramagnetically. With decreasing temperature, an increase in magnetization is observed and the slope of the curve changes at  $\sim 22\text{ K}$  which could be due to the appearance of weak FM. This anomaly is due to the transition from ICAFm into a  $c$ AAFm of the  $\text{Mn}^{+3}$  spins along  $c$ -axis [11]. Below this transition, the polarization of the  $\text{Gd}^{+3}$   $4f$ -spins by the canting of  $\text{Mn}^{+3}$  spins results into weak FM. Third anomaly was observed around 6 K, which is the long-range order of  $\text{Gd}^{+3}$  moments [16]. Below this temperature, there is a resultant configuration of net moment of canted  $\text{Gd}^{+3}$  spins antiparallel to that of canted  $\text{Mn}^{+3}$  spins.

We also performed ac-magnetization measurements to further confirm the observations from dc-magnetization behavior. The ac-magnetization for  $\text{DyMnO}_3$  was measured at 3 Oe ac field at a broad range of frequencies (figure 4.1.11).

The real component of the magnetization ( $M'$ ) exhibits a peak at  $\sim 5\text{ K}$  which we observed at 7 K in dc-measurement. The imaginary part of magnetization ( $M''$ ) exhibits peak at  $\sim 10\text{ K}$ . We did not observe any variation in the peak temperatures with frequency

confirming the AFM interaction between the  $\text{Dy}^{+3}$  ions at this temperature. We did not observe any anomaly  $\sim 43$  K, which was observed in dc-magnetization.

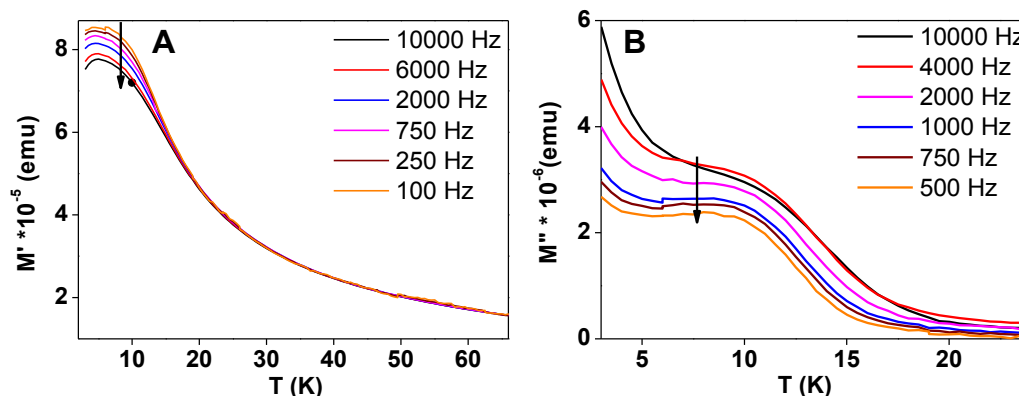


**Figure 4.1.11:** Temperature dependence of the A) real and B) imaginary part of the ac-magnetization measured in 3 Oe ac field and various frequencies as indicated in figure for  $\text{DyMnO}_3$  nanoparticles.

The real component of the magnetization ( $M'$ ) for  $\text{GdMnO}_3$  exhibits maximum at 6 K (figure 4.1.12) which was also observed in dc-magnetic magnetization measurements at same temperature. The imaginary part of magnetization ( $M''$ ) does not show this anomaly. Similar to  $\text{DyMnO}_3$ , for  $\text{GdMnO}_3$ , we did not observe any variation in the peak temperatures with frequency confirming the AFM interaction between the  $\text{Gd}^{+3}$  ions at this temperature.

Additionally, we did not observe any anomaly near  $T_N$  of  $\text{GdMnO}_3$ , which was observed in dc-magnetization measurements.

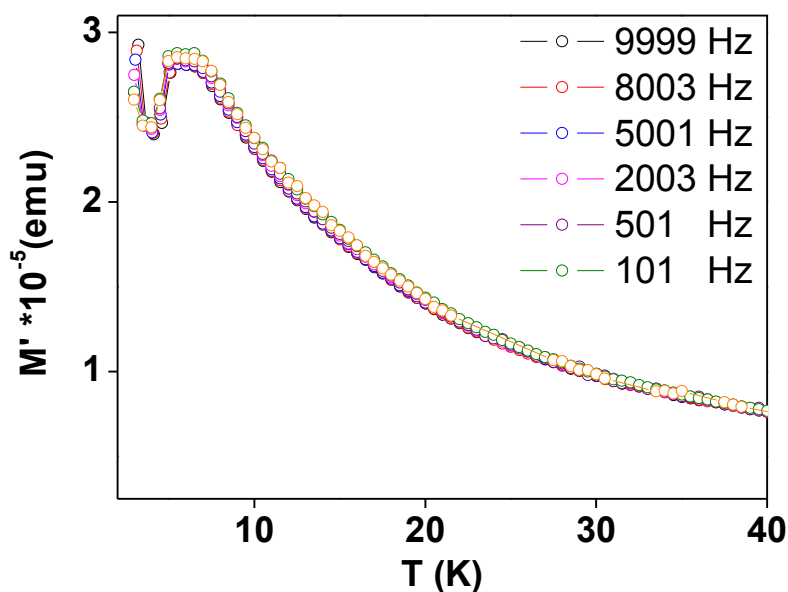


**Figure 4.1.12:** Temperature dependence of the real part of the ac-magnetization measured in 5 Oe ac field and various frequencies as indicated in figure for  $GdMnO_3$  nanoparticles.

#### 4.1.7 Conclusion

$DyMnO_3$  and  $GdMnO_3$  nanoparticles were prepared as single phase material using hydrothermal method. Particles of  $DyMnO_3$  are oval-like shaped (size ranging from 60 to 90 nm) and  $GdMnO_3$  are plate-like shaped (size ranging from 35 to 45 nm) as confirmed by TEM images. No anomaly near  $T_N$  for both  $DyMnO_3$  and  $GdMnO_3$  was observed in ac-magnetization measurements which were otherwise seen in dc-magnetization measurements. Results showed that nanoparticles of  $DyMnO_3$  and  $GdMnO_3$  retain the interesting magnetic properties as of its intrinsic bulk form.

---

## Section 4.2 Thermal hysteresis and exchange bias: $\text{EuMnO}_3$

---

Single phase orthorhombic  $\text{EuMnO}_3$  nanoparticles of average 45 nm size were synthesized using hydrothermal method. No signature of PM to ICAFM transition was observed in both real and imaginary part of ac magnetization. Real part of ac magnetization curves showed peak  $\sim 24.7$  K and anomalies  $\sim 46.8$  and  $21.8$  K were observed in imaginary part of ac magnetization. Reduction in the width of thermal hysteresis between field cooling and heating magnetization curve was observed in nanocrystallite ( $\sim 1$  K) as compare to bulk phase ( $\sim 3$  K)  $\text{EuMnO}_3$ . Isothermal magnetization showed large value of exchange bias (2799 Oe at 3 K) below ICAFM to cAAFm transition temperature.

---

### 4.2.1 Introduction

The complex interlinks among lattice distortions, magnetism, dielectric and transport properties of  $\text{RMnO}_3$  makes them an interesting material to study [28–30]. The boundary of magnetoelectric coupling in orthorhombic  $\text{RMnO}_3$ , is  $\text{EuMnO}_3$  which is nonmagnetoelectric and  $\text{GdMnO}_3$  is magnetoelectric [15]. In orthorhombic  $\text{RMnO}_3$  multiferroics, ferroelectricity is attributed to a complex spiral spin order that breaks the inversion symmetry [10, 31]. So, it is important to investigate temperature dependant magnetism of undoped  $\text{RMnO}_3$  compounds in order to understand its relation with dielectric and transport properties.

$\text{EuMnO}_3$  crystallises in orthorhombic perovskite structure with  $Pbnm$  symmetry [32]. At room temperature it is PE and PM. It undergoes a phase transition from PM to ICAFM state  $\sim 50$  K [5]. It further undergoes a transition from ICAFM to cAAFM order  $\sim 44$  K [18]. At  $\sim 24$  K, it shows a spin reorientation transition [18]. It shows a thermal hysteresis in field cooled heating and cooling magnetisation curves [18]. Detailed study of thermal hysteresis is not done so far. Study of thermal hysteresis and transitions are needed in order to understand the origin of magnetic ordering. Low temperature isothermal magnetization is also not studied so far in  $\text{EuMnO}_3$ , which could further give insight into these transitions.

Nanoparticles exhibit significant differences in their physical and chemical properties from their bulk counterparts due to their large surface to volume ratio [33, 34]. So, it is interesting to explore the corresponding effects like multiferroic properties in nanoparticle form in order to integrate them into nano-electronics and other applications with potential benefits. Despite of great interest to study them in nano regime there is no report on synthesis and magnetic property of  $\text{EuMnO}_3$  nanoparticles.

In this section, synthesis and magnetic property of  $\text{EuMnO}_3$  nanoparticles is demonstrated. A detailed study on thermal hysteresis and transitions of  $\text{EuMnO}_3$  nanoparticles is presented.

Isothermal magnetization shows large value of exchange bias below ICAFM to cAAFM transition temperature. The possible reason for exchange bias was also probed experimentally.

#### 4.2.2 Synthesis

EuMnO<sub>3</sub> nanoparticles was synthesized by modified hydrothermal method [22]. In a typical reaction, stoichiometric amounts of europium (III) nitrate pentahydrate (Eu(NO<sub>3</sub>)<sub>3</sub>· 5H<sub>2</sub>O, Sigma Aldrich, 99.9% purity) and manganese (II) nitrate *x* hydrate (Mn(NO<sub>3</sub>)<sub>2</sub>· *x*H<sub>2</sub>O, Sigma Aldrich, 99.9% purity) and an equal molar ratio of citric acid (C<sub>6</sub>H<sub>8</sub>O<sub>7</sub>, metal/citric acid molar ratio=1/1, Merck, 99.5% purity) were dissolved in deionized water. This solution was stirred for 6 h, followed by drop-wise addition of ammonia solution (28 wt %) to neutralize the unreacted citric acid as well as to raise the pH value of the solution near 9.2, resulting into a sol formation. Further sol was stirred for 3 h and transferred into an 80 mL capacity autoclave with a Teflon liner. After the hydrothermal treatment at 180 °C for 48 h, the precipitate was in turn filtered, washed with deionized water and was dried in vacuum oven. Finally, the powder sample was calcined at 750 °C for 6 h and used for further study.

#### 4.2.3 Structure and morphology

The X-ray diffraction pattern of as-synthesized powder with the reference data from orthorhombic (JCPDS file no. 261126) phases of bulk EuMnO<sub>3</sub> is shown in figure 4.2.1. The XRD pattern matches nicely with the orthorhombic EuMnO<sub>3</sub> with *Pbnm* symmetry. A small variation in the relative peak intensity due to shape anisotropy was observed. The diffraction

peaks are quite broad, showing the formation of  $\text{EuMnO}_3$  nanocrystallites with a mean crystallite size of  $\sim 35$  nm.

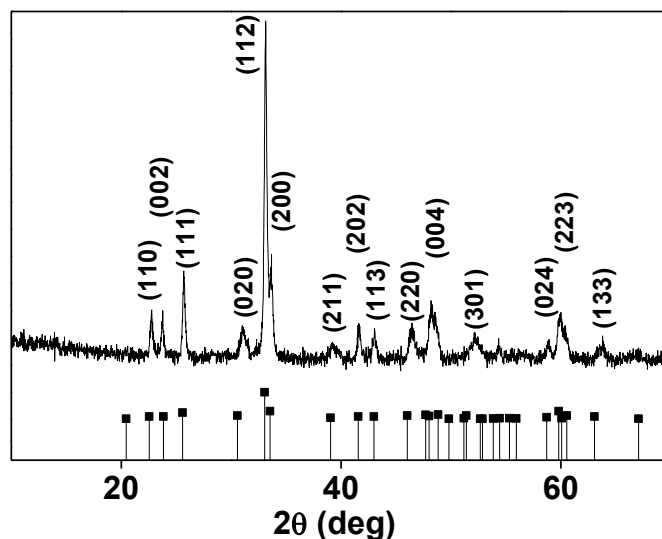


**Figure 4.2.1:** X-ray diffraction pattern of  $\text{EuMnO}_3$  nanoparticles with the data from JCPDS Card No. 261126 for the orthorhombic phase with  $Pbnm$  symmetry. Some peaks are not indexed for maintaining the clarity of figure.

The TEM images at different magnification (figures 4.2.2 A, B) suggest that particles have plate like morphology. The average particles size is  $\sim 45$  nm. Figure 4.2.2 C shows the lattice fringes of (202) plane of orthorhombic  $\text{EuMnO}_3$  nanoparticles, which further confirm phase and crystallinity of sample.

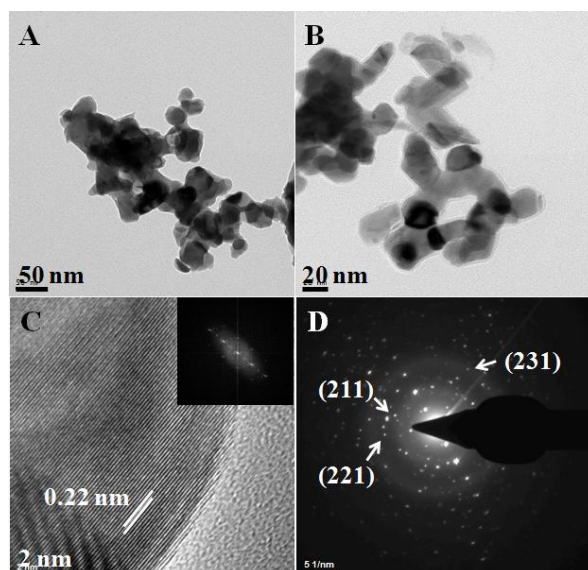


**Figure 4.2.2:** A, B) Transmission electron micrographs C) HRTEM image D) SAED pattern of orthorhombic  $\text{EuMnO}_3$  nanocrystals.

#### 4.2.4 Magnetic study

Figure 4.2.3 shows temperature dependence of magnetization in ZFC–FC modes at 500 Oe and 1 T applied magnetic field. At 500 Oe applied field ZFC–FC magnetization curves showed bifurcation at 53 K. ZFC magnetization curves showed two more anomalies as hump at 44.8 and 24.7 K. At 1 T applied field, ZFC–FC magnetization curves showed bifurcation at 43 K. ZFC curve shows broad hump at 13 K. Above 100 K, Curie-Weiss fitting of FC curve gave Weiss temperature of  $-40$  K, which is greater than reported value of  $-88$  K, for bulk ceramic sample [18]. Below bifurcation of ZFC–FC magnetization curves, FC magnetization curve shows a steep increase in magnetization value. As the temperature increases from 3 K, FC magnetization (500 Oe) shows decreasing trend and ZFC magnetization increases very slowly, showing maxima at 24.7 K.



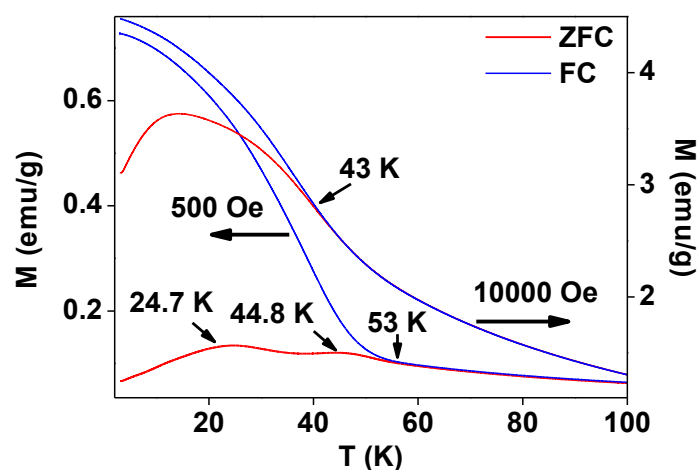


**Figure 4.2.3:** ZFC–FC magnetization curves at 500 Oe and 1 T applied fields for orthorhombic  $\text{EuMnO}_3$  nanoparticles.

Further heating cause decrease in magnetization and again shows a maxima at 44.8 K. Further it shows a decreasing trend. The increase in magnetization below  $\sim 3$  K in FC mode shows signature of FM interaction. The bifurcation of ZFC–FC magnetization curves at 53 K, is due to PM to ICAFM transition. This is in good agreement with reported values for bulk samples [5]. Maxima  $\sim 44.8$  K in ZFC magnetization curve can be attributed to ICAFM to cAAFM transition. Maximum at 24.7 K in ZFC curve can be assigned to spin reorientation transition [18]. It can be noted that for bulk ceramic samples, ZFC magnetization shows a decreasing trend as temperature increases from 3 K but in our nanocrystallite particles both ZFC–FC magnetization curves showed increasing

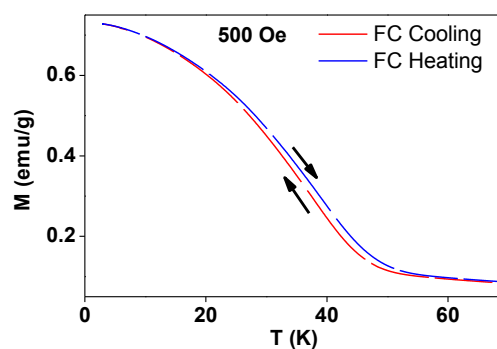


**Figure 4.2.4:** FC heating and cooling magnetization curves at 500 Oe applied fields for orthorhombic  $\text{EuMnO}_3$  nanoparticles.

trend. This can be explained by large value of Weiss temperature  $-40$  K, which shows

---

reduced strength of frustrated AFM. At low temperature *c*AAFM dominates and gave ferromagnetic like behavior. As the applied field is increased these transition were not seen in ZFC magnetization curve, which shows their weak interaction strength, so higher field can vanish them completely. At 1 T applied field ZFC–FC magnetization curves show bifurcation at 43 K and ZFC shows a maximum at 13 K. The field dependence of these transitions were probed further and discussed below. Field cooling and heating curve (figure 4.2.4) at 500 Oe applied field shows a thermal hysteresis between 19–56 K. The presence of thermal hysteresis can be explained by competitive interaction between different spin orders. In between 19-56 K, three phases PM, ICAFM and *c*AAFM compete with each other during heating and cooling cycle. So, in heating and cooling cycle, competitive interaction between different types of spin ordering results in thermal hysteresis. It is noteworthy that width of thermal hysteresis observed in nanocrystallite (~1 K) is lower than reported data on bulk samples (~3 K) [18]. As surface to volume ratio is higher in nanocrystallite, so surface disorder spins dominates over bulk spins. This is also evident from steep increase of FC magnetization curve. To probe field dependence of the transitions, we compared the ZFC magnetization curves in figure 4.2.5. The spin reorientation transition at 24.7 K does not show field dependency up to 1000 Oe applied field where as ICAFM to *c*AAFM transition varies from 48 K at 100 to 45 K at 1000 Oe applied field. At 1 T applied field ZFC magnetization shows a broad hump starting from 34 K with a pronounced peak ~2 K.

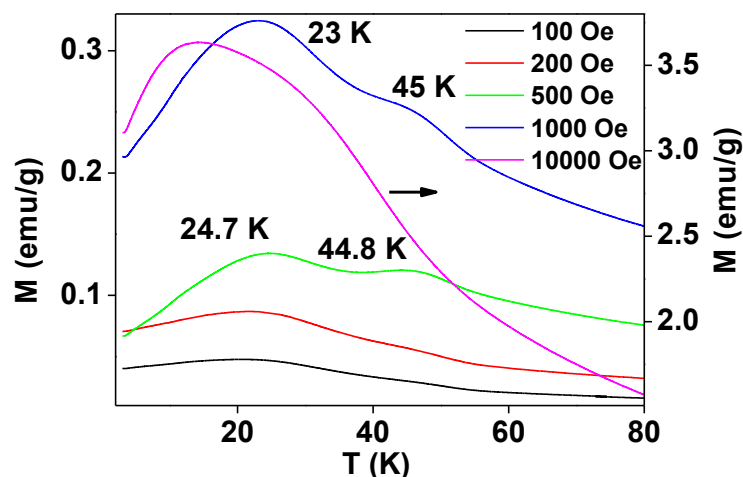


**Figure 4.2.5:** ZFC magnetization curves at various applied fields for orthorhombic  $\text{EuMnO}_3$  nanoparticles showing field dependency of transitions.

To further probe the nature of these transitions, ac magnetization was done in wide range of temperature at 5 Oe ac field at various frequencies. The real part of ac magnetization (figure 4.2.6 A) curves show a peak  $\sim 24.7$  K, which is spin reorientation transition observed in dc magnetization. Except this transition, no other transitions were observed in real part of ac magnetization curve which were seen in dc magnetization data. The absence of  $T_N$  ( $\sim 53$  K) in real part of ac magnetization was reported in many compounds of same class in both bulk and nano regime [35]. No frequency dependency was observed for spin reorientation transition. The imaginary part of ac magnetization (figure 4.2.6 B) shows anomalies  $\sim 46.8$  and  $21.8$  K. These can be associated to ICAFM to cAAFM and spin reorientation transitions respectively, which are in good agreement with dc magnetization data.

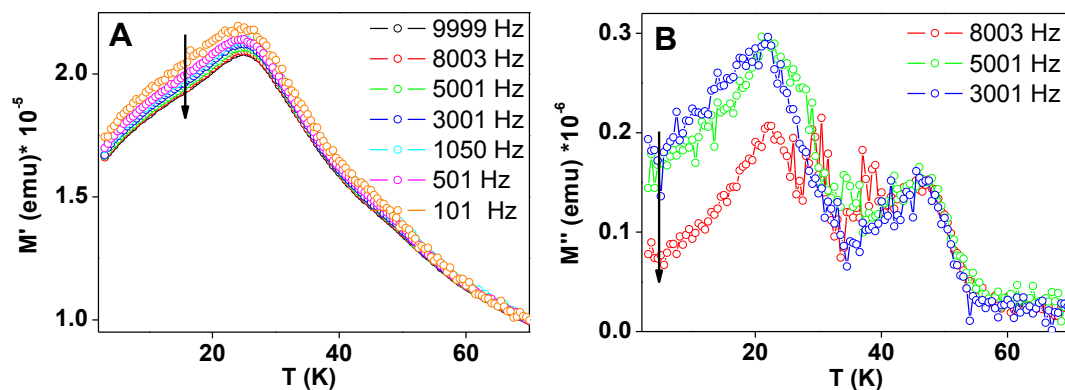


**Figure 4.2.6:** Temperature dependence of A) real and B) imaginary part of ac magnetization, measured in 5 Oe field and various frequencies as indicated in figure for orthorhombic  $\text{EuMnO}_3$  nanoparticles.

To probe further the nature of transitions, isothermal field dependency magnetization was performed around transition regions. The M–H curves (figure 4.2.7 A) shows non linearity below  $T_N$  and no saturation was observed in whole temperature range as expected for AFM compounds.

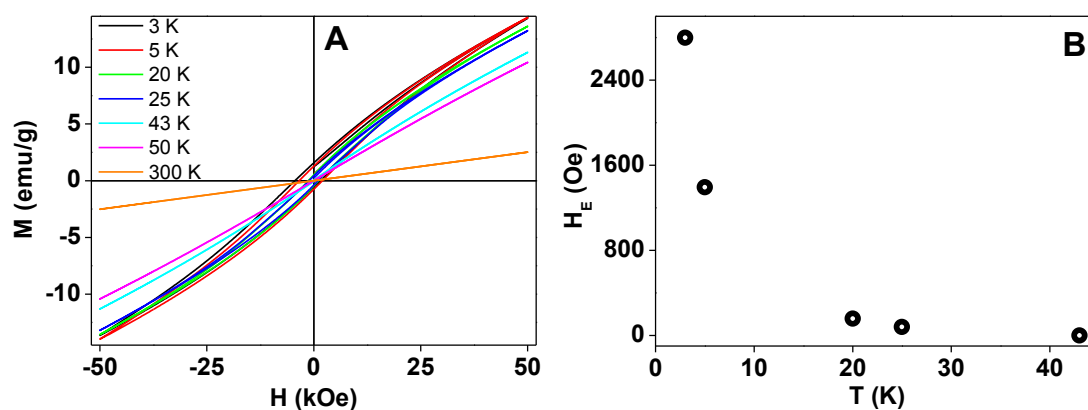


**Figure 4.2.7:** A) M–H loops for orthorhombic  $\text{EuMnO}_3$  nanoparticles at various temperatures B) temperature dependence of exchange bias.

At 25 K, coercivity value is 1025 Oe which increases to 2991 Oe at 3 K. The increase in coercivity value at low temperature can be due to *c*AAFM which became more pronounced at low temperature. Large exchange bias (figure 4.2.7 B) was observed below ICAFM to *c*AAFM (~43 K) transition. At 3 K, the value of exchange bias was ~2799 Oe and it decreases with increase in temperature and becomes zero at 43 K. The presence of exchange bias in nanocrystallite particles is well explained in the literature, due to presence of uncompensated surface spins which behave as, ferromagnetic-like surface layer. In literature for bulk  $\text{EuMnO}_3$ , exchange bias is not reported. It is proposed in several previous studies that in smaller dimensions, the AFM systems may show uncompensated spins at surface leading to net FM-like behavior at low temperature. Moreover, due to the absence of direct exchange interaction, the coupling is very weak and the shell-spins may not have any well-defined transition temperature. They are still part of the core lattice but due to the reduced coordination number of surface-atoms the surface spins remain disordered/canted leading to a FM-like surface layer [36–38]. Exchange bias effect was also observed in antiferromagnetic nanoparticles,  $\text{BiFe}_{0.8}\text{Mn}_{0.2}\text{O}_3$ ,  $\text{La}_{0.2}\text{Ca}_{0.8}\text{MnO}_3$  due to uncompensated surface spins [36, 37].  $\text{EuMnO}_3$  nanoparticles were cooled from 300 K to 3 K at desired applied field, then isothermal measurement was recorded. The applied field while cooling will align the surface uncompensated spins, which should increase the surface ferromagnetic-like character thereby increasing exchange bias. The M–H loops at 3 K under various field cooled conditions are shown in figure 4.2.8.

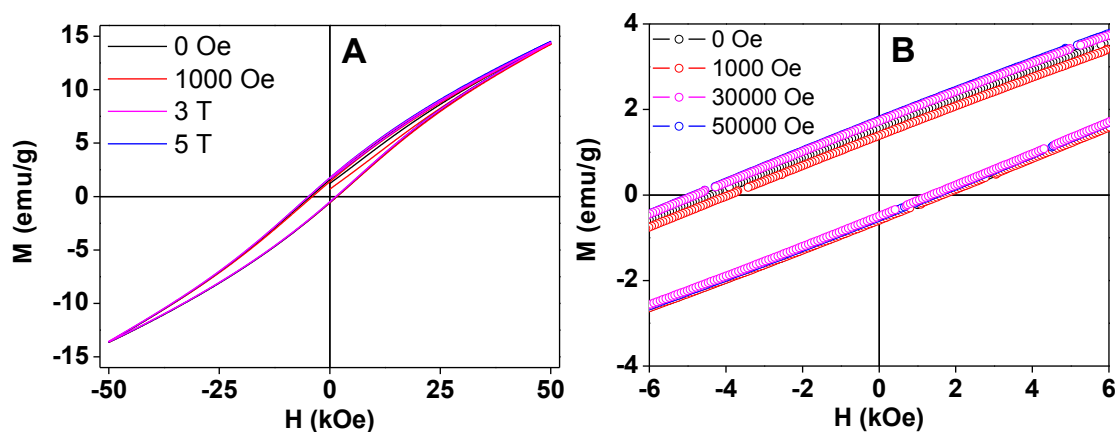


**Figure 4.2.8:** A)  $M$ – $H$  loops of orthorhombic  $\text{EuMnO}_3$  nanoparticles at 3 K at different field cooled conditions B) expanded plot of loop.

It was found that at 30000 Oe (3 T) and 50000 Oe (5 T) field cooled condition there was an enhanced exchange bias ( $\sim 3400$  Oe) at 3 K isothermal magnetization. At 1000 Oe field cooled, which is less than coercivity at 3 K, exchange bias decrease to 2260 Oe compared to 2799 Oe in zero field cooled  $M$ – $H$ . This could be due to the fact that, at field less than coercive field, the AFM spin could not align in field direction thereby decreasing exchange bias. Based on the above field cooled  $M$ – $H$  loops at 3 K, we can model a nanoparticle as a core-shell structure having an inner AFM core and FM-like surface layer (figure 4.2.9). The origin of exchange bias below ICAFM to cAAFM ( $\sim 43$  K) is due to onset of AFM nature in core of nanoparticles which is weakly coupled with uncompensated FM-like surface layer. The temperature dependency of exchange bias is due to increase in cAAFM ordering with decrease in temperature.

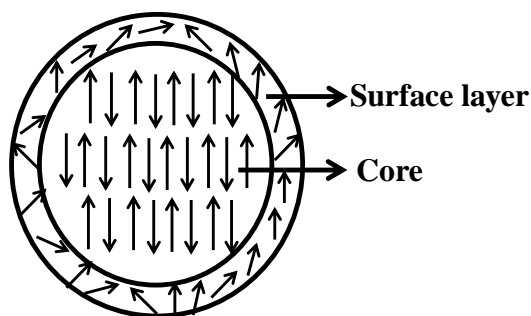


*Figure 4.2.9: Schematic model of an individual orthorhombic  $\text{EuMnO}_3$  nanoparticle.*

#### 4.2.5 Conclusion

We have synthesized single phase orthorhombic  $\text{EuMnO}_3$  nanoparticles. The ZFC–FC magnetization curves showed three anomalies  $\sim 53$ ,  $44.8$  and  $24.7$  K, were attributed to PM to ICAFM, ICAFM to cAAFM and spin reorientation transition respectively. Due to competitive interaction between different spin orderings a thermal hysteresis ( $\sim 1$  K) in between  $19$ – $56$  K was observed in field cooled heating and cooling magnetization. Based on field cooled M–H loop measurement, nanoparticle was modeled as core-shell structure. The origin of exchange bias below ICAFM to cAAFM ( $\sim 43$  K) transition is due to coupling between antiferromagnetic core with ferromagnetic surface layer of nanoparticles.

---

## Section 4.3 Effect of calcination on size and magnetic property of $\text{TbMnO}_3$

---

This section we have showed synthesis and detailed magnetic and Raman spectroscopy study on  $\text{TbMnO}_3$  particles of size  $\sim 25$  nm and  $2\text{--}3$   $\mu\text{m}$ . The incommensurate-commensurate (lock-in) transition was not observed in  $\chi T$  curve of  $\text{TbMnO}_3$  nanoparticles. The increased value of magnetization in samples annealed at  $800$   $^\circ\text{C}$  ( $2\text{--}3$   $\mu\text{m}$ ) was attributed to double exchange interaction between  $\text{Mn}^{+3}$  and  $\text{Mn}^{+4}$  spins. The presence of  $\text{Mn}^{+4}$  due to  $\text{Tb}^{+3}$  deficiencies in particles shells was confirmed by XPS measurements.

---



### 4.3.1 Introduction

As per the current understanding, researchers have identified four possible mechanisms behind the origin of ferroelectricity in magnetic materials (1) lone-pair effects, (2) geometric frustration, (3) charge ordering, and (4) magnetic ordering. Compounds such as TbMnO<sub>3</sub>, DyMnO<sub>3</sub> and TbMn<sub>2</sub>O<sub>5</sub> fall in the category of magnetic ordering where ferroelectricity is induced by magnetic long range order where arrangement of magnetic dipoles lacks reflection symmetry [3, 4].

TbMnO<sub>3</sub> (TMO) is a prototypical multiferroic material with perovskite structure and shows gigantic ME effect where both large GdFeO<sub>3</sub>-type and cooperative Jahn-Teller type distortions accompanied by the  $e_g$  orbital order of Mn<sup>+3</sup> ions. Competition between nearest-neighbor FM and next-nearest neighbor AFM interactions in a MnO<sub>2</sub> sheet normal to the  $c$  axis, makes the Mn<sup>+3</sup> ( $S=2$ ) spin system frustrated [1, 10]. Consequently, TMO has an incommensurate sinusoidal AFM structure with a propagation vector  $Q \sim 0.281$  between the AFM transition temperature  $T_N \sim 43$  K and the FE transition temperature  $T_C \sim 28$  K. The magnetic structure turns into an elliptical cycloid upon reaching  $T_C$  [39]. The FE polarization simultaneously appears along the  $c$ -axis, which can be explained by the inverse effect of the DM interaction [40]. Abe *et al.* showed in TMO that the rotating magnetic-field direction can reverse electric polarization [41]. They showed that the arrangement of Tb moments is modified by magnetic-field sweeping, thus Mn<sup>+3</sup> spin configuration is changed under the influence of the  $f$ - $d$  interaction. Consequently, the sign of electric polarization is reversed or memorized. Therefore, Tb  $4f$  has an important role in electric polarization flop [41].

At room temperature, TMO shows orthorhombic distorted perovskite structure with space group  $Pbnm$ . The electric configuration of the Mn<sup>+3</sup> sites in TMO is  $t^3_{2g} e^1_g$  which is same with its parent magneto resistive manganites LaMnO<sub>3</sub>. In LaMnO<sub>3</sub> the layered (A-type) AF order comes from the staggered orbital order of the type  $d_{3x^2-r^2}/d_{3y^2-r^2}$  but the spin

---

structure in TMO is a sinusoidal AF ordering of the  $\text{Mn}^{+3}$  moment that occurs at  $T_N$  with a wave vector  $q = (0, k_s, 1)$  in the orthorhombic  $Pbnm$  cell. At  $T_N$ , the wavenumber  $k_s$  ( $\sim 0.295$ ) is incommensurate and the value of  $k_s$  decreases with decreasing temperature and becomes constant ( $\sim 0.28$ ) around 30 K [10]. Kimura *et al.* showed that the spin frustration caused by the combination of a  $\text{GdFeO}_3$  type distortion and staggered orbital order is responsible for the emergence of long-period sinusoidal AFM order in TMO [1]. Quezel *et al.* showed in their neutron diffraction study, anomaly at 7 K which they attributed to the magnetic ordering of the  $\text{Tb}^{+3}$  ions [42].

Nanosize effects on both ferromagnetic and ferroelectric ordering of multiferroics were not studied in depth. The observation of Verwey metal to insulator transition and large spin dependent magnetoresistance in chemically synthesized and organically passivated  $\text{Fe}_3\text{O}_4$  nanoparticles with size as small as 6–8 nm and the shift in the Verwey transition temperature from 120 K (in bulk) to around 90 K (in nanoparticles) is reported [34]. Similarly, the observation of ferroelectric-paraelectric transition in biosynthesized  $\text{BaTiO}_3$  nanoparticles with size 5–6 nm and the shift of this transition at lower temperature is also reported [33]. The decrease in  $T_N$  as the particles size decreases is shown in the case of  $\text{BiFeO}_3$  [43]. As such, there are very few reports on the size dependent properties of multiferroic oxide because the synthesis of these materials in nano size with proper crystallinity and phase is non-trivial. As per our knowledge, there is only one report on TMO nanoparticles, where authors showed that TMO in nanosize also retains the multiferroic properties [44].

This section presents a detailed magnetic study of TMO and showed that the transitions at 45, 30 and 10 K which can be attributed to the sine-wave ordering of the  $\text{Mn}^{+3}$  moments, the incommensurate-commensurate lock-in transition and magnetic ordering of  $\text{Tb}^{+3}$  moments, respectively.

### 4.3.2 Synthesis

Terbium orthomanganite particles were synthesized using a modified hydrothermal process followed by annealing at 750, 800 °C. For this purpose, stoichiometric amounts of terbium (III) nitrate hydrate, ( $\text{Tb}(\text{NO}_3)_3 \cdot x\text{H}_2\text{O}$ , Aldrich, 99.9%), magnesium(II) nitrate x hydrate ( $\text{Mn}(\text{NO}_3)_2 \cdot x\text{H}_2\text{O}$ , Aldrich, 99.9%) and an equal amount of citric acid ( $\text{C}_6\text{H}_8\text{O}_7$ ) (metal/citric acid molar ratio=1/1)] (Merck, 99.5% ) were dissolved in deionized water so that the metal ions can be uniformly complexes together. The transparent solution was stirred for 6 h followed by drop-wise addition of ammonia solution (28 wt. %) to neutralize the unreacted citric acid as well as to raise the pH value of the solution near 9.2 resulting into a sol formation and further the sol was stirred for 3 h. The final solution was transferred to an 80 ml capacity autoclave with the Teflon liner. The autoclave was placed into an oven for the hydrothermal treatment at 160 °C for 20 h. After the completion of the reaction, the solution was dried at 100 °C. After that the powder sample was annealed at 700 °C for 6 h. The annealed sample was used for further characterization. To prepare the micron sized TMO particles, the nanoparticles were annealed for much longer time (12 h) at 800 °C.

### 4.3.3 Structure and morphology

Figure 4.3.1 shows the room temperature XRD pattern of hydrothermally synthesized TMO nanoparticles annealed at 700 and 800 °C. The XRD pattern is indexed with the orthorhombically distorted perovskite structure with space group *Pbnm* of terbium orthomanganite according to JCPDS file no. 250933 except one peak (around 29°) which could be attributed to phase contributions emanating from a small degree of unintended non-stoichiometry [44].

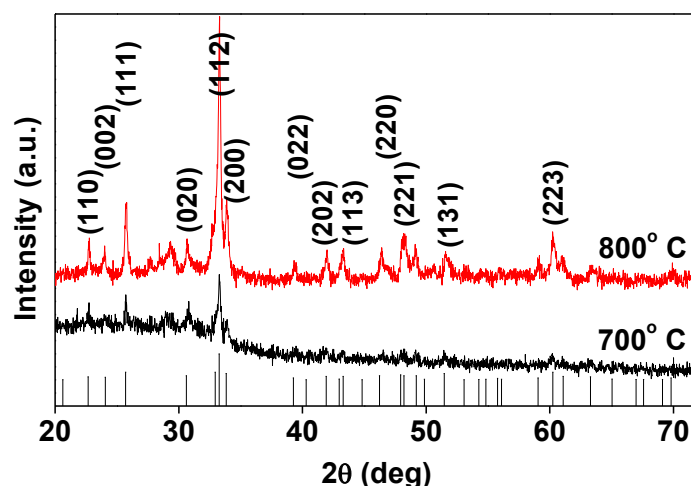


**Figure 4.3.1:** Comparative XRD patterns of  $TbMnO_3$  from the JCPDS#250933 database,  $TbMnO_3$  particles annealed at 700 and 800 °C, respectively.

The diffraction peaks of 700 °C annealed sample (figure 4.3.1) are quite broad showing the formation of TMO crystallites in nano size. The mean crystallite size calculated by means of Debye-Scherrer formula based on FWHM of different diffraction peaks of 700 °C annealed sample was found to be 25 nm. Figure 4.3.1 shows sharpening of peaks in 800 °C annealed sample due to the increase in particle size after long annealing at 800 °C for 12 h.

Figure 4.3.2 A, B shows the representative TEM images taken on the sample annealed at 700 °C suggesting that the particles are nanocrystalline in nature with plate like morphology and average size around 25 nm. Figure 4.3.2 C clearly shows the presence of lattice fringes with good crystallinity. The  $d$ -values calculated from this image (shown in the nm scale) matches with those obtained from powder XRD. Inset shows the FFT pattern of marked space of figure 4.3.2 C. Figure 4.3.2 D shows the SAED pattern of nanoparticles which matches with the XRD data. Figure 4.3.3 A, B shows the representative TEM images taken on the sample annealed at 800 °C suggesting that the particles are agglomerated in nature with size in micron range.

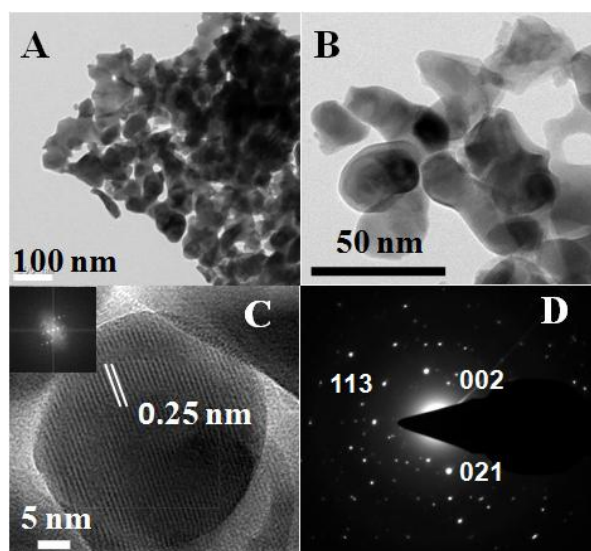


**Figure 4.3.2:** A, B) TEM images C) HRTEM image (D) SAED pattern of  $TbMnO_3$  nanoparticles annealed at 700 °C.

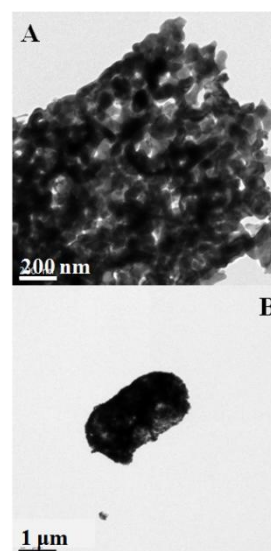


**Figure 4.3.3:** (A, B) TEM image of  $TbMnO_3$  particles annealed at 800 °C.

#### 4.3.4 Raman spectroscopy

Raman scattering is an excellent tool to study the crystal symmetry and lattice distortion. Raman active modes in  $RMnO_3$  come from the deviation from the ideal perovskite structure. The activation of each Raman modes can be assigned to rotation of the  $MnO_6$  octahedra around [101] or [010] direction and John-Teller distortion. The peaks indicated in the figure 4.3.4 correspond to the following modes the symmetric stretching of the basal oxygen O(2) of the octahedra around  $609\text{ cm}^{-1}$  ( $B_{1g}$ ); the asymmetric stretching around  $483\text{ cm}^{-1}$  ( $A_g$ ) associated with the JT distortion, that involves basal oxygen O(2) and apical ones O(1); the bending modes ( $A_g + B_{1g}$ ) at  $510$  and  $525\text{ cm}^{-1}$  in TMO and the tilt of the octahedra at around  $350\text{ cm}^{-1}$  ( $A_g$ ).

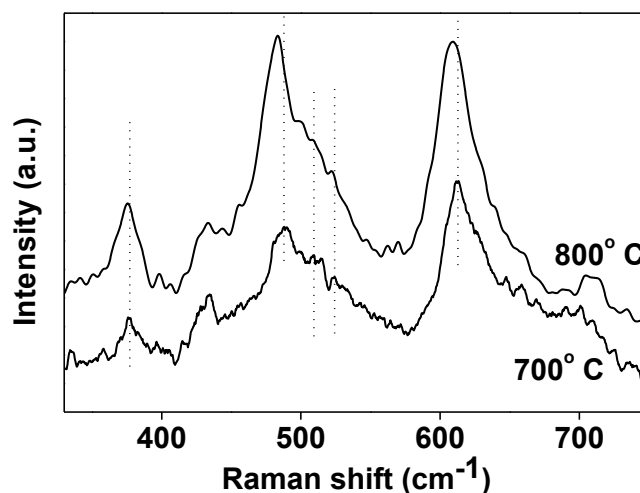


**Figure 4.3.4:** Room temperature Raman spectra of as-prepared  $TbMnO_3$  nanoparticles annealed at 700 and 800 °C. Vertical dashed lines are guide to eye.

From figure 4.3.4, it was observed that for 800 °C annealed particles there is a reduction in the Raman shift. This can be explained by assuming a decrease in the lattice distortion which results in a considerable reduction in the Raman shift in Raman spectra [45, 28]. This decrease in lattice distortion was also observed in temperature dependence of magnetization (discussed later).

#### 4.3.5 X-ray photoelectron spectroscopy (XPS)

The XPS spectra of  $Mn^{+3}$   $2p$  are shown in figure 4.3.5. Figures 4.3.5 A and B show peaks at 641.9 and 653.3 eV which are the characteristic peaks of  $Mn^{+3}$   $2p_{3/2}$  and  $2p_{1/2}$  [20]. Figure 4.3.5 B (for sample annealed at 800 °C) shows an extra peak at 642.7 eV which is characteristic of  $Mn^{+4}$   $2p_{3/2}$ . A mixture of  $Mn^{+3}$  and  $Mn^{+4}$  was obtained in the samples annealed at 800 °C but the sample annealed at 700 °C shows only the presence of  $Mn^{+3}$ .

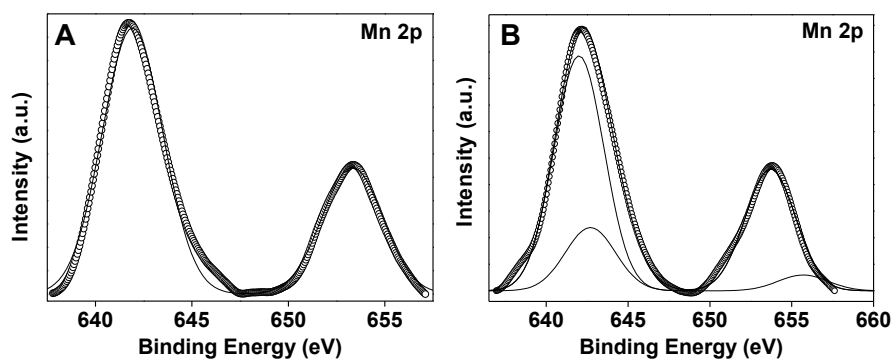


**Figure 4.3.5:** Room temperature XPS spectra for Mn 2p of as-prepared  $\text{TbMnO}_3$  nanoparticles annealed at 700 °C (A) and 800 °C (B) (scatter curves). The lines represent the deconvoluted peaks.

The partial conversion of  $\text{Mn}^{+3}$  to  $\text{Mn}^{+4}$  in 800 °C annealed sample can be explained on the basis of formation of  $\text{Tb}^{+3}$  deficient shell [44]. To compensate the  $\text{Tb}^{+3}$  deficiencies, some of  $\text{Mn}^{+3}$  ions go to  $\text{Mn}^{+4}$  state which leads to formation of  $\text{Tb}^{+3}_{1-x}\text{Mn}^{+3}_{1-x}\text{Mn}^{+4}_x\text{O}_3$  phase at the surface.

#### 4.3.6 Magnetic study

Figure 4.3.6 A shows M–H loops at representative temperatures. Figure 4.3.7 A shows initial magnetization curves at different temperature, showing straightening of curve at 45 K and above thereby indicating the onset of paramagnetic transition around this temperature.

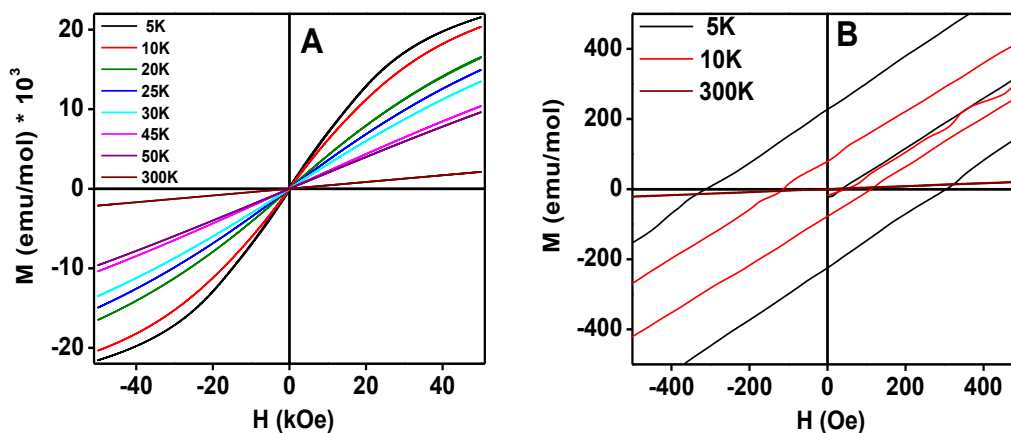


**Figure 4.3.6:** A) Hysteresis loops of as-prepared  $TbMnO_3$  nanoparticles annealed at  $700^\circ C$  at indicated temperature B) expanded plots of magnetization in higher magnification.

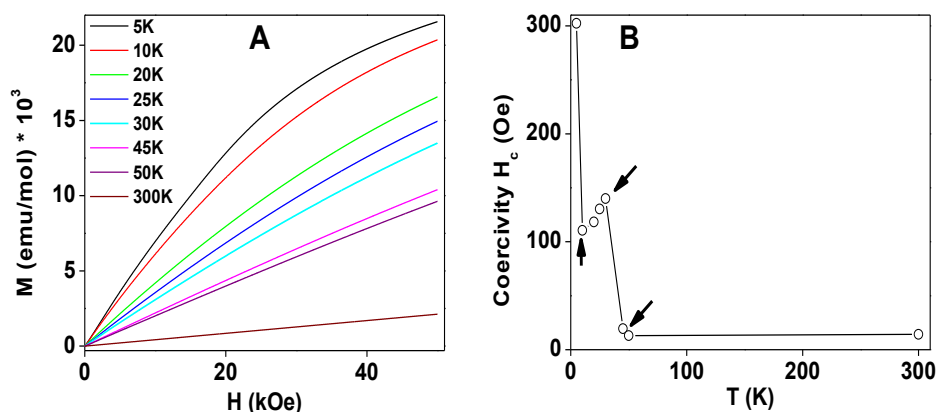


**Figure 4.3.7:** A) Initial magnetization curves B) coercivity as a function of temperature of  $TbMnO_3$  nanoparticles annealed at  $700^\circ C$ .

At higher temperature, it shows linear behavior due to PM phase as evident from zoom view (figure 4.3.6 A) of M-H curves at 45, 50, & 300 K (above  $T_N$ ), however at 45 K, we observed the emergence of small non-linear behavior and small opening-up of hysteresis loop which opens up at further low temperatures along with M-H curve showing more and more non-linear behavior. At 30 K, the coercivity ( $H_C$ ) was around 141 Oe and with further cooling



of the sample, the  $H_C$  decreases to 110 Oe at 10 K. Below 10 K, the  $H_C$  restrengthens and shows its maximum value of 303 Oe at 5 K. In figure 4.3.7 B,  $H_C$  vs.  $T$  curve shows three transitions at 45 K, 30 K and 10 K which were reported in literature as the sine-wave ordering of the  $Mn^{+3}$  moments ( $T_N$ ), the incommensurate-commensurate lock-in transition and magnetic ordering of  $Tb^{+3}$  moments, respectively [39]. These transitions were also observed in DC magnetic susceptibility ( $\chi$ ) vs.  $T$  measurements and are discussed in details in next section.

In figure 4.3.8, we have shown the  $\chi$ - $T$  of TMO calcined at 700 °C at 50 and 200 Oe applied field. In ZFC-FC magnetization curves, we observed first anomaly around 45 K (bifurcation), which is in the proximity to the bulk value of  $T_N$  of TMO. Below  $T_N$ ,  $Mn^{+3}$  sublattice AFM ordering starts to occur through SE interaction due to the spin reorientation of  $Mn^{+3}$  ions resulting into the bifurcation of ZFC-FC magnetization curves.

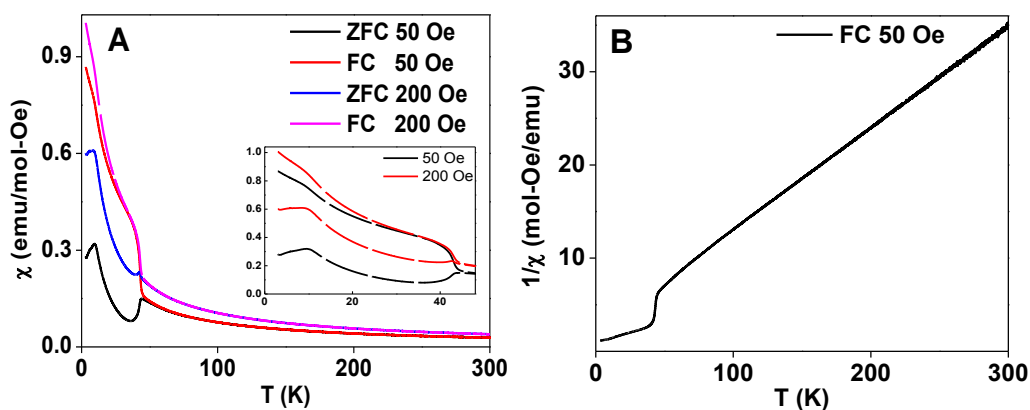


**Figure 4.3.8:** A) Temperature dependence of the susceptibility in ZFC-FC modes, with an applied field of 50 and 200 Oe for  $TbMnO_3$  nanoparticles. Inset shows the zoom view of ZFC-FC magnetization curves with bifurcation at  $T_N \sim 45$  K and ordering of  $Tb^{+3}$  moments at  $\sim 10$  K does not depend on applied external field B) inverse susceptibility  $1/\chi$  with straight line behavior above  $T_N$ .

The divergence of ZFC–FC magnetization curves below  $T_N$  shows the presence of overall weak ferromagnetism due to spin canting which also reflects in the opening up of the hysteresis loop in the M–H curves as shown in figure 4.3.6 B. At further low temperature around 10 K, the ZFC curves show a pronounced peak followed by a sharp decrease in the magnetization down to 3 K. This peak is due to the SE coupling between of  $Tb^{+3}$  ions resulting into another weak AFM ordering. The interaction between rare earth ions is usually observed at very low temperatures only. It should be noted that another magnetic anomaly near 27 K which was observed in single crystalline TMO corresponding to the incommensurate-commensurate (lock-in) transition, was not observed in our nanoparticles. As this transition is related to long length scale (magnetic modulation wave vector), therefore, due to the intrinsic strain in the nanoparticles, this type of transition is suppressed in smaller crystallite sized particles. However, we observed an anomaly in the  $H_C$  value around this temperature (figure 4.3.7 B). The  $1/\chi$ –T curve above  $T_N$  (~45 K) follows Curie-Weiss law (figure 4.3.8). To explore the field dependence of these transitions, we checked ZFC–FC measurements at two different applied fields. We observed that the  $T_N$  (~45 K) and AFM ordering temperature  $Tb^{+3}$  moments (~10 K) does not vary till 200 Oe (figure 4.3.8 A).

### 4.3.7 Size dependent magnetic property

It is important to check the fate of magnetic anomalies with the increased grain size (nano to micron). In figures 4.3.9 A and B, we show the comparative M–H loops (zoom view of 10 and 50 K data) nano sized (calcined at 700 °C for 6 h) and micron sized (calcined at 800 °C for 12 h) TMO which show that the values of magnetization, coercivity, and remanance increase in the micron sized TMO.

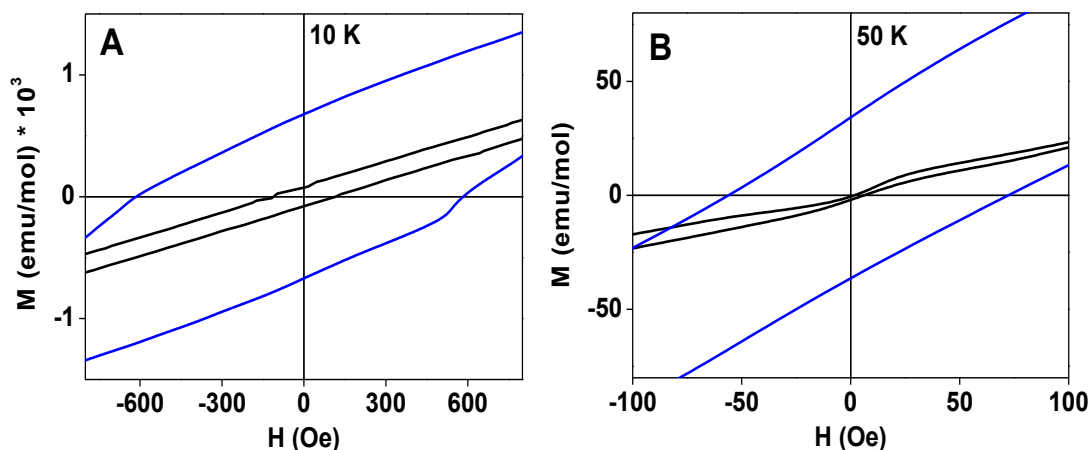


**Figure 4.3.9:** A comparison of  $M$ – $H$  hysteresis loops (zoom view) of  $TbMnO_3$  nanoparticles annealed at 700 (black line), 800 °C (blue line) at temperature A) 10 K and B) 50 K.

The increase in magnetization is due to the double exchange interaction between  $Mn^{+3}$  and  $Mn^{+4}$  ions. As evident from our XPS analysis and previous study by Kharrazi *et al.* that longer annealing of TMO at high temperature results into Tb deficiency shell to balance that some  $Mn^{+3}$  goes to  $Mn^{+4}$  state [44]. The value of  $H_C$  at 10 K, which was 113 Oe for 25 nm TMO particles becomes 582 Oe in samples annealed at 800 °C. Coercivity of 68 Oe was observed at 50 K in micron sized particles. It can also be noted that  $M$ – $H$  curve nonlinearity which disappeared in samples annealed at 700 °C particles above 45 K reappears for the micron sized particles and persists up to 80 K. It indicates the shift in the order-disorder transition temperature. To investigate it further in figure 4.3.10, we have compared the ZFC–FC  $\chi$ – $T$  curves (200 Oe) which clearly show that for micron sized TMO particles (with shell contribution of  $Tb_{1-x}Mn^{+3}_{1-x}Mn^{+4}_xO_3$ ) the ZFC–FC magnetization curves bifurcate at around 80 K instead of 45 K (nanosized particles) this is due to the enhanced magnetic interaction induced by the presence of  $Mn^{+4}$ .

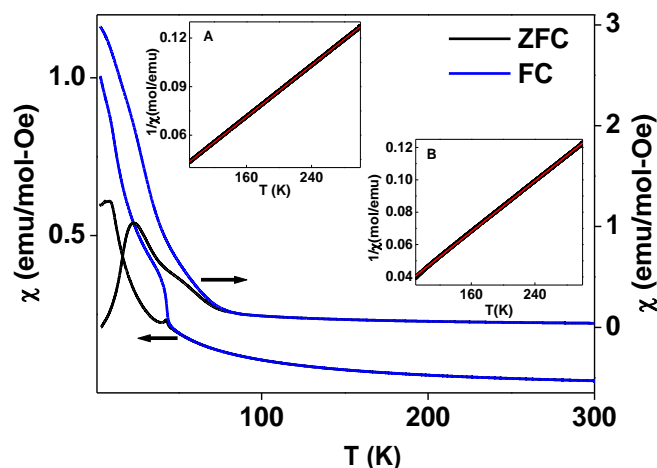


**Figure 4.3.10:** Temperature dependence of the ZFC–FC susceptibility, with an applied field of 200 Oe for  $\text{TbMnO}_3$  nanoparticles annealed at 700 °C (left Y-axis) and 800 °C (right Y-axis). Insets A) and B) show the inverse of susceptibility and their Curie-Weiss fits (red solid line) for  $\text{TbMnO}_3$  nanoparticles annealed at 700 and 800 °C, respectively.

However, the hump at 45 K (observed in the ZFC magnetization curves for nanosized samples) is still visible for the samples annealed at 800 °C as the  $\text{Mn}^{+3}$ – $\text{Mn}^{+3}$  SE interaction due to the TMO sublattice as in the case of pure TMO. However, in both the cases below  $T_N$  the  $\chi$  value increases dramatically indicating presence of weak ferromagnetism due to spin canting as discussed above. The Curie-Weiss fitting of FC magnetization curve above  $T_N$  gives Weiss temperature  $\theta$  and Curie constant  $C$  values –20 K, 2516 emu K/mol and –14 K, 2561 emu K/mol respectively for TMO samples calcined at 700 °C and 800 °C respectively. In samples annealed at 700 °C,  $\theta$  value (in negative) increases which indicates that AFM character in nanosize particles increases as the double exchange between  $\text{Mn}^{+3}$  and  $\text{Mn}^{+4}$  ions which results in FM nature in samples annealed at 800 °C decreases. The anomaly near 27 K which was observed in single crystalline TMO corresponding to the incommensurate-commensurate (lock-in) transition was not observed in samples annealed at 700 °C but

---

observed in samples annealed at 800 °C. As discussed earlier, this transition is related to long length scale (magnetic modulation wave vector) due to the annealing for longer duration at high temperature intrinsic strain in the particles decreases and the transition which was suppressed in smaller crystallite sized particles appeared in micron sized particles. Another important observation was disappearance of 10 K transition (due to  $Tb^{+3}$ - $Tb^{+3}$  spins interaction) in samples annealed at 800 °C. It might have shifted below 3 K. The reason behind the disappearance of this weak transition is not clear to us at present.

#### 4.3.8 Conclusion

Single phase  $TbMnO_3$  nanoparticles were synthesized using modified hydrothermal method. Particles are of plate like shaped with good crystallinity. We conclude that the presence of  $Mn^{+4}$  in particles annealed at 800 °C, enhances magnetic interaction which was observed as the increase of ZFC-FC magnetization bifurcation temperature. The anomaly near 27 K corresponding to incommensurate-commensurate (lock-in) transition was not observed in samples annealed at 700 °C but observed in samples annealed at 800 °C, probably due to the particle size effects.

---

#### 4.4 References

- [1] Kimura, T.; Ishihara, S.; Shintani, H.; Arima, T.; Takahashi, K. T.; Ishizaka, K.; Tokura, Y. *Phys. Rev. B* **2003**, *68*, 060403(R).
- [2] Fiebig, M.; Lottermoser, T.; Frohlich, D.; Goltsev, A. V.; Pisarev, R. V. *Nature* **2002**, *419*, 818.
- [3] Hill, N. A. *J. Phys. Chem. B* **2000**, *104*, 6694.
- [4] Ramesh, R. *Nature* **2009**, *461*, 1218.
- [5] Goto, T.; Kimura, T.; Lawes, G.; Ramirez, A. P.; Tokura, Y. *Phys. Rev. Lett.* **2004**, *92*, 257201.
- [6] Mostovoy, M. *Phys. Rev. Lett.* **2006**, *96*, 067601.
- [7] Kenzelmann, M.; Harris, A. B.; Jonas, S.; Broholm, C.; Schefer, J.; Kim, S. B.; Zhang, C. L.; Cheong, S. W.; Vajk, O. P.; Lynn, J. W. *Phys. Rev. Lett.* **2005**, *95*, 087206.
- [8] Plumer, M. L.; Walker, M. B. *J. Phys. C-Solid State Phys.* **1982**, *15*, 7181.
- [9] Walker, M. B. *Phys. Rev. B* **1980**, *22*, 1338.
- [10] Kimura, T.; Goto, T.; Shintani, H.; Ishizaka, K.; Arima, T.; Tokura, Y. *Nature* **2003**, *426*, 55.
- [11] Feyerherm, R.; Dudzik, E.; Aliouane, N.; Argyriou, D. N. *Phys. Rev. B* **2006**, *73*, 180401.
- [12] Pimenov, A.; Mukhin, A. A.; Ivanov, V. Y.; Travkin, V. D.; Balbashov, A. M.; Loidl, A. *Nat. Phys.* **2006**, *2*, 97.
- [13] Kimura, T.; Lawes, G.; Goto, T.; Tokura, Y.; Ramirez, A. P. *Phys. Rev. B* **2005**, *71*, 224425.
- [14] Ribeiro, J. L. *Phys. Rev. B* **2007**, *76*, 144417.

- 
- [15] Arima, T.; Goto, T.; Yamasaki, Y.; Miyasaka, S.; Ishii, K.; Tsubota, M.; Inami, T.; Murakami, Y.; Tokura, Y. *Phys. Rev. B* **2005**, *72*, 100102(R).
- [16] Kadomtseva, A. M.; Popov, Y. F.; Vorob'ev, G. P.; Kamilov, K. I.; Pyatakov, A. P.; Ivanov, V. Y.; Mukhin, A. A.; Balbashov, A. M. *Jetp. Lett.* **2005**, *81*, 19.
- [17] Pimenov, A.; Rudolf, T.; Mayr, F.; Loidl, A.; Mukhin, A. A.; Balbashov, A. M. *Phys. Rev. B* **2006**, *74*, 100403(R).
- [18] Ferreira, W. S.; Moreira, J. A.; Almeida, A.; Chaves, M. R.; Araujo, J. P.; Oliveira, J. B.; Da Silva, J. M. M.; Sa, M. A.; Mendonca, T. M.; Carvalho, P. S.; Kreisel, J.; Ribeiro, J. L.; Vieira, L. G.; Tavares, P. B.; Mendonca, S. *Phys. Rev. B* **2009**, *79*, 054303.
- [19] Wang, X. L.; Li, D.; Cui, T. Y.; Kharel, P.; Liu, W.; Zhang, Z. D. *J. Appl. Phys.* **2010**, *107*, 09B510.
- [20] Oku, M.; Hirokawa, K.; Ikeda, S. *J. Electron Spectrosc. Relat. Phenom.* **1975**, *7*, 465.
- [21] Martin-Carron, L.; Andres, A. de; Martinez-Lope, M. J.; Casais M. T.; Alonso, J. A. *Phys. Rev. B* **2002**, *66*, 174303.
- [22] Jaiswal, A.; Das, R.; Vivekanand, K.; Abraham, P. M.; Adyanthaya, S.; Poddar, P. J. *Phys. Chem. C* **2010**, *114*, 2108.
- [23] Park, T. J.; Papaefthymiou, G. C.; Viescas, A. J.; Moodenbaugh, A. R.; Wong, S. S. *Nano Lett.* **2007**, *7*, 766.
- [24] Uusi-Esko, K.; Malm, J.; Imamura, N.; Yamauchi, H.; Karppinen, M. *Mater. Chem. Phys.* **2008**, *112*, 1029.
- [25] Dyakonov, V.; Szytuła, A.; Baran, S.; Kravchenko, Z.; Zubov, E.; Iessenchuk, O.; Bazela, W.; Dul, M.; Zarzycki, A.; Szymczak, H. *Acta Physica Polonica A* **2010**, *117*, 607.
- [26] Stremper, J.; Bohnenbuck, B.; Mostovoy, M.; Aliouane, N.; Argryriou, D. N.; Schrettle, F.; Hemberger, J.; Krimmel, A.; von Zimmermann, M. *Phys. Rev. B* **2007**, *75*, 212402.
-

- 
- [27] Prokhnenko, O.; Feyerherm, R.; Dudzik, E.; Landsgesell, S.; Aliouane, N.; Chapon, L. C.; Argyriou, D. N. *Phys. Rev. Lett.* **2007**, *98*, 057206.
- [28] Iliev, M. N.; Abrashev, M. V.; Laverdière, J.; Jand, S.; Gospodinov, M. M.; Wang, Y. Q.; Sun, Y. Y. *Phys. Rev. B* **2006**, *73*, 064302.
- [29] Munoz, A.; Alonso, J. A.; Casais, M. T.; Martinez-Lope, M. J.; Martínez, J. L.; Fernández-Díaz, M. T. *J. Phys.: Condens. Matter.* **2002**, *14*, 3285.
- [30] Dabrowski, B.; Kolesnik, S.; Baszczuk, A.; Chmaissem, O.; Maxwell, T.; Mais, J. J. *Solid State Chem.* **2005**, *178*, 629.
- [31] Cheong, S. W.; Mostovoy, M. *Nat. Mater.* **2007**, *6*, 13.
- [32] Noda, K.; Nakamura, S.; Nagayama, J.; Kuwahara, H. *J. Appl. Phys.* **2005**, *97*, 10C103.
- [33] Bansal, V.; Poddar, P.; Ahmad, A.; Sastry, M. *J. Am. Chem. Soc.* **2006**, *128*, 11958.
- [34] Poddar, P.; Fried, T.; Markovich, G. *Phys. Rev. B* **2002**, *65*, 172405.
- [35] Harikrishnan, S.; Rößler, S.; Kumar, C. M. N.; Bhat, H. L.; Rößler, U. K.; Wirth, S.; Steglich, F.; Elizabeth, S. *J. Phys.: Condens. Matter.* **2009**, *21*, 096002.
- [36] Manna, P. K.; Yusuf, S. M.; Shukla, R.; Tyagi, A. K. *Phys. Rev. B* **2011**, *83*, 184412.
- [37] Markovich, V.; Puzniak, R.; Mogilyansky, D.; Wu, X.; Suzuki, K.; Fita, I.; Wisniewski, A.; Chen, S.; Gorodetsky, G. *J. Phys. Chem. C* **2011**, *115*, 1582.
- [38] Ahmadvand, H.; Salamati, H.; Kameli, P.; Poddar, A.; Acet, M.; Zakeri, K. *J. Phys. D: Appl. Phys.* **2010**, *43*, 245002.
- [39] Arima, T.; Tokunaga, A.; Goto, T.; Kimura, H.; Noda, Y.; Tokura, Y. *Phys. Rev. Lett.* **2006**, *96*, 097202.
- [40] Katsura, H.; Nagaosa, N.; Balatsky, A. V. *Phys. Rev. Lett.* **2005**, *95*, 057205.
-



- 
- [41] Abe, N.; Taniguchi, K.; Ohtani, S.; Takenobu, T.; Iwasa, Y.; Arima, T. *Phys. Rev. Lett.* **2007**, *99*, 227206.
- [42] Quezel, S.; Tcheou, F.; Rossat-Mignod, J.; Quezel, G.; Roudaut, E. *Physica B & C* **1977**, *86-88B*, 916.
- [43] Selbach, S. M.; Tybell, T.; Einarsrud, M. A.; Grande, T. *Chem. Mater.* **2007**, *19*, 6478.
- [44] Kharrazi, S.; Kundaliya, D. C.; Gosavi, S. W.; Kulkarni, S. K.; Venkatesan, T.; Ogale, S. B.; Urban, J.; Park, S.; Cheong, S. W. *Solid State Commun.* **2006**, *138*, 395.
- [45] Chan, T. S.; Liu, R. S.; Yang, C. C.; Li, W. H.; Lien, Y. H.; Huang, C. Y.; Lee, J. F. *J. Phys. Chem. B* **2007**, *111*, 2262.

# Chapter 5. Effect of R and B site substitution on magnetic properties of $RBO_3$ ( $R = Gd, Dy$ and $B = Mn, Cr$ )

---

The motivation of the chapter is to study the effect of R and B site substitution on the magnetic transitions of  $GdMnO_3$ . Orthorhombic  $DyMnO_3$  and  $GdMnO_3$  individually have almost similar antiferromagnetic transition temperature,  $\sim 39$  and  $\sim 42$  K, respectively. Below Néel transition,  $GdMnO_3$  undergoes a transition from incommensurate-antiferromagnetic phase (ICAFM) into a canted A-type AFM ordering (*c*AAFM) at  $\sim 22$  K. We have studied how the  $T_N$  and  $R^{+3}-R^{+3}$  ion interaction varies with R-site substitution in  $GdMnO_3$  with Dy.

$DyMnO_3$  and  $DyCrO_3$  have their individual  $T_N$  at  $\sim 39$  and  $\sim 142$  K, respectively. The effect of Cr substitution on  $T_N$  of  $DyMnO_3$  is also studied.

---

---

## Section 5.1 R-site substitution: $\text{Gd}_{1-x}\text{Dy}_x\text{MnO}_3$

---

Orthorhombic  $\text{DyMnO}_3$  and  $\text{GdMnO}_3$  individually have almost similar antiferromagnetic transition temperature,  $\sim 39$  and  $\sim 42$  K, respectively. Below  $T_N$   $\text{GdMnO}_3$  undergoes a transition from incommensurate-antiferromagnetic phase (ICAFM) into a canted A-type AFM ordering (*c*AAFM)  $\sim 22$  K. We have studied how the  $T_N$  and  $\text{R}^{+3}\text{-R}^{+3}$  ions interaction temperature varies with R-site substitution in  $\text{GdMnO}_3$  by Dy.

---

### 5.1.1 Introduction

Crystal structure of rare-earth manganites,  $\text{RMnO}_3$  (R=rare-earth) is determined by ionic radius of rare-earth ion. Materials with large  $\text{R}^{+3}$  ionic radius (R=La–Dy) crystallizes in orthorhombic structure whereas, materials with small  $\text{R}^{+3}$  ionic radius (R=Ho–Lu) crystallizes in hexagonal structure [1–14]. Multiferroic materials with strong coupling between magnetic and electric ordering attracted much attention due to its application in MERAM and fundamental physics [15–22]. Family of orthorhombic rare-earth manganites with (R=Gd, Tb, Dy) are particularly interesting due to its spiral spin structure which gives ferroelectricity in this class [23, 24]. With decreasing temperature these materials undergo a transition from paramagnetic state to a collinear spin sinusoidal incommensurate state ( $T_N=40\text{--}50$  K) and then to a spiral spin state with a lock in period ( $T_{\text{lock}}=15\text{--}30$  K). Below this  $T_{\text{lock}}$  it shows ferroelectric ordering. In collinear spin sinusoidal incommensurate state ( $T_{\text{lock}} < T < T_N$ ) wavelength of sinusoidal modulation changes monotonously with decreasing temperature and below  $T_{\text{lock}}$  wavelength of sinusoidal modulation remain unchanged [25–36]. Spiral spin ordering breaks inversion symmetry which results in electric polarization can be explained by two phenomenon a) spin-orbit coupling b) cation displacement driven by DM interaction.

$\text{DyMnO}_3$  and  $\text{GdMnO}_3$  are multiferroic rare-earth manganites from the family of  $\text{RMnO}_3$  with R=Gd, Tb, and Dy; where magnetic and ferroelectric order coexist [34]. For R=Tb and Dy, the multiferroic behavior is already present in zero magnetic field, while a finite magnetic field along the  $b$ -axis is necessary to induce multiferroicity in  $\text{GdMnO}_3$  [30, 31]. In  $\text{DyMnO}_3$ , the magnetic ordering of the  $\text{Mn}^{+3}$  moments with incommensurate propagation vector  $q_m^{\text{Mn}} \mathbf{b}^*$  is associated with a second-harmonic lattice modulation  $q_l^{\text{Mn}} = 2q_m^{\text{Mn}}$ , i.e., with a quadratic magnetoelastic coupling [25, 26]. On cooling below  $T_N \sim 39$  K, the incommensurate values of  $q^{\text{Mn}}$  vary with temperature, and below a characteristic

---

temperature  $T_f \sim 18$  K, a spontaneous electric polarization is observed in zero applied magnetic field [27]. The  $\text{Dy}^{+3}$  ordering cause significant anomalies in the dielectric-constant and electric-polarization. Therefore, the coupling between the  $\text{Dy}^{+3}$  and the  $\text{Mn}^{+3}$  ions appears to be more important in  $\text{DyMnO}_3$  than other manganite perovskites of the same class such as  $\text{Gd}$ ,  $\text{TbMnO}_3$ . At zero magnetic field,  $\text{GdMnO}_3$  remains PE and PM. At  $\sim 42$  K ( $T_N$ ),  $\text{GdMnO}_3$  undergoes a phase-transition from PM to an ICAFM phase, with a modulation wave vector directed along the  $b$ -axis [29, 30]. This modulation corresponds to a collinear arrangement of the  $\text{Mn}^{+3}$  spins. This is a consequence of competing exchange interactions between successive neighbor spins, which leads to a frustrated spin system. The modulated spin order below  $T_N$  remains collinear until the system enters into an  $A$ -type antiferromagnetic phase at about 27 K. Around 22 K, it under goes further transition from ICAFM into a  $c$ AAFM of the  $\text{Mn}^{+3}$  spins along the  $c$ -axis [29, 35]. Below this transition, the polarization of the  $\text{Gd}^{+3}$   $4f$  spins by the canting of  $\text{Mn}^{+3}$  spins results into weak ferromagnetism (FM). Around  $\sim 6$  K, the long-range ordering of  $\text{Gd}^{+3}$  spins occurs [33]. Below this temperature, there is a resultant configuration of canted  $\text{Gd}^{+3}$  spins antiparallel to that of canted  $\text{Mn}^{+3}$  spins. The application of a strong magnetic field,  $H \geq 5$  T along the  $a$ -axis induces a FE phase with a polarization oriented along the  $c$ -axis. Structural studies showed that this magnetically induced FE phase is accompanied by a commensurate modulation of the  $\text{Mn}^{+3}$  moments [31].

In this section we have studied how the Néel transition, ICAFM to  $c$ AAFM transition and  $\text{R}^{+3}$  to  $\text{R}^{+3}$  ion interaction temperature varies with R-site substitution in  $\text{GdMnO}_3$  by Dy.

### 5.1.2 Chemicals used

Dysprosium (III) oxide, ( $\geq 99.99\%$  trace metals basis, Sigma Aldrich), gadolinium (III) oxide powder, ( $\geq 99.99\%$  trace metals basis, Sigma Aldrich), and manganese (III) oxide ( $99.99\%$  trace metals, Sigma Aldrich).

### 5.1.3 Synthesis

Bulk polycrystalline samples of  $\text{Gd}_{1-x}\text{Dy}_x\text{MnO}_3$  ( $x=0-1$ ) were synthesized by the conventional solid-state reaction method, using stoichiometric mixture of high purity metal oxide starting materials. The compounds were ground thoroughly in a mortar and calcined at  $850\text{ }^\circ\text{C}$  for 24 h. Again the sample was ground and calcined at  $1300\text{ }^\circ\text{C}$  for 24 h. Finally, the ground sample was compressed into pellet and was sintered at  $1400\text{ }^\circ\text{C}$  for 24 h.

### 5.1.4 Crystal structure

Figure 5.1.1 shows the powder XRD pattern of orthorhombic  $\text{Gd}_{1-x}\text{Dy}_x\text{MnO}_3$  with ( $x=0-1$ ). All XRD patterns showed the formation of perovskite orthorhombic structure without any secondary phases. As both  $\text{DyMnO}_3$  and  $\text{GdMnO}_3$  crystallize in orthorhombic structure, so it was expected that the substituted compounds will also crystallize in orthorhombic.

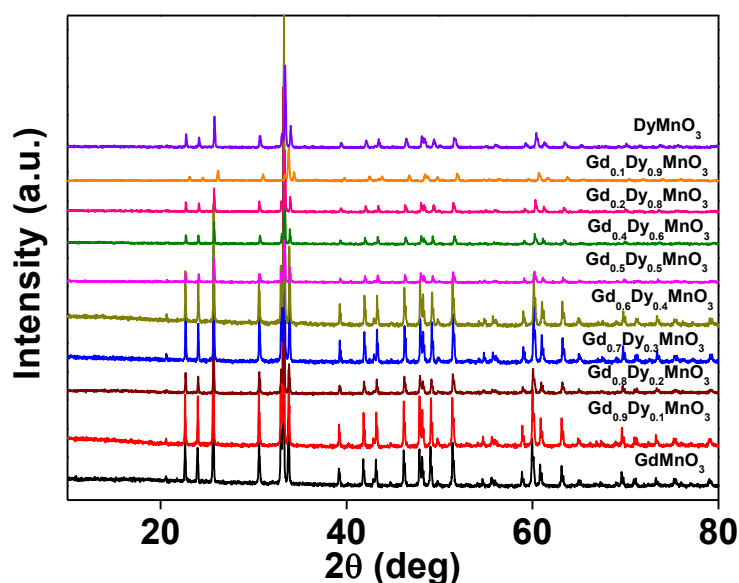


**Figure 5.1.1:** Room temperature XRD patterns of orthorhombic  $Gd_{1-x}Dy_xMnO_3$  ( $x=0-1$ ).

### 5.1.5 Raman spectroscopy

Room temperature Raman spectra of orthorhombic  $Gd_{1-x}Dy_xMnO_3$  with ( $x=0-1$ ) is shown in figure 5.1.2. There are 24 ( $7A_g + 5B_{1g} + 7B_{2g} + 5B_{3g}$ ) Raman active modes in orthorhombic manganites [37]. Raman active modes in orthorhombic manganites originate from rotation of [010], [101], Jahn-Teller distortion and R-shift [38]. Raman spectra of orthorhombic  $Gd_{1-x}Dy_xMnO_3$  with ( $x=0-1$ ) showed peaks  $\sim 610, 485, 368$  and  $275 \text{ cm}^{-1}$  which can be assigned to in-plane  $O_2$  stretching ( $B_{2g}1$ ),  $MnO_6$  bending ( $A_g3$ ), out-of-plane  $MnO_6$   $x$  rotation and in-plane  $MnO_6$   $y$  rotation ( $A_g7$ ) respectively [38]. Variation of above four phonon modes Raman shifts with  $x$  in  $Gd_{1-x}Dy_xMnO_3$  is shown figure 5.1.3. In all four modes, there was anomaly at  $x = 0.3$ . These all modes should harden with increase in  $x$  as ionic size of  $Dy^{+3}$  is smaller than  $Gd^{+3}$  ions, which results in increase distortion and bond length shortening. All these modes except  $A_g7$  are related to Jahn-Teller distortion so anomaly near  $x=0.3$  could be related to structural distortion. As the substitution of  $Gd^{+3}$  by  $Dy^{+3}$  in  $Gd_{1-x}Dy_xMnO_3$  increases

distortion in the structure increases. XRD pattern does not showed any evidence of peak shift in  $x=0.3$  sample, so synchrotron data is required to know possible reason of the anomaly.

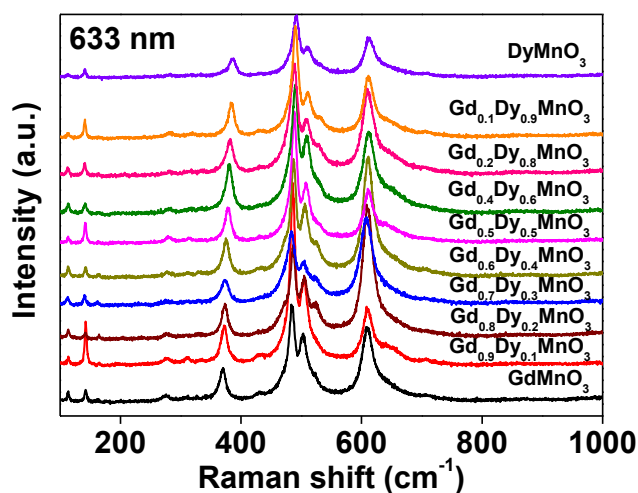


**Figure 5.1.2:** Room temperature Raman spectra of orthorhombic  $Gd_{1-x}Dy_xMnO_3$  ( $x=0-1$ ).

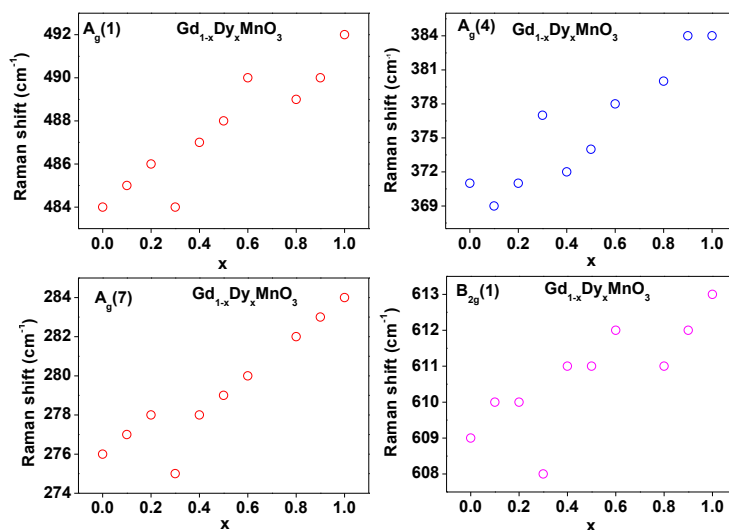


**Figure 5.1.3:** Variation of phonon mode frequency with  $x$  in orthorhombic  $Gd_{1-x}Dy_xMnO_3$  ( $x=0-1$ ).



The peaks  $\sim 110$  and  $142\text{ cm}^{-1}$  can be assigned to  $B_{2g}$  and  $A_g$  modes of  $R(z)$  [39]. There is no change in Raman shift of these modes with  $x$  in  $Gd_{1-x}Dy_xMnO_3$ .

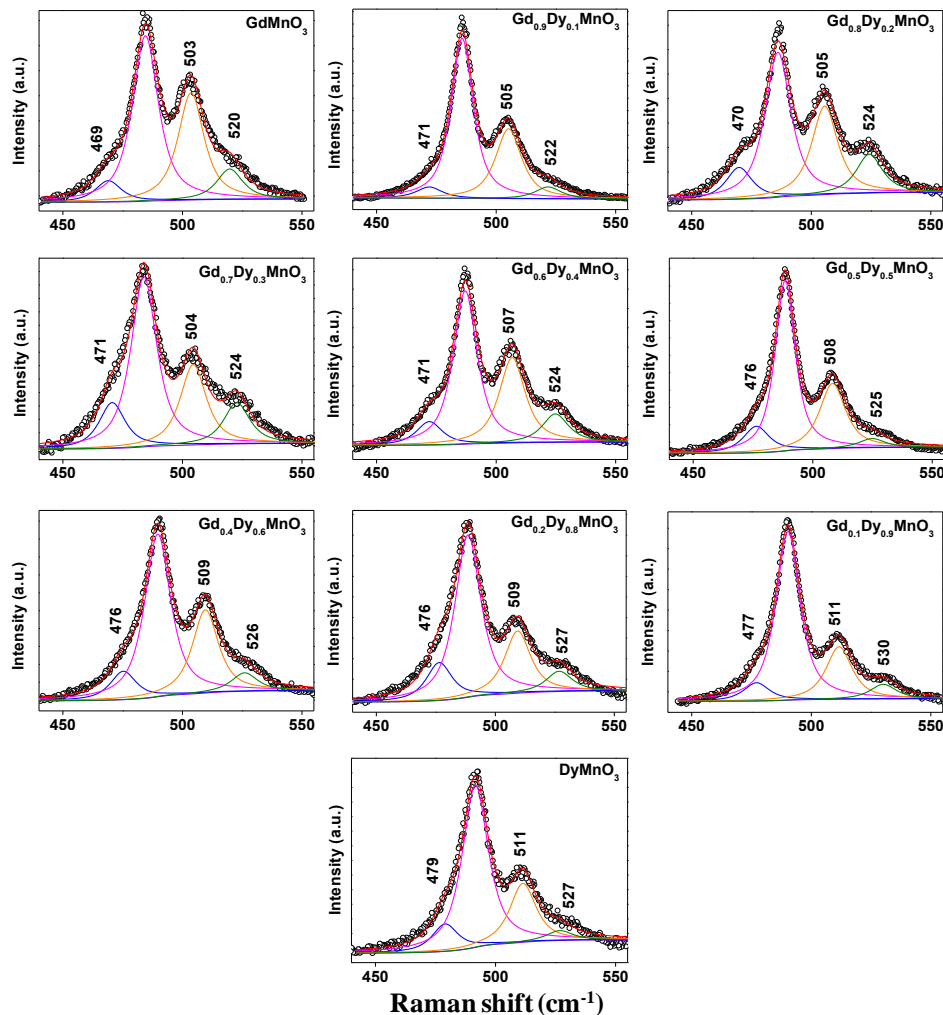


**Figure 5.1.4:** Variation of phonon mode frequency with  $x$  in orthorhombic  $Gd_{1-x}Dy_xMnO_3$  ( $x=0-1$ ).

Figure 5.1.4 shows the deconvoluted Raman modes of 470, 490, 505 and  $524\text{ cm}^{-1}$ . Raman modes  $\sim 470$  ( $E_g$  bending), 505 and  $524\text{ cm}^{-1}$  can be assigned to  $B_{2g}$  modes [37]. These modes show gradual hardening with increase of  $x$ , which is in agreement with literature. As  $x$  increases, distortion increase and bond length shortens.

Figure 5.1.5 shows the deconvoluted Raman modes  $\sim 615$  and  $640 \text{ cm}^{-1}$  which can be assigned to in-plane O2 stretching ( $B_{2g}$ ) and  $E_g$  antistretching mode. The Raman mode  $\sim 640 \text{ cm}^{-1}$  is due to  $E_g$  antistretching mode of orthorhombic  $\text{RMnO}_3$ . This mode peak does not show any trend in Raman shift position with increasing  $x$  in  $\text{Gd}_{1-x}\text{Dy}_x\text{MnO}_3$  ( $x=0-1$ ).

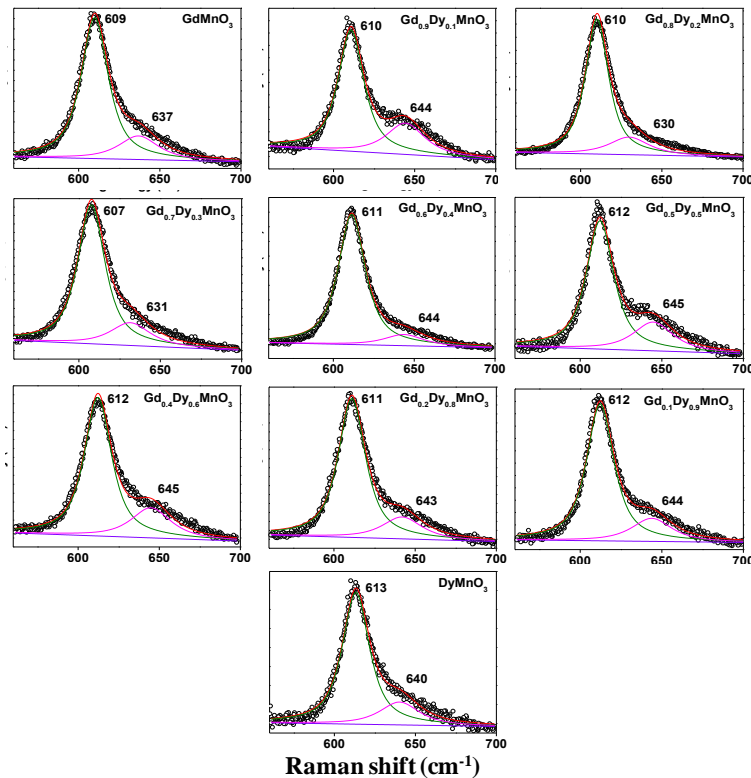


**Figure 5.1.5:** Variation of phonon mode frequency with  $x$  in orthorhombic  $\text{Gd}_{1-x}\text{Dy}_x\text{MnO}_3$  ( $x=0-1$ ).

### 5.1.6 Magnetic study

To see the role of magnetic field on AFM ordering, study of magnetic field dependence of magnetization was done at 3, 5, 7 and 10 K. Figure 5.1.6 shows field-induced metamagnetic transition at 3, 5, 7 and 10 K isothermal magnetization. This type of metamagnetic transition

was also observed in polycrystalline sample of  $\text{DyMnO}_3$  [40]. At  $\sim 3$  K, below a critical field magnetization increases slowly with field, above which initially magnetization increases rapidly and then slowly with increasing field. At  $\sim 3$  K, critical field and the field-induced metamagnetic transition is less sharp for  $\text{DyMnO}_3$  than  $\text{GdMnO}_3$ . With substitution of  $\text{Dy}^{+3}$  ions in  $\text{Gd}^{+3}$  site of  $\text{GdMnO}_3$  the sharpness of field-induced metamagnetic transition decreases monotonously with anomaly at  $x=0.3$ . Anomaly at  $x=0.3$  was also observed in Raman peak position. At low field region, moment values for  $\text{Gd}_{1-x}\text{Dy}_x\text{MnO}_3$  decrease monotonously with increasing  $x$ , but at high field value, moment value does not follow any trend. At the critical field these compounds show field induced transition from AFM to FM state [40].

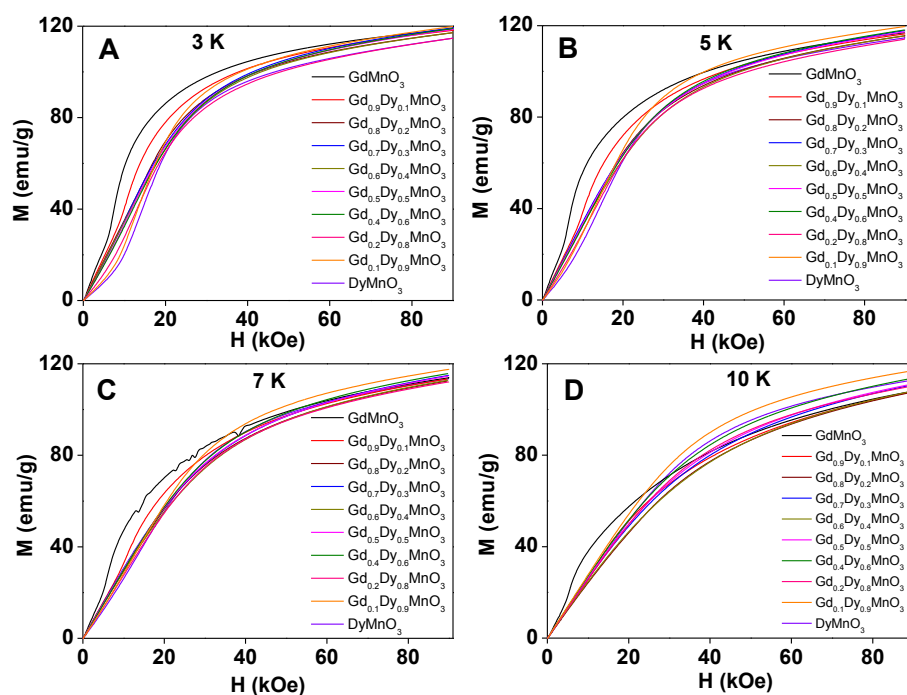


**Figure 5.1.6:** Initial magnetization as a function of applied field for orthorhombic  $\text{Gd}_{1-x}\text{Dy}_x\text{MnO}_3$  ( $x=0-1$ ) at A) 3 K B) 5 K C) 7 K and D) 10 K.

This implies, in FM state, magnetization values for  $\text{Gd}_{1-x}\text{Dy}_x\text{MnO}_3$  do not show any trend with increasing  $x$ . At 3 K, among  $\text{Gd}_{1-x}\text{Dy}_x\text{MnO}_3$  ( $x=0-1$ ), the critical field required for AFM to FM transition is highest in  $\text{DyMnO}_3$  and lowest for  $\text{GdMnO}_3$ . With increasing  $x$  in  $\text{Gd}_{1-x}\text{Dy}_x\text{MnO}_3$  ( $x=0-1$ ), the critical field required for AFM to FM transition showed monotonous increase. At 5 K, the trend of  $H$  dependence of magnetization remains almost same as 3 K but the critical field of AFM to FM transition decreased at 5 K compared to 3 K. At 7 and 10 K, only  $\text{GdMnO}_3$  shows field-induced transition whereas, other does not show any field-induced transition.

ZFC magnetization curves for orthorhombic  $\text{Gd}_{1-x}\text{Dy}_x\text{MnO}_3$  ( $x=0-1$ ) at 100 Oe is shown in figure 5.1.7. ZFC-FC magnetization curves showed bifurcation below  $T_N$  in all the samples,  $\text{Gd}_{1-x}\text{Dy}_x\text{MnO}_3$  ( $x=0-1$ ). ZFC magnetization curves showed a hump below 10 K, which is signature of  $R^{+3}-R^{+3}$  ordering.  $\text{Gd}^{+3}-\text{Gd}^{+3}$  ordering in  $\text{GdMnO}_3$  was observed at 4.3 K whereas,  $\text{Dy}^{+3}-\text{Dy}^{+3}$  ordering in  $\text{DyMnO}_3$  was observed at 7.7 K. At  $x=0.1, 0.2$  and  $0.4$ ,  $R^{+3}-R^{+3}$  ordering was observed below the  $\text{Gd}^{+3}-\text{Gd}^{+3}$  ordering temperature whereas in other samples  $R^{+3}-R^{+3}$  ordering temperature increases with increasing  $x$ .

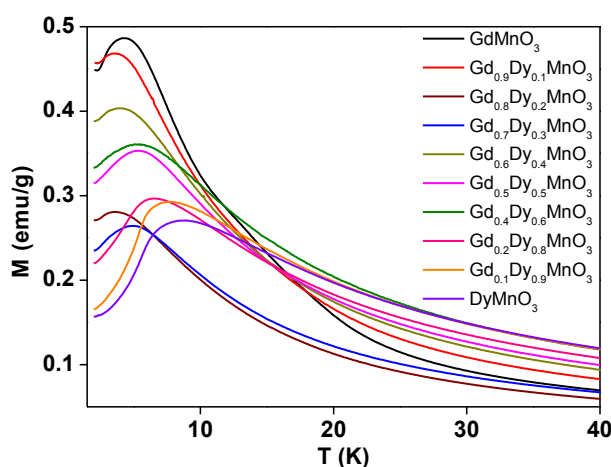


**Figure 5.1.7:** ZFC magnetization curves for orthorhombic  $\text{Gd}_{1-x}\text{Dy}_x\text{MnO}_3$  ( $x=0-1$ ) at 100 Oe applied field.

There is no signature of  $T_N$  in real part of ac magnetization in all samples. But below 10 K, signature of  $R^{+3}-R^{+3}$  interaction was observed as hump in real part of ac magnetization. The hump, signature of  $R^{+3}-R^{+3}$  interaction increases monotonously for  $x \geq 0.5$  but below 0.5 it does not follow any specific trend.

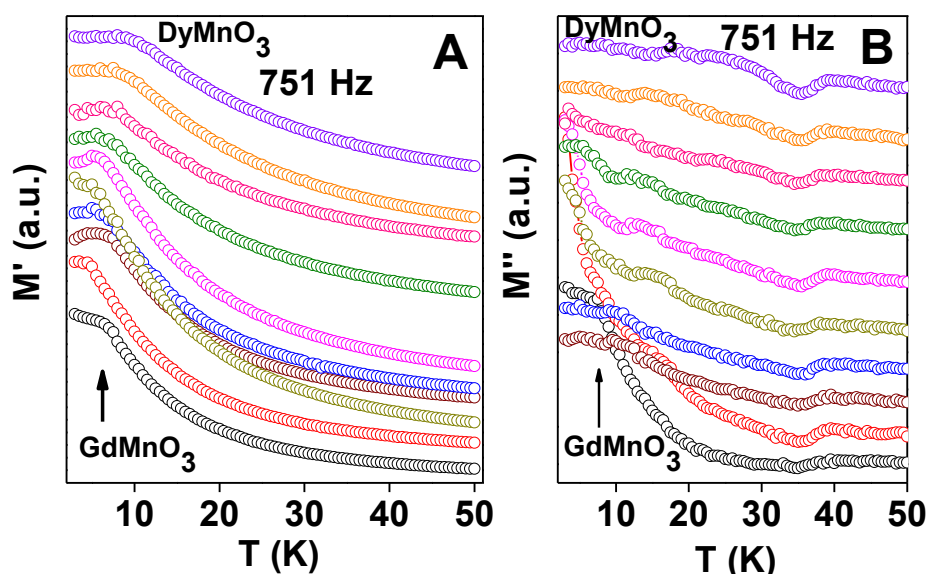


**Figure 5.1.8:** Temperature dependence of A) Real part and B) imaginary part of ac magnetization at ac field of 5 Oe and frequency 751 Hz.

Imaginary part of ac magnetization showed a hump  $\sim 40$  K, Néel transition of Gd/DyMnO<sub>3</sub>. The position of the hump is almost same for all the samples. Imaginary part of ac magnetization also showed signature of  $R^{+3}-R^{+3}$  interaction.

### 5.1.7 Conclusion

Magnetic measurements showed that, there is no change in  $T_N$  for orthorhombic Gd<sub>1-x</sub>Dy<sub>x</sub>MnO<sub>3</sub> with  $x=0-1$ .  $R^{+3}-R^{+3}$  ordering temperature changes with substitution of Dy in GdMnO<sub>3</sub> but the change is not monotonous.

---

## Section 5.2 B-site substitution: $\text{DyMn}_{1-x}\text{Cr}_x\text{O}_3$

---

$\text{DyMnO}_3$  and  $\text{DyCrO}_3$  have Néel transitions at  $\sim 39$  and  $\sim 142$  K respectively. The motivation of this study is to see effect of Cr substitution in B-site on  $T_N$  of  $\text{DyMnO}_3$ .

---

### 5.2.1 Introduction

There is a renewed interest among physicists and chemists to study complex oxides such as rare-earth manganites, chromites and ferrites, due to their potential use in magnetoelectric and optoelectronic devices. Several of these compounds show ferroelectric, ferroelastic, and magnetic ordering in single phase (multiferroicity), apart from interesting optoelectronic properties. Some of these compounds show ME effect.

The structural, electrical and magnetic properties of  $\text{RCrO}_3$  compounds are well studied. Rao *et al.* based on the resistivity measurements showed ferroelectric ordering due to distorted  $\text{CrO}_6$  octahedral in  $\text{DyCrO}_3$ ,  $\text{HoCrO}_3$ ,  $\text{YbCrO}_3$  and  $\text{LuCrO}_3$ .  $\text{DyCrO}_3$ .  $\text{RCrO}_3$  compounds crystallize in an orthorhombic structure with the space group  $Pbnm$  [40]. Single crystal of  $\text{DyCrO}_3$  exhibits weak ferromagnetism, where  $\text{Cr}^{+3}$  ions are order just below the  $T_N$ , 142 K and the  $\text{Dy}^{+3}$  ions order below 4.2 K in an antiferromagnetic structure [41–43].

$\text{DyMnO}_3$  crystallizes in orthorhombic phase with space group  $Pbnm$ . In  $\text{DyMnO}_3$  the spiral magnetic ordering is stabilized by competing exchange interactions, which forces opposite charge ions to shift in opposite directions, can be easily influenced by applied magnetic fields. In the orthorhombic rare-earth manganites  $\text{RMnO}_3$  ( $R=\text{Gd}$ ,  $\text{Tb}$ , and  $\text{Dy}$ ), which crystallize in a distorted perovskite structure, ferroelectricity has been shown to originate from a spiral magnetic structure.  $\text{DyMnO}_3$  show  $T_N \sim 43$  K due the ordering of  $\text{Mn}^{+3}$  moments and  $\sim 7$  K AFM interaction between the  $\text{Dy}^{+3}$  ions.

As  $\text{DyMnO}_3$  and  $\text{DyCrO}_3$  have  $T_N$  at 39 and 142 K respectively. The motivation of this study is to see effect of Cr substitution on  $T_N$  of  $\text{DyMnO}_3$ .

### 5.2.2 Chemicals used

Dysprosium (III) oxide,  $\geq 99.99\%$  trace metals basis (Sigma Aldrich), manganese (III) oxide  $99.99\%$  trace metals basis (Sigma Aldrich) and chromium (III) oxide purum,  $\geq 99\%$  (iodometric) (Sigma Aldrich).

### 5.2.3 Synthesis

Bulk polycrystalline samples of  $\text{DyMn}_{1-x}\text{Cr}_x\text{O}_3$  were synthesized by the conventional solid-state reaction method, using stoichiometric mixtures of high purity metal oxide starting materials. The compounds were ground thoroughly in a mortar and calcined at  $850\text{ }^\circ\text{C}$  for 24 h. Again the sample was ground and calcined at  $1300\text{ }^\circ\text{C}$  for 24 h. Finally, the ground sample was compressed into pellet and was sintered at  $1400\text{ }^\circ\text{C}$  for 24 h.

### 5.2.4 X-ray diffraction

Figure 1 shows the powder XRD pattern of orthorhombic  $\text{DyMn}_{1-x}\text{Cr}_x\text{O}_3$  ( $x=0.03, 0.05, 0.1$ ). All XRD patterns show the formation of perovskite orthorhombic structure without any secondary phases. No signature of  $\text{DyCrO}_3$  phase was observed in XRD pattern.



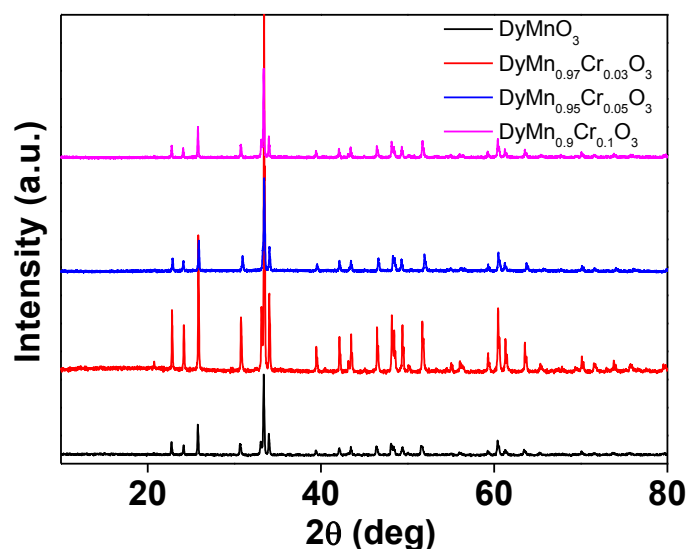


**Figure 5.2.1:** Room temperature XRD pattern of orthorhombic  $\text{DyMn}_{1-x}\text{Cr}_x\text{O}_3$  ( $x=0, 0.03, 0.05, 0.1$ ).

### 5.2.5 Raman spectroscopy

Room temperature Raman spectra of orthorhombic  $\text{DyMn}_{1-x}\text{Cr}_x\text{O}_3$  ( $x=0, 0.03, 0.05, 0.1$ ) is shown in figure 5.2.2. Raman active modes in orthorhombic manganites originate from rotation of  $[010]$ ,  $[101]$ , Jahn-Teller distortion and R-shift. Raman spectra of orthorhombic  $\text{DyMn}_{1-x}\text{Cr}_x\text{O}_3$  ( $x=0, 0.03, 0.05, 0.1$ ) showed peaks  $\sim 113, 140, 385, 492, 509$  and  $611 \text{ cm}^{-1}$ . Raman modes  $\sim 113, 140 \text{ cm}^{-1}$  can be assigned to  $B_{2g}$  and  $A_g$  modes of  $R(z)$ . There is no notable change in position of these modes (within the error resolution limit of instrument) with  $x$ , which can be due to the fact that these modes related to  $\text{Dy}^{+3}$  ions.

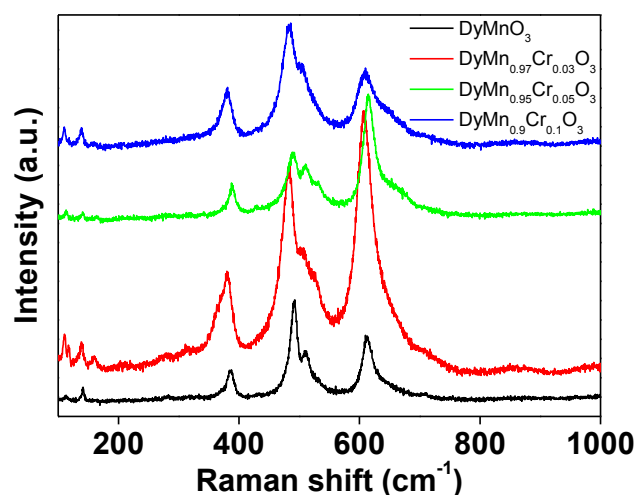


**Figure 5.2.2:** Room temperature Raman spectra of  $\text{DyMn}_{1-x}\text{Cr}_x\text{O}_3$  ( $x=0, 0.03, 0.05, 0.1$ ).

Raman peaks at  $385, 492 \text{ cm}^{-1}$  can be assigned to out-of-plane  $\text{MnO}_6$   $x$  rotation,  $\text{MnO}_6$  bending ( $A_g3$ ) respectively. Out-of-plane  $\text{MnO}_6$   $x$  rotation mode of  $\text{DyMnO}_3$  at  $385 \text{ cm}^{-1}$  shifts to  $380 \text{ cm}^{-1}$  for  $x=0.03, 0.1$  and  $390 \text{ cm}^{-1}$  for  $x=0.05$ .  $\text{MnO}_6$  bending ( $A_g3$ ) mode of  $\text{DyMnO}_3$  at  $492 \text{ cm}^{-1}$  shifts to  $482 \text{ cm}^{-1}$  for  $x=0.03, 0.1$  and  $489 \text{ cm}^{-1}$  for  $x=0.05$ . The trend observed in shift of these two modes are similar in both cases. The softening of Raman mode of  $\text{DyMn}_{1-x}\text{Cr}_x\text{O}_3$  for  $x=0.03, 0.1$  was expected as size of  $\text{Cr}^{+3}$  ion is smaller than  $\text{Mn}^{+3}$  ions. The peak  $\sim 612 \text{ cm}^{-1}$  is due to in-plane O2 stretching ( $B_{2g}1$ ) which is related to Jahn-Teller distortion does not shift of more than  $\pm 3 \text{ cm}^{-1}$ . This is due to the fact that  $\text{Cr}^{+3}$  ion is not Jahn-Teller active.

### 5.2.6 Magnetic study

Figure 5.2.3 shows field-induced metamagnetic transition at 3, 5, 7 and 10 K isothermal magnetization. Below  $\text{Dy}^{+3}-\text{Dy}^{+3}$  interaction, polycrystalline sample of  $\text{DyMnO}_3$  shows field dependent metamagnetic transition [44]. Below a critical field moment increases slowly

followed by a jump after which with increase in field moment increases slowly [44]. At 3 and 5 K,  $\text{DyMn}_{1-x}\text{Cr}_x\text{O}_3$  at ( $x=0.03$ ) showed metamagnetic transition whereas in samples ( $x=0.05$ , 0.1) no metamagnetic transition was observed. At all temperatures,  $\text{DyMn}_{1-x}\text{Cr}_x\text{O}_3$  at ( $x=0.03$ ) shows higher moment value than  $\text{DyMnO}_3$ . At 7 and 10 K, which is above  $\text{Dy}^{+3}$ - $\text{Dy}^{+3}$  antiferromagnetic interaction, no metamagnetic transition was observed in all the sample.

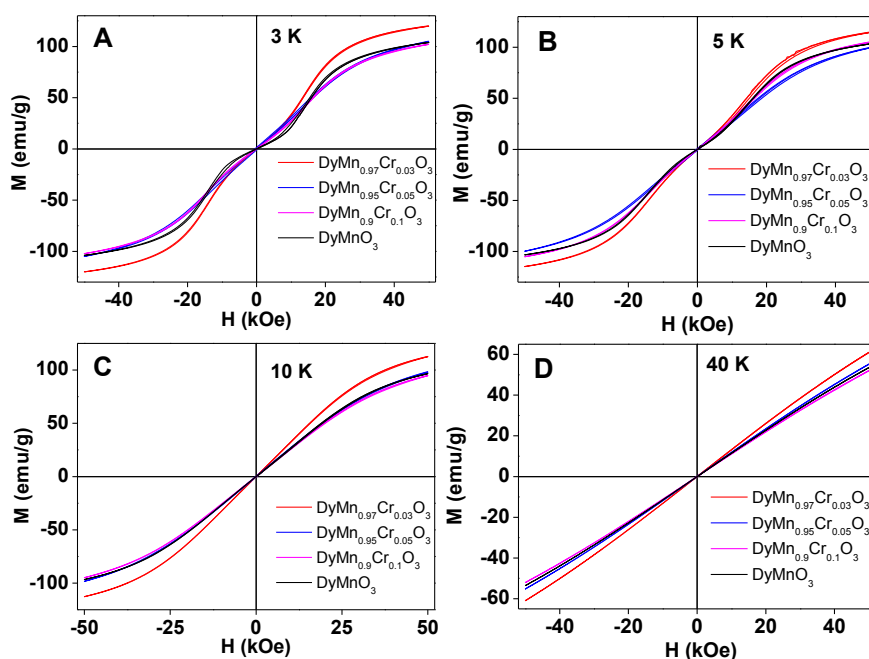


**Figure 5.2.3:** Magnetization as a function of applied field for orthorhombic  $\text{DyMn}_{1-x}\text{Cr}_x\text{O}_3$  ( $x=0, 0.03, 0.05, 0.1$ ) at A) 3 K, B) 5 K, C) 10 K and D) 40 K.

Temperature dependence of magnetization of  $\text{DyMn}_{1-x}\text{Cr}_x\text{O}_3$  at ( $x=0.03, 0.5, 0.1$ ) is shown in figure 5.2.4. With  $\text{Cr}^{+3}$  doping the bifurcation of ZFC–FC magnetization curves increases but with increasing doping the bifurcation temperature decreases. The decrease in bifurcation temperature of ZFC–FC magnetization curves with  $\text{Cr}^{+3}$  doping in  $\text{Mn}^{+3}$  site shows weakening of ordering strength of  $\text{Mn}^{+3}$  with  $\text{Cr}^{+3}$  ions. As the size of  $\text{Cr}^{+3}$  ion is less than  $\text{Mn}^{+3}$  ions, the introduction of  $\text{Cr}^{+3}$  ions in lattice does not give stress to the structure. In

$\text{DyCrO}_3$ ,  $\text{Cr}^{+3}$  ordering temperature is  $\sim 156$  K, but in  $\text{DyMn}_{1-x}\text{Cr}_x\text{O}_3$ , B-site ordering temperature decreases which can be due to combined effect of  $\text{Mn}^{+3}\text{--Mn}^{+3}$  and  $\text{Mn}^{+3}\text{--Cr}^{+3}$  interaction. With increasing  $\text{Cr}^{+3}$  doping in  $\text{Mn}^{+3}$  site, weakening strength of B-site ordering is due to weaker strength of  $\text{Mn}^{+3}\text{--Cr}^{+3}$  than  $\text{Mn}^{+3}\text{--Mn}^{+3}$ . With  $\text{Cr}^{+3}$  doping in  $\text{Mn}^{+3}$  site,  $\text{Dy}^{+3}\text{--Dy}^{+3}$  ordering temperature decreases. The decrease of  $\text{Dy}^{+3}\text{--Dy}^{+3}$  ordering temperature with  $\text{Cr}^{+3}$  doping in  $\text{Mn}^{+3}$  site shows that B-site also influence the ordering of R-site.

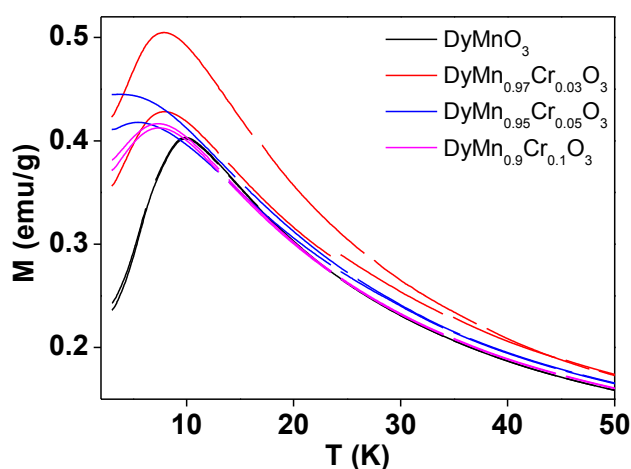


**Figure 5.2.4:** ZFC–FC magnetization curves for orthorhombic  $\text{DyMn}_{1-x}\text{Cr}_x\text{O}_3$  ( $x=0, 0.03, 0.05, 0.1$ ) at 200 Oe applied field.

No signature of  $T_N$  was observed in real part of ac magnetization in all samples. A hump was observed below 10 K, signature of  $\text{Dy}^{+3}\text{--Dy}^{+3}$  interaction in real part of ac magnetization.  $\text{Dy}^{+3}\text{--Dy}^{+3}$  interaction temperature does not change with  $x=0.03$  whereas, for  $x=0.05, 0.1$  interaction temperature decreased to 7.5 K in comparison to 8.5 K for  $x=0$  and 0.03. This decrease of ordering temperature of  $\text{Dy}^{+3}\text{--Dy}^{+3}$  interaction with  $\text{Cr}^{+3}$  doping in  $\text{Mn}^{+3}$  site shows possible interaction of  $\text{Dy}^{+3}$  with  $\text{Mn}^{+3}$  in  $\text{DyMnO}_3$ .

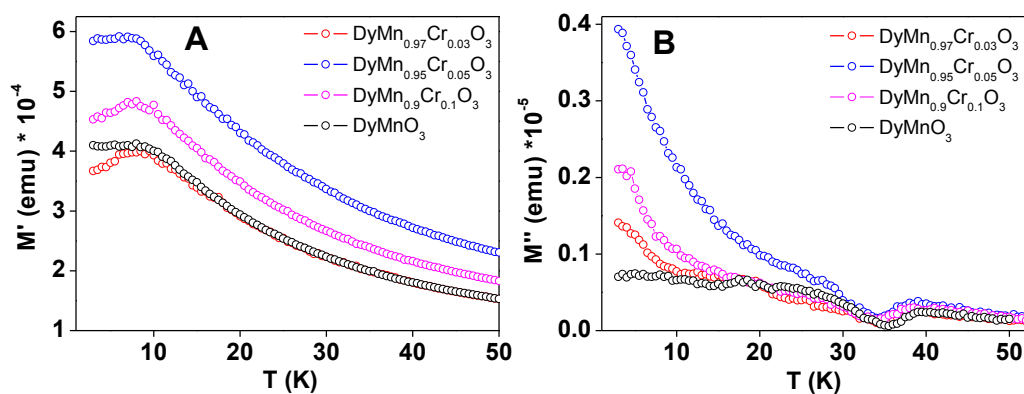


**Figure 5.2.5:** Temperature dependence of A) Real part and B) imaginary part of ac magnetization at ac field of 5 Oe and frequency 751 Hz.

Imaginary part of ac magnetization clearly showed the decrease of  $T_N$  with  $\text{Cr}^{+3}$  doping in  $\text{Mn}^{+3}$  site which was seen dc magnetization as weakening of B-site interaction. Hump in imaginary part of ac magnetization,  $T_N$  for  $\text{DyMnO}_3$  is  $\sim 39$  K which slightly decreases with  $\text{Cr}^{+3}$  doping in  $\text{Mn}^{+3}$  site to  $\sim 38.5, 38, 37$  K for  $x=0.3, 0.5, 0.1$   $\text{DyMn}_{1-x}\text{Cr}_x\text{O}_3$  respectively. The reason for this decrease in B-site ordering temperature is discussed above.

### 5.2.7 Conclusion

We have synthesized single phase orthorhombic  $\text{DyMn}_{1-x}\text{Cr}_x\text{O}_3$  ( $x=0.03, 0.05, 0.1$ ) by solid-state reaction route. With increase  $\text{Cr}^{+3}$  doping in  $\text{Mn}^{+3}$  site of  $\text{DyMnO}_3$ , the  $T_N$  decreased. The ordering temperature of  $\text{Dy}^{+3}-\text{Dy}^{+3}$  interaction decreased with  $\text{Cr}^{+3}$  doping in  $\text{Mn}^{+3}$  site shows possible interaction of R and B-site in  $\text{DyMnO}_3$ .

---

### 5.3 References

- [1] Yakel, H. L.; Koehler, W. C.; Bertaut, E. F.; Forrat, E. F. *Acta Crystallogr.* **1963**, *16*, 957.
- [2] Waintal, A.; Chenavas, J.; Seances, C. R. *Acad. Sci., Ser. B* **1967**, *264*, 168.
- [3] M. A. Gilleo, *Acta Crystallogr.* **1957**, *10*, 161.
- [4] Moussa, F.; Hennion, M.; Rodriguez-Carvajal, J.; Moudden, H.; Pinsard, L.; Revcolevschi, A. *Phys. Rev. B* **1996**, *54*, 15 149.
- [5] Rao, C.N.R.; Serrao, C. R. *J. Mater. Chem.* **2007**, *17*, 4931.
- [6] Chakrabortya, K. R.; Yusufa, S.M.; Tyagi, A. K. *J. Magn. Magn. Mater.* **2008**, *320*, 1163.
- [7] Sahu, J. R.; Ghosh, A.; Sundaresan, A.; Rao, C. N. R. *Mater. Res. Bull.* **2009**, *44*, 2123.
- [8] Uusi-Esko, K.; Malm, J.; Imamura, N.; Yamauchi, H.; Karppinen, M. *Mater. Chem. Phys.* **2008**, *112*, 1029.
- [9] van Aken, B. B.; Palstra, T. T. M. *Phys. Rev. B* **2004**, *69*, 134113.
- [10] van Aken, B. B.; Meetsma, A.; Palstra, T. T. M. *Acta Crystallogr. Sect. C: Cryst. Struct. Commun.* **2001**, *57*, 230.
- [11] Singh, A. K.; Patnaik, S.; Kaushik, S. D.; Siruguri, V. *Phys. Rev. B* **2010**, *81*, 184406.
- [12] Chung-Yuan, R. *Phys. Rev. B* **2009**, *79*, 125113.
- [13] Gao, P.; Chen, Z.; Tyson, T. A.; Wu, T.; Ahn, K. H.; Liu, Z.; Tappero, R.; Kim, S. B.; Cheong, S. W. *Phys. Rev. B* **2011**, *83*, 224113.
- [14] Oleaga, A.; Salazar, A.; Prabhakaran, D.; Cheng, J. G.; Zhou, J. S. *Phys. Rev. B* **2012**, *85*, 184425.

- 
- [15] Kleemann, W.; Borisov, P. *Smart Materials for Energy, Communications and Security NATO Science for Peace and Security Series B: Physics and Biophysics* 2008, 3.
- [16] Eerenstein, W.; Mathur, N. D.; Scott, J. F. *Nature* **2006**, 442,759.
- [17] Rado, G. T.; Folen, V. J. *Phys. Rev. Lett.* **1961**, 7, 310.
- [18] Astrov, D. N. *JETP* **1960**, 11, 708–709.
- [19] Gajek, M.; Bibes, M.; Fusil, S.; Bouzehouane, K.; Fontcuberta, J.; Barthélémy, A. Fert, A. *Nature Mater.* **2007**, 6, 296.
- [20] Noguès, J.; Schuller, I. K. *J. Magn. Magn. Mater.* **1999**, 192, 203.
- [21] Binek, C.; Hochstrat, A.; Chen, X.; Borisov, P.; Kleemann, W. *J. Appl. Phys.* **2005**, 97, 10C514.
- [22] Binek, C.; Doudin, B. *J. Phys.: Cond. Matter* **2005**, 17, L39.
- [23] Mostovoy, M. *Phys. Rev. Lett.* **2006**, 96, 067601.
- [24] Kenzelmann, M.; Harris, A. B.; Jonas, S.; Broholm, C.; Schefer, J.; Kim, S. B.; Zhang, C. L.; Cheong, S. W.; Vajk, O. P.; Lynn, J. W. *Phys. Rev. Lett.* **2005**, 95, 087206.
- [25] Plumer, M. L.; Walker, M. B. *J. Phys. C-Solid State Phys.* **1982**, 15, 7181.
- [26] Walker, M. B. *Phys. Rev. B* **1980**, 22, 1338.
- [27] Kimura, T.; Goto, T.; Shintani, H.; Ishizaka, K.; Arima, T.; Tokura, Y. *Nature* **2003**, 426, 55.
- [28] Feyerherm, R.; Dudzik, E.; Aliouane, N.; Argyriou, D. N. *Phys. Rev. B* **2006**, 73, 180401.
- [29] Pimenov, A.; Mukhin, A. A.; Ivanov, V. Y.; Travkin, V. D.; Balbashov, A. M.; Loidl, A. *Nat. Phys.* **2006**, 2, 97.

- 
- [30] Kimura, T.; Lawes, G.; Goto, T.; Tokura, Y.; Ramirez, A. P. *Phys. Rev. B* **2005**, *71*, 224425.
- [31] Ribeiro, J. L. *Phys. Rev. B* **2007**, *76*, 144417.
- [32] Arima, T.; Goto, T.; Yamasaki, Y.; Miyasaka, S.; Ishii, K.; Tsubota, M.; Inami, T.; Murakami, Y.; Tokura, Y. *Phys. Rev. B* **2005**, *72*, 100102(R).
- [33] Kadomtseva, A. M.; Popov, Y. F.; Vorob'ev, G. P.; Kamilov, K. I.; Pyatakoy, A. P.; Ivanov, V. Y.; Mukhin, A. A.; Balbashov, A. M. *Jetp. Lett.* **2005**, *81*, 19.
- [34] Pimenov, A.; Rudolf, T.; Mayr, F.; Loidl, A.; Mukhin, A. A.; Balbashov, A. M. *Phys. Rev. B* **2006**, *74*, 100403(R).
- [35] Ferreira, W. S.; Moreira, J. A.; Almeida, A.; Chaves, M. R.; Araujo, J. P.; Oliveira, J. B.; Da Silva, J. M. M.; Sa, M. A.; Mendonca, T. M.; Carvalho, P. S.; Kreisel, J.; Ribeiro, J. L.; Vieira, L. G.; Tavares, P. B.; Mendonca, S. *Phys. Rev. B* **2009**, *79*, 054303.
- [36] Kimura, T.; Ishihara, S.; Shintani, H.; Arima, T.; Takahashi, K. T.; Ishizaka, K.; Tokura, Y. *Phys. Rev. B* **2003**, *68*, 060403(R).
- [37] Iliev, M. N.; Abrashev, M. V.; *J. Raman Spectrosc.* **2001**, *32*, 805.
- [38] Iliev, M. N.; Abrashev, M. V.; Laverdière, J.; Jandl, S.; Gospodinov, M. M.; Wang, Y.-Q.; Sun, Y.-Y. *Phys. Rev. B* **2006**, *73*, 064302.
- [39] Iliev, M. N.; Abrashev, M. V.; Lee, H.-G.; Popov, V. N.; Sun, Y. Y.; Thomsen, C.; Meng, R. L.; Chu, C. W. *Phys. Rev. B* **1998**, *57*, 2872.
- [40] Rao, G. V. S.; Chandrashekhar, G. V.; Rao, C. N. R. *Solid State Commun.* **1968**, *6*, 177.
- [41] Naish, V. E.; Turov, E. A. *Fiz. Met. Metalloved.* **1961**, *11*, 321.
- [42] Bertaut, E. F. *Treatise in Magnetism Vol. III*, eds. Rado, G. T.; Shull, H.; Academic press, New York, **1963**, 149.
- [43] Yamaguchi, T. *J. Phys. Soc. Jpn.* **1975**, *38*, 1270.
- [44] Midya, A.; Das, S. N.; Mandal, P. *Phys. Rev. B* **2011**, *84*, 235127.
-



## **Chapter 6. Conclusion and future prospective**

---

This chapter presents the conclusive remarks and the salient features of the work described in the thesis. The scope for future potential developments in this field are also presented.

---

## 6.1 Conclusion

Multiferroics are rare because of the criteria for existence of electric and magnetic ordering are uncorrelated. Nano-size effects on both magnetic and ferroelectric property are subject of interest in recent studies due to their potential application in memory devices. Report on Verwey transition in chemically synthesized  $\text{Fe}_3\text{O}_4$  nanoparticles (6–8 nm) and similarly FE-PE transition in  $\text{BaTiO}_3$  nanoparticles (5–6 nm) drew large attention for the investigation of size dependent properties of multiferroic materials. Park *et al.* have reported that, below 100 K nanosized  $\text{BiFeO}_3$  exhibits sizable hysteresis and finite coercivity. Ferromagnetic ordering in nano-sized  $\text{BiFeO}_3$  (< ~62 nm) is observed due to breaking of helical ordering or incomplete rotation of spins along the AFM axis which gives rise to net magnetization. The reduction in particle size below the periodicity of helical ordering gives rise to the suppression of modulated spin structure, which improves the magnetization in nanoscale particles. There are very few reports on the size dependent multiferroic property of rare-earth manganites, due to the challenges associated with the synthetic chemistry, as high temperature calcination is required to form these phases. Several compounds from rare-earth manganites,  $\text{RMnO}_3$  (R=rare-earth ion) family are believed to show multiferroic properties. However, the size dependent magnetic properties remain underexplored due to the challenges associated in their wet chemical synthesis with an appropriate control over crystalline phase.

The objective of this thesis is to study the size and morphology dependent magnetic property of rare-earth manganites in nano dimension. We have developed a modified hydrothermal method for the synthesis of nanocrystalline rare-earth manganites. Our study clearly showed size and morphology dependent magnetic property of rare-earth manganites in nano-dimension. The highlights of the study are discussed below.

In this work, hexagonal  $\text{RMnO}_3$  (R=Er, Y, Yb, Lu) nanoparticles were synthesized by modified hydrothermal method. Signatures of  $T_N$  were observed  $\sim 69$  and  $\sim 82$  K respectively for  $\text{ErMnO}_3$  and  $\text{YMnO}_3$  nanoparticles as peak in derivative of real part of ac magnetization. Magnetic measurements revealed that triggering of  $\text{Er}^{+3}$  (4b) spin ordering by  $\text{Mn}^{+3}$  spins at  $T_N$  could be suppressed by an external magnetic field  $\geq 1500$  Oe. The bifurcation of ZFC–FC magnetization curves below  $\sim 40$  and  $\sim 20$  K for  $\text{ErMnO}_3$  and  $\text{YMnO}_3$  nanoparticles, respectively were attributed to the spin-reorientation of  $\text{Mn}^{+3}$  spins due to DM interactions. The hump at  $\sim 8$  and  $\sim 10$  K in ZFC–FC magnetization curves and real part of ac-magnetization curves respectively, for  $\text{YMnO}_3$  nanoparticles could be due to AFM ordering of  $\text{Mn}^{+3}$  spins in *ab*-plane. Temperature dependent dielectric spectroscopy showed anomaly at  $T_N$  for both  $\text{ErMnO}_3$  and  $\text{YMnO}_3$  nanocrystals indicating the presence of ME coupling.

We demonstrated a new method for the morphology-controlled synthesis of  $\text{YbMnO}_3$  by complete ionic control without the use of surfactant or template. Single crystalline nanorods, nanoplates of  $\text{YbMnO}_3$  synthesis were successfully achieved by ionic chemistry. Role of chloride and nitrate ions as structure directing agent for the formation of  $\text{YbMnO}_3$  nanorods and nanoplates, respectively were studied. We have shown morphology dependent magnetic property of  $\text{YbMnO}_3$  nanoparticles. Magnetic measurements showed presence of ferromagnetic interaction between  $\text{Mn}^{+3}$  and  $\text{Yb}^{+3}$  moments below  $\sim 35$  K in  $\text{YbMnO}_3$  nanorods.

As per our knowledge, we have reported first wet chemical synthesis of hexagonal  $\text{LuMnO}_3$  nanoparticles by modified hydrothermal method. Room temperature Raman spectroscopy data was consistent with the calculated values of isomorphous hexagonal  $\text{RMnO}_3$  (R=rare-earth atom) compounds with  $P6_3cm$  symmetry. Room temperature UV-vis-NIR spectra recorded in diffused reflectance mode showed electronic transitions at 1.7 eV (729 nm), 2.3 eV (539 nm) and 5 eV (258 nm), which are unique for hexagonal phase of

RMnO<sub>3</sub> compounds. We observed two unique and field dependent magnetic anomalies ~44, 12 K in M–T curve. The first anomaly is observed as a sharp bifurcation in ZFC–FC magnetization curves below 44 K at 100 Oe applied field which is accompanied with a sudden rise in the coercivity and magnetization. Second transition is observed at 12 K as a sharp peak in ZFC magnetization curves which is accompanied with a dip in coercivity. We attribute the transition at 44 K to the reorientation of the Mn<sup>+3</sup> ions due to DM interaction and transition at 12 K is explained by weak AFM coupling between Mn–O–Mn in *ab* plane which becomes dominant at lower temperature.

We reported for the first time, synthesis of orthorhombic EuMnO<sub>3</sub> nanoparticles. Large exchange bias was observed below ICAFM to cAAFM (~43 K) transition. On the basis of field cooled M–H loop measurements, it was proposed that coupling between antiferromagnetic core and uncompensated ferromagnetic surface spins of nanoparticles is responsible for exchange bias. Reduction in thermal hysteresis between field cooling and heating magnetization curve is observed in nanocrystallite (~1 K) as compare to bulk phase (~3 K) of EuMnO<sub>3</sub>. The reason for this reduction in width of thermal hysteresis could be due to the contribution from surface disorder spins over bulk spins.

Study on nanoparticles of DyMnO<sub>3</sub> and GdMnO<sub>3</sub> synthesized by modified hydrothermal method showed that interesting magnetic properties of its intrinsic bulk form is retained in its nano-dimension. Room temperature Raman spectra of DyMnO<sub>3</sub> nanoparticles showed, symmetric and the antisymmetric or Jahn-Teller stretching mode involving Mn–O bond stretching and also showed tilt and out of phase bending of MnO<sub>6</sub>. TEM measurements clearly showed that, the edge of the nanoparticles does not have any defects. Unlike the previous report by Wang *et al.* on ~52 nm GdMnO<sub>3</sub> nanoparticles where authors observed the opening of hysteresis loop below 10 K, we observed opening of hysteresis loop around 40 K, which could be due to the effect of particle size (35–45 nm). Detail magnetic study of

---

DyMnO<sub>3</sub> nanoparticles showed that the anomaly at 43 K (bifurcation of ZFC–FC magnetization curves) and 7 K (peak in ZFC magnetization curves) in the M–T curves can be attributed to the ordering of Mn<sup>+3</sup> moments and antiferromagnetic interaction between the Dy<sup>+3</sup> ions, respectively. GdMnO<sub>3</sub> nanoparticles showed transitions at 42, 22 and 6 K which can be attributed to the phase transition from PM to an ICAFm, is the transition from ICAFm into a cAAFm of the Mn<sup>+3</sup> spins and magnetic ordering of Gd<sup>+3</sup> moments, respectively. We observed that ac-magnetization does not show any anomaly both in real and imaginary part of magnetization near T<sub>N</sub> for DyMnO<sub>3</sub> and GdMnO<sub>3</sub> nanoparticles.

Recently gigantic ME effect was reported in TbMnO<sub>3</sub>, which makes this material interesting to study in nano form for its application. Modified hydrothermal method was used for the synthesis TbMnO<sub>3</sub>. The room temperature Raman spectroscopy data of nano and micron size orthorhombic TbMnO<sub>3</sub> particles showed that, there is softening in the Raman modes in micron sized particles due to decrease in the lattice distortion. Room temperature XPS study showed partial conversion of Mn<sup>+3</sup> to Mn<sup>+4</sup> in micron sized particles which can be due to formation of Tb<sup>+3</sup> deficient shell. We observed that, the presence of Mn<sup>+4</sup> in micron-sized particles, enhances magnetic interaction which was observed as the increase of ZFC–FC magnetization curves bifurcation temperature. The anomaly near 27 K, corresponding to the incommensurate-commensurate (lock-in) transition was not observed in nano sized particles but seen in micron sized particles, probably due to the decrease in the lattice distortion after longer annealing period at higher temperature.

## 6.2 Future prospective

Synthesis of rare-earth manganites is challenging as high temperature annealing is required to form these phases. There is no report on the size and morphology controlled synthesis of  $\text{RMnO}_3$  (R=rare-earth ions) compounds. There is an enormous need for the development of synthesis method, which can be used for the synthesis of wide range of rare-earth manganites. Hydrothermal method used in this thesis can be a potential method for the synthesis of  $\text{RMnO}_3$  compounds but poor control over particle size and morphology can be subject of future study. Sol-gel method can also be used for the synthesis of rare-earth manganites, but control of particle size and morphology is challenging.

Temperature dependent Raman spectroscopy will be able to probably explain the origin of anomalies at  $\sim 40$  and  $20$  K for  $\text{ErMnO}_3$  and  $\text{YMnO}_3$  nanoparticles, respectively which we attributed to spin reorientation of  $\text{Mn}^{+3}$  spins due to DM interactions. Temperature dependent neutron diffraction studies in the presence magnetic field will reveal the triggering mechanism of  $\text{Er}^{+3}$  (4b) spins ordering by  $\text{Mn}^{+3}$  spins at  $T_N$ .

Comparison of the lattice constants of three  $\text{YbMnO}_3$  samples (nanorods/nanoplates/bulk) as well as spin-polarized neutron measurements will explain the origin of morphology dependent magnetic property. High resolution XRD studies will give more insight into the structure and distortion of nanorods, nanoplates and bulk  $\text{YbMnO}_3$  particles.

Low-temperature Raman and dielectric investigations will further confirm the origin of the anomalies seen below  $T_N$  in  $\text{LuMnO}_3$  nanoparticles and possible phonon-magnon coupling.

The proposed mechanism for the origin of exchange bias in  $\text{EuMnO}_3$  nanoparticles, where AFM systems may show uncompensated spins at surface leading to core-shell

---

structure at low temperature where surface uncompensated spins act as ferromagnetic layer. This theory is subjected for a careful neutron scattering studies to prove the thickness of magnetic roughening. Spin-polarized neutron scattering experiments on this system will give more insight into the problem. The reduction of width of thermal hysteresis in  $\text{EuMnO}_3$  nanoparticles is not understood completely. Particle size dependent study will give more interesting results.

High-resolution TEM and XPS study on surface of  $\text{TbMnO}_3$  nanoparticles will give an idea of the effect of annealing on its magnetic property. Angle dependent XPS using hard synchrotron x-rays will give depth dependent oxidation states of  $\text{Mn}^{+3}$  ions, which in-turn will give more insight into core-shell structure of nanoparticles.

Why some rare-earth manganites do not show signature of  $T_N$  in dc and ac  $M-T$ , is not clear so far. AC magnetization is more sensitive to probe magnetic anomaly, but we observed that in many cases of rare-earth manganites ,it does not give signature of  $T_N$ . We could not understand the possible reason behind the absence of anomaly near  $T_N$  in ac magnetization in some of rare-earth manganites which were observed in dc magnetization. This could be a topic of future study.

In this thesis we have studied mostly the size and morphology dependent magnetic properties but study of dielectric property and electrical polarization as a function of temperature and electric field can answer many unanswered questions. There are very few reports on temperature dependent Neutron study of nano-dimensional  $\text{RMnO}_3$ . Detailed neutron diffraction study can solve many mysteries of size and morphology dependent magnetic structure of rare-earth manganites. There is a need to do high-resolution X-ray photoelectron spectroscopy to characterize the surface of nanoparticles of  $\text{RMnO}_3$ . This study will answer the origin of surface FM in AFM systems.

## Appendix I

---

### List of Publications (categorized by research area):

#### Multiferroics

(1) “Effect of Reduced Particle Size on the Magnetic Properties of Chemically Synthesized BiFeO<sub>3</sub> Nanocrystals” Adhish Jaiswal, **Raja Das**, K. Vivekanand, Priya Mary Abraham, Suguna Adyanthaya and Pankaj Poddar\*, *J. Phys. Chem. C* 2010, 114, 2108-2115.

DOI: [10.1021/jp910745g](https://doi.org/10.1021/jp910745g)

(2) “Temperature-Dependent Raman and Dielectric Spectroscopy of BiFeO<sub>3</sub> Nanoparticles: Signatures of Spin-Phonon and Magnetoelectric Coupling” Adhish Jaiswal<sup>^</sup>, **Raja Das**<sup>^</sup>, Tuhin Maity, K. Vivekanand, Suguna Adyanthaya, and Pankaj Poddar\* *J. Phys. Chem. C* 2010, 114, 12432-12439. (<sup>^</sup> A.J. and R.D. contributed equally to the work) DOI:

[10.1021/jp102450z](https://doi.org/10.1021/jp102450z)

(3) “Origin of Magnetic Anomalies below the Neel Temperature in Nanocrystalline LuMnO<sub>3</sub>” **Raja Das**, Adhish Jaiswal, Suguna Adyanthaya, and Pankaj Poddar\* *J. Phys. Chem. C* 2010, 114, 12104-12109. DOI: [10.1021/jp103037r](https://doi.org/10.1021/jp103037r)

(4) “Grain growth related effect on spin and phonon behavior in TbMnO<sub>3</sub> nanoparticles” **Raja Das**, Adhish Jaiswal, Suguna Adyanthaya, Pankaj Poddar\* *J. Appl. Phys.*, 2011 109, 064309. DOI: [10.1063/1.3563571](https://doi.org/10.1063/1.3563571)

(5) “Static and dynamic magnetic properties and interplay of Dy<sup>3+</sup>, Gd<sup>3+</sup> and Mn<sup>3+</sup> spins in orthorhombic DyMnO<sub>3</sub> and GdMnO<sub>3</sub> nanoparticles” **Raja Das**, Adhish Jaiswal, and Pankaj Poddar\* *J. Phys. D: Appl. Phys.* 2013, 45, 045301. DOI: [10.1088/0022-3727/46/4/045301](https://doi.org/10.1088/0022-3727/46/4/045301)

(6) “Magnetic and dielectric properties and Raman spectroscopy of GdCrO<sub>3</sub> nanoparticles” Adhish Jaiswal, **Raja Das**, K. Vivekanand, Tuhin Maity, Priya Mary Abraham, Suguna Adyanthaya, and Pankaj Poddar\* *J. Appl. Phys.* 2010, 107, 013912. DOI: [10.1063/1.3275926](https://doi.org/10.1063/1.3275926)

(7) “Synthesis and optical studies of GdCrO<sub>3</sub> nanoparticles” Adhish Jaiswal, **Raja Das**, Suguna Adyanthaya, Pankaj Poddar\* *J Nanopart Res*, 2010, 13, 1019. DOI: [10.1007/s11051-010-0090-4](https://doi.org/10.1007/s11051-010-0090-4)



- (8) "Surface Effects on Morin Transition, Exchange Bias and Enhanced Spin Reorientation in Chemically Synthesized  $DyFeO_3$  nanoparticles" Adhish Jaiswal, **Raja Das**, Suguna Adyanthaya and Pankaj Poddar\* *J. Phys. Chem. C*, 2011, 115, 2954. DOI: [10.1021/jp109313w](https://doi.org/10.1021/jp109313w)
- (9) "Dielectric and spin relaxation behaviour in  $DyFeO_3$  nanocrystals" Adhish Jaiswal, **Raja Das**, Tuhin Maity, and Pankaj Poddar\* *J. Appl. Phys.* 2011, 110, 124301. DOI: [10.1063/1.3669154](https://doi.org/10.1063/1.3669154)
- (10) "Observation of enhanced dielectric coupling and room temperature ferromagnetism in chemically synthesized  $BiFeO_3@SiO_2$  core-shell particles" Mandar M Shirolkar, **Raja Das**, Tuhin Maity, Pankaj Poddar, and Sulabha K. Kulkarni *J. Phys. Chem. C*, 2012, 116, 19503-19511. DOI: [10.1021/jp3025683](https://doi.org/10.1021/jp3025683)
- (11) "Static and dynamic magnetic properties and effect of surface chemistry on the morphology and crystallinity of  $DyCrO_3$  nanoplatelets" Preeti Gupta, Richa Bhargava, **Raja Das**, Pankaj Poddar *RSC Adv.* 2013, 3, 26427-26432. DOI: [10.1039/C3RA43088J](https://doi.org/10.1039/C3RA43088J)
- (12) "Observation of exchange bias below incommensurate antiferromagnetic (ICAFM) to canted A-type antiferromagnetic (cAAFM) transition in nanocrystalline orthorhombic  $EuMnO_3$ " **Raja Das**, and Pankaj Poddar (*RSC Adv.* 2014, 4, 10614-10618. DOI: [10.1039/C3RA45435E](https://doi.org/10.1039/C3RA45435E)).
- (13) "Ionic control on the morphology of ytterbium manganese oxide nanorods and nanoplates in a surfactant-free synthesis and their magnetic properties" **Raja Das**, and Pankaj Poddar\*(accepted *J. Phys. Chem. C*).
- (14) "Magnetic and dielectric study of nanocrystalline hexagonal  $ErMnO_3$  and  $YMnO_3$ " **Raja Das**, and Pankaj Poddar\*(communicated).

---

### Rare-earth-free Hard Magnet

- (15) "Colossal increase in energy product of  $Fe_3Se_4$  by Fe-site doping" Mousumi Sen Bishwas<sup>^</sup>, **Raja Das**<sup>^</sup>, and Pankaj Poddar\*( *J. Phys. Chem. C* 2014, 118, 4016-4022. DOI: [10.1021/jp411956q](https://doi.org/10.1021/jp411956q)). (<sup>^</sup> M.B.S. and R.D. contributed equally to the work)

(16) "Large Magnetocaloric Effect, Moment, and Coercivity Enhancement after Coating Ni Nanoparticles with Ag" S. Srinath, Pankaj Poddar\*, Raja Das, B. L. V. Prasad, James Gass and Hariharan Srikanth\* (*Chem. Phys. Chem.* accepted DOI: [10.1002/cphc.201300886](https://doi.org/10.1002/cphc.201300886))

-----

### Co-ordination polymer

(17) "Metal and metal oxide nanoparticle synthesis from metal organic frameworks (MOFs): finding the border of metal and metal oxides" **Raja Das**, Pradip Pachfule, Rahul Banerjee\*, Pankaj Poddar\* *Nanoscale*, 2012, 4, 591. DOI: [10.1039/C1NR10944H](https://doi.org/10.1039/C1NR10944H)

(18) "Design and in situ synthesis of a Cu-based porous framework featuring isolated double chain magnetic character" Chandan Dey<sup>^</sup>, **Raja Das**<sup>^</sup>, Binoy Krishna Saha, Pankaj Poddar\* and Rahul Banerjee\* *ChemComm*, 2011. (<sup>^</sup> C.D. and R.D. contributed equally to the work) DOI: [10.1039/C1CC13418C](https://doi.org/10.1039/C1CC13418C)

(19) "Solvothermal Synthesis, Structure, and Properties of Metal Organic Framework Isomers Derived from a Partially Fluorinated Link" Pradip Pachfule, **Raja Das**, Pankaj Poddar and Rahul Banerjee\* *Cryst. Growth Des.* 2011, 11, 1215–1222. DOI: [10.1021/cg101414x](https://doi.org/10.1021/cg101414x)

(20) "Structural and Selective Gas Adsorption Studies of Polyoxometalate and Tris (ethylenediamine) Cobalt(III) Based Ionic Crystals" Chandan Dey, **Raja Das**, Pradip Pachfule, Pankaj Poddar and Rahul Banerjee\* *Cryst. Growth Des.* 2011, 11, 139–146. DOI: [10.1021/cg101201b](https://doi.org/10.1021/cg101201b)

(21) "Structural, Magnetic, and Gas Adsorption Study of a Series of Partially Fluorinated Metal Organic Frameworks (HF-MOFs)" Pradip Pachfule, **Raja Das**, Pankaj Poddar and Rahul Banerjee\* *Inorg. Chem.* 2011, 50, 3855–3865. DOI: [10.1021/ic1017246](https://doi.org/10.1021/ic1017246)

(22) "Structural, Magnetic, and Gas Adsorption Study of a Two-Dimensional Tetrazole-Pyrimidine Based Metal-Organic Framework" Pradip Pachfule, **Raja Das**, Pankaj Poddar, and Rahul Banerjee\* *Cryst. Growth Des.* 2010, 10, 2475–2478. DOI: [10.1021/cg1003726](https://doi.org/10.1021/cg1003726)

(23) "Solid Phase Morphological Diversity of a Rare Vanadium Cubane (V<sub>4</sub>O<sub>16</sub>) Based Metal Organic Framework" Chandan Dey, **Raja Das**, Pankaj Poddar, and Rahul Banerjee\* *Cryst. Growth Des.* 2012, 12, 12–17. DOI: [10.1021/cg201030u](https://doi.org/10.1021/cg201030u)

(24) "Bistable Dynamic Coordination Polymer Showing Reversible Structural and Functional Transformations" Sanjog S. Nagarkar, **Raja Das**, Pankaj Poddar, and Sujit K. Ghosh\* *Inorg. Chem.* 2012, 51, 8317–8321. DOI: [10.1021/ic301481p](https://doi.org/10.1021/ic301481p)

(25) "Synthesis, characterization, and magnetic studies of coordination polymers with Co(II) and Mn(II) ions" Musheer Ahmad, **Raja Das**, Prem Lama, Pankaj Poddar\* and Parimal K. Bharadwaj\* *Cryst. Growth Des.* 2012, 12, 4624-4632. DOI: [10.1021/cg300829c](https://doi.org/10.1021/cg300829c)

(26) "Syntheses, Crystal Structures, and Magnetic Properties of Metal– Organic Hybrid Materials of Co(II) Using Flexible and Rigid Nitrogen- Based Ditopic Ligands as Spacers" Musheer Ahmad, Manish K. Sharma, **Raja Das**, Pankaj Poddar,\* and Parimal K. Bharadwaj\* *Cryst. Growth Des.* 2012, 12, 1571-1578. DOI: [10.1021/cg201619x](https://doi.org/10.1021/cg201619x)

(27) "Inter-Chain Relay of Antiferromagnetic Ordering in 1D Co(II) Coordination Polymers via  $\pi$ - $\pi$  Weak Interactions" Musheer Ahmad, **Raja Das**, Jerzy Mrozinski, Alina Bienko, Pankaj Poddar and Parimal K. Bharadwaj\* (communicated)

(28) "In vitro DNA and HSA binding, pBR322 plasmid cleavage, molecular modeling study of novel Cu(I)–Schiff base complex: Validation of a specific chemotherapeutic agent for human cervical tumor cell line (SiHa)" Sartaj Tabassum,\* Musheer Ahmad, **Raja Das**, Mohd. Afzal, Ruchi Singh, Mehvash Zaki, Pankaj Poddar, Parimal K. Bharadwaj\* (communicated)

-----

## Semiconductors

(29) "Ligand-free one-step synthesis of {001} faceted semiconducting BiOCl single crystals and their photocatalytic activity" Anupam Biswas<sup>^</sup>, **Raja Das**<sup>^</sup>, Chandan Dey, Rahul Banerjee and Pankaj Poddar\*(accepted in *Cryst. Growth Des.*). (<sup>^</sup> A.B. and R.D. contributed equally to the work) DOI: [10.1021/cg4014366](https://doi.org/10.1021/cg4014366)

(30) "Room Temperature Ferromagnetism in undoped and Fe doped ZnO Nanorods: Microwave Assisted Synthesis" Mukta V. Limaye, Shashi B. Singh, **Raja Das**, Pankaj Poddar and Sulabha K. Kulkarni\* *J. Solid State Chem.* 2011,184, 391-400. DOI: [10.1016/j.jssc.2010.11.008](https://doi.org/10.1016/j.jssc.2010.11.008)

(31) "Investigations of magnetic and dielectric properties of cupric oxide nanoparticles" Rohini S. Bhalerao-Panajkar, Mandar M. Shirolkar, **Raja Das**, Tuhin Maity, Pankaj Poddar

and S.K. Kulkarni\* *Solid State Communications* 2011, 151, 55–60.  
DOI: [10.1016/j.ssc.2010.10.024](https://doi.org/10.1016/j.ssc.2010.10.024)

-----

**Biophysics/chemistry (enzyme, Raman spectroscopy)**

(32) "*Mechanistic Study of Surface Functionalization of Enzyme –Lysozyme Synthesized Ag and Au Nanoparticles Using Surface Enhanced Raman Spectroscopy*" **Raja Das**, Ramya Jagannathan, Chandrashekhar Sharan, Umesh Kumar, Pankaj Poddar\*, *J. Phys. Chem. C* 2009, 113, 21493–21500. DOI: [10.1021/jp905806t](https://doi.org/10.1021/jp905806t)

(33) "*Attomolar Detection of D-glucose and TNT using Self -assembled Vertically Aligned Gold Nanorods by Solvent Evaporation*" Amey Apte, Prashant Bhaskar, **Raja Das**, Smita Chaturvedi, Pankaj Poddar and Sulabha Kulkarni (*communicated*)